An *ab initio* approach to modelling time-dependent cosmic-ray modulation in the heliosphere

KD Moloto

orcid.org 0000-0002-4840-6355

Thesis accepted in fulfilment of the requirements for the degree *Doctor of Philosophy in Space Physics* at the North-West University

Promoter: Prof NE Engelbrecht

Co-promoter: Prof RA Burger

Graduation December 2020

20661533

Acknowledgements

I would like to thank:

- My supervisors, Prof N. E. Engelbrecht and Prof R. A. Burger, for the expert guidance, motivation, and the patient support they have showed throughout this study.
- My nGAP mentor Prof R. D. Strauss, for all the discussions on how to become a better academic.
- Mary Vorster, for checking my language and grammar.
- Mrs Petro Sieberhagen (Mama Petro) for handling all my financial inquiries most efficiently.
- My family and friends, for all the support.
- The NRF. This work is based on the research supported in part by the National Research Foundation of South Africa (Grant Number 121920). Opinions expressed and conclusions arrived at are those of the author and are not necessarily to be attributed to the NRF.
- The Centre for High Performance Computing (CHPC) in South Africa for providing computational resources for this study.
- The Department of Higher Education and Training (DHET) and the new Generation of Academics Programme (nGAP) that has enabled me to pursue a career in academics.

Katlego Daniel Moloto
Centre for Space Physics, North-West University,
Potchefstroom Campus,
2520, South Africa

Abstract

The *ab initio* approach to cosmic ray modulation places a strong, primary emphasis on understanding the basic causes of cosmic-ray modulation. This requires knowledge and an understanding of both the large and small-scale structure of the heliosphere. A key part of this is understanding lies in how turbulence influences cosmic-ray modulation over the solar-cycle. Our understanding of the role of turbulence in cosmic-ray modulation has now reached a level where we can provide some answers to the questions of how various turbulence quantities that govern diffusion and drift in the heliosphere influence cosmic-ray modulation over time scales associated with the solar activity cycle and the solar magnetic cycle. The present study presents a three-dimensional, time-dependent, *ab initio* cosmic ray modulation model, developing this code from an effective-value steady-state approach to full time-dependence, in the process fully characterising the numerical complexities implicit to this process. In such a model, scattering and drift coefficients are required that depend realistically on turbulence input quantities such as magnetic variances and correlation scales. These are scaled both spatially and temporally following observations of these quantities, and using parametric fits to results computed from state-of-the art two-component turbulence transport models. Large-scale heliospheric quantities such as the solar wind speed, heliospheric magnetic field magnitude, and tilt angle are also modelled using observationally-motivated solar cycle and spatial dependences. The time-evolution of the wavy current sheet also plays a key role in the solar-cycle dependent modulation of cosmic rays, and is here for the first time implemented with its fully three-dimensional and time-dependent structure in a time-dependent modulation model. The end result of this study is the most realistic solar-cycle dependent three-dimensional cosmic-ray modulation model to date, that is able to self-consistently reproduce the major salient features of the observed cosmic ray intensity temporal profiles. A better understanding of the primary drivers of cosmic-ray modulation over decadal time-scales also leads to a better understanding of how intensities could vary over time-scales of centuries, as is here demonstrated. These insights are essential to being able to reliably predict future cosmic ray intensities, as meaningful extrapolations can only be done by modelling the fundamental physics in a self-consistent manner.

Keywords: Cosmic ray modulation, current sheet, diffusion, drift, turbulence

Acronyms and Abbreviations

The acronyms and abbreviations used in the text are listed below. For the purposes of clarity, any such usages are written out in full when they first appear.

3D	three-dimensional
ACR	anomalous cosmic-rays
au	astronomical unit
CHPC	Center for High Performance Computing
CIR	corotating interaction region
CR	cosmic-ray
GCR	galactic cosmic-ray
HCS	heliospheric current sheet
HMF	heliospheric magnetic field
HP	heliopause
ICME	interplanetary coronal mass ejection
MHD	magnetohydrodynamic
MIR	merged interaction region
NLGC	nonlinear guiding centre
SDE	stochastic differential equation
TPE	transport equation
TS	termination shock
V1	Voyager 1 spacecraft
V2	Voyager 2 spacecraft

Declaration by co-authors

This thesis has been written in accordance with the article format style as prescribed by North-West University. The articles are in published format, with the structure and style according to the author instructions of the specific journals. The co-authors of the article(s) listed bellow hereby give consent that K.D Moloto may submit this work as part of his thesis.

- Moloto, K. D.; Engelbrecht, N. E.; Burger, R. A. A Simplified Ab Initio Cosmic-ray Modulation Model with Simulated Time Dependence and Predictive Capability. The Astrophysical Journal, Volume 859, Issue 2, p. 12, (2018).
- Moloto, K. D.; Engelbrecht, N. E.; Strauss, R. D.; Moeketsi, D. M.; van den Berg, J. P. Numerical integration of stochastic differential equations: A parallel cosmic ray modulation implementation on Africa's fastest computer. Advances in Space Research, Volume 63, Issue 1, p. 626-639, (2019).
- Moloto, K. D.; Engelbrecht, N. E. Towards a fully time-dependent cosmic-ray modulation Model. To be submitted to: The Astrophysical Journal, (2020).

Engelbrecht, N. E.		Date 22/01/2020
Burger, R. A.		Date 28/01/2020
Strauss, R. D.		Date 22/01/2020
Moeketsi, D. M.		Date 22/01/2020
van den Berg, J. P.		Date 2020-01-22

Contents

CHAPTER 1

Introduction

THE subject of this study is the development and implementation of a fully time-dependent *ab initio* galactic cosmic-ray (CR) model. Due the complexity implicit to taking an *ab initio* approach to modelling the various processes involved in CR transport and modulation, such a project also requires a fully three-dimensional and energy-dependent treatment of the Parker (1965) CR transport equation (TPE). Such a model would need sound theory-based inputs for both large-scale (like the heliospheric magnetic field) and small-scale (such as the turbulence) heliospheric conditions. The development of such a model is outlined in the three main chapters of this thesis that have been published in peer reviewed journals.

Chapter 2 introduces the basic ideas and knowledge that one needs to be able to follow on in the rest of the thesis. It introduces and describes the main structures in the heliosphere that have been found to be the major contributors to long-term cosmic ray modulation. The Sun's cyclical behavior is introduced first, as that is what drives the rest of the processes. These include the solar wind, which drags along with it the heliospheric magnetic field (HMF) and heliospheric current sheet into the outer heliosphere. The transport equation and classification of CRs is discussed next, followed by a discussion on drift and diffusion. Lastly a number of relevant space age missions are introduced and followed by a discussion on pre-space records of cosmogenic nuclides on a centennial basis.

Chapter 3 is an article published in 2018 in The Astrophysical Journal, 859:107. It introduces a simplified, physics-first CR modulation model that uses as inputs effective values for the solar wind speed, magnetic field magnitude and heliospheric tilt angle, as well as values for turbulence quantities taken during the last three solar minima. These are used to simulate the time-dependence in a steady-state, three-dimensional stochastic solver of the Parker transport equation. Parametric fits to results from a two component turbulence transport model are used as inputs for diffusion coefficients derived from the Quasilinear and Nonlinear Guiding center (NLGC)

theories. The 1987, 1997 and 2009 solar minima are studied self-consistently, and relatively good agreement is found with observations for all three solar minima. The higher-than-usual intensities observed during the unusual 2009 solar minimum follow naturally from this model. This points to the relative importance of turbulence inputs in cosmic ray modulation models. The predictive capability of the model is also studied, with various predictions made for the current solar minimum based on reasonable extrapolations of the behaviour of the heliospheric magnetic field magnitude, tilt angle, and magnetic variance.

In **Chapter 4**, published in 2019 in Advances in Space Research 63, 626 - 639, the stochastic solver technique introduced in **Chapter 3** is tested at the Centre for High Performance Computing (CHPC). The growing demand for computational resources at this South African national facility, and others similar to it globally, makes it prudent to test the efficiency and scalability of models for large parallel platforms. Two setups of the model introduced in **Chapter 2** are used for the test. One that uses simple *ad hoc* diffusion coefficients, to demonstrate the scalability of the code for parallel computing and the the other that uses a computationally expensive setup, employing diffusion coefficients derived from first principles to model proton latitude gradients and relative amplitudes of recurrent cosmic-ray variations. These are found to be in qualitative agreement with spacecraft observations. Lastly an introduction and background is given on the CHPC.

A three-dimensional, fully time-dependent *ab initio* cosmic-ray modulation model is introduced in **Chapter 5**. The model uses simple theoretically and observationally motivated temporal profiles for the large-scale and small-scale heliospheric parameters that feed into diffusion and drift coefficients. The model reproduces the major salient features observed by spacecraft in proton differential intensities for the period 1977 to 2001. Estimates for the historical heliospheric magnetic field magnitude derived from calculations based on observed cosmogenic nuclide counts are used in the model to test the relative importance of drift effects on cosmic ray modulation in the pre-space age. The alternating peaks and plateaux in the results are clearly evidence of the significance of this mechanism. The intensity profiles also peak during the Dalton minimum as would be expected from the inverse relation to solar cycle activity. These results are published in 2020 in The Astrophysical Journal, 894:121.

This thesis concludes with a chapter that gives a summary of the main results of this thesis, and the conclusions drawn therefrom. Refinements and possible improvements to the model are mentioned briefly in **Chapter 6**.

CHAPTER 2

Structures and Properties of the Heliosphere and Solar Cycle Relevant to Time-Dependent Cosmic-Ray Modulation

2.1 Introduction

Our local star, the Sun, is the only one which can be studied in great detail and thus can be considered as a proxy for cool stars. The use of the Sun as a paradigm for cool stars leads to a better understanding of the processes driving the broader population of cool sun-like stars [e.g. *Hanslmeier*, 2002]. This may help in answering the fundamental question of whether we are alone in the Universe [e.g. *Airapetian et al.*, 2020; *Scheucher et al.*, 2020]. The Sun is also the only star which is close enough to observe fine details on its surface such as sunspots, faculae, prominences, coronal holes, flares etc., which are all described as solar activity phenomena. It is a rotating magnetic star of which the atmosphere constantly blows radially away, forming a huge bubble of supersonic plasma, the solar wind [see, e.g., *Parker*, 1958], which engulfs the Earth and the other planets, shaping their immediate space environments.

The term heliosphere describes this region of interstellar space directly influenced by the Sun. Embedded in the solar wind is the Sun's turbulent magnetic field, which is transported with it into space and which in turn plays a major role in the transport of cosmic rays. Apart from more recent, anthropogenic influences, the Sun is the driving factor of the climate on Earth and the structure and shape of the Earth's magnetosphere, thus determining and influencing the near-Earth space environment. The modulation of cosmic rays can modify the radiation environment on Earth and needs to be taken into account for planning and maintaining space missions and even transpolar jet flights [*Badhwar et al.*, 1992, 2001; *Zeitlin et al.*, 2013; *Cucinotta*, 2014]. Solar activity can cause, through coupling of the solar wind and the Earth's magnetosphere, strong geomagnetic storms in

the magnetosphere and ionosphere, which may disturb radio-wave propagation and navigation-system stability, or induce dangerous currents in long pipes or power lines [see, e.g., *Barnard et al.*, 2011; *Siluszyk et al.*, 2019].

2.2 Solar Activity

The concept of solar activity is neither straightforwardly interpreted nor unambiguously defined. A variety of indices quantifying solar activity have been proposed in order to represent different observables and caused effects. For instance, solar-surface magnetic variability, eruption phenomena, coronal activity or even interplanetary transients and geomagnetic disturbances can be related to the concept of solar activity [*Usoskin*, 2017]. Most of these indices are highly correlated to each other due to the dominant 11-year cycle discussed below. These indices can be divided into physical and synthetic according to the way they are obtained/calculated. Physical indices quantify the directly-measurable values of a real physical observable, such as, e.g., the radio flux [*Usoskin*, 2017]. Synthetic indices (the most common being the sunspot number) are calculated using an algorithm from observed data or phenomena. They can also be either direct (i.e., directly relating to the Sun) or indirect (relating to indirect effects caused by solar activity)[see, e.g., *Hathaway*, 2015; *Usoskin*, 2017].

The most commonly used direct index of solar activity is the sunspot number. Sunspots are dark areas (of size up to tens of thousands of km, lifetime up to half-a-year) of irregular shape seen on the photosphere of the Sun [*Hathaway*, 2015; *Cliver and Herbst*, 2018]. These regions are associated with strong magnetic fields and are direct indicators of the level of solar activity [*Schrijver et al.*, 1998]. If these fields have strengths of $\sim$0.3 T, they limit effective heat conduction. This implies a local temperature reduction and thus that these regions are cooler than the rest of the surface [*Meyer-Vernet*, 2007]. Traditionally, sunspot numbers are given as daily numbers, monthly averages, yearly averages, and smoothed numbers. The Wolf, Zürich, or International Sunspot Numbers have been obtained daily since 1849. The relative sunspot number R is defined as

$$R = k\,(10g + n)\,, \tag{2.1}$$

where g is the number of identified sunspot groups, n is the number of individual sunspots in all groups visible on the solar disc and k is a correction factor for the individual observer, which compensates for differences in observational techniques and instruments used by different observers, and is used to normalize different observations to each other. Wolf extended the sunspot record back another 100 years to 1749 but much of that earlier data is incomplete. Wolf often filled in gaps in the sunspot observations using geomagnetic activity measurements as proxies for the sunspot number [*Usoskin*, 2017; *Cliver and Herbst*, 2018].

The sunspot number for the day was that found by the primary observer. If the primary observer was unable to make a count then the count from a designated secondary or tertiary observer was used instead. The use of only one observer for each day aims to make R a homogeneous time series. But such an approach ignores all other observations available for the day, thus possible errors of the primary observer cannot be caught or estimated. The observational uncertainties in the monthly R can be up to 25% [*Usoskin*, 2017]. Beginning

in 1981, and continuing through the present, the process was changed from using the numbers from a single primary/secondary/tertiary observer to using a weighted average of many observers but with their k-factors associated with the primary observer [*Hathaway*, 2015].

Due to these uncertainties, alternative sunspot numbers do exist; there is the Boulder Sunspot Number, the American Sunspot Number and the Group Sunspot Number. The scientific community needs a 'consensus' series of solar activity, there is currently a significant effort to reconcile the differences in the sunspot numbers and to provide a more reliable sunspot record (with error estimates) from 1610 to the present. Any kind of revisions will have far-reaching impact as sunspot numbers are used as inputs into estimations of the Sun's contribution to climate change and to the modulation of galactic cosmic rays and the radioisotopes they produce in Earth's atmosphere [*Hathaway*, 2015; *Usoskin*, 2017; *Cliver and Herbst*, 2018].

Figure 2.1 shows annual averages of sunspot numbers and from these observations it is clearly evident that the Sun has a quasi-periodic ∼11 year solar activity cycle. The Sun goes through a period of fewer and smaller sunspots numbers during solar minimum followed by a period of more and larger sunspots during solar maximum. The leading spots in sunspot pairs have opposite polarities in opposite hemispheres. The magnetic polarities of sunspot pairs alternate in a hemisphere every ∼11 years due to the solar activity cycle [*Hale*, 1908]. If for instance, the leading sunspot in a pair in the northern hemisphere has a positive polarity in one solar activity cycle, the leading sunspot will have a negative polarity in the next cycle, known today as Hale's sunspot polarity law. Conversely, the leading sunspot in the southern hemisphere will have a negative polarity in the first solar activity cycle and positive polarity in the second one. The solar magnetic field thus oscillates with a mean period of ∼22 years, reversing polarity every ∼11 years. Sunspots also show a clear latitudinal dependence during a solar cycle, called Spörer's Law, shown in Figure 2.2. Sunspots form in two bands on either side of the solar equator, starting at mid-latitudes and progressing towards the solar equator during solar maximum, but with a zone of avoidance near the equator. When these sunspots fade, sunspots of the new cycle start appearing at mid-latitudes, creating the Maunder butterfly diagram [*Maunder*, 1904].

As evident from Figures 2.1 and 2.2, the solar cycle is far from being just a simple periodic phenomenon, as there are variations in the cycle length and amplitude, varying dramatically between nearly spotless grand minima and very large values during grand maxima. Stochastic or chaotic processes seem to be behind the occurrence of these grand minima and maxima and not the result of cyclic variations that produce the 11 year cycle. The Sun seems to spends about a third of its time at moderate solar activity levels, about a sixth of its time in a grand minimum and about a tenth in a grand maximum, with the solar activity in solar cycle 23 corresponding to a grand maximum [see, e.g., *McCracken and Beer*, 2015; *Usoskin*, 2017; *Caballero-Lopez et al.*, 2019, and references therein].

2.3 The Solar Wind

The heliosphere is formed as a result of the interaction between the solar and interstellar plasma and can be defined as the local region of interstellar space influenced by the Sun. A simplistic understanding of the

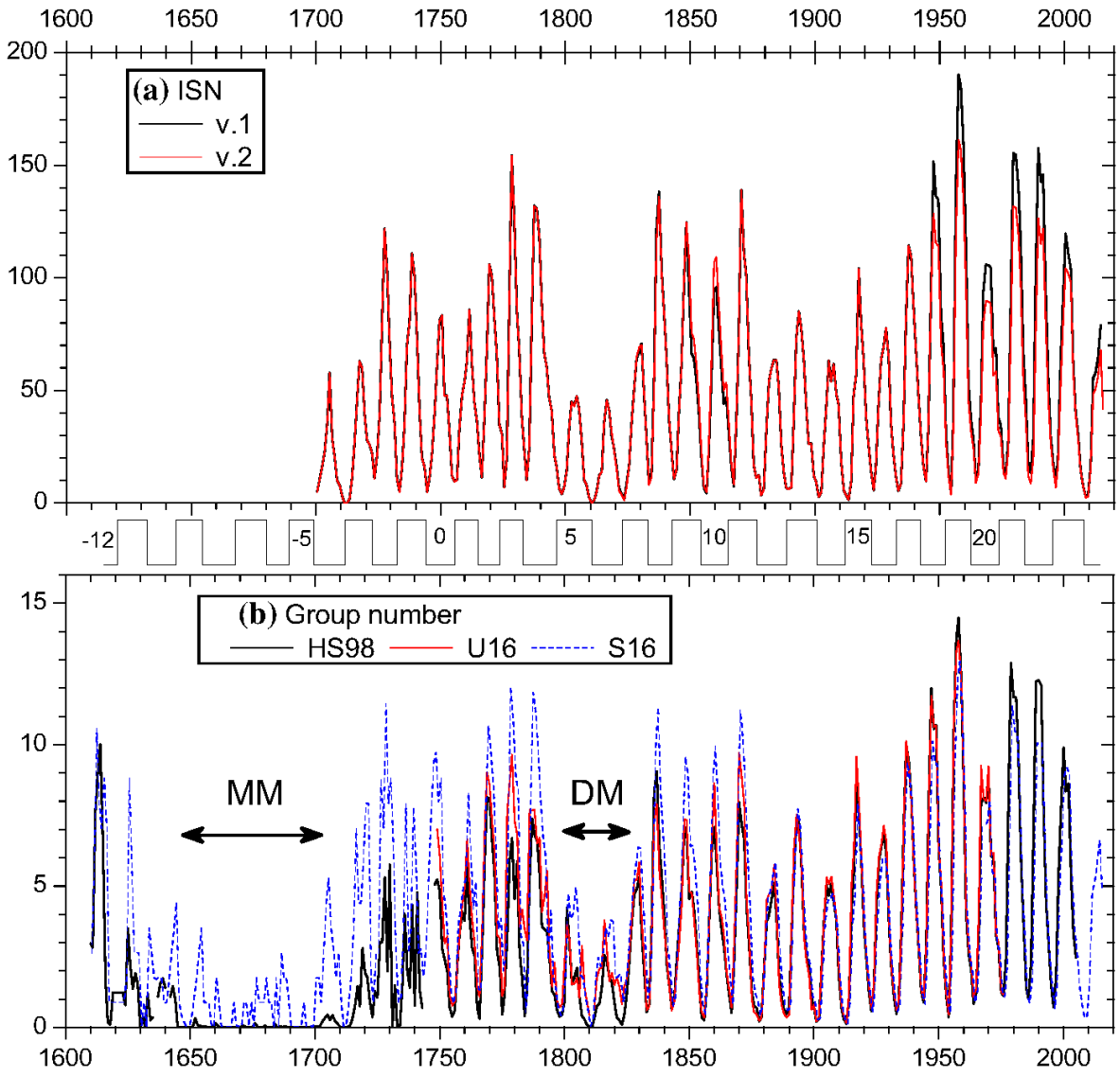

Figure 2.1: *Annually averaged International Sunspot Number series version 1 and 2 (the latter is scaled with a 0.6 factor, see SILSO, http://sidc.be/silso/datafiles) top panel and sunspot group number: HS98—(Hoyt and Schatten [1998]); U16—(Usoskin I. G. et al. [2016]); S16—(Svalgaard Leif and Schatten Kenneth H. [2016]).The first official solar cycle started in 1755, we are currently nearing the end of cycle number 24. Standard (Zürich) cycle numbering is shown between the panels. The Maunder (MM) and Dalton minimum (DM) are also shown in the lower panel [Usoskin, 2017].*

formation of the heliosphere is that the solar wind flows radially outward from the Sun and therefore blows a spherical bubble that continually expands. But as the solar wind expands into space, its pressure decreases with radial distance from the Sun. This is because interstellar space is not empty, but contains matter in the form of the interstellar medium (ISM) [*Pogorelov et al.*, 2017]. The Sun is the main driver of the heliosphere, and consequently its global structure is heavily influenced by the Sun's temporal variations (discussed earlier in this chapter), most notable the ∼11 year solar activity cycle [*Owens and Forsyth*, 2013; *Opher et al.*, 2020].

The concept of a solar wind, originally called solar corpuscular radiation [e.g. *Parker*, 1960], was introduced ∼60 years ago to account for the fact that comets' tails always point radially away from the Sun, regardless

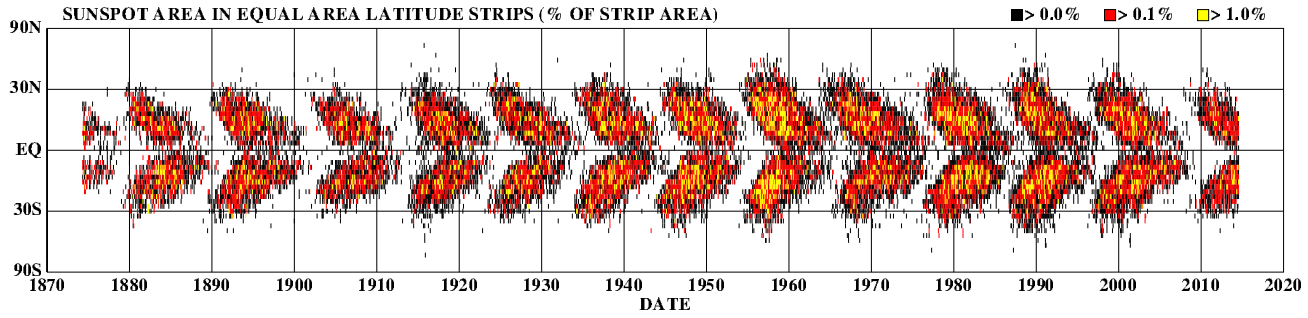

Figure 2.2: *Sunspot area as a function of latitude and time. Sunspots form in two bands, one in each hemisphere, and migrate toward the equator as the cycle progresses [Hathaway, 2015].*

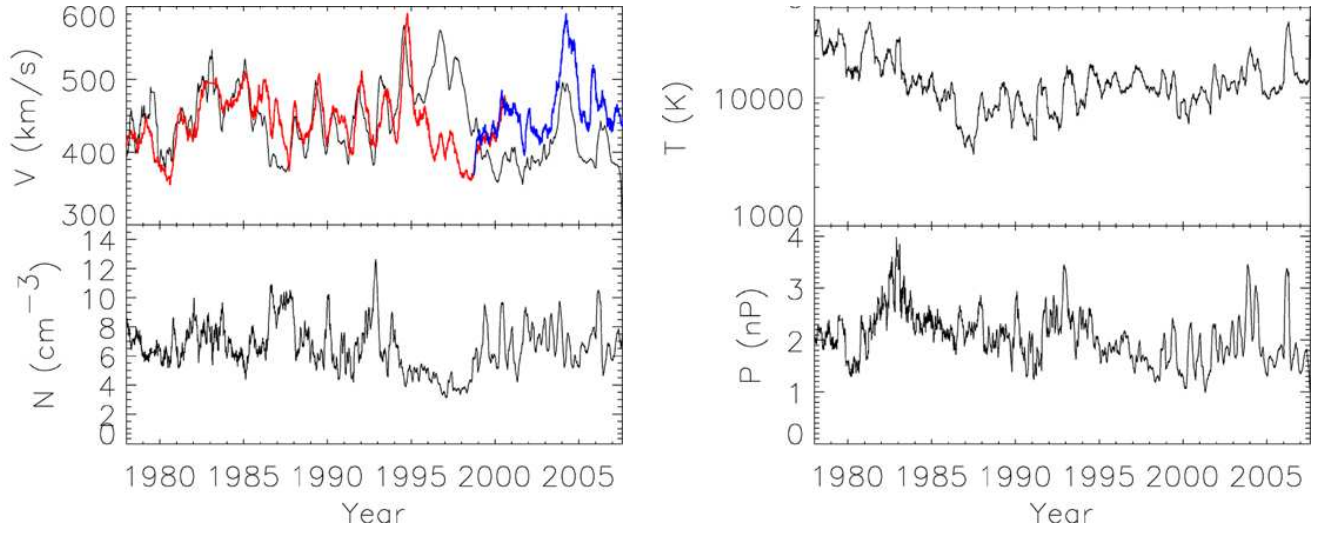

Figure 2.3: *Running 101-day averages of the solar wind speed, density, temperature and dynamic pressure observed by* Voyager 2. *The top left panel also shows speeds at 1 au from* IMP 8 *(red) and* ACE *(blue). Adapted from Richardson and Stone [2009].*

of the position of the comet. The name 'solar wind' was first introduced by *Parker* [1958] who argued that the atmosphere of the Sun could not be in static equilibrium and was in fact expanding at supersonic speed. The first *in situ* observations of the supersonic solar wind were made by the *Mariner 2* spacecraft [see, e.g., *Gombosi*, 1998] and we have continuous *in situ* observations from different spacecraft at 1 au to the present. For a review on the early work done on the solar wind, the reader is referred to *Parker* [1961] and *Parker* [2001].

Early estimates of the solar wind speed, based on its effect on comets, were in the region of 400 km s^{-1} to 1000 km s^{-1}, which is not too far from the observed values in the region of 400 km s^{-1} to 800 km s^{-1}. Observations by the *Ulysses* spacecraft [see, e.g., *McComas et al.*, 2000] have revealed unambiguously that the solar wind speed is not uniform over all latitudes but its speed is influenced close to the Sun by the solar magnetic field, which is in the form of a dipole during solar minimum conditions [see, e.g., *Gosling and Pizzo*, 1999]. In the solar equatorial regions, the radial plasma flow and the Sun's magnetic field are orientated almost perpendicular to each other and the magnetic field thus inhibits the expansion of the corona. These field lines

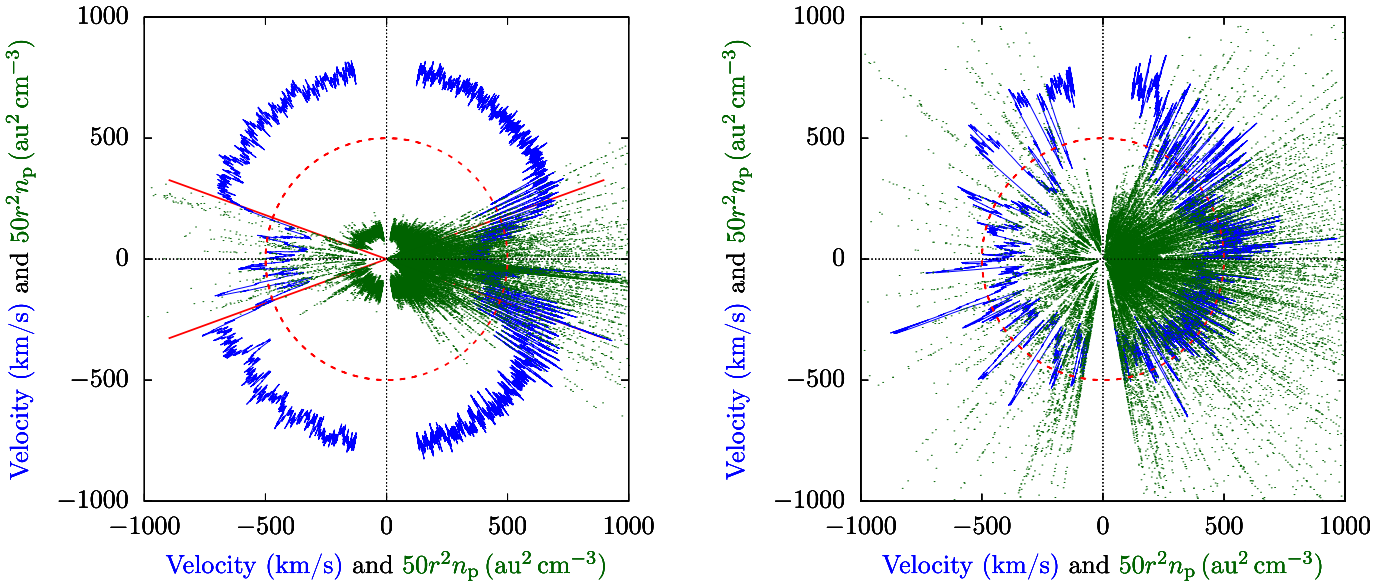

Figure 2.4: *Solar wind radial velocity (blue) and proton density (green) at different heliographic latitudes, as observed by* Ulysses/SWOOP. *The density is multiplied by r^2 to compensate for observations at varying r. The red circle represents a solar wind velocity of 500 km s^{-1} and a "density" of 10 au^{2}cm^{-3} . While straight red lines represents the sector boundaries at ±20° latitude. Left panel:* Ulysses' *first polar orbit during solar minimum (1990-12-20 through 1997-12-15). Right panel:* Ulysses' *second polar orbit during solar maximum (1997-12-15 through 2004-02-22) [Verscharen et al., 2019].*

are in the form of loops which begin and end on the solar surface and stretch around the Sun to form the streamer belts. These regions are in turn regarded as the most plausible sources of the slow solar wind in the broader heliosphere, which has typical average speed of up to 400 km s^{-1}. Other indications are that the slow solar wind may arise from the edges of coronal holes [see, e.g., *Smith*, 2000; *Schwenn*, 2006; *Wang*, 2011].

In the polar regions, however, the Sun's magnetic field is dominated by polar coronal holes which form open magnetic field lines directed parallel to the out-flowing solar wind and so do not inhibit it's flow, giving rise to the fast solar wind streams in these regions. The latitudinal dependence of the solar wind speed is thus defined by the latitudinal distribution of polar coronal holes on the Sun's surface [see, e.g., *Cranmer*, 2009; *Wang*, 2009]. During solar maximum conditions the polar coronal holes show no clear distribution, and neither does the solar wind. The fast solar wind has a characteristic average speed of around 800 km s^{-1}. The fast solar wind can sometimes extend close to the equator and overtake the earlier emitted slower stream, resulting in corotating interaction regions (CIRs) [see, e.g., *Fujiki et al.*, 2003; *McComas et al.*, 2008; *Heber*, 2011].

In the ecliptic the slow solar wind reaches an asymptotic speed of about 400 km s^{-1} and, to first order, maintains that speed up to the termination shock (TS) [*Richardson and Stone*, 2009]. Figure 2.3 shows 101-day averages of the solar wind speed, density, temperature and dynamic pressure observed by *Voyager 2* (*V2*). The top left panel also shows 101-day averages of the solar wind speed at 1 au. Near the Sun (out to around 30 au the speeds at Earth and those at *V2* are very similar. These parameters have display a large amount of variation, but to first order the speed is constant, and the density initially decreases as r^{-2} [*Richardson and Stone*, 2009; *Zank et al.*, 2018], this radial dependence flattening out at larger radial distances due to the potential heating of

solar wind protons by the turbulent cascade of waves formed during the generation of pickup ions [*Richardson et al.*, 1995; *Smith et al.*, 2001; *Isenberg*, 2005].

The solar wind changes over a solar cycle. The dynamic pressure, which determines the distance to the TS and heliopause (HP) [*Washimi et al.*, 2017], is at its smallest near solar maximum, after which it increases for 2–3 years after solar maximum, then decreasing into the next solar maximum [*Richardson and Wang*, 1999]. At solar maximum, the solar wind is slow and dense at all heliolatitudes, but during solar minimum it is slow and dense near the equator but fast and tenuous near the poles due to the presence of high-latitude coronal holes [*Phillips et al.*, 1995], with a transition region near $20° - 30°$ heliolatitude [*McComas et al.*, 2000]. During solar maximum conditions, the coronal holes are smaller and more or less uniformly distributed in the corona, so that no clear latitude dependence can be distinguished [see, e.g., *Marsden and Harrison*, 1995; *Balogh et al.*, 2001, for more detail]. This can clearly be seen in Figure 2.4 which shows solar wind observations by the *Ulysses* spacecraft as a function of latitude during times of minimum (left panel) and maximum (right panel) solar activity.

This gradient in speed with heliolatitude at solar minimum causes the difference in solar wind speeds at Earth and *V2* in 1986–87 and 1995–97 shown in the top panel of Figure 2.3. In 1986–87, *V2* was at a lower average heliolatitude than Earth and observed lower speeds whereas from 1995–97 *V2* was at a higher heliolatitude than Earth and observed much higher speeds. Solar activity varies over a solar cycle and the structure of the solar wind is solar cycle dependent as it is modified by interplanetary coronal mass ejections (ICMEs) near solar maximum, with many more ICMEs at solar maximum than at solar minimum [*Cane and Richardson*, 2003; *Richardson and Cane*, 2010]. At times of high solar activity the Sun sometimes emits a series of ICMEs. The latter ICMEs can catch up to earlier ICMEs and merge, compressing the solar wind ahead of them to form regions of high magnetic field and (often) density called merged interaction regions (MIRs) [*Burlaga et al.*, 1984; *Burlaga*, 1995; *Richardson et al.*, 2002]. Near solar maximum these structures dominate the solar wind profile, so that during solar maximum as much as 40% of the solar wind observed by *V2* is from ICMEs [*Richardson et al.*, 2003].

At some stage the speed of the supersonic solar wind plasma decreases to subsonic speeds and a heliospheric shock, called the solar wind termination shock (TS), forms [see, e.g., *Parker*, 1961; *Choudhuri*, 1998; *Parker*, 2001; *Pogorelov et al.*, 2017]. Beyond this point, which two measurements show occurs at a distance of between 83.7 au to 94 au [e.g., *Stone et al.*, 2005; *Stone et al.*, 2008], the solar wind propagation direction in the front/nose of the heliosphere shifts to the meridional and azimuthal directions as it is "turned around" by its encounter with the ISM. The other structures that comprise the heliosphere in this region are; the heliopause (HP, which separates the solar and interstellar plasmas) and the bow-shock (BS, where the interstellar medium flow speed drops to subsonic values).

Until recently, the consensus was that the shape of the heliosphere is comet-like [see, e.g., *Ferreira et al.*, 2007; *Pogorelov et al.*, 2017]. However, *Opher et al.* [2020] argue, based on magnetohydrodynamic (MHD) simulations, that the twisted magnetic field of the Sun confines the solar wind plasma beyond the termination shock and drives jets to the north and south of the heliosphere, very much like some observed astrophysical jets. These jets are deflected into the tail region by the motion of the Sun through the ISM. The interstellar

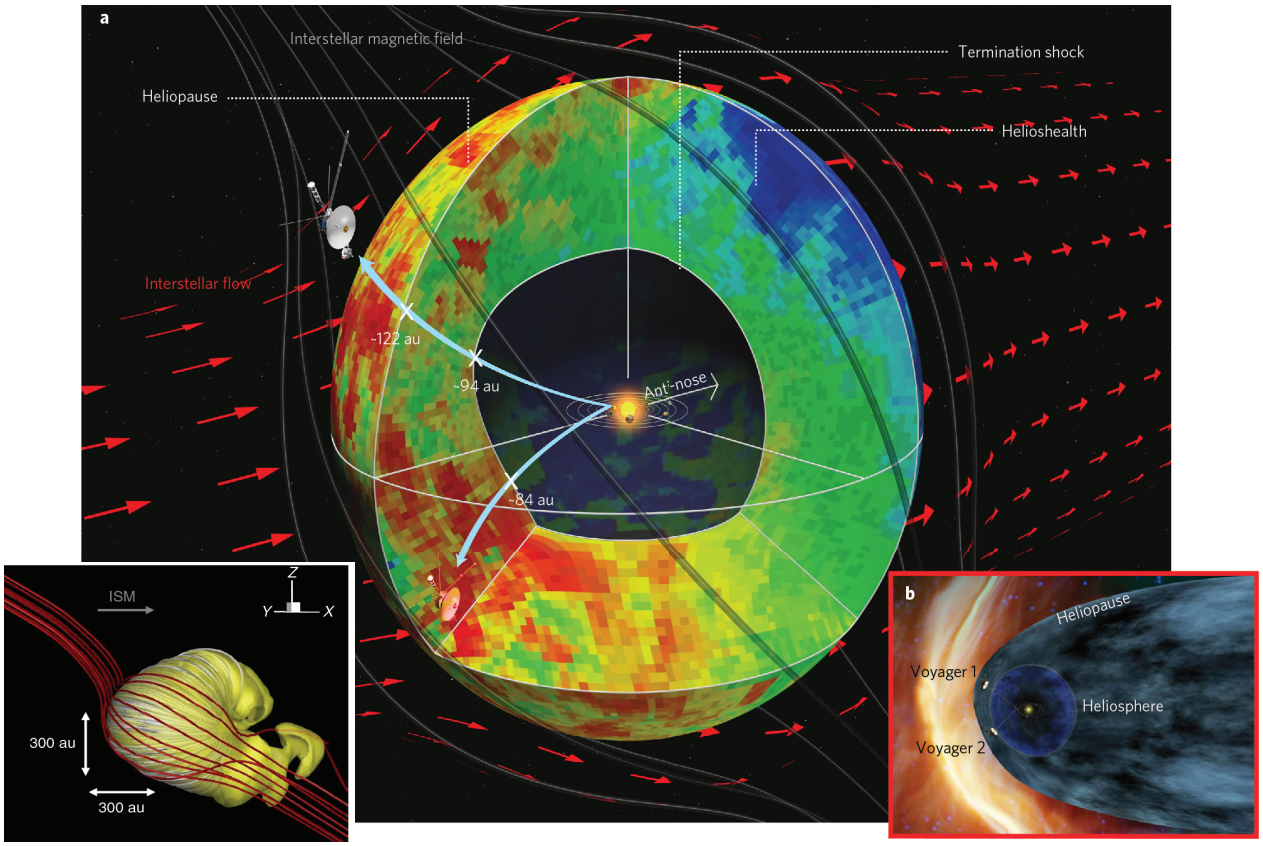

Figure 2.5: ***a****: Gross shape and basic properties of the global heliosphere in three dimensions based on both remote ENA and in situ ion measurements from Cassini/INCA and LECP/*V1 *and* V2*, respectively. The termination shock location is 10 au further out in the* V1 *direction, The red arrows represent the interstellar plasma flow deflected around the heliosphere.* ***b****: left panel, two-lobe structure heliosphere with an interstellar magnetic field resulting from MHD simulations. The HP is shown by the yellow surface. The white lines represent the solar magnetic field. The red lines represent the interstellar magnetic field.* ***b****: right panel. the standard view of a comet-like configuration including an elongated heliotail extending thousands of astronomical units, widely adopted as one of two possibilities put forward by Parker in 1961. The supersonic solar wind region is represented by the blue region around the Sun. The extended region beyond the blue region represents the HS. Adapted from Dialynas et al. [2017] and Opher et al. [2020].*

wind blows the two jets into the tail but is not strong enough to force the lobes into a single comet-like tail. This is in contrast to the traditional view of the shape of the heliosphere being a comet-like object aligned in the direction of the Sun's trajectory through the ISM [*Parker*, 1961; *Baranov and Malama*, 1993] with a long tail extending for thousands of au. Instead, the interstellar wind flows around the heliosphere and into the equatorial region between the two jets, thus separating them as can be seen in the bottom left-hand panel of Figure 2.5, consistent with the energetic neutral atom (ENA) images of the heliotail from *IBEX* where two lobes are visible in the north and south. There is also a suggestion from the *Cassini* ENA observations that the heliosphere lacks a tail [*Krimigis et al.*, 2009; *McComas et al.*, 2013]. The lobes are turbulent (due to large-scale MHD instabilities and reconnection) and strongly mix the solar wind with the ISM beyond ∼400 au. The distance from the Sun to the HP in this new description of the heliosphere is nearly the same in all directions. This new rounder and smaller shape is also in agreement with the shape suggested by the ENA observations by the Cassini spacecraft [*Dialynas et al.*, 2017] This shape of the heliosphere is consistent with the less-adopted

shape suggested by *Parker* [1961], which presents a bubble-like structure, formed under the influence of a large-scale interstellar magnetic field (depicted by the red lines). This confines the heliosheath plasma nearly symmetrically in all directions while allowing the solar wind to be evacuated in the direction of the interstellar magnetic field.

2.4 The Heliospheric Magnetic Field: Parker Model

The solar wind drags the coronal magnetic field out into the heliosphere, forming the heliospheric magnetic field (HMF). Thus, the large scale structure and dynamics of the HMF are governed by the solar wind flow, which in turn originates in the magnetic structure of the corona. The simplest steady-state picture is observed under solar minimum conditions when the coronal magnetic field is closest to being dipolar [e.g., *Stix*, 2004; *Kislov et al.*, 2019], typically with the magnetic dipole axis tilted by a few degrees to the solar rotation axis. At this time the fast solar wind fills most of the heliosphere, flowing outwards from the Sun from the regions of open magnetic field lines originating in the polar coronal holes [*Balogh et al.*, 1995]. In the region corresponding to the solar magnetic equator, however, there is a belt of slower solar wind of about 20° latitudinal width. The magnetic field boundary separating oppositely directed magnetic field lines originating from the northern and southern polar coronal holes is carried out by this slower solar wind to form the heliospheric current sheet (HCS), a large scale magnetic boundary which extends throughout the heliosphere, separately discussed in section 2.5. Latitudinal differences in the rotation speed of the Sun causes stretching and distortions in the field lines and eventually kinks and twists develop. This differential solar rotation winds the magnetic field around the Sun's equator, adding more complexity to its structure [see, e.g., *Snodgrass*, 1983; *Phillips et al.*, 1995; *Burger et al.*, 2008].

There are a variety of models for the HMF [for a review see, e.g., *Burger and Sello*, 2005; *Hitge and Burger*, 2010], including that of *Fisk* [1996]. However, for most long-term cosmic-ray modulation studies, the model of *Parker* [1958] is used because evidence for more complex HMF models remains somewhat ambiguous [see, e.g., *Burger et al.*, 2008; *Sternal et al.*, 2011]. Observationally, the Parker spiral model well approximates the mean and large-scale structure of the HMF of our solar system [*Ness*, 2006]. However, Fisk fields and their variants can in principle explain short-term intensity variations observed by the same instruments used to study long-term modulation [see, e.g., *Engelbrecht and Burger*, 2010].

The *Parker* [1958] spiral model is one of the simplest models for the heliospheric magnetic field and can be written in heliocentric spherical coordinates as

$$\mathbf{B} = A \left(\frac{r_e}{r}\right)^2 (\mathbf{e}_r - \tan\psi \mathbf{e}_\phi)\,, \tag{2.2}$$

with $r_e = 1\,\mathrm{au}$, $\mathbf{e}_r$ and $\mathbf{e}_\phi$ unit vectors in the radial and in the azimuthal direction, respectively, and $|A|$ the magnitude of the radial component of the field at Earth. The sign of A indicates the HMF polarity: When it is positive, the field in the northern hemisphere points away from the Sun and inward in the southern

hemisphere, with the opposite applying when A is negative. In what follows, the notation $A > 0$ for positive polarity cycles and $A < 0$ for negative polarity cycles will be used. The basic structure of the HMF is that of Archimedean spirals lying on cones of constant heliographic latitude. These spiral field lines do not cross, due to the divergence-free nature of this field.

The quantity ψ is the Parker spiral angle, which is the angle between the radial direction and that of the average HMF at a certain position. The spiral angle gives an indication of how tightly wound the HMF spiral is [e.g. *Smith and Bieber*, 1991], and is defined by

$$\tan\psi = \frac{\Omega\,(r - r_{\mathrm{o}})\sin\theta}{V_{sw}}, \tag{2.3}$$

where V_{sw} is the solar wind speed, $\Omega = 2.67 \times 10^{-6}\,\mathrm{rad\,s^{-1}}$ is the average angular rotation speed of the Sun, and r_{o} is the radial distance at which the field is assumed to be purely radial, and which defines the assumed spherical HMF source surface. This theoretical description of the HMF is usually assumed to apply from this surface onward. Since the source surface is at a fraction of an au, r_o is often neglected compared to the overall $\sim$122 au scale of the heliosphere. Note that the ratio Ω/V_{sw} is very close to $1\,\mathrm{au^{-1}}$ for a $400\,\mathrm{km\,s^{-1}}$ solar wind, expressed in $\mathrm{au\,s^{-1}}$. Since at Earth $r = 1$ au and the polar angle $\theta = 90°$, a typical value of ψ is 45° at Earth and tends to 90° when $r \geq 10$ au in the equatorial plane.

The HMF in the solar ecliptic plane, particularly at Earth orbit, is well sampled, and observations have confirmed the existence of a Parker spiral HMF at mid to low heliolatitudes. The magnitude of the HMF at Earth has an average value of $B_e \approx 5\,\mathrm{nT}$ to 6 nT during typical solar minimum conditions, but increases with time by up to a factor of $\sim$2 towards solar maximum conditions. Beyond a few au, the magnitude decreases as r^{-2} in the solar equatorial region, but as r^{-1} over the solar poles where $\sin\theta$ is close to zero. Figure 2.6 shows the comparison of the Parker model with the magnetic field in the equatorial plane as observed by *Voyager 1* (*V1*), the latter indicated by dots. The HMF estimate from Parker's model (shown as a solid line) is based upon the observed HMF at Earth and solar wind speeds measured (within 10 au) or estimated (beyond 10 au) using *V1* data. Estimated field magnitudes due to lower ($400\,\mathrm{km\,s^{-1}}$) or higher ($800\,\mathrm{km\,s^{-1}}$) average solar wind speeds are indicated by the two dotted lines. It is clear from Figure 2.6 that the Parker model provides a reasonably accurate description of the observed HMF magnitude in the solar ecliptic plane. Note that the two local maxima and two local minima in the HMF magnitude shown in the figure during 1990 and 2000, and 1987 and 1997, respectively, correspond to 11-year variations associated with solar activity. The behaviour of the HMF at polar latitudes, however, is still the subject of much debate [see, e.g., *Ness and Wilcox*, 1965; *Thomas and Smith*, 1980; *Roberts et al.*, 2007; *Burger et al.*, 2008; *Smith*, 2011; *Sternal et al.*, 2011]. This is due to the fact that observations of the high latitude HMF are limited to the few measurements made by the *Ulysses* spacecraft, which made three fast latitude scans between its launch in 1990 and the end of that mission in 2009 [*Forsyth et al.*, 1996].

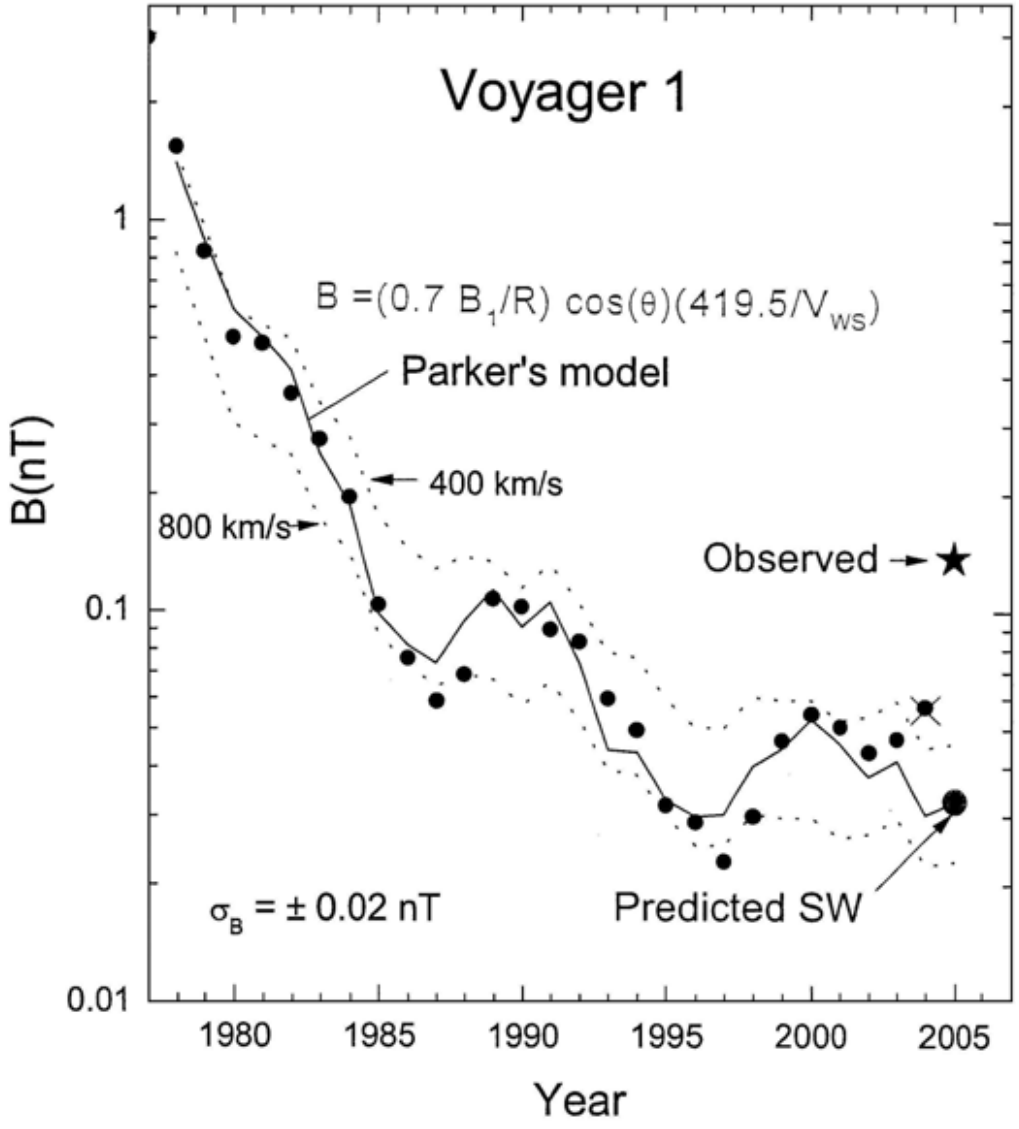

Figure 2.6: *Comparison of* V1 *yearly averages of HMF magnitude since launch with the Parker model using measured HMF at 1 au. The dots show the yearly averages measured by* V1 *and the solid curve is Parker's model. The dashed curves are the predictions of Parker's model for a solar wind speed of 400 km s^{-1} and 800 km s^{-1}, respectively. Solar cycle changes with a period of ∼11 years can be seen to be superimposed on the long-term decrease [Ness, 2006].*

2.5 Heliospheric Current Sheet and the Tilt Angle

The heliospheric current sheet (HSC) is a major three-dimensional corotating structure in the heliosphere, separating the two hemispheres of opposite magnetic polarities [see, e.g., the reviews by *Smith*, 2001; *Malandraki et al.*, 2019]. The origin of the HCS lies in the open magnetic field lines that originate on the solar surface at high latitude and get dragged towards the ecliptic plane. Being part of the HMF, it is frozen into the solar wind and propagates radially outward.

The rotational and magnetic axes of the Sun are misaligned by the tilt angle α. As the Sun rotates, the HCS also rotates, resulting in a wavy or warped structure. At 1 au the thickness of the HCS is ∼10 000 km [*Smith*,

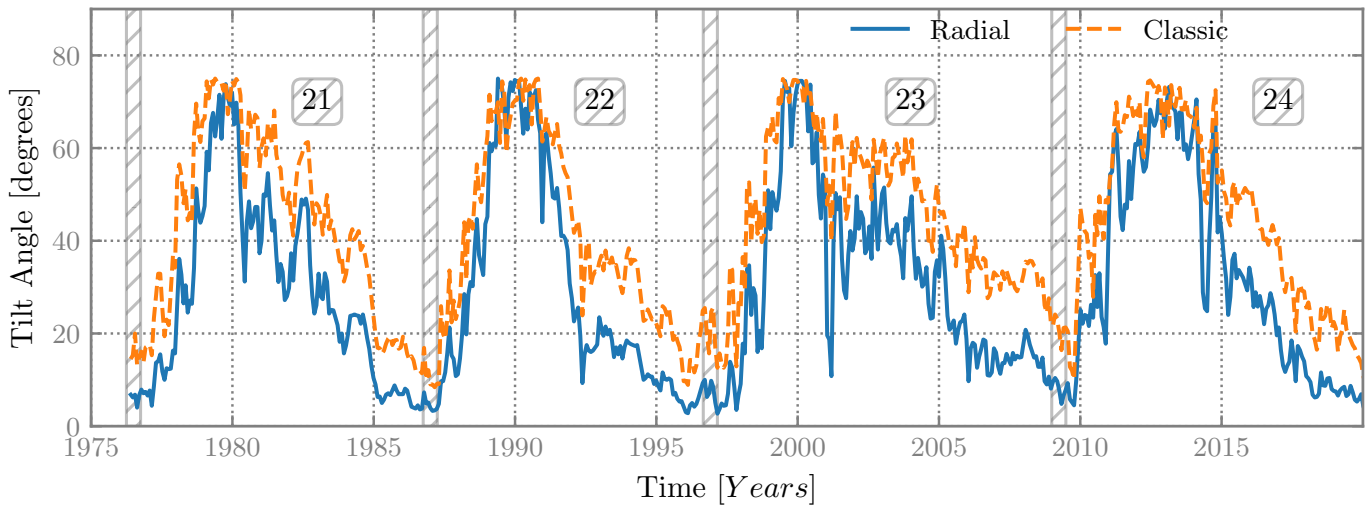

Figure 2.7: *Two different models for the tilt angle α. The "classic" uses a line-of-sight boundary condition at the photosphere and includes a significant polar field correction. The newer, possibly more accurate "radial" model uses a radial boundary condition at the photosphere, and requires no polar field correction. The shaded areas represent the start and end of solar cycles, respectively. Tilt angle data from* `http://wso.stanford.edu/Tilts.html`.

2001; *Battarbee et al.*, 2017; *Engelbrecht et al.*, 2019]. The structure of the HCS varies greatly during a solar cycle due to the fact that the tilt angle α increases with increasing solar activity, greatly warping the structure of the current sheet.

Figure 2.7 shows observations of the tilt angle using two different models to compute it from solar magnetic field maps [*Hoeksema*, 1992]. The "classic" model uses a line-of-sight boundary conditions, with a source surface at 2.5 solar radii, while the new "radial" (possibly more accurate) model uses the radial boundary conditions at the photosphere, with a source surface at 3.5 solar radii. Note that data are only available as from mid-1976. This is obviously a restriction for studies of long-term cosmic-ray modulation that require observed tilt angles as input. Increasing solar activity may also affect the dipolar structure of the solar magnetic field, introducing quadrupole moments which may result in multiple current sheets in the heliosphere [*Kóta and Jokipii*, 2001; *Khabarova et al.*, 2017; *Kislov et al.*, 2019]. As solar minimum conditions return, the solar magnetic and rotational axes almost align, producing a fairly simple, single current sheet. If the magnetic and rotational axes of the Sun would be aligned, the HCS would form as a flat sheet located at $\theta = \pi/2$, thus lying in the equatorial plane. An expression for the wavy HCS was first derived by *Jokipii and Thomas* [1981]. *Krüger* [2005] derives an expression for the structure of such a current sheet in terms of the polar angle θ, such that

$$\theta = \frac{\pi}{2} - \tan^{-1}\left[\tan\alpha \sin\left(\phi_o + \frac{\Omega r}{V_{sw}}\right)\right]. \tag{2.4}$$

Where ϕ_o is an arbitrary azimuthal angle in a fixed observer's frame [see *Jokipii and Thomas*, 1981]. The HCS is shown in Figure 2.8 as a shaded surface for a tilt angle of 20°. The tilt angle varies from a minimum value of ∼5° during solar minimum periods to an upper limit of ∼75° during solar maximum periods, the latter value resulting from a limitation of the observation techniques [*Hoeksema*, 1992].

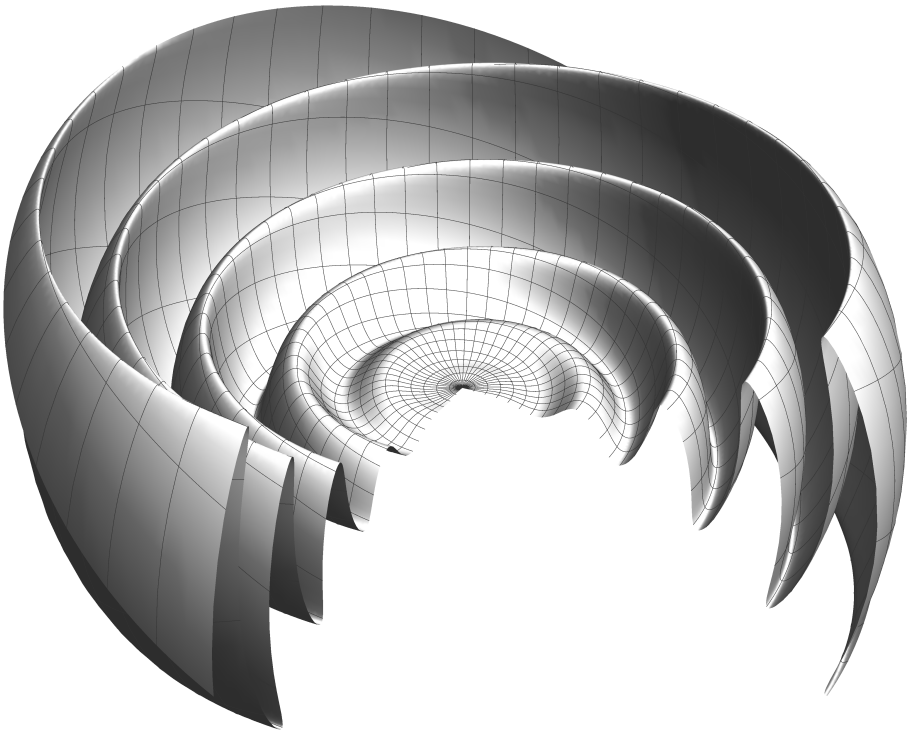

Figure 2.8: *Heliospheric current sheet, for a tilt angle of 20°, up to a radial distance of 30 au. A section of the sheet has been removed to accentuate its wavy structure [R.A. Burger (2015), private communication].*

Figure 2.9 shows the evolution of a steady-state (orange lines) and a time-dependent (blue lines) HCS over the 11 year solar cycle, based on tilt angle inputs modeled as proposed by *Burger et al.* [2008], which in turn are based on fits of observed temporal variations in the tilt angle:

$$\alpha\left(T\right)=\alpha_{min}+\left(\frac{\pi}{4.8}-\frac{\alpha_{min}}{2}\right)\times\begin{cases}1-\cos\left(\frac{\pi}{4}T\right),\ 0\leq T\leq 4\\ 1-\cos\left(\frac{\pi}{7}\left(T-11\right)\right),\ 4<T\leq 11,\end{cases}\tag{2.5}$$

where the angles are expressed in radians, and time T is in fractional years past solar maximum. The tilt angle is assumed to vary between 5° and 75°, (the limits to which the radial model tilt angle extends) as shown in the top panel of Figure 2.7. To model any quantity time-dependently in the heliosphere, we need to consider the speed at which information propagates. In a steady-state heliosphere, this information moves instantaneously, so that if something happens at Earth, a particle that is on the boundary is immediately aware of what has happen and can react to the new conditions. In a time-dependent heliosphere however this information only propagates outward at the solar wind speed. Hence the value of a quantity such as the inclination of the current sheet at some position (r,θ,ϕ) and time T_i can be related, with appropriate scaling, to the value of that quantity at Earth at a time $T=T_i-T_\eta$, where $T_\eta=r_i/V_{sw}$, assuming a radially constant solar wind speed, which is approximately accurate within the termination shock [*Richardson and Stone*, 2009]. So the 'local' tilt angle for a particle at position (r,θ,ϕ) and time T_i is equal to the tilt angle at 1 au at a time T, and the latter angle would then be used to calculate the current sheet angle. For a heliosphere that is 100 au, T_η is equal

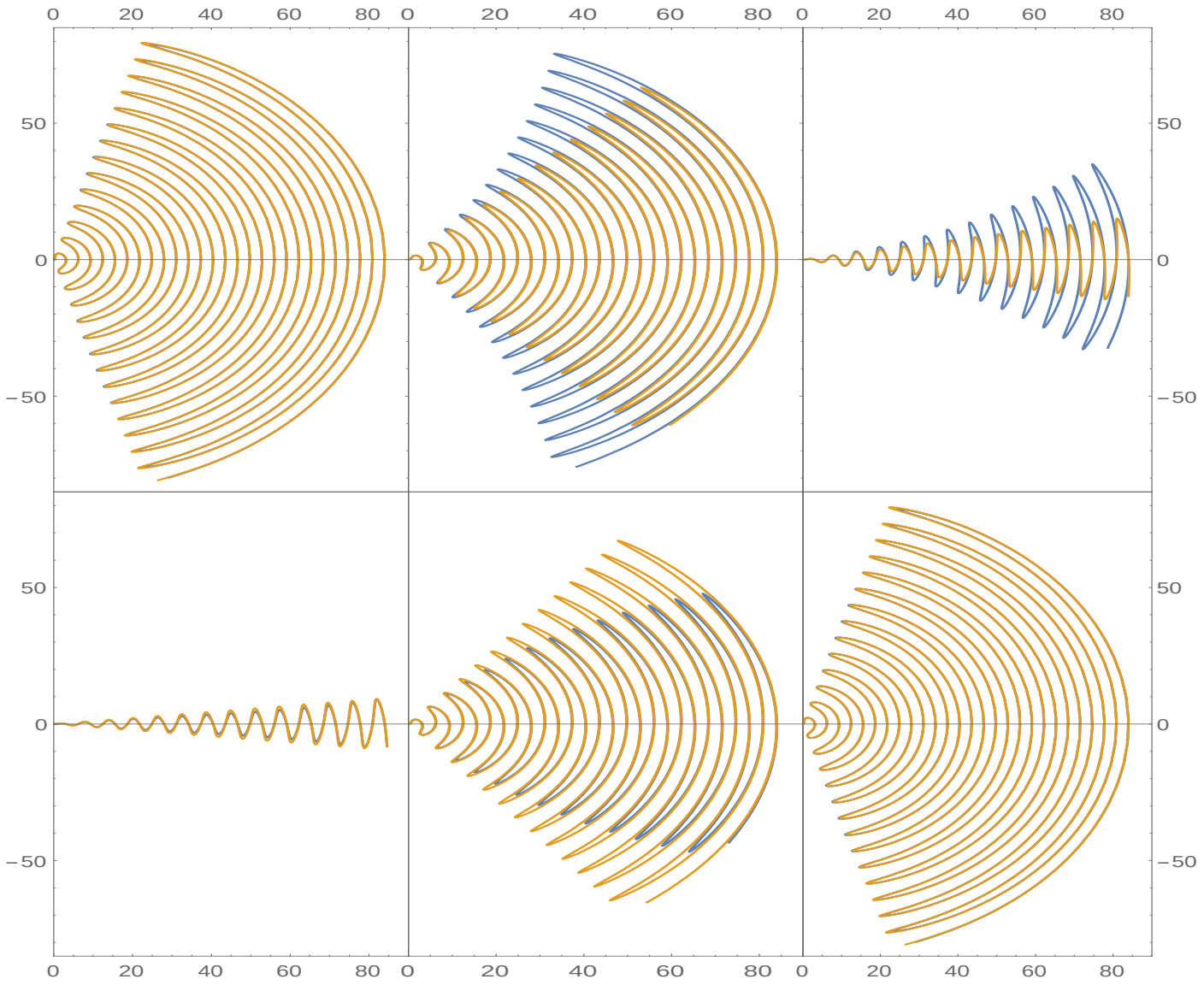

Figure 2.9: *Evolution of a steady-state (orange lines) and a time-dependent (blue lines) HCS over the 11 year solar cycle. See text for details.*

to about a year. So starting at full solar maximum, the top left panel of Figure 2.9, the steady-state (orange line) and the time-dependent (blue line) HCS are virtually the same, reflecting the relatively flat temporal behaviour of the tilt angle during periods of high solar activity seen in Figure 2.7. At about two and half years after solar maximum (top middle panel), the steady state and time-dependent HCS are equal in the inner heliosphere, where T_η is small, while the time-dependent HCS it is larger in the outer heliosphere. This is due to the fact that it takes time T_η for the new tilt angle conditions to reach the outer heliosphere. This is again the case at about four and half years after solar maximum (top right panel). After about seven years after solar maximum, solar minimum is reached and again the steady-state and time-dependent HCS are approximately equal (bottom left panel), as tilt angles reach a local minimum here. Now the descending phase of the tilt angle is over and the ascending phase has begun. At about nine years after solar maximum (bottom middle panel), the time-dependent HCS is now smaller than the steady-state HCS, again this is because the new higher tilt

angle conditions have not reached the outer heliosphere yet. Then 11 years after solar maximum we are back at solar maximum and the HCSs are roughly equal again (bottom right panel). The steady-state HCS essentially underestimates the HCS during the descending phase of the tilt angle and overestimates during the ascending phase. This time-dependent approach is discussed and implemented for all large and small scale quantities in the heliosphere in **Chapter 5**, *Moloto and Engelbrecht* [2020].

2.6 Turbulence Models

Any attempt at modelling the transport of CRs in a self-consistent manner requires a treatment of turbulence in the heliosphere, given that the scattering theories used to derive expressions for CR diffusion coefficients require as basic inputs information pertaining to the behaviour of the turbulence power spectrum [e.g., *Matthaeus and Velli*, 2011]. Given the complexity of this field, this study does not attempt an exhaustive review of the subject, confining itself rather to selected topics relevant to the transport and modulation of cosmic rays. For more extensive reviews, consult *Batchelor* [1970], *Frisch* [1995], *Davidson* [2004], *Bruno and Carbone* [2013] and *Verscharen et al.* [2019].

The turbulent HMF can be written in terms of a background component B_o that is uniform over relatively long timescales, and a fluctuating component,

$$\mathbf{B} = B_o \mathbf{e}_z + \mathbf{b}(x, y, z), \tag{2.6}$$

where for the sake of convention the uniform component is assumed to be in the z-direction of a cartesian coordinate system, and $\langle \mathbf{b} \rangle = 0$. For the purposes of this study, only transverse turbulent fluctuations are considered, so that

$$\mathbf{B} = B_o \mathbf{e}_z + b_x \mathbf{e}_x + b_y \mathbf{e}_y. \tag{2.7}$$

This is a reasonable assumption within the supersonic solar wind [e.g. *Bruno and Carbone*, 2013], but *Voyager* observations indicate that this is not so in the heliosheath [e.g. *Gallana et al.*, 2016; *Burlaga et al.*, 2018; *Fraternale et al.*, 2019].

Observational studies of turbulent fluctuations in the HMF often focus on the turbulence power spectrum. Correlations between magnetic fluctuations can be quantitfied using a correlation tensor defined as [see, *e.g.*, *Matthaeus et al.*, 2007]

$$R_{ij}\left(\mathbf{r}\right) = \left\langle \delta \mathbf{b}_i(\mathbf{x}) \delta \mathbf{b}_j(\mathbf{x}+\mathbf{r}) \right\rangle, \tag{2.8}$$

with the brackets denoting an ensemble average, and $\mathbf{r}$ a spatial lag. At zero lag, the value of the correlation function corresponds to the magnetic variance $R_{ii}(0) = \delta b_i^2$, and the distance at which the correlation function drops to $1/e$ of this initial value corresponds to the correlation length. The Fourier transform of this correlation function is the turbulence spectral tensor [see, e.g., *Batchelor*, 1970]. The spectrum represents a cascade of energy from large scales to smaller scales [see, e.g., *Davidson*, 2004], and has been observed in the solar wind.

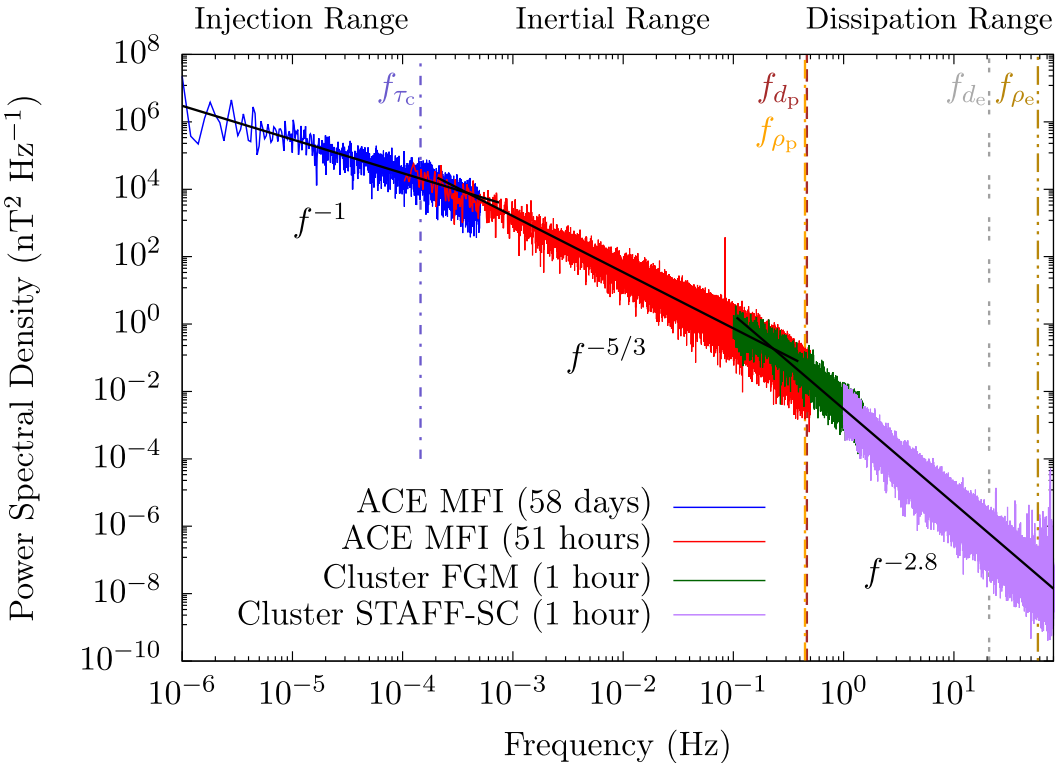

Figure 2.10: *Power spectrum of HMF fluctuations in the solar wind at 1 au. The black lines show the power laws that are associated with injection (−1), inertial (−5/3) and dissipation ranges (−2.8) Verscharen et al. [2019].*

Figure 2.10 shows an example of such a spectrum, computed using magnetic observations at 1 au from various spacecraft [*Verscharen et al.*, 2019], and displays several distinct ranges. The most important of these, to this study, are the energy-containing range, where large-scale driving of the turbulence occurs [see, *e.g.*, *Goldstein and Roberts*, 1999; *Matthaeus et al.*, 2007], and the inertial range. In this range, no more driving occurs, and the eddies simply decay, transferring energy to smaller and smaller scales with a frequency/wavenumber dependence of $f^{-5/3}/k^{-5/3}$ [see, *e.g.*, *Kolmogorov*, 1941]. Below these lengthscales, the dissipation range occurs, where fluctuation energy is dissipated into the background plasma, heating it [see, e.g., *Leamon et al.*, 2000; *Smith et al.*, 2006]. As fluctuations at these scales are not expected to affect the transport of galactic CR protons [see, e.g., *Bieber et al.*, 1994; *Engelbrecht and Burger*, 2013], and therefore will not be considered in this study.

Turbulent fluctuations in the solar wind display anisotropic behaviour [see, e.g., *Matthaeus et al.*, 1990; *Bieber et al.*, 1996], in that turbulence quantities vary when observed at different angles to the background magnetic field [see, e.g., *Narita et al.*, 2010]. This is usually modelled, for transverse turbulence, using either the slab or Alfvenic turbulence model, two-dimensional turbulence model, or the composite (two-component) turbulence model, which is a combination of previous two [see, e.g., *Bieber et al.*, 1994]. In the case of slab turbulence,

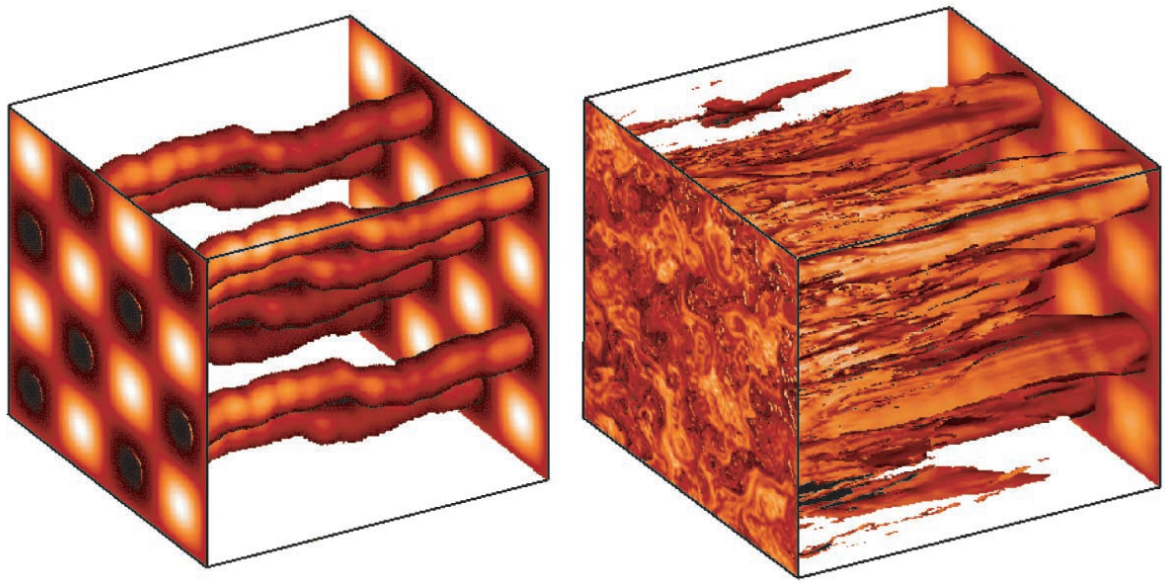

Figure 2.11: *Magnetic flux tubes for pure slab turbulence (left-hand panel) and 80/20 composite 2D/slab turbulence (right-hand panel). Note that flux tubes are initially circular on the right-hand side of the Figure, and that the field lines that define the flux tubes are followed from right to left [Matthaeus et al., 2003].*

the fluctuating component is only a function of z, and the total field is given by

$$\begin{aligned} \mathbf{B} &= B_o \mathbf{e}_z + \delta \mathbf{b}_{slab}(z), \\ &= B_o \mathbf{e}_z + \delta b_{slab,x}(z)\mathbf{e}_x + \delta b_{slab,y}(z)\mathbf{e}_y, \end{aligned} \tag{2.9}$$

with the variance given by

$$\delta B^2_{slab} = \delta b^2_{slab,x} + \delta b^2_{slab,y} = 2\delta b^2_{slab,x} = 2\delta b^2_{slab,y}. \tag{2.10}$$

assuming axisymmetric turbulenct fluctuations with respect to the mean magnetic field direction z. For a treatment of nonaxisymmetric turbulence, see *Ruffolo et al.* [2008] and *Strauss et al.* [2017]. The left panel of Figure 2.11, taken from *Matthaeus et al.* [2003], illustrates the effects of pure slab turbulence on magnetic flux tubes. As function of x and y for a given z, the tubes are identical, and they all vary in step as function of z.

For the 2D model, fluctuations are assumed to be functions of transverses coordinate (x, y) only, such that the total magnetic field can be written as

$$\begin{aligned} \mathbf{B} &= B_o \mathbf{e}_z + \delta \mathbf{b}_{2D}(x, y), \\ &= B_o \mathbf{e}_z + \delta b_{x,2D}(x, y)\mathbf{e}_x + \delta b_{y,2D}(x, y)\mathbf{e}_y. \end{aligned} \tag{2.11}$$

In contrast to the case for slab turbulence, the 2D fluctuations are a function of coordinates perpendicular to the uniform background magnetic field, remaining constant for any particular value of z, while varying in the

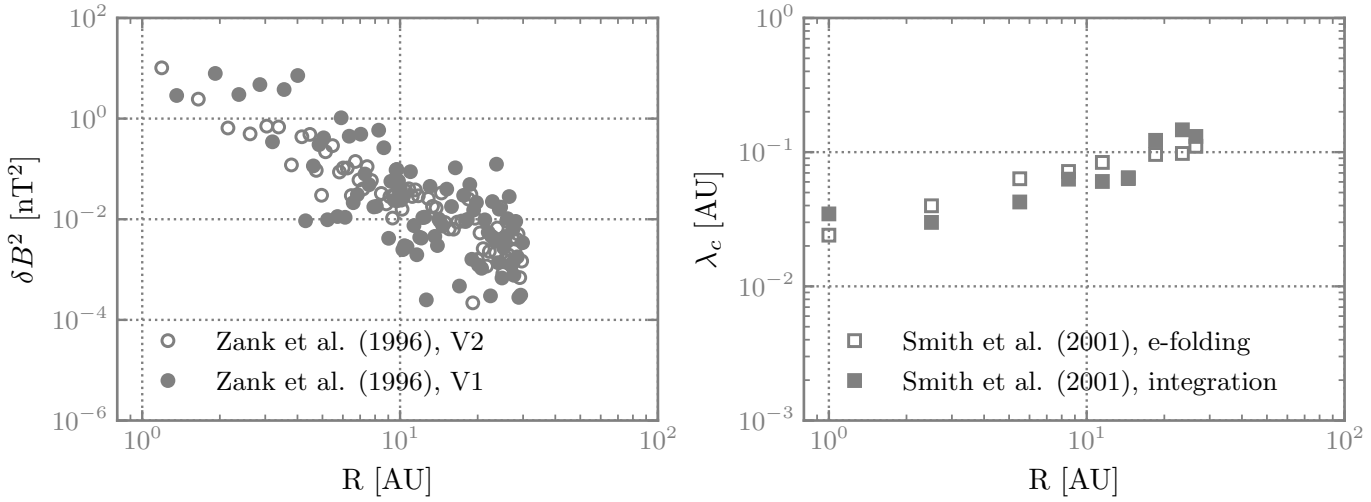

Figure 2.12: *Left panel: Total magnetic variances observed in the ecliptic, for the N-component of the observed magnetic field as a function of radial distance Zank et al. [1996]. Note that the above-mentioned authors reported variances normalised to the magnetic field magnitude at Earth, while the above Figure illustrates these data when denormalised, using a solar minimum value for the HMF magnitude at Earth of 5 nT^2. Right panel: Correlation lengths as a function of radial distance in the ecliptic. Black and white circles represent correlation scales computed with the e-folding and integration methods, respectively Smith et al. [2001].*

(x, y) plane. Assuming again axisymmetric fluctuations, the 2D variance then is

$$\delta B_{2D}^2 = \delta b_{2D,x}^2 + \delta b_{2D,y}^2 = 2\delta b_{2D,x}^2 = 2\delta b_{2D,y}^2. \tag{2.12}$$

By combining the slab and 2D turbulence models, a so-called composite turbulence model is obtained, such that

$$\delta \mathbf{b} = \delta \mathbf{b}_{slab}(z) + \delta \mathbf{b}_{2D}(x, y). \tag{2.13}$$

The influence of composite turbulence on magnetic flux tubes is illustrated in the right panel of Figure 2.11. The (x, y) dependence of the fluctuating component of the magnetic field quickly 'braids and shreds' the flux tubes, leaving no trace of the almost coherent behaviour seen in the left panel of this Figure. Observations suggest that a composite turbulence model with some $70\% - 90\%$ of the energy in the inertial range residing in 2D fluctuations, and the remainder in slab turbulence [see, e.g., *Matthaeus et al.*, 1990; *Bieber et al.*, 1996; *Oughton et al.*, 2015].

The various scattering theories used to derive cosmic ray diffusion coefficients generally require as a basic input some expression modelling the slab and/or 2D turbulence power spectrum [*Shalchi*, 2009]. Any modulation study using such coefficients would then necessarily have to model the spatial and time dependence's of basic turbulence quantities these coefficients are functions of. Typically, information on the spatial variation of at least the magnetic variances and correlation scales is required for modelling purposes. In general, *Voyager* observations show that variances decrease with radial distance, while correlations scales increase [see, e.g., *Zank et al.*, 1996; *Smith et al.*, 2001]. These observations are shown in Figure 2.12.

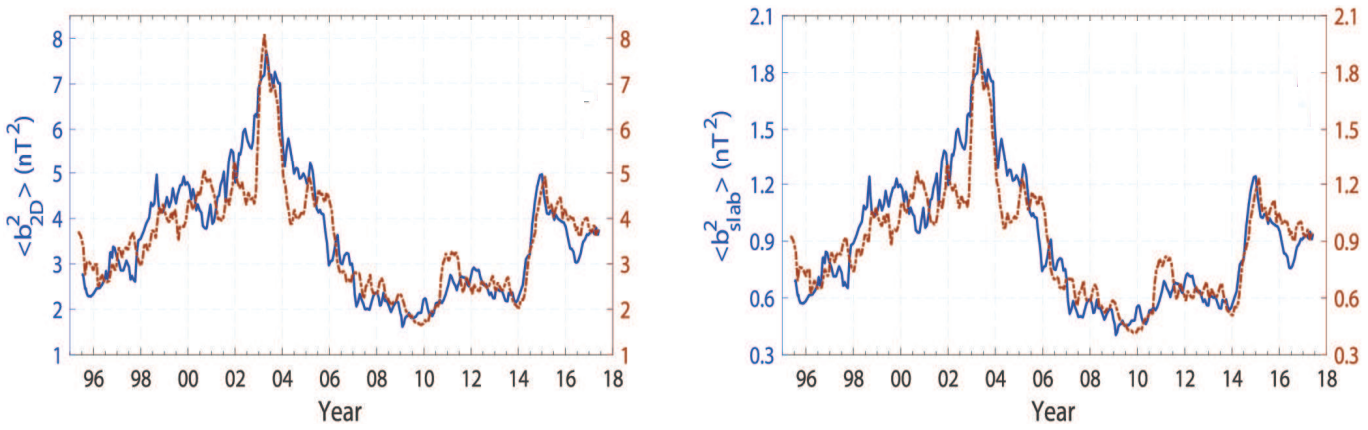

Figure 2.13: *Temporal evolution of the 2D and slab turbulence magnetic energy left and right panels respectively for inward (red dashed) and outward (blue dashed) lines directed HMF. A ratio of 2D and slab energy of* 80% : 20% *has been assumed Zhao et al. [2018].*

Ulysses observations also indicate a strong latitudinal dependence for these quantities [e.g., *Bavassano et al.*, 2000a, b]. These dependences can either be modelled using relatively simple power law fits to observations [e.g. *Burger et al.*, 2008; *Engelbrecht and Burger*, 2010; *Qin and Shen*, 2017; *Shen et al.*, 2019], or by employing one of a growing number of turbulence transport models [e.g. *Engelbrecht and Burger*, 2013, 2015]. Such models can be numerically solved for various turbulence quantities, and have evolved from relatively simple single component models such as those of *Zank et al.* [1996] and *Breech* [2008], to sophisticated two-component models that take into account the anisotropic nature of solar wind turbulence [see, e.g., *Oughton et al.*, 2011; *Zank et al.*, 2012; *Zank et al.*, 2017, 2018], some of which have been coupled with MHD codes [e.g. *Wiengarten et al.*, 2016; *Chhiber et al.*, 2017]. Such models can be used to extrapolate for the spatial behaviour of turbulence quantities in regions of the heliosphere where no spacecraft observations have been made yet. This approach, however, is quite complicated, and computationally expensive. An alternative is to employ parametrised fits to already-existing solutions to these models. This approach is taken in this study, using radial dependences motivated by the solutions to the *Oughton et al.* [2011] model presented by *Engelbrecht and Burger* [2013] and *Engelbrecht and Burger* [2015] as well as solutions to the *Zank et al.* [2017] turbulence transport model presented by *Adhikari et al.* [2017]. Various observational studies have also reported time dependences for various turbulence quantities [see, e.g., *Nel*, 2015; *Zhao et al.*, 2018].

Figure 2.13, taken from *Zhao et al.* [2018], shows a clear the time dependence in both the 2D and slab magnetic energy variances in the left and right panels respectively. Calculated for both inward directed and outward directed HMF with a ratio of 80% : 20% 2D and slab energy. Solar maximum carries around four times more turbulent energy than solar minimum as can be seen for 2003 and 2009 respectively. The present study takes these into account by modelling the behaviour seen in observations using simple sinusoidal temporal scalings. These authors do not report a solar cycle dependence for the correlation scales, and neither does *Wicks et al.* [2011], although such a dependence is reported by *Burger and Engelbrecht* [2018].

2.7 Classification and Transport of Cosmic Rays

Protons make up $\sim 92\%$ of the cosmic rays and carry about $\sim 73\%$ of their total mass and energy, while helium carries about $\sim 17\%$ of the energy and the rest of the other heavier nuclei, make up just 0.4% of the particles and $\sim 7\%$ of the energy respectively. These particles have energies ranging over 14 orders of magnitude in energy up to $\sim 10^{26} eV$ [see, e.g., *Kallenrode*, 2001; *Cummings et al.*, 2016]. There are various types of cosmic rays and they are classified according to their energies and origin.

Galactic cosmic rays (GCRs) enter the heliosphere almost isotropically from interstellar space, and are believed to be accelerated by shocks in the galaxy (like supernova remnants, pulsars, and active galactic nuclei) to very high energies [*Axford*, 1981; *Busching and Potgieter*, 2008; *Fisk and Gloeckler*, 2012]. GCRs have been detected with energies up to 10^{15} eV and beyond. Above this energy, they are believed to originate from extragalactic sources [see, e.g., *Schlaepfer*, 2003; *Aharonian et al.*, 2012]. In this work we are only interested in the modulation of GCRs. As their name suggests, solar energetic particles (SEPs) originate at the Sun, and are accelerated mainly by solar flares, coronal mass ejections and shocks in the interplanetary medium. They have energies up to several hundred MeV, and are observed at Earth for periods varying from hours to a few days at a time, mainly during times of maximum solar activity periods [see, e.g., *Forbush*, 1946; *Balogh et al.*, 2008; *Cliver*, 2008; *Grechnev et al.*, 2008; *Usoskin*, 2008]. Anomalous cosmic rays (ACRs) are formed due to the ionisation of interstellar neutral gas relatively close to the Sun. Neutral particles are ionised by photo-ionisation or by charge exchange and then the new-born ions (called pick-up ions) are transported to the outer heliosphere [see, e.g., *Engelbrecht and Strauss*, 2015]. There they are believed to be accelerated at the solar wind termination shock [see, e.g., *Fisk et al.*, 1974; *Fichtner*, 2001; *Florinski*, 2009; *Gloeckler et al.*, 2009; *Potgieter*, 2010; *Strauss et al.*, 2010]. Jovian electrons are continuously emitted into interplanetary space at a heliocentric radial distance of $\sim$5 au by Jupiter's magnetosphere, and were discovered during the Jupiter fly-by of the *Pioneer 10* spacecraft in 1973 [*Simpson et al.*, 1974]. The Jovian magnetosphere is a relatively strong source of electrons with energies up to $\sim$30 MeV. They are observed at Earth and up to $\sim$10 au from the Sun [see, e.g., *Moses*, 1987; *Ferreira et al.*, 2001; *Ferreira*, 2005; *Heber and Potgieter*, 2008; *Dunzlaff et al.*, 2010; *Vogt et al.*, 2018].

Four major processes govern the modulation of cosmic rays in the heliosphere, namely (1) convection, due to the radially expanding solar wind, (2) energy changes due to adiabatic cooling, (3) diffusion due to the turbulent HMF, and (4) drift due to gradients and curvatures in HMF or any abrupt changes in the field direction [see, e.g., *Potgieter*, 1984; *Ferreira*, 2002; *Langner*, 2004; *Strauss*, 2010]. These processes are described by the [*Parker*, 1965] transport equation (TPE),

$$\frac{\partial f_0(\mathbf{r},p,t)}{\partial t} = \nabla\cdot(\mathbf{K}\cdot\nabla f_0(\mathbf{r},p,t)) - \mathbf{V}_{sw}\cdot\nabla f_0(\mathbf{r},p,t) + \frac{1}{3}(\nabla\cdot\mathbf{V}_{sw})\frac{\partial f_0(\mathbf{r},p,t)}{\partial \ln p} + Q, \tag{2.14}$$

where $f_0(\mathbf{r},p,t)$ is the omnidirectional cosmic-ray distribution function in terms of particle momentum p, and Q is a function denoting cosmic ray sources within the heliosphere itself, set to zero when only galactic cosmic rays are considered. The solar wind velocity is denoted by $\mathbf{V}_{sw}$ and $\mathbf{K}$ is the cosmic-ray diffusion tensor. The term $\mathbf{V}_{sw}\cdot\nabla f_0(\mathbf{r},p,t)$ describes the outward convection of cosmic-rays by the solar wind, whereas the

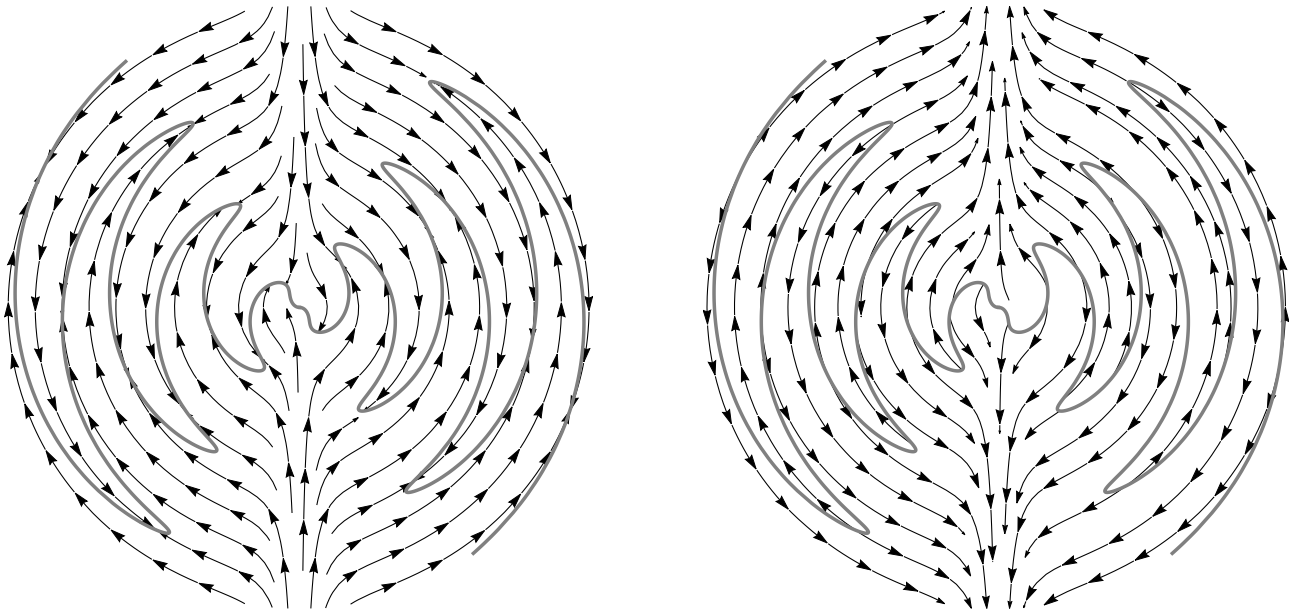

Figure 2.14: *Left panel: Drift pattern for protons during an $A > 0$ solar polarity cycle. Right panel: Drift pattern for protons during an $A < 0$ solar polarity cycle. Although not shown, the drift direction along the wavy current sheet, denoted by the grey solid line, is inwards towards the Sun during $A < 0$ and outwards, away from the Sun, during $A > 0$. Note that the tilt angle is here assumed to be 60° [R.A. Burger (2015), private communication].*

term $1/3\,(\nabla \cdot \mathbf{V}_{sw})\,\partial f_0(\mathbf{r}, p, t)/\partial \ln p$ describes adiabatic energy changes the cosmic rays experience within the heliosphere. The remaining term, $\nabla \cdot (\mathbf{K} \cdot \nabla f_0(\mathbf{r}, p, t))$, describes both cosmic-ray drift and diffusion. The density gradients and curvature in the background HMF result in a drift flux component of which the direction depends on the polarity of the HMF epoch. When the HMF is directed outward from the Sun in the northern hemisphere and inward in the southern hemisphere, positively charge particles are expected to drift into the inner heliosphere mainly over the solar poles and out along the HCS. This period is referred to as a $A > 0$ magnetic polarity epoch. In this phase of the solar cycle, the drift pattern of negatively charged particles is in the opposite direction [see, e.g., *Jokipii and Thomas*, 1981]. When the HMF is directed inward in the northern hemisphere region and outward in the southern hemisphere region, the magnetic polarity is referred to as $A < 0$. This is shown in Figure 2.14 where a positively charged particle would drift along over the poles in the left panel and along the current sheet in the right panel. This is the main contribution to the peak and plateau seen in cosmic ray intensities over the 11 and 22 year cycle [see, e.g., *Reinecke and Potgieter*, 1994; *Potgieter et al.*, 2001].

The diffusion tensor $\mathbf{K}$ is in spherical coordinates in Equation 2.14. The transformation given by *Burger et al.* [2008] is used to convert the diffusion tensor into HMF-aligned coordinates $\mathbf{K}'$, written as

$$\mathsf{K}' = \begin{bmatrix} \kappa_{\parallel} & 0 & 0 \\ 0 & \kappa_{\perp,2} & \kappa_A \\ 0 & -\kappa_A & \kappa_{\perp,3} \end{bmatrix} \tag{2.15}$$

where parallel and perpendicular subscripts indicate diffusion coefficients parallel and perpendicular to the assumed HMF, and κ_A is the drift coefficient [see, e.g., *Forman et al.*, 1974], to a diffusion tensor in spherical coordinates. The present study assumes axisymmetric turbulence and consequently axisymmetric perpendicular diffusion, so that $\kappa_{\perp,2} = \kappa_{\perp,3}$. For more details of the physical meaning of these parameters see, for instance, *Jokipii and Thomas* [1981], *Engelbrecht and Burger* [2013], *Burger* [2012] and *Engelbrecht et al.* [2017]. Note that elements of the above tensor are related to the mean free paths discussed below by $\kappa = v\lambda/3$, with v the particle speed.

The coefficients in the field-aligned tensor can be related to those of the tensor in heliocentric spherical coordinates by [*Burger et al.*, 2008]

$$\begin{aligned}
\kappa_{rr} &= (\kappa_{\parallel}\cos^2\psi + \kappa_{\perp,3}\sin^2\psi)\cos^2\zeta + \kappa_{\perp,2}\sin^2\zeta \\
\kappa_{r\theta} &= (\kappa_{\parallel}\cos^2\psi + \kappa_{\perp,3}\sin^2\psi - \kappa_{\perp,2})\sin\zeta\cos\zeta - \kappa_A\sin\psi \\
\kappa_{r\phi} &= (-\kappa_{\parallel} + \kappa_{\perp,3})\sin\psi\cos\psi\cos\zeta - \kappa_A\cos\psi\sin\zeta \\
\kappa_{\theta r} &= (\kappa_{\parallel}\cos^2\psi + \kappa_{\perp,3}\sin^2\psi - \kappa_{\perp,2})\sin\zeta\cos\zeta + \kappa_A\sin\psi \\
\kappa_{\theta\theta} &= (\kappa_{\parallel}\cos^2\psi + \kappa_{\perp,3}\sin^2\psi)\sin^2\zeta + \kappa_{\perp,2}\cos^2\zeta \\
\kappa_{\theta\phi} &= (-\kappa_{\parallel} + \kappa_{\perp,3})\sin\psi\cos\psi\sin\zeta + \kappa_A\cos\psi\cos\zeta \\
\kappa_{\phi r} &= (-\kappa_{\parallel} + \kappa_{\perp,3})\sin\psi\cos\psi\cos\zeta + \kappa_A\cos\psi\sin\zeta \\
\kappa_{\phi\theta} &= (-\kappa_{\parallel} + \kappa_{\perp,3})\sin\psi\cos\psi\sin\zeta - \kappa_A\cos\psi\cos\zeta \\
\kappa_{\phi\phi} &= \kappa_{\parallel}\sin^2\psi + \kappa_{\perp,3}\cos^2\psi,
\end{aligned} \tag{2.16}$$

with ψ denoting the HMF winding angle, and ζ defined by

$$\begin{aligned}
\sin\psi &= -\frac{B_\phi}{B}; & \cos\psi &= \frac{\sqrt{B_r^2 + B_\theta^2}}{B} \\
\cos\zeta &= \frac{B_r}{\sqrt{B_r^2 + B_\theta^2}}; & \cos\zeta &= \frac{B_\theta}{\sqrt{B_r^2 + B_\theta^2}}.
\end{aligned} \tag{2.17}$$

Note that ζ reduces to zero for a Parker field. The tangent of the winding angle is then

$$\tan\psi = -\frac{B_\phi}{\sqrt{B_r^2 + B_\theta^2}}, \tag{2.18}$$

which reduces to the standard expression given earlier should $B_\theta = 0$, as is the case for a Parker field. The various elements of the diffusion tensor in heliocentric spherical coordinates can then be written as [*Burger et al.*, 2008]

$$\begin{aligned}
\kappa_{rr} &= \kappa_{\parallel} \cos^2\psi + \kappa_{\perp,3} \sin^2\psi \\
\kappa_{r\theta} &= -\kappa_A \sin\psi \\
\kappa_{r\phi} &= (-\kappa_{\parallel} + \kappa_{\perp,3}) \sin\psi \cos\psi \\
\kappa_{\theta r} &= \kappa_A \sin\psi \\
\kappa_{\theta\theta} &= \kappa_{\perp,2} \\
\kappa_{\theta\phi} &= \kappa_A \cos\psi \\
\kappa_{\phi r} &= (-\kappa_{\parallel} + \kappa_{\perp,3}) \sin\psi \cos\psi \\
\kappa_{\phi\theta} &= -\kappa_A \cos\psi \\
\kappa_{\phi\phi} &= \kappa_{\parallel} \sin^2\psi + \kappa_{\perp,3} \cos^2\psi.
\end{aligned} \tag{2.19}$$

The above transformation is valid for heliospheric magnetic field models that, unlike the Parker HMF, have a non-zero θ-component, such as the *Fisk* [1996]-type fields.

The Parker transport equation 2.14 is here solved using the stochastic approach (and code) of *Engelbrecht and Burger* [2015], and can be written in terms of a set of equivalent Itō stochastic differential equations [see, e.g., *Zhang*, 1999a; *Gardiner*, 2004; *Strauss and Effenberger*, 2017]

$$dx_i = A_i(x_i)dt + \sum_j B_{ij}(x_i) \cdot dW_i, \tag{2.20}$$

with $i \in [r, \theta, \phi, E]$ referring to heliocentric spherical polar coordinates (r, θ, ϕ), CR kinetic energy E and $x_i(t)$ describing Itō processes, and dW_i Wiener processes, such that [e.g. *Gardiner*, 2004]

$$dW_i(t) = \eta(t)\sqrt{dt}, \tag{2.21}$$

represents the discretization of a Wiener process, which is a time-stationary Levy process where the time increments have a zero-mean normal distribution [see, e.g., *Gardiner*, 2004; *Zhang*, 1999a; *Strauss and Effenberger*, 2017]. Furthermore, η represents a Gaussian-distributed pseudo-random number that is generated numerically using the Mersenne Twister algorithm developed by *Matsumoto and Nishimura* [1998] in this thesis. Equation 2.20 is solved using the so-called time-backwards approach where the evolution of N pseudo-particles in phase-space is iteratively traced from an initially specified point until they exit at a boundary, whereupon the average cosmic ray intensity at the initial point is calculated using the Euler-Maruyama approximation [*Maruyama Gisiro*, 1955] to perform the numerical integration [for more details see *Pei et al.*, 2010; *Strauss et al.*, 2011; *Engelbrecht and Burger*, 2015; *Strauss and Effenberger*, 2017]:

$$j(x_i^o, t^o) = \frac{1}{N} \sum_{k=1}^{N} j_B(x_{i,k}^e, t_k^e), \tag{2.22}$$

where (x_i^o, t^o) and (x_i^e, t^e) denote the initial and final phase space points and times respectively, and j_B the boundary intensity. Where the choice of N (the number of pseudoparticles) should be motivated by keeping the statistical errors ($\sim 1/\sqrt{N}$ [e.g., *Strauss and Effenberger*, 2017]) low. The tensor $\mathbf{B}$ and vector $\mathbf{A}$ are related to the CR transport coefficients, and are linked to the diffusion tensor $\mathbf{K}$ discussed above such that [*Engelbrecht and Burger*, 2015]

$$\begin{aligned}
\mathsf{B}_{1,1} &= \frac{\sqrt{2(\kappa_{\phi\phi}\kappa_{r\theta}^2 - 2\kappa_{r\phi}\kappa_{r\theta}\kappa_{\theta\phi} + \kappa_{rr}\kappa_{\theta\phi}^2 + \kappa_{\theta\theta}\kappa_{r\phi}^2 - \kappa_{rr}\kappa_{\theta\theta}\kappa_{\phi\phi})}}{\sqrt{\kappa_{\theta\phi}^2 - \kappa_{\theta\theta}\kappa_{\phi\phi}}}, \\
\mathsf{B}_{1,2} &= \frac{\kappa_{r\phi}\kappa_{\theta\phi} - \kappa_{r\theta}\kappa_{\phi\phi}}{\kappa_{\theta\phi}^2 - \kappa_{\theta\theta}\kappa_{\phi\phi}} \sqrt{2(\kappa_{\theta\theta} - \frac{\kappa_{\theta\phi}^2}{\kappa_{\phi\phi}})}, \\
\mathsf{B}_{1,3} &= \frac{\sqrt{2}\kappa_{r\phi}}{\sqrt{\kappa_{\phi\phi}}}, \\
\mathsf{B}_{2,2} &= \frac{\sqrt{2(\kappa_{\theta\theta} - \kappa_{\theta\phi}^2/\kappa_{\phi\phi})}}{r}, \\
\mathsf{B}_{2,3} &= \frac{\kappa_{\theta\phi}}{r}\sqrt{\frac{2}{\kappa_{\phi\phi}}}, \\
\mathsf{B}_{3,3} &= \frac{\sqrt{2\kappa_{\phi\phi}}}{r\sin\theta}, \\
\mathsf{B}_{2,1} &= B_{3,1} = B_{3,2} = 0
\end{aligned} \tag{2.23}$$

and

$$\begin{aligned}
A_r &= \frac{1}{r^2}\frac{\partial}{\partial r}r^2\kappa_{rr} + \frac{1}{r\sin\theta}\frac{\partial}{\partial\phi}\kappa_{r\phi} + \frac{1}{r\sin\theta}\frac{\partial}{\partial\theta}\kappa_{r\theta}\sin\theta - V_{sw} - V_{d,r}, \\
A_\theta &= \frac{1}{r^2}\frac{\partial}{\partial r}r^2\kappa_{r\theta} + \frac{1}{r^2\sin\theta}\frac{\partial}{\partial\theta}\kappa_{\theta\theta}\sin\theta + \frac{1}{r^2\sin\theta}\frac{\partial}{\partial\phi}\kappa_{\theta\phi} - \frac{V_{d,\theta}}{r}, \\
A_\phi &= \frac{1}{r^2\sin^2\theta}\frac{\partial}{\partial\phi}\kappa_{\phi\phi} + \frac{1}{r^2\sin^2\theta}\frac{\partial}{\partial r}r\kappa_{\phi\phi} + \frac{1}{r^2\sin^2\theta}\frac{\partial}{\partial\theta}\kappa_{\theta\phi} - \frac{V_{d,\phi}}{r\sin\theta}, \\
A_E &= \frac{1}{3r^2}\frac{\partial}{\partial r}(r^2V_{sw})\frac{(E+2E_o)}{E+E_o}E,
\end{aligned} \tag{2.24}$$

for a fully three dimensional HMF, with E_o being the CR rest-mass energy. Note that the signs of A_E, as well as of the solar wind and drift speeds V_{sw} and V_d, are chosen to reflect the time-backward nature of the approach taken to solving Equation 2.20, and thus Equation 2.14.

The boundary intensity j_B in Equation 2.22 is constructed to agree with *Voyager* proton observations reported by *Webber et al.* [2008] at 85 au:

$$j_B(85\,\text{au}) = \frac{17.0(P/P_o)^{-2.4}}{2.2 + 2.1(P/P_o)^{-3}}, \tag{2.25}$$

with units of particles $\mathrm{m^2\,s^{-1}\,sr^{-1}\,MeV^{-1}}$, where P_o =1 GV and P in GV. This boundary spectrum is set close to the nominal location of the heliospheric termination shock. A similar approach is taken in previous studies study [see, e.g., *Engelbrecht and Burger*, 2015; *Qin and Shen*, 2017; *Guo and Florinski*, 2016]. This is due to the fact that a considerable amount of modulation has been observed to occur in the heliosheath [see, e.g., *McDonald et al.*, 2000; *Caballero-Lopez et al.*, 2010; *Stone et al.*, 2013; *Zhang et al.*, 2015]. The boundary spectrum is expected to have an 11 year solar cycle dependence based on the report by *Webber et al.* [2008], who see a $\sim 60\%$ to $\sim 70\%$ intensity increase from solar maximum to solar minimum for protons with energies below 400-540 GeV $\mathrm{nuc^{-1}}$. Modelling this time dependence would however require assumptions as to time-dependent modulation conditions in the heliosheath, which are not currently well understood [see, e.g., *Gallana et al.*, 2016; *Burlaga et al.*, 2018]. Thus this boundary spectrum will potentially overestimate GCR proton intensities at 85 au during periods of higher solar activity. Furthermore, assuming a boundary spectrum that is constant as function of latitude may not be an ideal assumption [e.g. *Quenby and Webber*, 2015]. It nevertheless takes into account, to a greater degree, the significant effects of GCR modulation in the heliosheath while limiting the number of *ad hoc* assumptions that need to be made as to the modulation of GCRs in this region of the heliosphere.

2.8 Drift and Diffusion

Given the key role of drift and diffusion in the transport of cosmic rays, the choice of drift and diffusion coefficients used in a numerical modulation code is of utmost importance. Many theories have been proposed to describe how charged particles are scattered in turbulent magnetic fields [for extensive reviews, see e.g. *Shalchi*, 2009; *Shalchi*, 2020], several of which having been used in CR modulation studies. These include quasilinear theory [*Jokipii*, 1966], nonlinear guiding center theory [*Matthaeus et al.*, 2003], extended nonlinear guiding center theory [*Shalchi*, 2006], unified nonlinear theory [*Shalchi*, 2010], and various modifications to NLGC theory [e.g. *Ruffolo et al.*, 2012; *Qin and Zhang*, 2014]. These theories often yield mathematically intractable results [see, e.g., *Engelbrecht and Burger*, 2015; *Dempers and Engelbrecht*, 2020], and require as basic input an expression for the turbulence power spectrum, which in turn requires inputs as to basic turbulence quantities such as the magnetic variances and correlation lengths. These results are usually compared with various estimations of the parallel and perpendicular diffusion coefficients, either from particle transport models, or inferred from particle observations [see, e.g., *Palmer*, 1982; *Chen and Bieber*, 1993; *Bieber et al.*, 1994], or they can be compared with diffusion coefficients calculated using numerical simulations of the transport of test particles in synthetic magnetic turbulence [see, e.g., *Qin et al.*, 2002; *Minnie et al.*, 2007a; *Snodin et al.*, 2016].

In order to acquire simple, tractable expressions for CR mean free paths with realistic spatial and time dependences, a composite slab/2D model for transverse magnetostatic turbulence is assumed [see, e.g., *Matthaeus et al.*, 1995], the slab/2D turbulence power spectra are assumed to have wavenumber-independent energy-containing ranges, and Kolmogorov inertial ranges. This second assumption differs from spacecraft observations [see, e.g., *Bieber et al.*, 1993; *Bruno and Carbone*, 2013], but leads to relatively simple, tractable expressions for the parallel and perpendicular mean free paths [see, e.g, *Engelbrecht and Burger*, 2015, for mean free paths

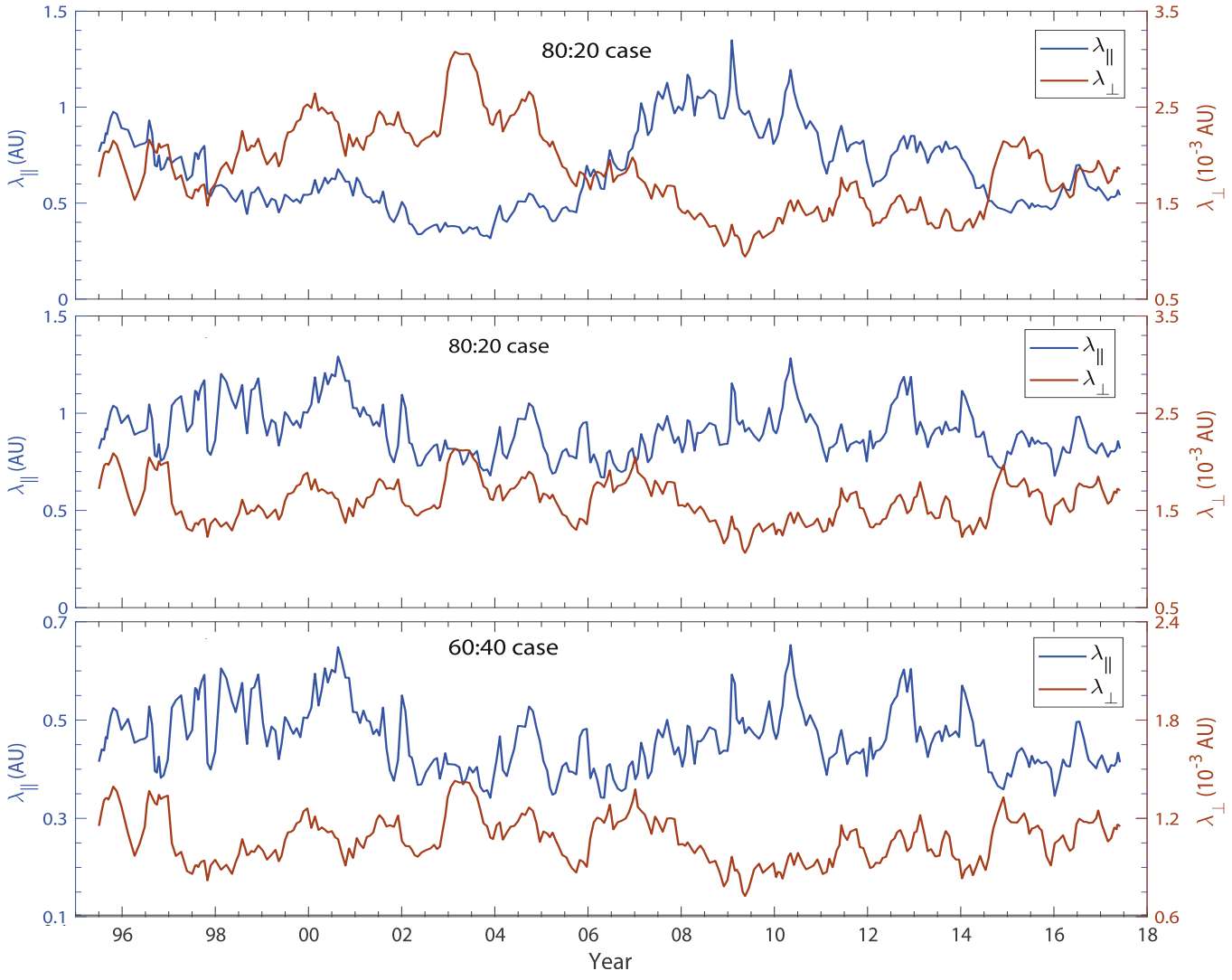

Figure 2.15: *Temporal mean free path evolution profiles for a protons with rigidity 445 MV (corresponding to a 100 MeV protons) in the ecliptic plane at 1 au for outwardly directed HMF. Top panel shows $\lambda_{\parallel}$ (blue line), and perpendicular $\lambda_{\perp}$ (red line), with a 80:20 2D and slab energy ratio in a constant HMF background magnitude of B_0 =5.5 nT. The middle panel is the same as the top panel but for a solar-cycle-dependent background HMF magnitude. The bottom panel is the same as the middle panel, but now with a 60:40 2D and slab energy ratio. Adapted from Zhao et al. [2018].*

derived using more realistic spectral forms]. The parallel MFP expression used here is that constructed by *Burger et al.* [2008] from the *Jokipii* [1966] Quasilinear Theory results of *Teufel and Schlickeiser* [2003] for magnetostatic slab turbulence,

$$\lambda_{\parallel} = \frac{3s}{(s-1)} \frac{R^2}{k_m} \frac{B_o^2}{\delta B_{sl}^2} \left[\frac{1}{4\pi} + \frac{2R^{-s}}{\pi(2-s)(4-s)} \right], \tag{2.26}$$

where $s = 5/3$ is the absolute value of the (Kolmogorov) inertial range spectral index, $R = R_L k_m$ in terms of the maximal proton Larmor radius R_L, and $k_m = 1/\lambda_{sl}$ the wavenumber at which the slab spectrum inertial range commences.

For the perpendicular MFP, the Nonlinear Guiding Center result of *Shalchi et al.* [2004a], as modified by

Burger et al. [2008] to take into account a general ratio of slab to 2D energies [see, e.g., *Bieber et al.*, 1996]. This theory has been shown to provide a reasonably good description of the perpendicular mean free path of charged particles in simulations [*Minnie et al.*, 2007a]. This expression, similar to one derived from the same theory and used by *Zank et al.* [2004], is given by

$$\lambda_{\perp} = \left[\alpha^2\sqrt{3\pi}\frac{2\nu-1}{\nu}\frac{\Gamma(\nu)}{\Gamma(\nu-1/2)}\lambda_{2D}\frac{\delta B_{2D}^2}{B_0^2}\right]^{2/3}\lambda_{\parallel}^{1/3}, \tag{2.27}$$

where $\nu = 5/6$ denotes half the absolute value of the Kolmogorov inertial range spectral index, and $\alpha^2 = 1/3$ after *Matthaeus et al.* [2003]. The above two expressions for the parallel and perpendicular mean free paths have previously been used in numerical cosmic ray modulation studies [*Burger et al.*, 2008; *Engelbrecht and Burger*, 2010; *Sternal et al.*, 2011, e.g.]. Recently, *Zhao et al.* [2018] investigated the solar cycle dependences of similar expressions, shown in Figure 2.15, where observed 2D and slab turbulence fluctuation energies and the corresponding correlation lengths were used to calculate MFPs in the ecliptic plane at 1 au. In the top panel the MFPs are calculated using a constant HMF background magnitude of B_0 =5.5 nT to highlight the effects of the small-scale turbulence quantities on diffusion coefficients. The solar cycle dependence of $\lambda_{\parallel}$ and $\lambda_{\perp}$ can clearly be seen, with $\lambda_{\parallel}$ lower during solar maximum (i.e., 2003) than during solar minimum (i.e., 2009), while $\lambda_{\perp}$ is higher at solar maximum than solar minimum. Note that $\lambda_{\parallel}$ is nearly three orders of magnitude larger than the $\lambda_{\perp}$ at 1 au. In the middle panel a solar-cycle-dependent background HMF magnitude is used to calculate the parallel $\lambda_{\parallel}$ and perpendicular $\lambda_{\perp}$ MFPs. The solar cycle dependence of the MFPs is reduced but still identifiable, since the background HMF magnitude B_0 and turbulence energy δB_{2D}^2 or δB_{slab}^2 occur in ratios in both $\lambda_{\parallel}$ and $\lambda_{\perp}$ expressions. There is a clear anti-correlation between the parallel and perpendicular MFPs. The effect of turbulence anisotropy on MFPs is shown in the bottom panel which is similar to the middle panel but now for a 60:40 2D and slab energy ratio. There is little difference in the temporal tendency of 80:20 and 60:40 2D and slab energy ratio scenarios, apart from a reduction in magnitude for both MFPs for the latter case.

CR drift coefficients have long been known to be reduced in the presence of turbulent fluctuation [see, e.g., *Bieber and Matthaeus*, 1997; *Minnie et al.*, 2007b; *Burger and Visser*, 2010; *Tautz and Shalchi*, 2012]. Recently, *Engelbrecht et al.* [2017] derived an expression for the turbulence-reduced drift lengthscale, following the approach of *Bieber and Matthaeus* [1997], but assuming that the perpendicular decorrelation lengthscale for charged particles travelling in a turbulent magnetic field is proportional to the perpendicular mean free path, as opposed to the field line random walk [see, e.g., *Matthaeus et al.*, 1995] perpendicular diffusion coefficient. According to *Engelbrecht et al.* [2017], the lengthscale corresponding to the turbulence-reduced drift coefficient is given by

$$\lambda_D = R_L\left[1+\frac{\lambda_{\perp}^2}{R_L^2}\frac{\delta B_T^2}{B_0^2}\right]^{-1}, \tag{2.28}$$

with $\delta B_T^2 = \delta B_{sl}^2 + \delta B_{2D}^2$ the total magnetic variance, where the drift lengthscale in the absence of turbuelnce is then R_L [*Forman et al.*, 1974]. This expression provides results in reasonable agreement with numerical test particle simulations [e.g. *Minnie et al.*, 2007b; *Tautz and Shalchi*, 2012] for a broad range of turbulence conditions expected in the heliosphere.

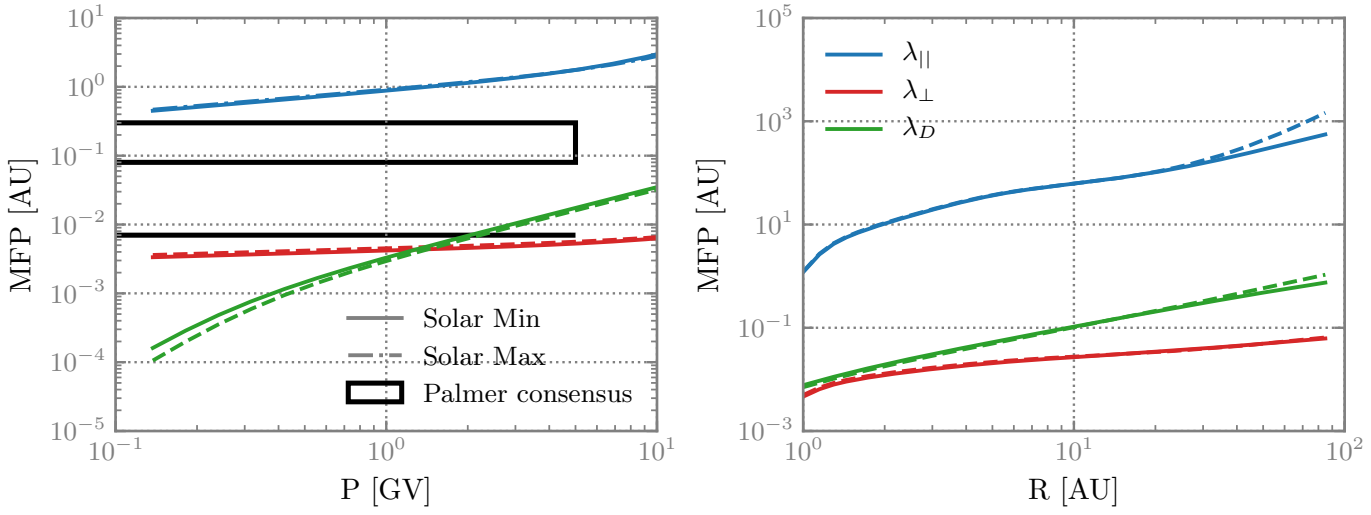

Figure 2.16: *Proton parallel $\lambda_{\parallel}$ and perpendicular $\lambda_{\perp}$ MFPs (blue and red lines) and drift scales λ_D (green lines). Left panel shows these as a function of rigidity at Earth, right panel shows the 1.28 GV MFPs as function of radial distance in the ecliptic plane. Black line and box in the left panel denote Palmer [1982] consensus values for $\lambda_{\perp}$ and $\lambda_{\parallel}$, respectively.*

The diffusion and drift lengthscales discussed above are shown as function of rigidity at Earth (left panel), and radial distance in the ecliptic plane for 1.2 GV protons (right panel) in Figure 2.16, using as inputs various spatial and temporal scalings for large and small scale heliospheric plasma quantities from solar maximum (indicated with dashed lines) to solar minimum (indicated by solid lines). The *Palmer* [1982] consensus of expected values for the MFPs at 1 au in the ecliptic is indicated by the solid black line and box for the perpendicular and parallel MFPs, respectively. The parallel MFP shows the expected $P^{1/3}$ rigidity dependence and is slightly above the Palmer consensus. The perpendicular MFP in accordance with the Palmer consensus displays a relatively flat $P^{1/9}$ dependence. Both the parallel and perpendicular MFP show relatively little solar cycle dependence, with solar maximum perpendicular MFPs only slightly higher than solar minimum MFPs, similar to the behaviour reported by *Zhao et al.* [2018]. The drift scale does however show a clear solar cycle dependence below 1 GV, where it deviates from the expected P^1 dependence the most during solar maximum. This implies, for the case considered here, that drift-reduction over the solar cycle will only play a role in the transport of lower-energy CRs. The parallel MFP and drift scale display a relatively gradual increase toward the outer heliosphere, while the perpendicular MFP remains relatively constant as a function of heliocentric radial distance. The perpendicular MFP again shows very little solar cycle dependence, while the drift scale and the parallel MFP show a moderate solar cycle dependence above ∼30 au, with solar maximum values higher than solar minimum values. These MFPs will be discussed and characterised in greater detail in subsequent chapters.

2.9 Observations

Since the early 1960's the HMF and the solar wind plasma have been measured directly by *in situ* spacecraft. Most of these data at 1 au are available on the OMNI dataset [see, e.g., *King and Papitashvili*, 2005]. A full review of the all the spacecraft missions that have contributed to our understanding of modulation and the heliosphere is beyond the scope of this thesis. What follows is a brief review of some of these spacecraft missions that are relevant to this study, in no particular order. Thereafter, some relevant studies that infer the historic, pre-space age behaviour of quantities such as the heliospheric magnetic field magnitude at Earth will also be summarized.

2.9.1 Space Age Observations

V1 and *V2* [*Behannon et al.*, 1977] were launched in 1977. Both have scientific instruments that are mostly still operating. They have measured solar wind, magnetic fields and energetic particles for more than four decades. These observations have contributed to the understanding of the spatial and temporal variations of GCRs and ACRs at distances now extending to beyond the HP. They are the first to study the outer solar system, the TS, the heliosheath and now the ISM. *V1* travels at 34° heliolatitude out of the ecliptic plane whereas *V2* travels at −28° heliolatitude out of the ecliptic plane. *V1* crossed the termination shock in 2004 at 94.5 au and recently became the first spacecraft to cross the heliopause at 121.6 au and enter interstellar space. *V2*, following behind, crossed the termination shock at ∼84 au in 2007 confirming that the TS is not stationary and that the heliosphere is asymmetric [*Richardson and Stone*, 2009; *Stone et al.*, 2008; *Krimigis et al.*, 2011].

The *International Monitoring Platform spacecraft* (*IMP*) was a series of ten proposed missions in the 60's and early 70's. The *IMP 8* spacecraft was the last these missions to be launched in 1973. There were several energetic particle experiments on-board as well as three plasma experiments and a magnetometer. The mission officially ended in 2001 [*Lockwood and Webber*, 1992; *Webber and Lockwood*, 1995; *Richardson et al.*, 2007; *Ahluwalia and Lopate*, 2007].

Ulysses [*Balogh et al.*, 1992], launched in 1990 into an approximately 6-year orbit of the Sun, was the first spacecraft to explore the 3-dimensional structure of the heliosphere over a large latitude range. It remains the only spacecraft to pass into the north and south polar regions of the Sun, executing fast latitude scans [see, e.g., *Forsyth et al.*, 1996; *Heber et al.*, 1996; *Bavassano et al.*, 2000a]. It has moved towards each of these polar regions three times in a 17-year period before operations ceased in 2009, which included fast latitude scans during two minima and one maximum in the 11-year solar activity cycle.

Instruments aboard the *Advanced Composition Explorer* (*ACE*) [*Stone et al.*, 1998] spacecraft measure the composition of energetic nuclei as they bombard the Earth, providing clues to their origin and subsequent transformations, both near the Sun and in the solar wind. Other *ACE* instruments monitor magnetic fields and shocks in the solar wind at the Earth's orbit. For instance, *ACE* produced the first direct evidence that magnetic fields in the solar wind can merge and join together near the Earth's orbit causing shocks that lead to

particle acceleration [*Fisk and Gloeckler*, 2008], and still provides extremely useful data for turbulence analyses [e.g. *MacBride et al.*, 2008].

The *PAMELA* mission was launched in 2006 and is optimized particularly to measure cosmic rays and their antiparticles, such as positrons and anti-protons [*Casolino et al.*, 2008]. It is also suited to study particles of solar origin and particles trapped in the Earth's magnetosphere. One of the major discovery was the large positron excess with respect to electrons between 10 GeV and 100 GeV as well as the discovery of antiprotons being trapped in the radiation belts around the Earth [*Adriani et al.*, 2011]. For a full comprehensive review of the mission see *Adriani et al.* [2014]

2.9.2 Inferred Historic Observations

Many studies have established that the HMF intensity and many solar wind properties are highly correlated with the solar cycle, for instance the HMF magnitude is correlated to sunspot numbers. These studies analyse *in situ* spacecraft observations [*Smith and Balogh*, 2008; *Lockwood et al.*, 2009; *Connick et al.*, 2009; *Smith et al.*, 2013], ground-based observations [*Lockwood*, 2003], and cosmogenic data such as ^{10}Be and ^{14}C from tree rings and ice cores [*McCracken*, 2007; *McCracken et al.*, 2013; *Caballero-Lopez et al.*, 2019]. From these correlations it is possible to reconstruct the HMF magnitude and solar wind speed well into the past [*Goelzer et al.*, 2013; *Usoskin*, 2017] using sunspot numbers and using geomagnetic data [*Svalgaard and Cliver*, 2010]. There are also modulation-theory derived estimates based on comparisons with cosmogenic nuclides like ^{10}Be, where the HMF magnitude is calculated by inverting solutions of the *Parker* [1965] CR transport equation (TPE) [see, e.g., *Caballero-Lopez et al.*, 2004]. *Cliver and Herbst* [2018, and references therein] provide a comprehensive review of these studies.

Such estimates provide a valuable basis for the comparison of recent solar activity with that of the past [see, e.g., *Svalgaard and Cliver*, 2010; *Barnard et al.*, 2011; *Barnard et al.*, 2018; *Cliver and Herbst*, 2018]. This information can be used to reconstruct cosmic ray modulation on the centennial scale and could also be used to predict future intensities [see, e.g., *Schwadron et al.*, 2014; *Moloto et al.*, 2018, and references therein]. Figure 2.17 shows a compilation of the HMF magnitude, with uncertainties from various estimates going back $\sim$ 600 years, taken from *Cliver and Herbst* [2018]. For the period (1390–2016), reconstructions are based on cosmogenic ^{10}Be observations [*McCracken and Beer*, 2015] (1391–1748); from ^{14}C observations [*Muscheler et al.*, 2016] (1390–1748); from sunspot number counts [*Owens et al.*, 2016a] (1749–1844); from geomagnetic data [*Owens et al.*, 2016b] (1845–1964); and from various spacecraft observations near-Earth for the most recent period (1965–2016). The uncertainty in these estimates increases the further back in history you go, or the more assumptions you need to make about the underlying correlations. These estimates go back far enough to cover the both the Spörer and Maunder grand minima, which some believe should give us a lower limit on solar activity.

Cliver and Ling [2011] derive a lower limit value of $\sim$2.8 nT to which the HMF in the ecliptic would drop if the 11 year solar cycle were to cease. This value is in reasonable agreement with minimum yearly values in Figure 2.17, from *McCracken and Beer* [2015], for both the Maunder and Spörer Grand Minima, but it lies above

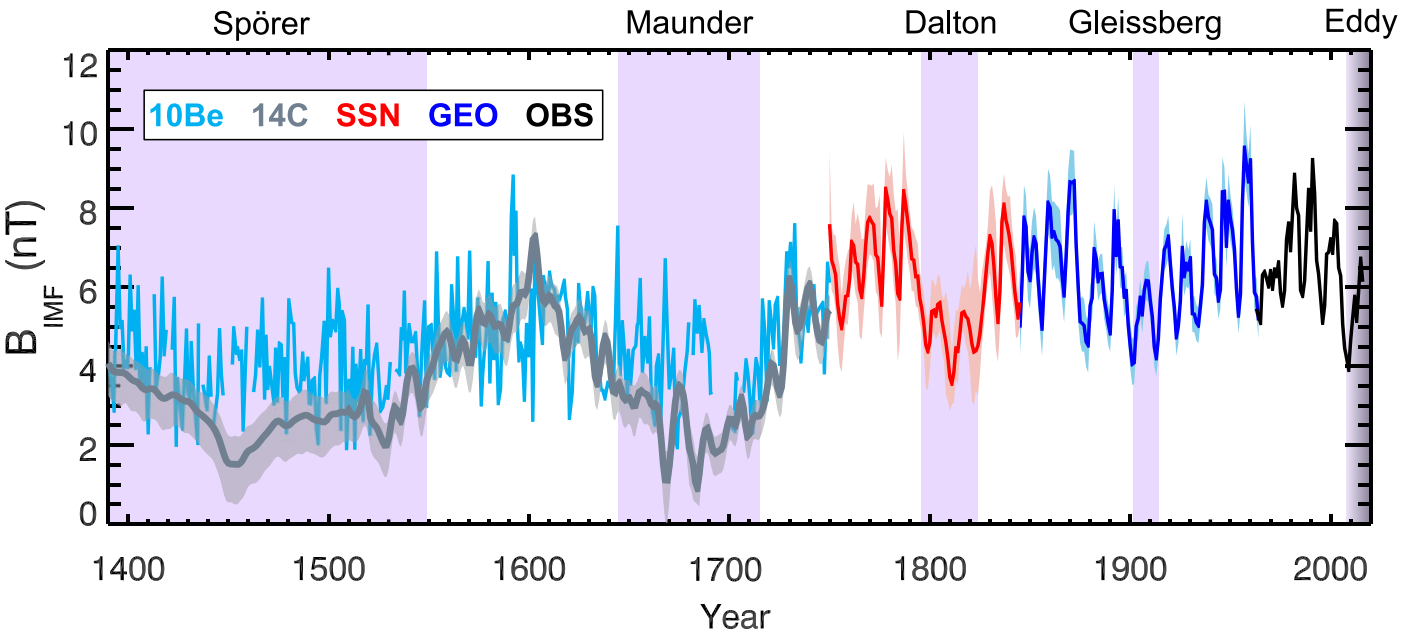

Figure 2.17: *HMF magnitude, with uncertainties, reconstructed from various sources as listed in the text. The grand Spörer, Maunder, Dalton, Gleissberg, and (the proposed) Eddy minima are also indicated [Cliver and Herbst, 2018].*

those of *Muscheler et al.* [2016]. Recent thermodynamic MHD models under extreme scenarios suggest that the lower limit for the HMF might actually be as low as zero nT [e.g. *Rahmanifard et al.*, 2017; *Riley et al.*, 2015], although others expect a 'floor' in the value of the HMF magnitude at some point [e.g. *Svalgaard and Cliver*, 2007]. The implications for cosmic-ray modulation, with a lower HMF limit of zero nT would be very interesting, as the unusual 2009 solar minimum, with a lower HMF magnitude at Earth of ∼3.5 nT, produced the highest cosmic-ray intensities in recorded history, and given the HMF magnitude dependence of the CR transport coefficients, discussed in the next section.

2.10 Summary

A brief overview of the basic topics and concepts important to the heliospheric modulation of CRs is presented in this chapter. The general shape and structure of the heliosphere was introduced, and the implications of solar activity on said structure in terms of the HMF, the solar wind and the heliospheric tilt angle were also discussed.

CR modulation, with particular focus on the transport of galactic cosmic rays, was introduced. The stochastic approach to cosmic ray transport was outlined and a physics-first approach to modelling diffusion coefficients and drift scales, as well as the basic turbulence quantities these, transport parameters are functions of, was introduced. In the chapters that follow these topics will be expanded where the need arises, as they are used to demonstrate the development and implementation of a fully time-dependent *ab initio* cosmic ray modulation model, as well as various applications of this model.

References

Adhikari, L., G. P. Zank, P. Hunana, D. Shiota, R. Bruno, Q. Hu, and D. Telloni, II. transport of nearly incompressible magnetohydrodynamic turbulence from 1 to 75 au, *Astrophys. J.*, *841*, 85, doi: 10.3847/1538-4357/aa6f5d, 2017.

Adriani, O., et al., Cosmic-Ray Electron Flux Measured by the PAMELA Experiment between 1 and 625 GeV, *Phys. Rev. Lett.*, *106*(20), 201101, doi:10.1103/PhysRevLett.106.201101, 2011.

Adriani, O., et al., The PAMELA Mission: Heralding a new era in precision cosmic ray physics, *Phys. Rep.*, *544*(4), 323–370, doi:10.1016/j.physrep.2014.06.003, 2014.

Aharonian, F., A. Bykov, E. Parizot, V. S. Ptuskin, and A. Watson, Cosmic rays in galactic and extragalactic magnetic fields, *Space Sci. Rev.*, *166*, 97–132, 2012.

Ahluwalia, H. S., and C. Lopate, Response of IMP 8 penetrating proton channel to galactic cosmic ray modulation, in *Proceedings of the 30-th International Cosmic Ray Conference (Mexico City)*, vol. 1, pp. 331–334, 2007.

Airapetian, V. S., et al., Impact of space weather on climate and habitability of terrestrial-type exoplanets, *International Journal of Astrobiology*, *19*(2), 136–194, doi:10.1017/S1473550419000132, 2020.

Axford, W. I., The acceleration of galactic cosmic rays, in *Origin of Cosmic Rays*, *IAU Sumposium*, vol. 94, edited by G. Setti, G. Spada, and A. W. Wolfendale, pp. 339–358, 1981.

Badhwar, G. D., D. Stuart Nachtwey, and T. Chui-Hsu Yang, Radiation issues for piloted Mars mission, *Advances in Space Research*, *12*(2-3), 195–200, doi:10.1016/0273-1177(92)90108-A, 1992.

Badhwar, G. D., J. E. Keith, and T. F. Cleghorn, Neutron measurements onboard the space shuttle, *Radiation Measurements*, *33*(3), 235–241, doi:10.1016/S1350-4487(00)00159-1, 2001.

Balogh, A., T. J. Beek, R. J. Forsyth, P. C. Hedgecock, R. J. Marquedant, E. J. Smith, D. J. Southwood, and B. T. Tsurutani, The magnetic field investigation on the ULYSSES mission - Instrumentation and preliminary scientific results, *Astron. Astrophys. Supp.*, *92*(2), 221–236, 1992.

Balogh, A., E. J. Smith, B. T. Tsurutani, D. J. Southwood, R. J. Forsyth, and T. S. Horbury, The heliospheric magnetic field over the south polar region of the Sun, *Science*, *268*, 1007–1010, 1995.

Balogh, A., R. G. Marsden, and E. J. Smith, *The heliosphere near solar minimum. The Ulysses perspective*, 2001.

Balogh, A., L. J. Lanzerotti, and S. T. Suess, *The heliosphere through the solar activity cycle*, Springer-Praxis Books and Springer Science+Business Media, 2008.

Baranov, V. B., and Y. G. Malama, Model of the solar wind interaction with the local interstellar medium - Numerical solution of self-consistent problem, *J. Geophys. Res.*, *98*, 15,157, doi:10.1029/93JA01171, 1993.

Barnard, L., M. Lockwood, M. A. Hapgood, M. J. Owens, C. J. Davis, and F. Steinhilber, Predicting space climate change, *Geophysical Research Letters*, *38*(16), doi:10.1029/2011GL048489, 2011.

Barnard, L., K. McCracken, M. Owens, and M. Lockwood, What can the annual 10be solar activity reconstructions tell us about historic space weather?, *J. Space Weather Space Clim.*, *8*, A23, doi:10.1051/swsc/2018014, 2018.

Batchelor, G., *The theory of homogenous turbulence*, Cambridge University Press, 1970.

Battarbee, M., S. Dalla, and M. S. Marsh, Solar Energetic Particle Transport Near a Heliospheric Current Sheet, *Astrophys. J.*, *836*(1), 138, doi:10.3847/1538-4357/836/1/138, 2017.

Bavassano, B., E. Pietropaolo, and R. Bruno, On the evolution of outward and inward Alfvénic fluctuations in the polar wind, *J. Geophys. Res.*, *105*, 15,959–15,964, 2000a.

Bavassano, B., E. Pietropaolo, and R. Bruno, Alfvénic turbulence in the polar wind: A statistical study on cross helicity and residual energy variations, *J. Geophys. Res.*, *105*, 12,697–12,704, 2000b.

Behannon, K. W., M. H. Acuna, L. F. Burlaga, R. P. Lepping, N. F. Ness, and F. M. Neubauer, Magnetic Field Experiment for Voyagers 1 and 2, *Space Sci. Rev.*, *21*(3), 235–257, doi:10.1007/BF00211541, 1977.

Bieber, J. W., and W. H. Matthaeus, Perpendicular diffusion and drift at intermediate cosmic ray energies, *Astrophys. J.*, *485*, 655, 1997.

Bieber, J. W., J. Chen, W. H. Matthaeus, C. W. Smith, and M. A. Pomerantz, Long-term variations of interplanetary magnetic field spectra with implications for cosmic ray modulation, *J. Geophys. Res.*, *98*(A3), 3585–3603, 1993.

Bieber, J. W., W. H. Matthaeus, C. W. Smith, W. Wanner, M.-B. Kallenrode, and G. Wibberenz, Proton and electron mean free paths: The Palmer consensus revisited, *Astrophys. J.*, *420*(1), 294–306, 1994.

Bieber, J. W., W. Wanner, and W. H. Matthaeus, Dominant two-dimensional solar wind turbulence with implications for cosmic ray transport, *J. Geophys. Res.*, *101*(A2), 2511–2522, 1996.

Breech, B. A., Topics in solar wind turbulence, Ph.D. thesis, University of Delaware, 2008.

Bruno, R., and V. Carbone, The solar wind as a turbulence laboratory, *10*, doi:10.12942/lrsp-2013-2, 2013.

Burger, R. A., Modeling Drift along the Heliospheric Wavy Neutral Sheet, *Astrophys. J.*, *760*, 60, 2012.

Burger, R. A., and N. E. Engelbrecht, Solar-Cycle Dependence of the Correlation Length for the N-Component of the Magnetic Field From IMP and ACE Observations From 1973 to 2016, in *AGU Fall Meeting Abstracts*, vol. 2018, pp. SH21C–3300, 2018.

Burger, R. A., and P. C. Sello, The effect on cosmic ray modulation of a parker field modified by a latitudinal-dependent solar wind speed, *35*, 643–646, 2005.

Burger, R. A., and D. J. Visser, Reduction of Drift Effects due to Solar Wind Turbulence, *Astrophys. J.*, *725*(1), 1366–1372, doi:10.1088/0004-637X/725/1/1366, 2010.

Burger, R. A., T. P. J. Krüger, M. Hitge, and N. E. Engelbrecht, A Fisk-Parker hybrid heliospheric magnetic field with a solar-cycle dependence, *Astrophys. J.*, *674*, 511–519, 2008.

Burger, R. A., T. P. J. Krüger, M. Hitge, and N. E. Engelbrecht, A Fisk-Parker hybrid heliospheric magnetic field with a solar cycle dependance, *Astrophys. J.*, *674*, 511–519, 2008.

Burlaga, L. F., Interplanetary magnetohydrodynamics, *Interplanetary magnetohydrodynamics*, *3*, 1995.

Burlaga, L. F., F. B. McDonald, N. F. Ness, R. Schwenn, A. J. Lazarus, and F. Mariani, Interplanetary flow systems associated with cosmic ray modulation in 1977-1980, *J. Geophys. Res.*, *89*, 6579–6587, doi:10.1029/JA089iA08p06579, 1984.

Burlaga, L. F., V. Florinski, and N. F. Ness, Turbulence in the outer heliosheath, *Astrophys. J.*, *854*, 20, doi:10.3847/1538-4357/aaa45a, 2018.

Busching, I., and M. S. Potgieter, The variability of the proton cosmic ray flux on the Sun's way around the galactic center, *Adv. Space Res.*, *42*, 504–509, 2008.

Caballero-Lopez, R. A., H. Moraal, K. G. McCracken, and F. B. McDonald, The heliospheric magnetic field from 850 to 2000 AD inferred from ^{10}Be records, *J. Geophys. Res.*, *109*(A12102), doi:10.1029/2004JA010633, 2004.

Caballero-Lopez, R. A., H. Moraal, and F. B. McDonald, The Modulation of Galactic Cosmic-ray Electrons in the Heliosheath, *Astrophys. J.*, *725*, 121–127, 2010.

Caballero-Lopez, R. A., N. E. Engelbrecht, and J. D. Richardson, Correlation of Long-term Cosmic-Ray Modulation with Solar Activity Parameters, *Astrophys. J.*, *883*(1), 73, doi:10.3847/1538-4357/ab3c57, 2019.

Cane, H. V., and I. G. Richardson, Interplanetary coronal mass ejections in the near-Earth solar wind during 1996-2002, *Journal of Geophysical Research (Space Physics)*, *108*(A4), 1156, doi:10.1029/2002JA009817, 2003.

Casolino, M., et al., Launch of the space experiment PAMELA, *Advances in Space Research*, *42*(3), 455–466, doi:10.1016/j.asr.2007.07.023, 2008.

Chen, J., and J. W. Bieber, Cosmic-ray anisotropies and gradients in three dimensions, *Astrophys. J.*, *405*, 375–389, 1993.

Chhiber, R., P. Subedi, A. V. Usmanov, W. H. Matthaeus, D. Ruffolo, M. L. Goldstein, and T. N. Parashar, Cosmic-Ray Diffusion Coefficients throughout the Inner Heliosphere from a Global Solar Wind Simulation, *230*(2), 21, doi:10.3847/1538-4365/aa74d2, 2017.

Choudhuri, A. R., *The physics of fluids and plasmas*, 342–350 pp., Cambridge University Press, Cambridge, 1998.

Cliver, E. W., History of research on solar energetic particle (SEP) events: the evolving paradigm, in *Universal heliophysical processes*, *Proceedings IAU Symposium*, vol. 257, edited by N. Gopalswamy and D. F. Webb, pp. 401–412, 2008.

Cliver, E. W., and K. Herbst, Evolution of the Sunspot Number and Solar Wind B Time Series, *Space Science Reviews*, *214*(2), 56, doi:10.1007/s11214-018-0487-4, 2018.

Cliver, E. W., and A. G. Ling, The floor in the solar wind magnetic field revisited, *Solar Physics*, *274*(1), 285–301, doi:https://doi.org/10.1007/s11207-010-9657-610.1007/s11207-010-9657-6, 2011.

Connick, D. E., C. W. Smith, and N. A. Schwadron, The Flux of Open and Toroidal Interplanetary Magnetic Field as a Function of Heliolatitude and Solar Cycle, *Astrophys. J.*, *695*(1), 357–362, doi:10.1088/0004-637X/695/1/357, 2009.

Cranmer, S. R., Coronal holes, *Living Reviews in Solar Physics*, *6*, 3:1–66, 2009.

Cucinotta, F. A., Space Radiation Risks for Astronauts on Multiple International Space Station Missions, *PLoS ONE*, *9*(4), e96,099, doi:10.1371/journal.pone.0096099, 2014.

Cummings, A. C., E. C. Stone, B. C. Heikkila, N. Lal, W. R. Webber, G. Jóhannesson, I. V. Moskalenko, E. Orlando, and T. A. Porter, Galactic Cosmic Rays in the Local Interstellar Medium: Voyager 1 Observations and Model Results, *Astrophys. J.*, *831*(1), 18, doi:10.3847/0004-637X/831/1/18, 2016.

Davidson, P., *Turbulence: an introduction for scientists and engineers*, Oxford University Press, 2004.

Dempers, N., and N. E. Engelbrecht, On the effects of dynamical turbulence on the perpendicular diffusion of low-energy cosmic ray electrons, *65*(8), 2072–2079, doi:10.1016/j.asr.2020.01.040, 2020.

Dialynas, K., S. M. Krimigis, D. G. Mitchell, R. B. Decker, and E. C. Roelof, The bubble-like shape of the heliosphere observed by Voyager and Cassini, *Nature Astronomy*, *1*, 0115, doi:10.1038/s41550-017-0115, 2017.

Dunzlaff, P., A. Kopp, and B. Heber, Propagation of Jovian electron jets in heliospheric flux tube structures, *J. Geophys. Res.*, *115*(A10106), 1–11, 2010.

Engelbrecht, N. E., and R. A. Burger, Effects of various dissipation range onset models on the 26-day variations of low-energy galactic cosmic-ray electrons, *AdvSpRes*, *45*(8), 1015–1025, doi:10.1016/j.asr.2009.12.012, 2010.

Engelbrecht, N. E., and R. A. Burger, An ab initio model for the modulation of galactic cosmic-ray electrons, *Astrophys. J.*, *779*, 158, doi:10.1088/0004-637X/779/2/158, 2013.

Engelbrecht, N. E., and R. A. Burger, An Ab Initio Model for Cosmic-ray Modulation, *Astrophys. J.*, *772*, 46, doi:10.1088/0004-637X/772/1/46, 2013.

Engelbrecht, N. E., and R. A. Burger, Sensitivity of Cosmic-Ray Proton Spectra to the Low-wavenumber Behavior of the 2D Turbulence Power Spectrum, *Astrophys. J.*, *814*(2), 152, doi:10.1088/0004-637X/814/2/152, 2015.

Engelbrecht, N. E., and R. D. Strauss, A detailed calculation of neutral hydrogen ionization frequencies used in turbulence transport models in the heliosphere, *Astron. Astrophys.*, *579*, A120, doi:10.1051/0004-6361/201526056, 2015.

Engelbrecht, N. E., R. D. Strauss, J. A. le Roux, and R. A. Burger, Toward a Greater Understanding of the Reduction of Drift Coefficients in the Presence of Turbulence, *Astrophys. J.*, *841*(2), 107, doi:10.3847/1538-4357/aa7058, 2017.

Engelbrecht, N. E., S. T. Mohlolo, and S. E. S. Ferreira, An Improved Treatment of Neutral Sheet Drift in the Inner Heliosphere, *Astrophys. J. Lett.*, *884*(2), L54, doi:10.3847/2041-8213/ab4ad6, 2019.

Ferreira, S. E. S., The heliospheric transport of galactic cosmic rays and Jovian electrons, Ph.D. thesis, Potchefstroom University for CHE, South Africa, 2002.

Ferreira, S. E. S., The transport of galactic and jovian cosmic ray electrons in the heliosphere, *Adv. Space Res.*, *35*, 586–596, 2005.

Ferreira, S. E. S., M. S. Potgieter, R. A. Burger, B. Heber, and H. Fichtner, Modulation of Jovian and galactic electrons in the heliosphere: 1. Latitudinal transport of a few MeV electrons, *J. Geophys. Res.*, *106*, 24,979–24,987, 2001.

Ferreira, S. E. S., M. S. Potgieter, and K. Scherer, Modeling of the Heliospheric Interface, Magnetic Field, and Cosmic-Ray Transport, *Astrophys. J.*, *659*(2), 1777–1783, doi:10.1086/512848, 2007.

Fichtner, H., Anomalous cosmic rays: Messengers from the outer heliosphere, *Space Sci. Rev.*, *95*, 639–754, 2001.

Fisk, L. A., Motion of the footpoints of heliospheric magnetic field lines at the Sun: Implications for recurrent energetic particle events at high heliographic latitudes, *J. Geophys. Res.*, *101*, 15,547–15,553, 1996.

Fisk, L. A., and G. Gloeckler, Acceleration of Suprathermal Tails in the Solar Wind, *Astrophys. J.*, *686*(2), 1466–1473, doi:10.1086/591543, 2008.

Fisk, L. A., and G. Gloeckler, Acceleration of galactic cosmic rays in the interstellar medium, *Astrophys. J.*, *744*(127), 1–9, 2012.

Fisk, L. A., B. Kozlovsky, and R. Ramaty, An interpretation of the observed oxygen and nitrogen enhancements in low-energy cosmic rays, *Astrophys. J.*, *190*, L35–L37, 1974.

Florinski, V., Pickup ion acceleration at the termination shock and in the heliosheath, *Space Sci. Rev.*, *143*, 111–124, 2009.

Forbush, S. E., Three unusual cosmic-ray increases possibly due to charged particles from the Sun, *Physical Review Letters*, *70*, 771–772, 1946.

Forman, M. A., J. R. Jokipii, and A. J. Owens, Cosmic-ray streaming perpendicular to the mean magnetic field, *Astrophys. J.*, *192*(2), 535–540, 1974.

Forsyth, R. J., A. Balogh, E. J. Smith, G. Erdos, and D. J. McComas, The underlying Parker spiral structure in the Ulysses magnetic field observations, 1990-1994, *J. Geophys. Res.*, *101*(A1), 395–403, 1996.

Fraternale, F., N. V. Pogorelov, J. D. Richardson, and D. Tordella, Magnetic turbulence spectra and intermittency in the heliosheath and in the local interstellar medium, *Astrophys. J.*, *872*, 40, doi:10.3847/1538-4357/aafd30, 2019.

Frisch, U., *Turbulence. The legacy of A.N. Kolmogorov*, 1995.

Fujiki, K., M. Kojima, M. Tokumaru, T. Ohmi, A. Yokobe, K. Hayashi, D. J. McComas, and H. A. Elliott, How did the solar wind structure change around the solar maximum? From interplanetary scintillation observation, *Ann. Geophys.*, *21*, 1257–1261, 2003.

Gallana, L., F. Fraternale, M. Iovieno, S. M. Fosson, E. Magli, M. Opher, J. D. Richardson, and D. Tordella, Voyager 2 solar plasma and magnetic field spectral analysis for intermediate data sparsity, *J. Geophys. Res.*, *121*, 39053,919, doi:10.1002/2015JA021830, 2016.

Gardiner, C. W., *Handbook of Stochastic Methods for Physics, Chemistry and the Natural Sciences*, Springer Series in Synergetics, third ed., Springer, Berlin, 2004.

Gloeckler, G., L. A. Fisk, J. Geiss, M. E. Hill, D. C. Hamilton, R. B. Decker, and S. M. Krimigis, Composition of interstellar neutrals and the origin of anomalous cosmic rays, *Space Sci. Rev.*, *143*, 163–175, 2009.

Goelzer, M. L., C. W. Smith, N. A. Schwadron, and K. G. McCracken, An analysis of heliospheric magnetic field flux based on sunspot number from 1749 to today and prediction for the coming solar minimum, *Journal of Geophysical Research (Space Physics)*, *118*(12), 7525–7531, doi:10.1002/2013JA019404, 2013.

Goldstein, M. L., and D. A. Roberts, Magnetohydrodynamic turbulence in the solar wind, *6*, 4154, doi:10.1063/1.873680, 1999.

Gombosi, T. I., *Physics of the Space Environment*, 211–254 pp., Cambridge University Press, Cambridge, 1998.

Gosling, J. T., and V. J. Pizzo, Formation and Evolution of Corotating Interaction Regions and their Three Dimensional Structure, *Space Sci. Rev.*, *89*, 21–52, 1999.

Grechnev, V. V., et al., An extreme solar event of 20 January 2005: Properties of the flare and the origin of energetic particles, *Solar Physics*, *252*, 149–177, 2008.

Guo, X., and V. Florinski, Galactic Cosmic-Ray Intensity Modulation by Corotating Interaction Region Stream Interfaces at 1 au, *Astrophys. J.*, *826*(1), 65, doi:10.3847/0004-637X/826/1/65, 2016.

Hale, G. E., On the probable existence of a magnetic field in sun-spots, *Astrophys. J.*, *28*, 315, 1908.

Hanslmeier, A., *The Sun and Space Weather*, *Astrophysics and Space Science Library*, vol. 277, Springer Netherlands, 2002.

Hathaway, D. H., The Solar Cycle, *Living Reviews in Solar Physics*, *12*(1), 4, doi:10.1007/lrsp-2015-4, 2015.

Heber, B., Cosmic rays through the solar hale cycle, *Space Sci. Rev. Online*, pp. 1–14, 2011.

Heber, B., and M. S. Potgieter, *Galactic and anomalous cosmic rays throught the solar cycle: New insights from Ulysses*, The heliosphere through the solar activity cycle, Springer-Praxis Books and Springer Science+Business Media, 2008.

Heber, B., et al., Spatial variation of > 40 MeV/n nuclei fluxes observed during the Ulysses rapid latitude scan, *Astron. & Astrophys.*, *316*, 538–546, 1996.

Hitge, M., and R. A. Burger, Cosmic ray modulation with a Fisk-type heliospheric magnetic field and a latitude-dependent solar wind speed, *Adv. Space Res.*, *45*, 18–27, 2010.

Hoeksema, J. T., Large-scale structure of the heliospheric magnetic field: 1976-1991, *in Solar Wind Seven Colloquium*, pp. 191–196, 1992.

Hoyt, D., and K. Schatten, Group sunspot numbers: A new solar activity reconstruction, *Solar Physics*, *179*(1), 189–219, doi:https://doi.org/10.1023/A:100500752781610.1023/A:1005007527816, 1998.

Isenberg, P. A., Turbulence-driven Solar Wind Heating and Energization of Pickup Protons in the Outer Heliosphere, *Astrophys. J.*, *623*, 502–510, 2005.

Jokipii, J. R., Cosmic-Ray Propagation. I. Charged Particles in a Random Magnetic Field, *Astrophys. J.*, *146*, 480, doi:10.1086/148912, 1966.

Jokipii, J. R., and B. T. Thomas, Effects of drift on the transport of cosmic rays IV. Modulation by a wavy interplanetary current sheet, *Astrophys. J.*, *243*, 1115–1122, 1981.

Kallenrode, M. B., *Space physics: an introduction to plasmas and particles in the heliosphere and magnetospheres*, Springer, 2001.

Khabarova, O. V., et al., High-latitude Conic Current Sheets in the Solar Wind, *Astrophys. J.*, *836*(1), 108, doi:10.3847/1538-4357/836/1/108, 2017.

King, J. H., and N. E. Papitashvili, Solar wind spatial scales in and comparisons of hourly Wind and ACE plasma and magnetic field data, *Journal of Geophysical Research (Space Physics)*, *110*(A2), A02104, doi: 10.1029/2004JA010649, 2005.

Kislov, R. A., O. V. Khabarova, and H. V. Malova, Quasi-stationary Current Sheets of the Solar Origin in the Heliosphere, *Astrophys. J.*, *875*(1), 28, doi:10.3847/1538-4357/ab0dff, 2019.

Kolmogorov, A., The Local Structure of Turbulence in Incompressible Viscous Fluid for Very Large Reynolds' Numbers, *Akademiia Nauk SSSR Doklady*, *30*, 301–305, 1941.

Kóta, J., and J. R. Jokipii, Recurrent depressions of galactic cosmic rays in CIRs: 22-year cycle, in *Proceedings of the 27-th International Cosmic Ray Conference (Hamburg)*, vol. 9, pp. 3577–3580, 2001.

Krimigis, S. M., D. G. Mitchell, E. C. Roelof, K. C. Hsieh, and D. J. McComas, Imaging the Interaction of the Heliosphere with the Interstellar Medium from Saturn with Cassini, *Science*, *326*, 971–, doi:10.1126/science.1181079, 2009.

Krimigis, S. M., E. C. Roelof, R. B. Decker, and M. E. Hill, Zero outward flow velocity for plasma in a heliosheath transition layer, *Nature*, *474*, 359–361, 2011.

Krüger, T. P. J., The effect of a Fisk-Parker hybrid magnetic field on cosmic rays in the heliosphere, Master's thesis, North-West University (Potchefstroom Campus), 2005.

Langner, U. W., Effects of termination shock acceleration on cosmic rays in the heliosphere, Ph.D. thesis, Potchefstroom University for CHE, South Africa, 2004.

Leamon, R. J., W. H. Matthaeus, C. W. Smith, G. P. Zank, D. J. Mullan, and S. Oughton, MHD-driven kinetic dissipation in the solar wind and corona, *Astrophys. J.*, *537*, 1054–1062, 2000.

Lockwood, J. A., and W. R. Webber, On the interplanetary cosmic ray latitudinal gradient, *J. Geophys. Res.*, *97*(A6), 8221–8230, 1992.

Lockwood, M., Twenty-three cycles of changing open solar magnetic flux, *Journal of Geophysical Research (Space Physics)*, *108*(A3), 1128, doi:10.1029/2002JA009431, 2003.

Lockwood, M., A. P. Rouillard, and I. D. Finch, THE RISE AND FALL OF OPEN SOLAR FLUX DURING THE CURRENT GRAND SOLAR MAXIMUM, *The Astrophysical Journal*, *700*(2), 937–944, doi:10.1088/0004-637x/700/2/937, 2009.

MacBride, B. T., C. W. Smith, and M. A. Forman, The Turbulent Cascade at 1 AU: Energy Transfer and the Third-Order Scaling for MHD, *Astrophys. J.*, *679*(2), 1644–1660, doi:10.1086/529575, 2008.

Malandraki, O., et al., Current Sheets, Magnetic Islands, and Associated Particle Acceleration in the Solar Wind as Observed by Ulysses near the Ecliptic Plane, *Astrophys. J.*, *881*(2), 116, doi:10.3847/1538-4357/ab289a, 2019.

Marsden, R. G., and R. A. Harrison, Book-Review - the High Latitude Heliosphere, *The Observatory*, *115*, 346, 1995.

Maruyama Gisiro, Continuous markov processes and stochastic equations, *Rendiconti del Circolo Matematico di Palermo*, *4*(1), 48, doi:https://doi.org/10.1007/BF0284602810.1007/BF02846028, 1955.

Matsumoto, M., and T. Nishimura, Mersenne twister: A 623-dimensionally equidistributed uniform pseudo-random number generator, *ACM Trans. Model. Comput. Simul.*, *8*(1), 3–30, doi:10.1145/272991.272995, 1998.

Matthaeus, W. H., and M. Velli, Who needs turbulence? A review of turbulence effects in the heliosphere and on the fundamental process of reconnection, *Space Sci. Rev.*, *160*, 145–168, 2011.

Matthaeus, W. H., M. L. Goldstein, and D. A. Roberts, Evidence for the presence of quasi-two-dimensional nearly incompressible fluctuations in the solar wind, *J. Geophys. Res.*, *95*, 20,673–20,683, 1990.

Matthaeus, W. H., P. C. Gray, D. H. Pontius Jr., and J. W. Bieber, Spatial structure and field-line diffusion in transverse magnetic turbulence, *Phys. Rev. Lett.*, *75*(11), 2136–2139, 1995.

Matthaeus, W. H., G. Qin, J. W. Bieber, and G. P. Zank, Nonlinear collisionless perpendicular diffusion of charged particles, *Astrophys. J. Lett.*, *590*(1), L53–L56, 2003.

Matthaeus, W. H., J. W. Bieber, D. Ruffolo, P. Chuychai, and J. Minnie, Spectral Properties and Length Scales of Two-dimensional Magnetic Field Models, *Astrophys. J.*, *667*, 956–962, doi:10.1086/520924, 2007.

Maunder, E. W., Note on the distribution of sun-spots in heliographic latitude, 1874-1902, *64*, 747, 1904.

McComas, D. J., J. T. Gosling, and R. M. Skoug, Ulysses observations of the irregularly structured mid-latitude solar wind during the approach to solar maximum, *Geophys. Res. Lett.*, *27*(16), 2437–2440, doi:10.1029/2000GL000052, 2000.

McComas, D. J., R. W. Ebert, H. A. Elliott, B. E. Goldstein, J. T. Gosling, N. A. Schwadron, and R. M. Skoug, Weaker solar wind from the polar coronal holes and the whole Sun, *Geophys. Res. Lett.*, *35*(L18103), 1–5, 2008.

McComas, D. J., M. A. Dayeh, H. O. Funsten, G. Livadiotis, and N. A. Schwadron, The Heliotail Revealed by the Interstellar Boundary Explorer, *Astrophys. J.*, *771*, 77, doi:10.1088/0004-637X/771/2/77, 2013.

McCracken, K., J. Beer, F. Steinhilber, and J. Abreu, The Heliosphere in Time, *Space Sci. Rev.*, *176*(1-4), 59–71, doi:10.1007/s11214-011-9851-3, 2013.

McCracken, K. G., Heliomagnetic field near earth, 1428–2005, *Journal of Geophysical Research: Space Physics*, *112*(A9), doi:10.1029/2006JA012119, 2007.

McCracken, K. G., and J. Beer, The Annual Cosmic-Radiation Intensities 1391 - 2014; The Annual Heliospheric Magnetic Field Strengths 1391 - 1983, and Identification of Solar Cosmic-Ray Events in the Cosmogenic Record 1800 - 1983, *Solar Phys.*, *290*(10), 3051–3069, doi:10.1007/s11207-015-0777-x, 2015.

McDonald, F. B., B. Heikkila, N. Lal, and E. C. Stone, The relative recovery of galactic and anomalous cosmic rays in the distant heliosphere: Evidence for modulation in the heliosheath, *jgr*, *105*(A1), 1–8, doi:10.1029/1999JA900372, 2000.

Meyer-Vernet, N., *Basics of the Solar of the Wind*, Cambridge University Press, 2007.

Minnie, J., J. W. Bieber, W. H. Matthaeus, and R. A. Burger, On the Ability of Different Diffusion Theories to Account for Directly Simulated Diffusion Coefficients, *Astrophys. J.*, *663*(2), 1049–1054, doi:10.1086/518765, 2007a.

Minnie, J., J. W. Bieber, W. H. Matthaeus, and R. A. Burger, Suppression of Particle Drifts by Turbulence, *Astrophys. J.*, *670*(2), 1149–1158, doi:10.1086/522026, 2007b.

Moloto, K. D., and N. E. Engelbrecht, A Fully Time-dependent Ab Initio Cosmic-Ray Modulation Model Applied to Historical Cosmic-Ray Modulation, *Astrophys. J.*, *894*(2), 121, doi:10.3847/1538-4357/ab87a2, 2020.

Moloto, K. D., N. E. Engelbrecht, and R. A. Burger, A Simplified Ab Initio Cosmic-ray Modulation Model with Simulated Time Dependence and Predictive Capability, *Astrophys. J.*, *859*(2), 107, doi:10.3847/1538-4357/aac174, 2018.

Moses, D., Jovian Electrons at 1 AU: 1978–1984, *Astrophys. J.*, *313*, 471, doi:10.1086/164987, 1987.

Muscheler, R., F. Adolphi, K. Herbst, and A. Nilsson, The Revised Sunspot Record in Comparison to Cosmogenic Radionuclide-Based Solar Activity Reconstructions, *Solar Physics*, *291*(9-10), 3025–3043, doi:10.1007/s11207-016-0969-z, 2016.

Narita, Y., K.-H. Glassmeier, F. Sahraoui, and M. L. Goldstein, Wave-vector dependence of magnetic-turbulence spectra in the solar wind, *Phys. Rev. Lett.*, *104*, 171,101, doi:10.1103/PhysRevLett.104.171101, 2010.

Nel, A. E., The solar-cycle dependence of the heliospheric diffusion tensor, Master's thesis, North-West University (Potchefstroom Campus), 2015.

Ness, N. F., Heliospheric Magnetic Fields and Termination Shock Crossing: Voyager 1, *ISSI Scientific Reports Series*, *5*, 183–202, 2006.

Ness, N. F., and J. M. Wilcox, Sector structure of the quiet interplanetary magnetic field, *Science*, *148*(3677), 1592–1594, 1965.

Opher, M., A. Loeb, J. Drake, and G. Toth, A small and round heliosphere suggested by magnetohydrodynamic modelling of pick-up ions, *Nature Astronomy*, doi:10.1038/s41550-020-1036-0, 2020.

Oughton, S., W. H. Matthaeus, C. W. Smith, B. Breech, and P. A. Isenberg, Transport of solar wind fluctuations: A two-component model, *J. Geophys. Res.*, *116*, 8105, 2011.

Oughton, S., W. H. Matthaeus, M. Wan, and K. T. Osman, Anisotropy in solar wind plasma turbulence, *373*, 20140152, doi:10.1098/rsta.2014.0152, 2015.

Owens, M. J., and R. J. Forsyth, The Heliospheric Magnetic Field, *Living Reviews in Solar Physics*, *10*(1), 5, doi:10.12942/lrsp-2013-5, 2013.

Owens, M. J., et al., Near-earth heliospheric magnetic field intensity since 1750: 1. sunspot and geomagnetic reconstructions, *Journal of Geophysical Research: Space Physics*, *121*(7), 6048–6063, doi:10.1002/2016JA022529, 2016a.

Owens, M. J., et al., Near-earth heliospheric magnetic field intensity since 1750: 2. cosmogenic radionuclide reconstructions, *Journal of Geophysical Research: Space Physics*, *121*(7), 6064–6074, doi:10.1002/2016JA022550, 2016b.

Palmer, I. D., Transport coefficients of low-energy cosmic rays in interplanetary space, *20*, 335–351, doi:10.1029/RG020i002p00335, 1982.

Parker, E. N., Dynamics of the interplanetary gas and magnetic fields, *Astrophys. J.*, *128*, 664–676, 1958.

Parker, E. N., The Hydrodynamic Theory of Solar Corpuscular Radiation and Stellar Winds., *Astrophys. J.*, *132*, 821, doi:10.1086/146985, 1960.

Parker, E. N., The Stellar-Wind Regions., *Astrophys. J.*, *134*, 20, doi:10.1086/147124, 1961.

Parker, E. N., The passage of energetic charged particles through interplanetary space, *13*, 9–49, 1965.

Parker, E. N., A history of early work on the heliospheric magnetic field, *Astrophys. J.*, *106*(A8), 15,797–15,801, 2001.

Pei, C., J. W. Bieber, R. A. Burger, and J. Clem, A general time-dependent stochastic method for solving Parker's transport equation in spherical coordinates, *Journal of Geophysical Research (Space Physics)*, *115*(A12), A12107, doi:10.1029/2010JA015721, 2010.

Phillips, J. L., et al., Ulysses solar wind plasma observations from pole to pole, *Geophys. Res. Lett.*, *22*, 3301–3304, 1995.

Pogorelov, N. V., et al., Heliosheath Processes and the Structure of the Heliopause: Modeling Energetic Particles, Cosmic Rays, and Magnetic Fields, *Space Science Reviews*, *212*(1-2), 193–248, doi:10.1007/s11214-017-0354-8, 2017.

Potgieter, M. S., The modulation of galactic cosmic rays as described by a three-dimensional drift model, Ph.D. thesis, Potchefstroom University for CHE, South Africa, 1984.

Potgieter, M. S., The dynamic heliosphere, solar activity, and cosmic rays, *Adv. Space Res.*, *46*, 402–412, 2010.

Potgieter, M. S., R. A. Burger, and S. E. S. Ferreira, Modulation of Cosmic Rays in the Heliosphere From Solar Minimum to Maximum: a Theoretical Perspective, *Space Sci. Rev.*, *97*, 295–307, doi:10.1023/A:1011837303094, 2001.

Qin, G., and Z. N. Shen, Modulation of Galactic Cosmic Rays in the Inner Heliosphere, Comparing with PAMELA Measurements, *Astrophys. J.*, *846*(1), 56, doi:10.3847/1538-4357/aa83ad, 2017.

Qin, G., and L. H. Zhang, The Modification of the NonLinear Guiding Center Theory, *Astrophys. J.*, *787*(1), 12, doi:10.1088/0004-637X/787/1/12, 2014.

Qin, G., W. H. Matthaeus, and J. W. Bieber, Subdiffusive transport of charged particles perpendicular to the large scale magnetic field, *Geophys. Res. Lett.*, *29*, 10.1029/2001GL014,035, doi:10.1029/2001GL014035, 2002.

Quenby, J. J., and W. R. Webber, Transient heliosheath modulation, *Monthly Notices of the Royal Astronomical Society*, *453*(2), 1297–1304, doi:10.1093/mnras/stv1482, 2015.

Rahmanifard, F., N. A. Schwadron, C. W. Smith, K. G. McCracken, K. A. Duderstadt, N. Lugaz, and M. L. Goelzer, Inferring the heliospheric magnetic field back through maunder minimum, *The Astrophysical Journal*, *837*(2), 165, doi:10.3847/1538-4357/aa6191, 2017.

Reinecke, J. P. L., and M. S. Potgieter, An explanation for the difference in cosmic ray modulation at low and neutron monitor energies during consecutive solar minimum periods, *J. Geophys. Res.*, *99*(A8), 14,761–14,768, doi:10.1029/94JA00792, 1994.

Richardson, I. G., and H. V. Cane, Near-Earth Interplanetary Coronal Mass Ejections During Solar Cycle 23 (1996 - 2009): Catalog and Summary of Properties, *Solar Phys.*, *264*(1), 189–237, doi:10.1007/s11207-010-9568-6, 2010.

Richardson, I. G., H. V. Cane, T. T. von Rosenvinge, and R. McGuire, IMP 8 GME energetic particle observations over three solar cycles, in *Proceedings of the 30-th International Cosmic Ray Conference (Mexico City)*, vol. 1, pp. 323–326, 2007.

Richardson, J., and C. Wang, The global nature of solar cycle variations of the solar wind dynamic pressure, *Geophys. Res. Lett.*, *26*(5), 561–564, doi:10.1029/1999GL900052, 1999.

Richardson, J. D., and E. C. Stone, The Solar Wind in the Outer Heliosphere, *Space Sci. Rev.*, *143*(1-4), 7–20, doi:10.1007/s11214-008-9443-z, 2009.

Richardson, J. D., K. I. Paularena, A. J. Lazarus, and J. W. Belcher, Radial evolution of the solar wind from IMP 8 to Voyager 2, *Geophys. Res. Lett.*, *22*, 325–328, 1995.

Richardson, J. D., K. I. Paularena, C. Wang, and L. F. Burlaga, The life of a cme and the development of a mir: From the sun to 58 au, *Journal of Geophysical Research: Space Physics*, *107*(A4), SSH 1–1–SSH 1–9, doi:10.1029/2001JA000175, 2002.

Richardson, J. D., C. Wang, and L. F. Burlaga, Correlated solar wind speed, density, and magnetic field changes at Voyager 2, *Geophys. Res. Lett.*, *30*(23), 2207, doi:10.1029/2003GL018253, 2003.

Riley, P., et al., INFERRING THE STRUCTURE OF THE SOLAR CORONA AND INNER HELIOSPHERE DURING THE MAUNDER MINIMUM USING GLOBAL THERMODYNAMIC MAGNETOHYDRODYNAMIC SIMULATIONS, *The Astrophysical Journal*, *802*(2), 105, doi:10.1088/0004-637x/802/2/105, 2015.

Roberts, D. A., J. Giacalone, J. R. Jokipii, M. L. Goldstein, and T. D. Zepp, Spectra of polar heliospheric magnetic fields and implications for field structure, *J. Geophys. Res.*, *112*, 8103–+, doi:10.1029/2007JA012247, 2007.

Ruffolo, D., P. Chuychai, P. Wongpan, J. Minnie, J. W. Bieber, and W. H. Matthaeus, Perpendicular Transport of Energetic Charged Particles in Nonaxisymmetric Two-Component Magnetic Turbulence, *Astrophys. J.*, *686*(2), 1231–1244, doi:10.1086/591493, 2008.

Ruffolo, D., T. Pianpanit, W. H. Matthaeus, and P. Chuychai, Random Ballistic Interpretation of Nonlinear Guiding Center Theory, *Astrophys. J. Lett.*, *747*(2), L34, doi:10.1088/2041-8205/747/2/L34, 2012.

Scheucher, M., K. Herbst, V. Schmidt, J. L. Grenfell, F. Schreier, S. Banjac, B. Heber, H. Rauer, and M. Sinnhuber, Proxima Centauri b: A Strong Case for Including Cosmic-Ray-induced Chemistry in Atmospheric Biosignature Studies, *Astrophys. J.*, *893*(1), 12, doi:10.3847/1538-4357/ab7b74, 2020.

Schlaepfer, H., Cosmic rays, *Spatium*, *11*, 1–15, 2003.

Schrijver, C. J., A. M. Title, K. L. Harvey, N. R. Sheeley, Y. M. Wang, G. H. J. van den Oord, R. A. D. Shine, T. Tarbell, and N. E. Hurlburt, Large-scale coronal heating by the small-scale magnetic field of the sun, *Nature*, *394*, 152, 1998.

Schwadron, N. A., et al., Does the worsening galactic cosmic radiation environment observed by crater preclude future manned deep space exploration?, *Space Weather*, *12*(11), 622–632, doi:10.1002/2014SW001084, 2014.

Schwenn, R., Solar wind sources and their variations over the solar cycle, *Space Sci. Rev.*, *124*, 51–76, 2006.

Shalchi, A., Extended nonlinear guiding center theory of perpendicular diffusion, *Astron. & Astrophys.*, *453*(3), L43–L46, doi:10.1051/0004-6361:20065465, 2006.

Shalchi, A., *Nonlinear Cosmic Ray Diffusion Theories*, Springer, 2009.

Shalchi, A., A Unified Particle Diffusion Theory for Cross-field Scattering: Subdiffusion, Recovery of Diffusion, and Diffusion in Three-dimensional Turbulence, *Astrophys. J. Lett.*, *720*(2), L127–L130, doi:10.1088/2041-8205/720/2/L127, 2010.

Shalchi, A., Perpendicular Transport of Energetic Particles in Magnetic Turbulence, *Space Sci. Rev.*, *216*(2), 23, doi:10.1007/s11214-020-0644-4, 2020.

Shalchi, A., J. W. Bieber, and W. H. Matthaeus, Analytic forms of the perpendicular diffusion coefficient in magnetostatic turbulence, *Astrophys. J.*, *604*(2), 675–686, 2004a.

Shen, Z. N., G. Qin, P. Zuo, and F. Wei, Modulation of Galactic Cosmic Rays from Helium to Nickel in the Inner Heliosphere, *Astrophys. J.*, *887*(2), 132, doi:10.3847/1538-4357/ab5520, 2019.

Siluszyk, A., A. Gil, R. Modzelewska, S. Moskwa, M. Siluszyk, and A. Wawrzynczak, Neural net clustering in the study of electrical grids failures in relation to geomagnetic storms, in *Journal of Physics Conference Series*, *Journal of Physics Conference Series*, vol. 1391, p. 012107, doi:10.1088/1742-6596/1391/1/012107, 2019.

Simpson, J. A., D. L. Chenette, and T. F. Conlon, The detection of Jovian high energy electrons in interplanetary space $\geq$ 1 A.U. from the planet., in *Solar Wind Three*, edited by C. T. Russell, pp. 472–474, 1974.

Smith, C. W., and J. W. Bieber, Solar Cycle Variation of the Interplanetary Magnetic Field Spiral, *Astrophys. J.*, *370*, 435, doi:10.1086/169830, 1991.

Smith, C. W., K. Hamilton, B. J. Vasquez, and R. J. Leamon, Dependence of the dissipation range spectrum of interplanetary magnetic fluctuations on the rate of energy cascade, *Astrophys. J.*, *645*, L85–L88, 2006.

Smith, C. W., N. A. Schwadron, and C. E. DeForest, Decline and Recovery of the Interplanetary Magnetic Field during the Protracted Solar Minimum, *Astrophys. J.*, *775*(1), 59, doi:10.1088/0004-637X/775/1/59, 2013.

Smith, E. J., The sun, solar wind, and magnetic field. I, in *Course CXLII*, edited by A. Ferrari and E. Sindoni, 2000.

Smith, E. J., The heliospheric current sheet, *J. Geophys. Res.*, *106*(A8), 15,819–15,831, 2001.

Smith, E. J., Solar cycle evolution of the heliospheric magnetic field: The Ulysses legacy, *J. Atmospheric and Solar-Terrestrial Physics*, *73*, 277–289, 2011.

Smith, E. J., and A. Balogh, Decrease in heliospheric magnetic flux in this solar minimum: Recent Ulysses magnetic field observations, *Geophys. Res. Lett.*, *35*(22), L22103, doi:10.1029/2008GL035345, 2008.

Smith, W. S., W. H. Matthaeus, G. P. Zank, N. F. Ness, S. Oughton, and J. D. Richardson, Heating of the low-latitude solar wind by dissipation of turbulent magnetic fluctuations, *J. Geophys. Res.*, *106*(A5), 8253–8272, 2001.

Snodgrass, H. B., Magnetic rotation of the solar photosphere, *Astrophys. J.*, *270*(1), 288–299, 1983.

Snodin, A. P., D. Ruffolo, and W. H. Matthaeus, Evolution of the magnetic field line diffusion coefficient and non-Gaussian statistics, *Astrophys. J.*, *827*, 115, doi:10.3847/0004-637X/827/2/115, 2016.

Sternal, O., N. E. Engelbrecht, R. A. Burger, S. E. S. Ferreira, H. Fichtner, B. Heber, A. Kopp, M. S. Potgieter, and K. Scherer, Possible evidence for a Fisk-type heliospheric magnetic field. I. Analyzing Ulysses/KET electron observations, *Astrophys. J.*, *741*(23), 1–12, 2011.

Stix, M., *The Sun: An introduction*, Springer, 2004.

Stone, E. C., A. M. Frandsen, R. A. Mewaldt, E. R. Christian, D. Margolies, J. F. Ormes, and F. Snow, The Advanced Composition Explorer, *Space Sci. Rev.*, *86*, 1–22, doi:10.1023/A:1005082526237, 1998.

Stone, E. C., A. C. Cummings, F. B. McDonald, B. C. Heikkila, N. Lal, and W. R. Webber, Voyager 1 explores the termination shock region and the heliosheath beyond, *309*, 2017–2020, 2005.

Stone, E. C., A. C. Cummings, F. B. McDonald, B. C. Heikkila, N. Lal, and W. R. Webber, An asymmetric solar wind termination shock, *Nature*, *454*, 71–74, 2008.

Stone, E. C., A. C. Cummings, F. B. McDonald, B. C. Heikkila, N. Lal, and W. R. Webber, Voyager 1 Observes Low-Energy Galactic Cosmic Rays in a Region Depleted of Heliospheric Ions, *Science*, *341*(6142), 150–153, doi:10.1126/science.1236408, 2013.

Strauss, R. D., Modelling of anomalous cosmic rays, Master's thesis, North–West University (Potchefstroom Campus), South Africa, 2010.

Strauss, R. D., and F. Effenberger, A hitch-hiker's guide to stochastic differential equations, *Space Sci. Rev.*, *212*, 151–192, doi:10.1007/s11214-017-0351-y, 2017.

Strauss, R. D., M. S. Potgieter, S. E. S. Ferreira, and M. E. Hill, Modelling anomalous cosmic ray oxygen in the heliosheath, *Astron. Astrophys.*, *522*(A35), 1–8, 2010.

Strauss, R. D., M. S. Potgieter, A. Kopp, and I. Büsching, On the propagation times and energy losses of cosmic rays in the heliosphere, *Journal of Geophysical Research (Space Physics)*, *116*(A12), A12105, doi: 10.1029/2011JA016831, 2011.

Strauss, R. D. T., N. Dresing, and N. E. Engelbrecht, Perpendicular Diffusion of Solar Energetic Particles: Model Results and Implications for Electrons, *Astrophys. J.*, *837*(1), 43, doi:10.3847/1538-4357/aa5df5, 2017.

Svalgaard, L., and E. W. Cliver, A Floor in the Solar Wind Magnetic Field, *Astrophys. J. Lett.*, *661*(2), L203–L206, doi:10.1086/518786, 2007.

Svalgaard, L., and E. W. Cliver, Heliospheric magnetic field 1835–2009, *Journal of Geophysical Research: Space Physics*, *115*(A9), doi:10.1029/2009JA015069, 2010.

Svalgaard Leif, and Schatten Kenneth H., Reconstruction of the sunspot group number: The backbone method, *Solar Physics*, *291*(9), 2653–2684, doi:https://doi.org/10.1007/s11207-015-0815-810.1007/s11207-015-0815-8, 2016.

Tautz, R. C., and A. Shalchi, Drift Coefficients of Charged Particles in Turbulent Magnetic Fields, *Astrophys. J.*, *744*(2), 125, doi:10.1088/0004-637X/744/2/125, 2012.

Teufel, A., and R. Schlickeiser, Analytic calculation of the parallel mean free path of heliospheric cosmic rays. II. Dynamical magnetic slab turbulence and random sweeping slab turbulence with finite wave power at small wavenumbers, *Astron. & Astrophys.*, *397*, 15–25, 2003.

Thomas, B. T., and E. J. Smith, The Parker spiral configuration of the interplanetary magnetic field between 1 and 8.5 AU, *J. Geophys. Res.*, *85*(A12), 6861–6867, 1980.

Usoskin, I. G., A history of solar activity over millennia, *Living Reviews in Solar Physics*, *5*, 1–88, 2008.

Usoskin, I. G., A history of solar activity over millennia, *Living Reviews in Solar Physics*, *14*(1), 3, doi: 10.1007/s41116-017-0006-9, 2017.

Usoskin I. G., Kovaltsov G. A., Lockwood M., Mursula K., Owens M., and Solanki S. K., A new calibrated sunspot group series since 1749: Statistics of active day fractions, *Solar Physics*, *291*(9), 2685–2708, doi: https://doi.org/10.1007/s11207-015-0838-110.1007/s11207-015-0838-1, 2016.

Verscharen, D., K. G. Klein, and B. A. Maruca, The multi-scale nature of the solar wind, *Living Reviews in Solar Physics*, *16*(1), 5, doi:10.1007/s41116-019-0021-0, 2019.

Vogt, A., B. Heber, A. Kopp, M. S. Potgieter, and R. D. Strauss, Jovian electrons in the inner heliosphere. Proposing a new source spectrum based on 30 years of measurements, *Astron. Astrophys.*, *613*, A28, doi: 10.1051/0004-6361/201731736, 2018.

Wang, Y. M., Coronal holes and open magnetic flux, *Space Sci. Rpoev.*, *144*, 383–399, 2009.

Wang, Y. M., Semiempirical models of the slow and fast solar wind, *Space Sci. Rev.*, pp. 1–21, 2011.

Washimi, H., T. Tanaka, and G. P. Zank, Time-varying Heliospheric Distance to the Heliopause, *Astrophys. J. Lett.*, *846*(1), L9, doi:10.3847/2041-8213/aa8556, 2017.

Webber, W. R., and J. A. Lockwood, Intensity variations of > 70-MeV cosmic rays measured by Pioneer 10, Voyager 1 & 2 and IMP in the heliosphere during the recovery period from 1992-1995, *Geophys. Res. Lett.*, *22*, 2669–2672, 1995.

Webber, W. R., A. C. Cummings, F. B. McDonald, E. C. Stone, B. Heikkila, and N. Lal, Galactic cosmic ray H and He nuclei energy spectra measured by Voyagers 1 and 2 near the heliospheric termination shock in positive and negative solar magnetic polarity cycles, *Journal of Geophysical Research (Space Physics)*, *113*(A10), A10108, doi:10.1029/2008JA013395, 2008.

Wicks, R. T., T. S. Horbury, C. H. K. Chen, and A. A. Schekochihin, Anisotropy of Imbalanced Alfvénic Turbulence in Fast Solar Wind, *Phys. Rev. Lett.*, *106*, 045,001, 2011.

Wiengarten, T., S. Oughton, N. E. Engelbrecht, H. Fichtner, J. Kleimann, and K. Scherer, A generalized two-component model of solar wind turbulence and ab initio diffusion mean-free paths and drift lengthscales of cosmic rays, *Astrophys. J.*, *833*, 17, doi:10.3847/0004-637X/833/1/17, 2016.

Zank, G. P., W. H. Matthaeus, and C. W. Smith, Evolution of turbulent magnetic fluctuation power with heliospheric distance, *J. Geophys. Res.*, *101*(A8), 17,093–17,107, 1996.

Zank, G. P., G. Li, V. Florinski, W. H. Matthaeus, G. M. Webb, and J. A. Le Roux, Perpendicular diffusion coefficient for charged particles of arbitrary energy, *J. Geophys. Res.*, *109*(A4), A04107, doi:10.1029/2003JA010301, 2004.

Zank, G. P., A. Dosch, P. Hunana, V. Florinski, W. H. Matthaeus, and G. M. Webb, The Transport of Low-frequency Turbulence in Astrophysical Flows. I. Governing Equations, *Astrophys. J.*, *745*, 35, 2012.

Zank, G. P., L. Adhikari, P. Hunana, D. Shiota, R. Bruno, and D. Telloni, Theory and transport of nearly incompressible magnetohydrodynamic turbulence, *Astrophys. J.*, *835*, 147, doi:10.3847/1538-4357/835/2/147, 2017.

Zank, G. P., L. Adhikari, L.-L. Zhao, P. Mostafavi, E. J. Zirnstein, and D. J. McComas, The pickup ion-mediated solar wind, *The Astrophysical Journal*, *869*(1), 23, doi:10.3847/1538-4357/aaebfe, 2018.

Zeitlin, C., et al., Measurements of Energetic Particle Radiation in Transit to Mars on the Mars Science Laboratory, *Science*, *340*(6136), 1080–1084, doi:10.1126/science.1235989, 2013.

Zhang, M., A Path Integral Approach to the Theory of Heliospheric Cosmic-Ray Modulation, *Astrophys. J.*, *510*, 715–725, 1999a.

Zhang, M., X. Luo, and N. Pogorelov, Where is the cosmic-ray modulation boundary of the heliosphere?, *Physics of Plasmas*, *22*(9), 091501, doi:10.1063/1.4928945, 2015.

Zhao, L. L., L. Adhikari, G. P. Zank, Q. Hu, and X. S. Feng, Influence of the Solar Cycle on Turbulence Properties and Cosmic-Ray Diffusion, *Astrophys. J.*, *856*(2), 94, doi:10.3847/1538-4357/aab362, 2018.

CHAPTER 3

A Simplified Ab Initio Cosmic-ray Modulation Model with Simulated Time Dependence and Predictive Capability

The paper presented in this chapter has been published in The Astrophysical Journal: K.D. Moloto et al. — The Astrophysical Journal, 859:107

The Astrophysical Journal, 859:107 (12pp), 2018 June 1 https://doi.org/10.3847/1538-4357/aac174

A Simplified Ab Initio Cosmic-ray Modulation Model with Simulated Time Dependence and Predictive Capability

K. D. Moloto[1], N. E. Engelbrecht[1,2], and R. A. Burger[1]
[1] Center for Space Research, North-West University, Potchefstroom, 2522, South Africa
[2] National Institute for Theoretical Physics (NIThePP), Gauteng, South Africa; n.eugene.engelbrecht@gmail.com
Received 2018 March 6; revised 2018 April 27; accepted 2018 April 27; published 2018 May 30

Abstract

A simplified ab initio approach is followed to model cosmic-ray proton modulation, using a steady-state three-dimensional stochastic solver of the Parker transport equation that simulates some effects of time dependence. Standard diffusion coefficients based on Quasilinear Theory and Nonlinear Guiding Center Theory are employed. The spatial and temporal dependences of the various turbulence quantities required as inputs for the diffusion, as well as the turbulence-reduced drift coefficients, follow from parametric fits to results from a turbulence transport model as well as from spacecraft observations of these turbulence quantities. Effective values are used for the solar wind speed, magnetic field magnitude, and tilt angle in the modulation model to simulate temporal effects due to changes in the large-scale heliospheric plasma. The unusually high cosmic-ray intensities observed during the 2009 solar minimum follow naturally from the current model for most of the energies considered. This demonstrates that changes in turbulence contribute significantly to the high intensities during that solar minimum. We also discuss and illustrate how this model can be used to predict future cosmic-ray intensities, and comment on the reliability of such predictions.

Key words: cosmic rays – diffusion – solar wind – Sun: heliosphere – turbulence

1. Introduction

Astronauts in space encounter severe risks to their health due to their greater exposure to ionizing high-energy cosmic radiation during flights (see, e.g., Badhwar et al. 2001a), in the *International Space Station* itself (e.g., Cucinotta 2014), and especially when engaged in spacewalks (e.g., Zapp et al. 1998). These risks include an increased probability of getting cancer (Cucinotta & Durante 2006), developing issues with their central nervous systems (Cucinotta et al. 2014), and suffering damage to their eyes (Cucinotta et al. 2001a). This radiation also poses a risk to the integrity of electronic systems (Adams 1985; Holmes-Siedle & Adams 2009), which in turn could lead to catastrophic mission failures. These risks become even greater when possible manned missions to Mars are considered (e.g., Cucinotta et al. 2001b; Hellweg & Baumstark-Khan 2007; Zeitlin et al. 2013). Long transit times equal greater exposure to cosmic rays (CRs; Badhwar et al. 2001b; Wilson et al. 2001), and upon arrival, astronauts would receive almost no shielding from the Martian atmosphere, further increasing their exposure to radiation (Zeitlin et al. 2004). Given these risks, it is essential in the near future to have some indication of expected CR intensities so as to attempt to minimize the radiation exposure of future manned missions (see, e.g., Schwadron et al. 2014).

The development of a model to predict galactic CR intensity is the subject of this study. Such a project would require, due to the complexity of the various processes involved in CR transport and modulation, a fully three-dimensional, energy- and time-dependent treatment with a sound theoretical basis to allow reasonable and meaningful extrapolations of various quantities, such as diffusion coefficients, that play a vital role in these processes to be made. In terms of the first requirement for such a model, by employing stochastic techniques to solve the Parker (1965) CR transport equation (TPE), it has now become possible to attempt fully three-dimensional, energy- and time-dependent studies of CR modulation (e.g., Qin & Shen 2017; Strauss & Effenberger 2017, and references therein). This technique has the advantage over finite difference techniques previously used to study CR modulation in that it does not suffer from stability issues, which necessitated a reduction in dimensions or the assumption of a steady state in these prior models (see, e.g., Burger et al. 2008). As to the second condition, most existing models employ ad hoc expressions for diffusion coefficients, which are varied to achieve model agreement with spacecraft observations of CR intensities. Although this approach can lead to excellent agreement with data and some information on the rigidity dependence of diffusion coefficients (see, e.g., Potgieter 1996; Zhang et al. 2007), it is exceedingly difficult to extrapolate the possible future behavior of these diffusion coefficients except in very broad terms. Therefore, the second condition requires an ab initio approach to modulation. In this approach, diffusion and drift coefficients are derived from first principles using various scattering theories (e.g., Teufel & Schlickeiser 2003; Shalchi 2009; Ruffolo et al. 2012; Qin & Zhang 2014), using as inputs for these coefficients results from turbulence transport models (such as those proposed by, e.g., Breech et al. 2008; Oughton et al. 2011; Wiengarten et al. 2016; Weygand et al. 2016; Zank et al. 2017), with outputs in agreement with turbulence observations throughout the heliosphere (for a review of these, see Bruno & Carbone 2013). This has been done with some success by Engelbrecht & Burger (2013a, 2013b), who computed intensity spectra for galactic protons, antiprotons, electrons, and positrons. They found reasonable agreement with existing observations of the same in various parts of the heliosphere, using the same model and diffusion coefficients (taking into account the effects of dissipation range turbulence for low-mass leptons), albeit using a steady-state 3D Alternating Direction Implicit solver for the Parker TPE. The development of a CR modulation model with the particular purpose of providing an estimate of the CR exposure in

The Astrophysical Journal, 859:107 (12pp), 2018 June 1 Moloto, Engelbrecht, & Burger

spaceflight has been the subject of previous studies (see, e.g., Badhwar & O'Neill 1994; O'Neill 2006; Golge et al. 2015; Miyake et al. 2017), but these modulation codes have generally solved the Parker TPE in one spatial dimension or employed the highly simplified force-field approximation of Gleeson & Axford (1968). This is a severe limitation, as all of the relevant processes involved in CR modulation, such as drifts (see, e.g., Jokipii & Thomas 1981; Kóta 2013; Moraal 2013; Potgieter 2013), simply cannot be taken into account using such approaches.

An ab initio approach, then, can more fully model potential time dependences in diffusion and drift coefficients. The present study attempts to construct a first version of just such a model, attempting to simulate large-scale (like the heliospheric magnetic field, HMF) and small-scale (such as the turbulence) heliospheric conditions observed during the last three solar minima and using diffusion and drift coefficients that are theoretically well motivated; in doing so, we try to reproduce simultaneously and self-consistently the galactic CR proton observations taken at Earth during those minima. Incorporating fully time-dependent models for large- and small-scale heliospheric plasma quantities is no small task. Although progress has been made in this regard (see, e.g., Qin & Shen 2017), it is still not entirely clear how to self-consistently construct such a model so that, for instance, the time-dependent HMF model used is divergence free. As an initial step, then, this study implements an effective-value approach to modeling the temporal variations of heliospheric plasma phenomena and turbulence quantities encountered by galactic CR protons as they traverse the heliosphere, focusing on solar minimum conditions as a first step toward self-consistently modeling modulation for a full solar cycle, a complicated procedure in and of itself (see, e.g., Kóta & Jokipii 2001; Kóta 2013). The simulations performed with such a code then are steady state in the sense that the large-scale heliospheric quantities (such as, for example, the HMF magnitude) and small-scale quantities (such as the magnetic variances) are modeled in a steady-state manner relevant to the period of modulation considered. Even though, as an initial step only, solar minimum conditions are considered, the complexity inherent to this problem still provides an excellent test of our current understanding of CR modulation, as, for example, CR transport during different magnetic polarity cycles has to be properly modeled, and the unusual behavior of the last solar minimum also has to be addressed. The remainder of this paper consists of two parts. In the next section, the complete transport model will be described, beginning with assumptions on how the large- and small-scale plasma quantities are modeled and vary between the different solar minima based on spacecraft observations of the HMF magnitude, tilt angle, and various turbulence quantities, such as the magnetic variance. As a preliminary approach to building a fully time-dependent modulation model, this is done using an effective-value approach, which will be discussed in this section. These plasma quantities will be characterized throughout the heliosphere. Turbulence quantities will be modeled using parameterized expressions motivated by spacecraft observations, and where spacecraft data are unavailable, by outputs yielded by the two-component turbulence transport model (TTM) of Oughton et al. (2011). This is a refinement of the approaches taken by Burger et al. (2008), Engelbrecht & Burger (2010), Zhao et al. (2014), and Qin & Shen (2017), who do not consider the results of turbulence transport models in their choices of spatial dependences for turbulence quantities. The use of parameterized expressions for the turbulence quantities, as opposed to turbulence transport model solutions as was done by, e.g., Engelbrecht & Burger (2013a), is motivated by the inherent simplicity of such an approach and the ease of application in concert with the effective approach taken in modeling large-scale quantities in this study. The diffusion tensor used here will be introduced and motivated, and the effects of changes in the large- and small-scale heliospheric quantities on the parallel and perpendicular mean free paths (MFPs) as well as on the turbulence-reduced drift coefficients, will be demonstrated. The final section of this paper will present galactic proton intensities calculated using this model for the years 1987, 1997, and 2009, with comparisons to spacecraft observations. Furthermore, the model will be used to make tentative predictions of CR intensities that may be observed during the next solar minimum, using a range of various heliospheric parameters predicted in several studies as motivation.

2. The Transport Model

The Parker (1965) CR transport equation (TPE) is solved here using the stochastic approach outlined by Engelbrecht & Burger (2015b). This technique is discussed in great detail by, e.g., Zhang (1999), Pei et al. (2010), and Strauss & Effenberger (2017). Ignoring sources of energetic particles (like, for instance, the Jovian source of low-energy electrons (Simpson et al. 1974; Eraker 1982)), the Parker TPE is given by

$$\frac{\partial f_0}{\partial t} = \nabla \cdot (\boldsymbol{K} \cdot \nabla f_0) - \boldsymbol{V}_{\rm sw} \cdot \nabla f_0 + \frac{1}{3}(\nabla \cdot \boldsymbol{V}_{\rm sw}) \frac{\partial f_0}{\partial \ln p}, \quad (1)$$

with $f_0(\boldsymbol{r}, p, t)$ the omnidirectional CR phase-space density as a function of particle position $\boldsymbol{r}$, momentum p, and time t. This quantity is related to the observed CR differential intensity through the relation $j_T = p^2 f_0$ (see, e.g., Moraal 2013). In this equation, various processes act to modulate an incoming local interstellar spectrum (LIS). These are diffusion, drifts due to gradients and curvatures in the HMF as well as along the heliospheric current sheet (HCS), convection due to the solar wind (with speed $V_{\rm sw}$), and adiabatic energy changes. The quantity $\boldsymbol{K}$ denotes the diffusion tensor, given in HMF-aligned coordinates as (see, e.g., Burger et al. 2008)

$$\boldsymbol{K} = \begin{bmatrix} \kappa_{\parallel} & 0 & 0 \\ 0 & \kappa_{\perp,2} & \kappa_A \\ 0 & -\kappa_A & \kappa_{\perp,3} \end{bmatrix}. \quad (2)$$

Off-diagonal elements denote drift coefficients, while diagonal elements denote diffusion coefficients parallel and perpendicular to the background HMF. Note that these diffusion and drift coefficients can be related to a length scale such that $\kappa = v\lambda/3$, with v the particle speed. In the stochastic approach to solving Equation (1), the equation can be written in terms of a set of equivalent Itō stochastic differential equations (see, e.g., Zhang 1999; Gardiner 2004; Strauss & Effenberger 2017),

$$dx_i = A_i(x_i)dt + \sum_j B_{ij}(x_i) \cdot dW_i, \quad (3)$$

with $i \in [r, \theta, \phi, E]$, $x_i(t)$ describing Itō processes and dW_i describing Wiener processes. The quantities A_i and B_{ij} are

The Astrophysical Journal, 859:107 (12pp), 2018 June 1 Moloto, Engelbrecht, & Burger

treated in exactly the same manner as described by Engelbrecht & Burger (2015b). In the present study, Equation (3) is solved as described by Engelbrecht & Burger (2015b) in a time-backward manner. In this approach, the evolution of N pseudoparticles in phase space is iteratively traced from an initially specified point until they exit at a boundary, whereupon the average CR intensity at the initial point is calculated using (see, e.g., Strauss et al. 2011b; Engelbrecht & Burger 2015b; Strauss & Effenberger 2017)

$$j(x_i^o, t^o) = \frac{1}{N}\sum_{k=1}^{N} j_B(x_{i,k}^e, t_k^e), \tag{4}$$

where (x_i^o, t^o) and (x_i^e, t^e) denote the initial and final phase-space points and times, respectively, and j_B is the boundary intensity. In the present study, we choose $N = 10{,}000$ pseudoparticles per energy bin, following, e.g., Strauss & Effenberger (2017) and motivated by the fact that the statistical error is proportional to $1/\sqrt{N}$ (see, e.g., Strauss et al. 2011a and references therein).

This study, like that of Engelbrecht & Burger (2015b) and Qin & Shen (2017), employs a boundary spectrum set inside of the nominal location of the heliospheric termination shock, in this case at 85 au. A similar approach is taken by Guo & Florinski (2016). This is due to the fact that a considerable amount of modulation has been observed to occur in the heliosheath (see, e.g., McDonald et al. 2000; Caballero-Lopez et al. 2010; Stone et al. 2013; Zhang et al. 2015). The input spectrum used in this study has been constructed to agree with *Voyager* observations reported by Webber et al. (2008) at 85 au and is given by

$$j_B(85\ \mathrm{au}) = \frac{17.0(P/P_o)^{-2.4}}{2.2 + 2.1(P/P_o)^3}, \tag{5}$$

in units of particles $\mathrm{m^2\,s^{-1}\,sr^{-1}\,MeV^{-1}}$, $P_o = 1$ GV, and P in GV. As a first approach, we ignore the effects of charge-sign-dependent modulation on this input spectrum. Future studies will take this into account.

The present study seeks to model heliospheric conditions over consecutive solar minima. As such, during these periods, the solar wind speed has been observed to show a latitudinal dependence, assuming values of $\sim$800 $\mathrm{km\,s^{-1}}$ over the poles and $\sim$400 $\mathrm{km\,s^{-1}}$ in the ecliptic plane (see, e.g., McComas et al. 2000). This is modeled as a function of colatitude θ using a hyperbolic tangent function,

$$V_{\mathrm{sw}}(\theta) = 400\begin{cases}\dfrac{3}{2} - \dfrac{1}{2}\tanh\left[8(\theta - \pi/2 + \alpha + \delta_t)\right], & \theta \leqslant \pi/2;\\ \dfrac{3}{2} + \dfrac{1}{2}\tanh\left[8(\theta - \pi/2 - \alpha - \delta_t)\right], & \theta > \pi/2\end{cases}, \tag{6}$$

in units of $\mathrm{km\,s^{-1}}$, with $\delta_t = \pi/9$ radians and α denoting the heliospheric tilt angle. The HMF is here described by the Parker (1958) field. The temporal variations of these large-scale plasma quantities, including those of the HCS tilt angle, are modeled using an effective-value approach (see, e.g., Nagashima & Morishita 1980a, 1980b). This approach takes into account the fact that it takes the solar wind and the HMF embedded in it over a year to reach the outer limits of the heliosphere (Nagashima & Morishita 1980b). Thus, even if a CR particle could traverse the whole heliosphere instantaneously, it would still experience approximately at least the last year's worth of the solar wind, magnetic fields, and tilt angles. In this study, the intensities measured at a certain time are associated with the average of at least the preceding year's worth of tilt angle values as measured close to the Sun. Thus, any intensity measured on a particular day must be associated with a running average of at least the previous year's worth of tilt angle, magnetic field, and solar wind data, a fact supported by the heliospheric residence times of CRs reported by Strauss et al. (2011b). Figure 1 shows radial model values for the tilt angle as found on the Wilcox Solar Observatory Web site. The spot value, indicated by the blue line, shows the tilt angle as it is measured, and the 16 and 20 month effective tilt angles show the running average calculated over the 16 and 20 month window preceding the date shown, respectively, with these interval lengths being informed, as noted above, by CR residence times as well as by the time it takes the plasma to propagate from Earth out to 100 au. It is these 16 month-averaged tilt angles that we use as inputs for this quantity pertaining to particular points in time in the solar cycle. The short-term variations in the tilt angle are smoothed out, which is to be expected since we are applying an average. A consequence of applying the effective tilt angle is that it leads to a time shift with respect to the original data. The time shift is one-half of the period over which the effective tilt angle is calculated, thus taking a 16 month effective tilt angle is similar to taking an eight-month time shift. These time-shifted tilt angles are then used as inputs for the heliospheric current sheet, the angular extent of which is modeled here as in Burger (2012) and Engelbrecht & Burger (2015b) as

$$\theta_{ns} = \frac{\pi}{2}\tan^{-1}(\tan\alpha\sin\phi^*), \tag{7}$$

where $\phi^* = \phi + r\Omega/V_{\mathrm{sw}}$. Current sheet drifts and drifts due to gradients and curvatures in the HMF are dealt with as proposed by Burger (2012). An identical effective-value approach is used for the solar wind speed and HMF magnitude at Earth, taken from *OMNI* spacecraft observations, and shown in the middle and bottom panels of Figure 1. More specifically, effective values for the HMF magnitude, solar wind speed, and tilt angle during the solar minimum periods of interest to this study are listed in Table 1.

As to the diffusion tensor, we assume as a point of departure that the composite slab/2D model for turbulence is valid (e.g., Bieber et al. 1994). The parallel MFP used here is constructed from the Quasilinear Theory (QLT; Jokipii 1966) results derived by Teufel & Schlickeiser (2003) and by Burger et al. (2008), and subsequently employed in several numerical modulation studies (e.g., Engelbrecht & Burger 2013a, 2015b). This parallel MFP expression, derived assuming a slab turbulence spectrum with a wavenumber-independent energy-containing range and a Kolmogorov inertial range with spectral index $-s = -5/3$, is given by

$$\lambda_{\parallel} = \frac{3s}{(s-1)}\frac{R^2}{k_m}\frac{B_o^2}{\delta B_{\mathrm{sl}}^2}\left[\frac{1}{4\pi} + \frac{2R^{-s}}{\pi(2-s)(4-s)}\right], \tag{8}$$

where $R = R_L k_m$, with k_m the wavenumber at which the inertial range on the assumed slab spectrum commences, and R_L

The Astrophysical Journal, 859:107 (12pp), 2018 June 1 Moloto, Engelbrecht, & Burger

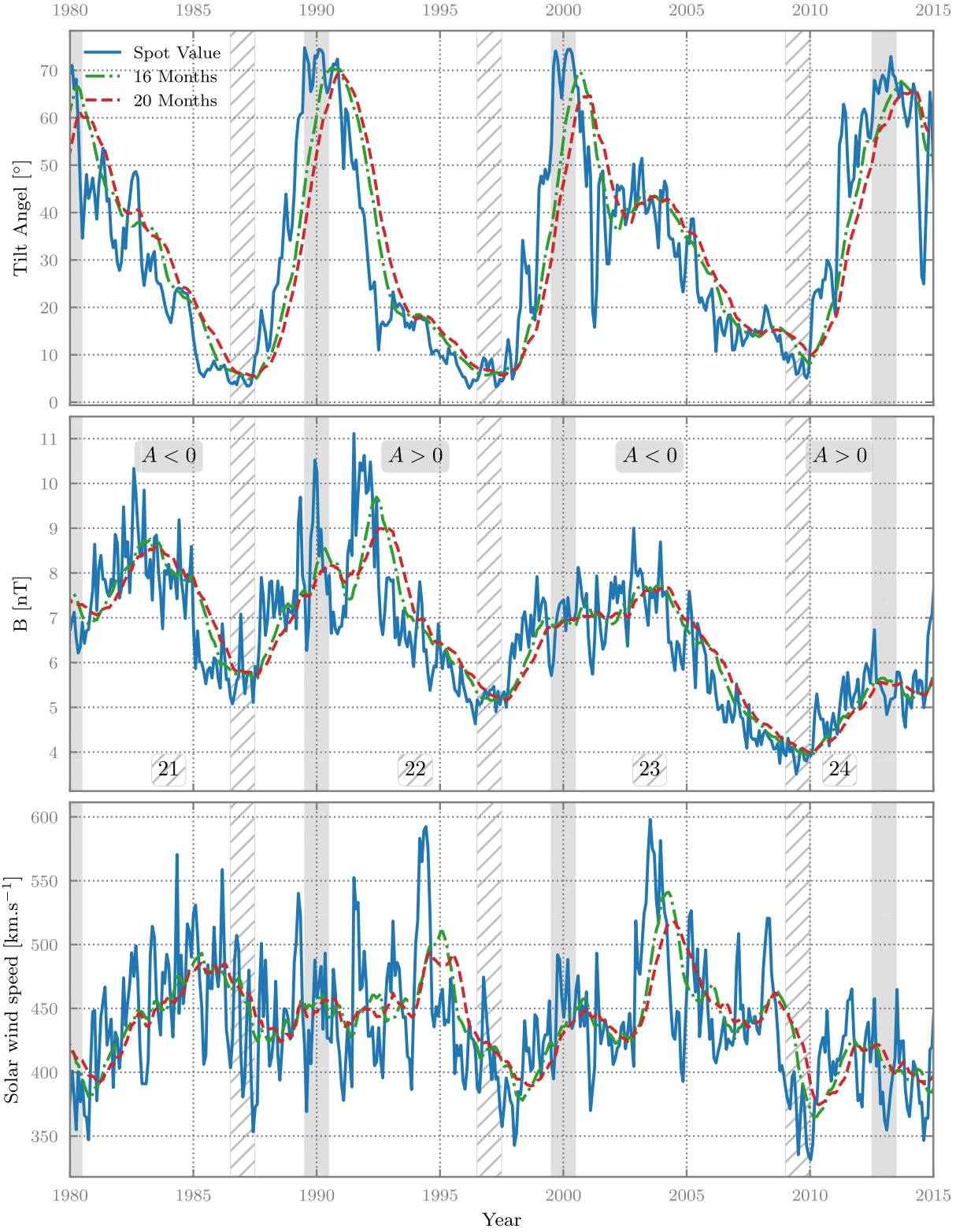

Figure 1. Effective tilt angles (top panel), HMF magnitudes (middle panel), and solar wind speeds (bottom panel) at Earth employed in this study. The hatched bars separate the numbered solar cycles, and the gray bars denote periods of full solar maximum. Red and green lines indicate lagged values. Spot values (blue lines) indicate unlagged quantities as observed at Earth. See the text for details.

denotes the maximal proton Larmor radius. Furthermore, $\delta B_{\rm sl}^2$ denotes the total slab variance, while B_o denotes the uniform background field.

To model the perpendicular MFP, the results for $\lambda_{\parallel}$ are used as inputs for the expression derived from the Nonlinear Guiding Center (NLGC) theory first proposed by Matthaeus et al. (2003) and employed in modulation studies by Burger et al. (2008), who modify the result presented by Shalchi et al. (2004) to take into account an arbitrary ratio of slab to 2D energy. This result is derived for a 2D turbulence power

The Astrophysical Journal, 859:107 (12pp), 2018 June 1 Moloto, Engelbrecht, & Burger

Table 1
Effective Values at Earth for the Magnetic Field, Total Variance, Solar Wind Speed, and the Tilt Angle used as Inputs for the Relevant Solar Minima Runs

	Magnetic Field (nT)	Variance (nT^2)	Solar Wind (km s^{-1})	Tilt Angle (degree)
1987	6.2	10.3	425	9.1
1997	5.1	7.0	412	6.3
2009	3.9	4.1	400	8.2

spectrum assumed to consist of a flat energy-containing range and a Kolmogorov inertial range only. This spectral form is not entirely realistic (see Matthaeus et al. 2007), and expressions for $\lambda_\perp$ assuming more realistic input power spectra have been previously derived (see, e.g., Shalchi et al. 2010; Engelbrecht & Burger 2013a, 2015b) by employing more recent scattering theories (see, e.g., Shalchi 2009, 2010; Qin & Zhang 2014). However, the NLGC expression still provides a tractable analytical expression that does not differ too greatly from the result derived by Engelbrecht & Burger (2013a) for a similar, yet more physically motivated, spectrum. The NLGC perpendicular MFP is given by

$$\lambda_\perp = \left[\alpha^2\sqrt{3\pi}\frac{2\nu-1}{\nu}\frac{\Gamma(\nu)}{\Gamma(\nu-1/2)}\lambda_{2D}\frac{\delta B_{2D}^2}{B_0^2}\right]^{2/3}\lambda_\parallel^{1/3}, \quad (9)$$

where $\nu = 5/6$ denotes half of the assumed inertial range spectral index, δB_{2D}^2 the total 2D variance, and λ_{2D} the length scale corresponding to the wavenumber at which the inertial range on the assumed 2D turbulence power spectrum commences. We follow Matthaeus et al. (2003) in assuming that $\alpha^2 = 1/3$, based on the results of their numerical test-particle simulations of the perpendicular diffusion coefficient.

Numerical test-particle simulations (see, e.g., Minnie et al. 2007b; Tautz & Shalchi 2012) and theory (e.g., Burger 1990; Jokipii 1993; Fisk & Schwadron 1995; le Roux & Webb 2007) show that CR drift coefficients are reduced from the weak-scattering value $\kappa_A = vR_L/3$ (Forman et al. 1974) in the presence of magnetic turbulence. Modeling this self-consistently, however, has proven to be difficult (see Engelbrecht & Burger 2015a, and references therein). In this study, an expression for the turbulence-reduced drift coefficient derived from first principles by Engelbrecht et al. (2017) is employed, providing results in reasonable agreement with numerical test-particle simulations for the range of turbulence conditions expected in the supersonic solar wind. Here, the length scale corresponding to the drift coefficient is given by

$$\lambda_D = R_L\left[1+\frac{\lambda_\perp^2}{R_L^2}\frac{\delta B_T^2}{B_0^2}\right]^{-1}, \quad (10)$$

where δB_T^2 denotes the total (slab and 2D) transverse variance. In conditions where turbulence levels are very low, this expression reduces to the Larmor radius, which is the weak-scattering drift length scale. Note that it is a function of the perpendicular MFP, and thus, from Equation (9), also a function of the parallel MFP.

The above diffusion tensor requires as inputs values for various turbulence quantities, such as the slab and 2D magnetic variances and turnover scales, throughout the heliosphere. The approach of this study entails using parameterized fits to the radial and colatitudinal profiles of the turbulence quantities yielded by the two-component turbulence transport model proposed by Oughton et al. (2011), as solved by, e.g., Engelbrecht & Burger (2013a) for generic solar minimum conditions. These fits are adjusted to be in agreement with observations of various turbulence quantities in different parts of the heliosphere as well as during different solar minima.

Table 2
Values Used in Equation (11) to Obtain Parametric Fits for the Magnetic Variances

		Slab/2D Ratio	ϵ_1
δB^2	Ecliptic	15/85	−2.4
δB^2	Polar	90/10	−2.9

The magnetic variances reported by Zank et al. (1996) can be fitted with a simple power law as a function of radial distance. In doing this, however, the contribution to the slab variance from waves generated due to the formation of pickup ions (see, e.g., Zank 1999; Isenberg 2005) is omitted. This contribution is expected from theory to predominate at high wavenumbers (e.g., Williams & Zank 1994). This is borne out by some observations (e.g., Cannon et al. 2014; Aggarwal et al. 2016; Cannon et al. 2017) and thus would not greatly affect the transport of the highly energetic galactic CR protons considered in this study as they should not affect the level of the slab fluctuation spectrum in the inertial and energy-containing ranges. However, the effects of such waves on lower-energy particles may perhaps be significant (Engelbrecht 2017). The power law used in this study to model the total variance is given by

$$\delta B_T^2 = \delta B_E^2\left(\frac{r}{r_0}\right)^{\epsilon_1}, \quad (11)$$

where δB_E^2 is the value this quantity assumes at Earth ($r_0 = 1$ au), and ϵ_1 is a constant. Effective values for δB_E^2 corresponding to the solar minimum years considered here are listed in Table 1, as reported by Burger et al. (2014). Note that stream-shear effects due to latitudinal increase of the solar wind speed (see, e.g., Breech et al. 2008) are not taken into account in this treatment, in contrast to what is done by Engelbrecht & Burger (2013a, 2015b) when full solutions to the Oughton et al. (2011) TTM are taken into account. The slab/2D anisotropy (see, e.g., Bieber et al. 1994) assumed in the ecliptic plane is that reported by Bieber et al. (1996; although these values vary considerably; see, e.g., Oughton et al. 2015). This ratio is held to a different value over the poles, as turbulence in the fast solar wind has been found to be different from that observed in the slow solar wind (Bavassono et al. 2000a, 2000b). Motivated by the findings of Dasso et al. (2005), who report a preponderance of fluctuations with wavenumbers quasi-parallel to the background magnetic field, we assume a 90/10 slab/2D ratio at high latitudes. Values for ϵ_1 are also chosen differently in the ecliptic region as opposed to those in the poles, since they are motivated by outputs yielded by the Oughton et al. (2011) TTM. These, and the values assumed for the slab/2D ratios, are listed in Table 2. Variances at 1 au over the poles are scaled up by a factor of 2 from the corresponding ecliptic values in Table 1 using a hyperbolic tangent function of the form of Equation (6), following the *Ulysses* observations of increased variances at high latitudes reported by, e.g., Forsyth

The Astrophysical Journal, 859:107 (12pp), 2018 June 1 Moloto, Engelbrecht, & Burger

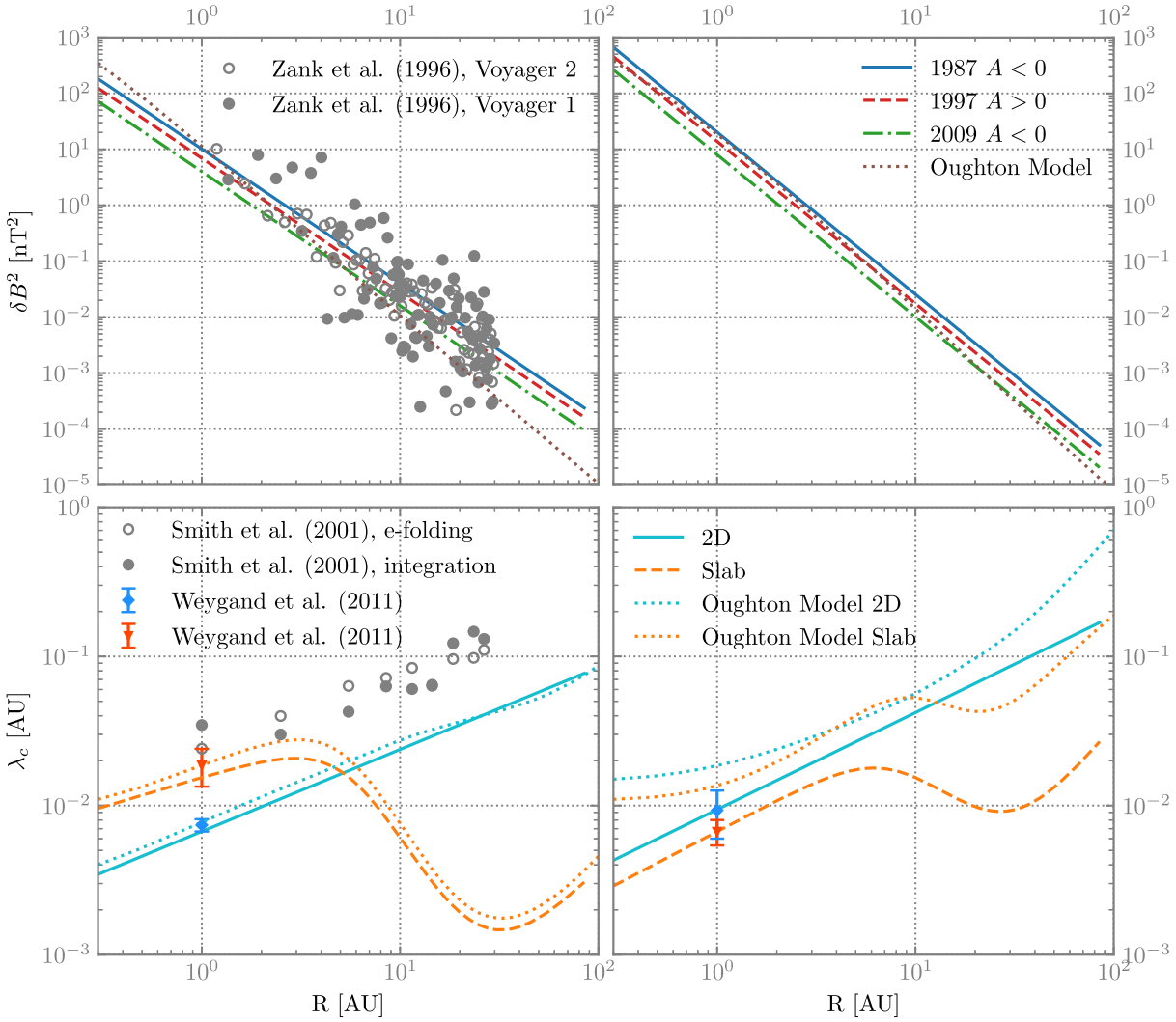

Figure 2. Parametric fits to magnetic variances (top panels) and correlation scales (bottom panels) as a function of heliocentric radial distance in the ecliptic plane (left panels) and at high latitudes (right panels). Observations of these quantities reported by Zank et al. (1996), Smith et al. (2001), and Weygand et al. (2011) are included where applicable. Solutions to the full Oughton et al. (2011) TTM as solved by Engelbrecht & Burger (2013a, 2015b) for generic solar minimum conditions are also shown.

et al. (1996) and Erdös & Balogh (2005). This approach to the latitudinal dependence of magnetic variances is markedly different from that taken by Qin & Shen (2017), who argue, based on observations reported by Perri & Balogh (2010), that this quantity would decrease as one moves toward the polar regions. We choose instead to follow the observations of, e.g., Erdös & Balogh (2005), as such a scaling has been found, when used in the numerical CR modulation model of Engelbrecht & Burger (2013a), to yield galactic CR proton latitude gradients in reasonable agreement with *Ulysses* observations of the same, as reported by Heber et al. (1996). The variances thus modeled are shown as a function of heliocentric radial distance in the top panels of Figure 2, in the ecliptic plane (right panel) and over the poles (left panel). In the inner heliosphere in the ecliptic plane, the modeled variances fall well within the range of *Voyager* observations as reported by Zank et al. (1996), whereas larger values are assumed over the poles.

The spatial dependence of the slab correlation scale yielded by the Oughton et al. (2011) TTM is the most complicated of all the turbulence quantities considered, as solutions where the effects of pickup-ion fluctuations are not ignored are parameterized here. This is under the assumption that, although fluctuations driven by pickup-ion formation may not affect the slab spectral level at the lower wavenumbers where galactic CR protons resonate, they will still affect the correlation function and hence the correlation scale. This is modeled as a combination of power laws that are a function of radial distance in three stages, each with its own power-law index:

$$\lambda_s = \lambda_s^E \left(\frac{r}{r_0}\right)^{\epsilon_1} \left[\frac{1+\left(\frac{r}{r_{c1}}\right)^{f_1}}{1+\left(\frac{r_0}{r_{c1}}\right)^{f_1}}\right]^{\frac{g_1}{f_1}} \left[\frac{1+\left(\frac{r}{r_{c2}}\right)^{f_2}}{1+\left(\frac{r_0}{r_{c2}}\right)^{f_2}}\right]^{\frac{g_2}{f_2}}, \quad (12)$$

where λ_s^E is the value of the 2D correlation scale at Earth, at a radial distance $r = r_0$, under the assumption that the slab correlation scale at Earth is ~2.3 times the 2D scale (within the error bars of the observations reported by Weygand et al. 2011); ϵ_1, ϵ_2, and ϵ_3 are the exponents of the three different radial dependences; r_{c1} and r_{c2} are the radial distance where the radial dependence changes from r^{ϵ_1} to r^{ϵ_2} to r^{ϵ_3} respectively; and $f_1\,(\geqslant 0)$ and $f_2\,(\geqslant 0)$ determine how sharp these transitions are. Large values for f result in abrupt transitions, while smaller

The Astrophysical Journal, 859:107 (12pp), 2018 June 1

Table 3
Values Used in Equation (12) for Parametric Fits to the Oughton et al. (2011) TTM Results Pertaining to the Slab Correlation Scales in the Ecliptic Plane as well as at High Heliographic Latitudes

	λ_s^E (au)	ϵ_1	ϵ_2	ϵ_3	f_1	f_2	r_{c1}	r_{c2}
Ecliptic	15.4×10^{-3}	0.4	−2.7	1.4	3.0	2.50	5.5	25.0
Polar	6.7×10^{-3}	0.7	−1.2	1.4	3.0	3.0	7.25	30.0

Table 4
Values Used in Equation (13) for Parametric Fits to the Oughton et al. (2011) TTM Results Pertaining to the 2D Correlation Scales in the Ecliptic Plane as well as at High Heliographic Latitudes

	λ_{2D}^E	ϵ_{2D}
Ecliptic	6.7×10^{-3}	0.55
Polar	9.4×10^{-3}	0.65

values result in smoother transitions. Values for the parameters used are given in Table 3. In contrast to the slab correlation scale, the 2D correlation scale is modeled as a single power law with indices following the radial dependence of the Oughton et al. (2011) TTM and remaining within the range of the observations of this quantity reported by Smith et al. (2001) such that

$$\lambda_{2D} = \lambda_{2D}^E \left(\frac{r}{r_0}\right)^{\epsilon_{2D}}, \tag{13}$$

with its value at Earth, as well as fitting parameters, given in Table 4. Observed correlation scales for components of the magnetic field at Earth (Wicks et al. 2013) show virtually no change from one solar minimum to the next. Therefore, the 1 au values employed here are kept the same for each solar minimum period considered here. Note that for both slab and 2D correlation scales, different fitting parameters are used in the polar regions, with values at 1 au set to have the ratio of the 2D to slab correlation scales agree with that reported by Dasso et al. (2005) and Weygand et al. (2011) for fast solar wind speed data intervals at Earth. This is motivated by observations indicating that the behavior of turbulence in these conditions is similar to that in the polar regions of the inner heliosphere, where the fast solar wind dominates (Bavassono et al. 2000a, 2000b). Latitudinal changes for both correlation scales are modeled using a hyperbolic tangent function of the form of Equation (6), as with the variances, to change values for λ_s^E and λ_{2D}^E

The bottom panels of Figure 2 show the slab and 2D correlation scales as a function of radial distance in the ecliptic plane and over the poles. Note the decrease in the slab correlation scale beyond ∼4 au for both the colatitudes shown in the figure, which, as noted above, models the effects of pickup-ion formation and occurs at different radial distances depending on latitude, reflecting the outputs yielded by the Oughton et al. (2011) TTM. This fit also takes into account that the slab correlation scale modeled by Engelbrecht & Burger (2013a) relaxes in the outer heliosphere at the resonant scale corresponding to the wavenumber at which the energy due to the formation of pickup ions is injected into the slab fluctuation spectrum (see, e.g., Oughton et al. 2011). The same panels show the monotonically increasing 2D correlation scale, which is consistent with the consistently decreasing 2D variance shown in the top panels of Figure 2. We also show in Figure 2 the corresponding solutions to the full Oughton et al. (2011) TTM as solved by Engelbrecht & Burger (2013a, 2015b) for generic solar minimum conditions usually assumed in CR modulation studies and not specific to a particular solar minimum, as required in this study. The variance scalings employed in this model do not greatly differ in magnitude from those yielded by the TTM, but reflect the different solar-cycle-specific values at Earth employed for this quantity. In the ecliptic plane (top-left panel of Figure 2), the radial dependences are somewhat different, but nevertheless yield results within the spread of the Zank et al. (1996) observations. As to the correlation scales in the ecliptic plane (bottom-left panel of Figure 2), the approximations and full solutions show very similar radial dependences, with deviations in magnitude well within the error bars of the Weygand et al. (2011) observations relevant to the slow solar wind. Over the poles (bottom-right panel of Figure 2), the parameterized solutions differ in magnitude from the TTM solutions, due to the fact that the parameterized solutions were set so as to agree with the Weygand et al. (2011) observations relevant to the fast solar wind. The radial dependences of both the TTM outputs and the parameterized solutions remain, however, very similar.

The effects of the turbulence quantities described above on the spatial and rigidity dependences of the parallel and perpendicular MFPs as well as the corresponding drift length scales described by Equations (8)–(10) are illustrated in Figure 3 for the parameters corresponding to the solar minima of 1987, 1997, and 2009, respectively. The quantities corresponding to these years are denoted in this figure by solid, dotted–dashed, and dashed lines, respectively, while the parallel MFP, perpendicular MFP, and drift scale curves are blue, orange, and green, respectively. Overall, these results are very similar to those reported by Engelbrecht & Burger (2013a), confirming that the current approach, regardless of its simplicity, is a reasonable alternative to the full TTM. The top panel of Figure 3 shows the radial dependences of the 1 GV values of these quantities in the ecliptic plane. Below ∼10 au, $\lambda_\parallel$ remains relatively constant as a function of radial distance, as the monotonic decrease in the slab variance is matched by a corresponding increase in the slab correlation scale. Beyond this distance, however, the effects of the pickup-ion-induced decrease in the slab correlation scale modeled in Equation (12), combined with the continued decrease in the slab variance, cause the parallel MFP to increase steeply until ∼40 au, where the increase in the slab correlation scale seen in Figure 2 causes $\lambda_\parallel$ to flatten out somewhat. The increase of $\lambda_\perp$ with radial distance is less prominent, as the 2D correlation scale is here modeled to increase monotonically with radial distance. The slight kink in the perpendicular MFP beyond ∼10 au is, however, due to the $\lambda_\parallel^{1/3}$ dependence seen in Equation (9). The drift scale at this rigidity assumes weak-scattering values beyond ∼2 au, differing between the different solar minima due to the different values assumed for the HMF magnitude, as listed in Table 1. This is simply due to the fact that, from Equation (10), turbulence levels are too low to significantly reduce the drift coefficient, only becoming large enough to do so in the very inner heliosphere. Note that, for the parameters used here, the drift scale becomes larger than the perpendicular MFP at ∼2 au. In terms of the temporal differences in these quantities, the 1987 parameters yield the smallest drift scales

The Astrophysical Journal, 859:107 (12pp), 2018 June 1

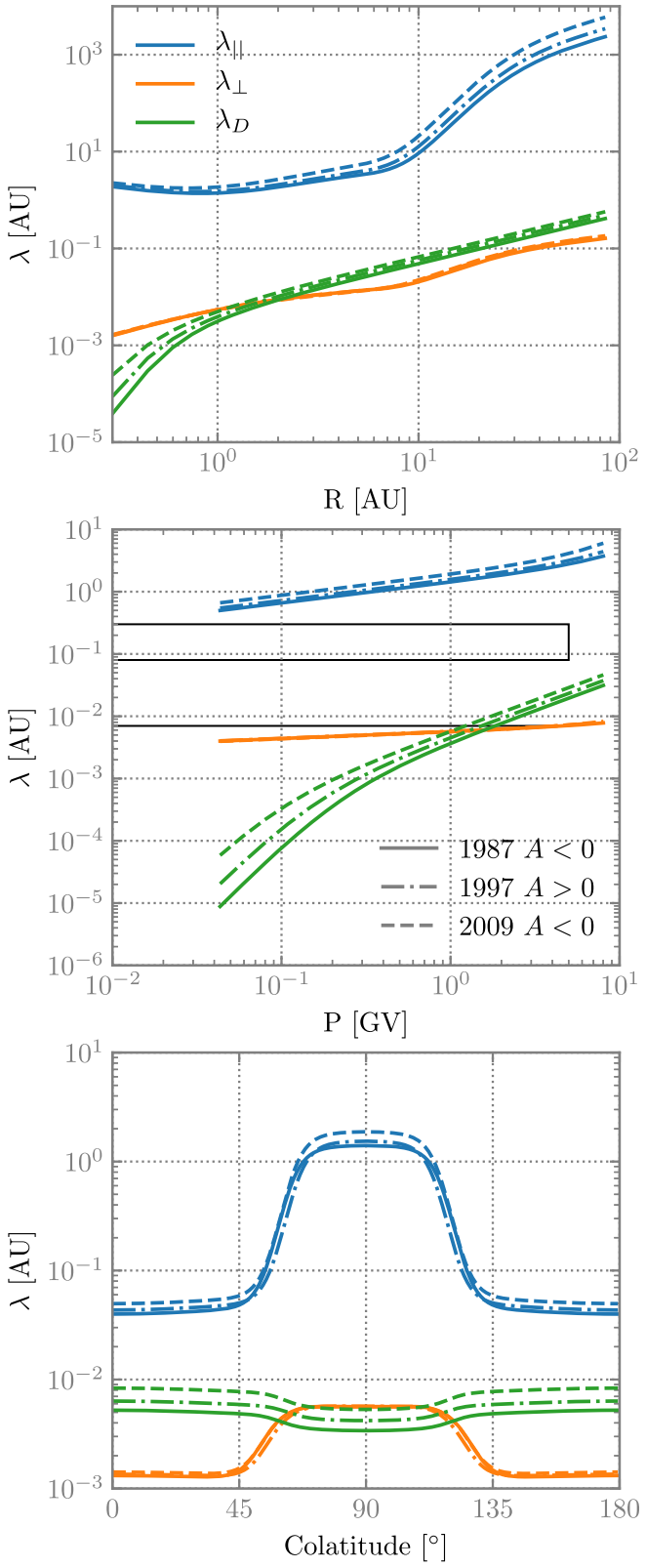

Figure 3. Parallel and perpendicular MFPs (blue and orange lines, respectively) and drift scales (green lines) for protons used in this study. The top panel shows the values for these quantities at 1 GV as a function of radial distance in the ecliptic plane, the middle panel shows them as a function of rigidity at Earth, and the bottom panel shows the 1 GV length scales as a function of colatitude at 1 au. The black line and box in the middle panel denotes the Palmer (1982) consensus values for $\lambda_\perp$ and $\lambda_\parallel$, respectively.

and parallel MFPs, while the 2009 parameters yield the largest values for these quantities, effectively bounding the curves for the 1997 parameters. The perpendicular MFPs for these years remain very similar, with only slight changes discernible.

Considering the rigidity dependences of these quantities at Earth, as shown in the middle panel of Figure 3, the proton parallel MFP shows the expected $P^{1/3}$ dependence throughout the rigidity range considered and remains slightly above the Palmer (1982) consensus range (black box) for the rigidity range considered in this study. The Palmer consensus range, however, does not take into account possible solar-cycle dependences of the MFPs (see, e.g., Bieber et al. 1994 for more details). Chen & Bieber (1993), from an analysis of CR intensities, and Burger et al. (2014) and Zhao et al. (2018), from direct analyses of solar wind turbulence, do, however, report larger MFPs during solar minimum, in qualitative agreement with what is reported here. The perpendicular MFP displays a relatively flat $P^{1/9}$ dependence, in accordance with the Palmer consensus and as expected from Equations (8) and (9). Turning to the drift scale, this quantity displays the P^1 dependence expected of the weak-scattering length scale (which is equal to the Larmor radius of the particle in question) beyond ~2 GV, deviating significantly from that dependence below this rigidity. This implies that, for the parameters of this model, drift-reduction effects due to turbulence will only play a significant role in the transport of lower-energy CRs. Temporally, the picture here is the same as when the radial dependences are considered, with the use of the 1997 parameters yielding results intermediate between the larger 2009 and the smaller 1987 parallel MFPs and drift scales, with relatively little effect on the perpendicular MFPs.

Shown as a function of colatitude at 1 au in the bottom panel of Figure 3, the 1 GV parallel MFP assumes values considerably larger in the ecliptic plane than over the poles, as expected from the slab variance dependence of Equation (8) and in qualitative agreement with the findings of Erdös & Balogh (2005). The perpendicular MFP behaves in a similar fashion, which, from the variance dependence in Equation (9) and the fact that the 2D variance in the polar regions is here modeled to be larger than that in the ecliptic plane, would appear to be counterintuitive, but is simply due to the $\lambda_\parallel^{1/3}$ dependence of $\lambda_\perp$. Although the colatitudinal dependence of these MFPs is by construction very similar to that of these quantities as reported by Engelbrecht & Burger (2013a) as seen in Figure 5 of that paper, with larger values for $\lambda_\parallel$ in the ecliptic plane than over the poles, and with values for $\lambda_\perp$ in the ecliptic plane being smaller than those over the poles. Note that for the MFPs used in this study, there are no increases in these quantities at intermediate colatitudes as reported by Engelbrecht & Burger (2013a), as stream-shear effects due to the latitudinal increase of the solar wind speed are not taken into account here. Drift scales behave quite differently from the perpendicular MFP, assuming larger values over the poles than in the ecliptic plane, reflecting the change in HMF magnitude more than the increase in turbulence levels due to the larger Larmor radius of 1 GV CRs. For lower-energy particles, this changes, with smaller drift scales over the poles than in the ecliptic plane.

In the following section, results from the complete modulation model described here will be presented.

The Astrophysical Journal, 859:107 (12pp), 2018 June 1 Moloto, Engelbrecht, & Burger

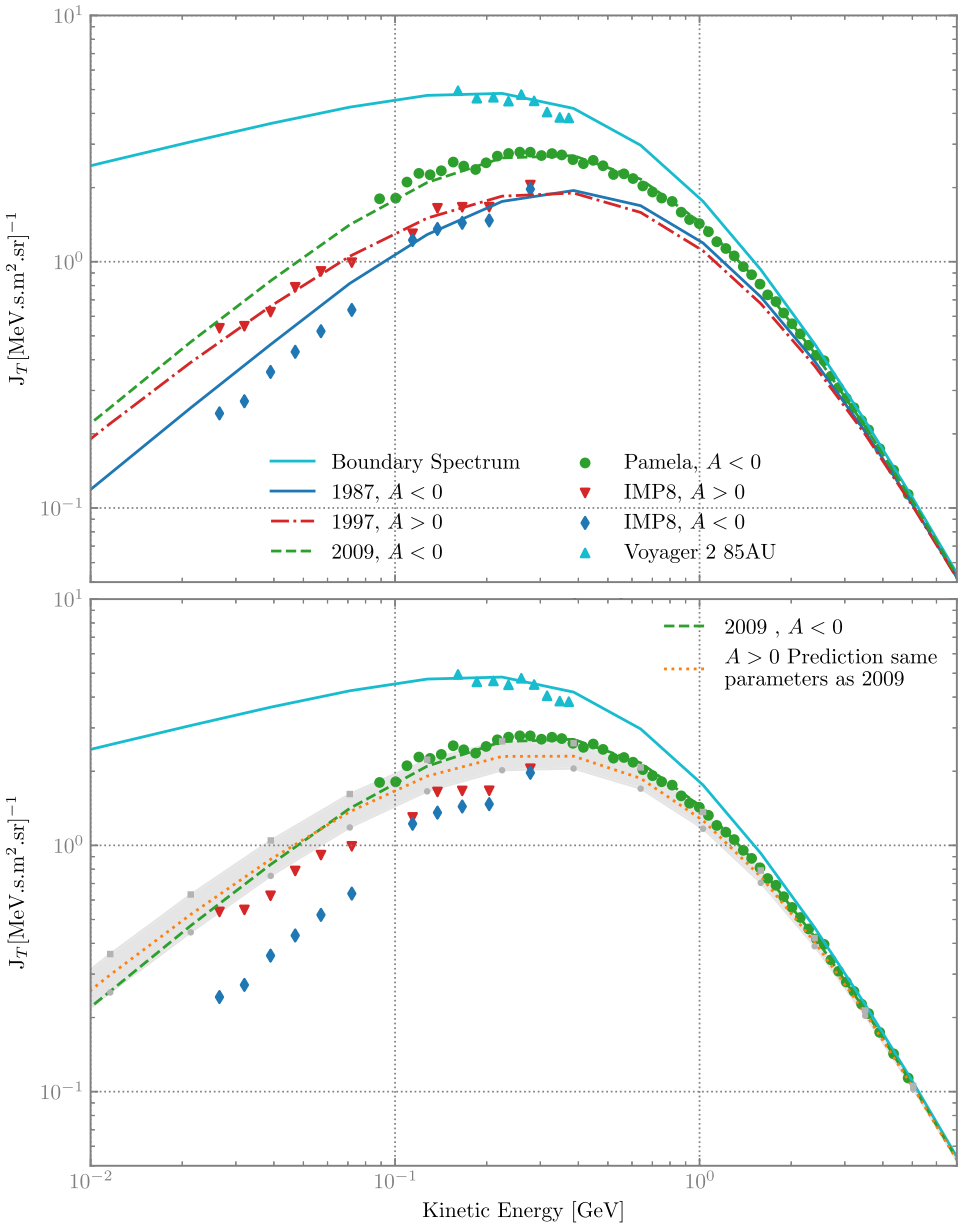

Figure 4. Top panel: computed galactic cosmic-ray proton intensities at Earth for the years 1987 (dark blue), 1997 (red), and 2009 (green). The light blue line indicates the input spectrum used (Equation (5)) at 85 au. Also shown are spacecraft observations for the relevant periods, as reported by McDonald et al. (1992; *IMP-8*), Adriani et al. (2013; PAMELA) and Webber et al. (2008; *Voyager 2*). Bottom panel: the same, but with the gray range denoting possible predicted intensities during the next solar minimum when the magnetic variance and HMF magnitude is varied up (gray squares) or down (gray circles) by 20%. The orange line denotes intensities calculated for an $A > 0$ magnetic polarity cycle under the assumption of heliospheric conditions identical to those prevalent in 2009.

3. Modulation Results and Discussion

Galactic CR proton intensities at Earth computed for the three different solar minimum years considered in this study, using the model as described above, are shown in the top panel of Figure 4. Observations shown are from *IMP-8* (McDonald et al. 1992) and PAMELA (Adriani et al. 2013) reported at Earth, and *Voyager 2* at 85 au (Webber et al. 2008). The light blue line represents the boundary spectrum used in the modulation code, Equation (5), which passes through the *Voyager* data, as it is constructed to do. Model results for the solar minima of 2009 ($A < 0$) and 1997 ($A > 0$) are in excellent agreement with observations at all energies considered, while those for 1987 ($A < 0$) agree best with observations at higher energies. At higher energies (beyond ~0.3 GeV), the 1987 results are slightly larger than those for 1997, in accordance with neutron monitor observations (see, e.g.,Potgieter 2008 and references therein), with the opposite being true at lower energies, characteristic of the effects of drifts on CR modulation (e.g., Kóta & Jokipii 1983). Given that the turbulence input to the present modulation model is based on reasonable assumptions and is guided by observations, the fact that the present model yields results in good agreement with the unusually high 2009 intensities leads us to conclude that the higher than expected CR intensity during the 2009 solar minimum can be quantitatively linked to turbulence parameters that differ from solar minimum to solar minimum, in agreement with the conclusions drawn by Zhao et al. (2014) and Moloto (2015).

The Astrophysical Journal, 859:107 (12pp), 2018 June 1

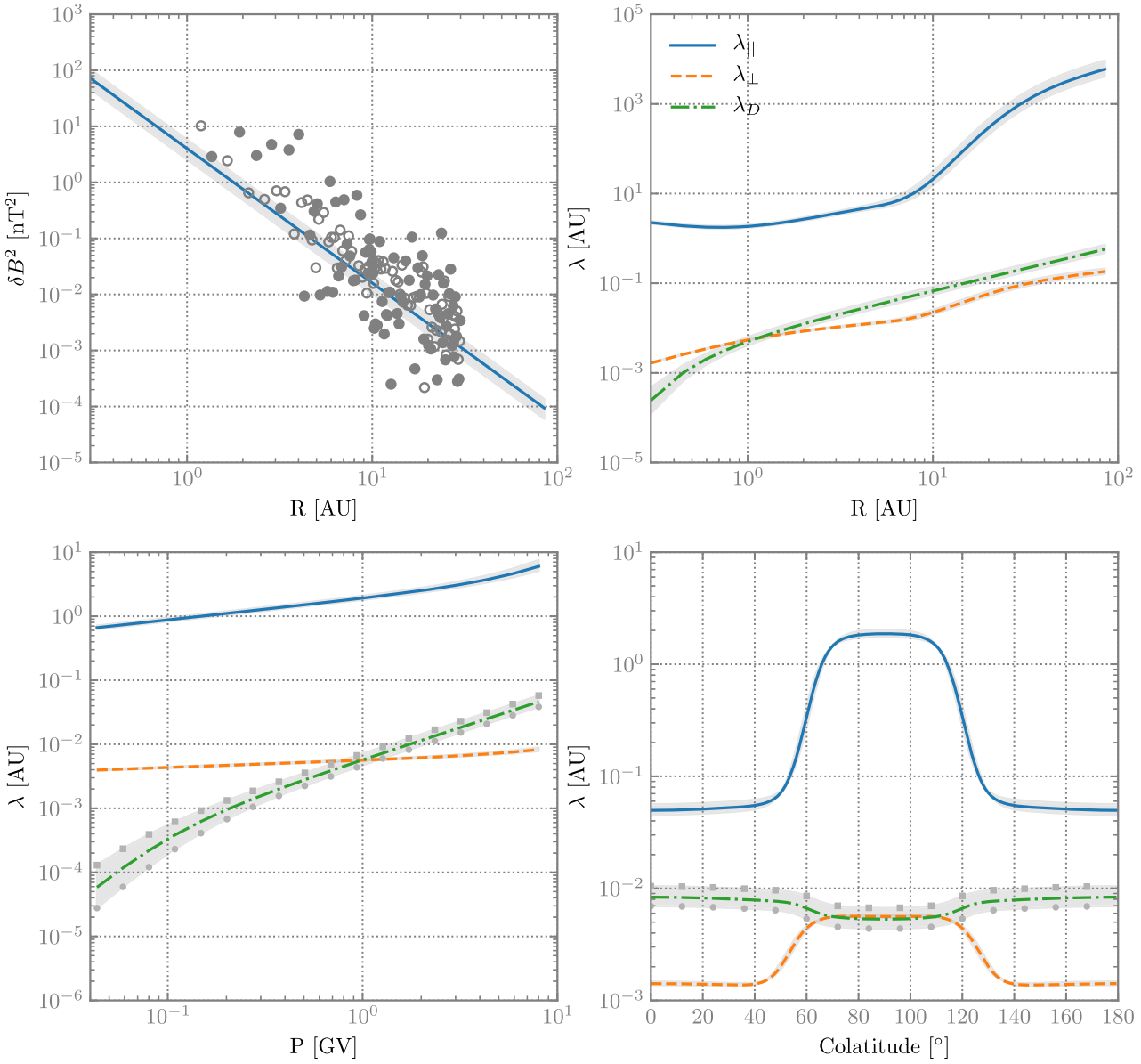

Figure 5. Assumptions for turbulence quantities and mean free paths for the minimum of solar cycle 25. Top-left panel: total magnetic variance as a function of radial distance, with observations of the same reported by Zank et al. (1996). Top-right panel: 1 GV mean free paths and drift scales as a function of heliocentric radial distance; bottom-right panel: 1 GV mean free paths and drift scales as a function of colatitude at 1 au; and bottom-left panel: mean free paths and drift scales as a function of rigidity at Earth. The gray range denotes possible predicted values for these quantities during the next solar minimum when the magnetic variance and HMF magnitude is varied up (gray squares) or down (gray circles) by 20%. Colored lines indicate values calculated under the assumption of heliospheric conditions identical to those prevalent in 2009.

Given the ab initio nature of the present model and its ability to reproduce observed intensity spectra during the previous three solar minima, the question arises as to what predictions can be made for the next solar minimum. This process, however, requires making extrapolations regarding the behavior of the HMF magnitude, tilt angle, and turbulence quantities during that time. Hathaway & Upton (2016) and Cameron et al. (2016), using surface flux transport models to predict the Sun's axial dipole strength during the next sunspot cycle minimum, argue that solar cycle 25 would be very similar to solar cycle 24. Therefore, a reasonable point of departure would be to assume that all the parameters relevant to modulation remain as they were modeled for 2009, except that now, a positive magnetic polarity cycle is assumed. The differential intensities calculated thus are shown as the orange dashed line on the bottom panel of Figure 4. Interestingly, the $A < 0$ 2009 spectrum remains larger than the equivalent $A > 0$ spectrum down to $\sim$0.07 GeV. As this crossover occurs at larger energies when observations from previous solar minima are considered, from the simulations of Reinecke & Potgieter (1994), this implies that for this set of parameters, diffusion effects play a larger role than drift effects. As there is a large degree of uncertainty when predictions on future levels of solar activity are made (Cameron et al. 2016), and indeed it has even been predicted that cycle 25 could be even less active than cycle 24 (Ahluwalia 2016), the model was run with a change in HMF magnitude and variance of 20%. This yields the gray band in

The Astrophysical Journal, 859:107 (12pp), 2018 June 1 Moloto, Engelbrecht, & Burger

Figure 4, where the gray squares denote the solution with a 20% larger HMF magnitude and variance and the gray dotted line the solution with a 20% smaller HMF magnitude and variance. The larger values for these quantities lead to computed intensities similar to the PAMELA observations from 2009, with this particular $A > 0$ solution crossing the $A < 0$ solution at an energy of ~0.2 GV, higher than the crossing energy for the $A > 0$ intensities calculated for 2009 conditions. Decreasing the variance and HMF magnitude by 20% leads to intensities significantly lower than the 2009 values, with a crossover occurring only at ~0.01 GeV. The reason for this behavior can be deduced from the drift and diffusion coefficients. The corresponding changes to the drift length scale and the MFPs affected by the different projected solar cycle 25 parameters, as well as the total variances, are shown in Figure 5 as a function of radial distance, rigidity, and colatitude. As both the HMF magnitude and the magnetic variances are changed simultaneously, the ratio of these quantities remains unchanged, leading to only relatively small changes in the MFPs. The largest changes are to be seen in the drift coefficients, with the 20% increase leading to a larger drift scale and the 20% decrease leading to a smaller drift scale. This would imply that in the former case, drift effects would play a larger role in the modulation of galactic CRs, leading, as shown by Reinecke & Potgieter (1994), to a shift of the crossover point in the spectra to a higher energy. The converse also holds, as the relatively decreased effects of drift implied by the smaller drift scale acquired when the HMF magnitude and variance are decreased by 20% lead to a shift toward a lower energy of the crossover point, again in agreement with the findings of Reinecke & Potgieter (1994).

4. Summary and Conclusions

Taken as a whole, the agreement of model results with data for all three solar minima is good. Furthermore, the fact that careful, observationally motivated modeling of the turbulence quantities as they differ from one solar cycle to the next naturally leads to larger intensities relative to previous solar minima observed during the unusual solar minimum of 2009 leads us to conclude that the higher than expected CR intensity observed during this solar minimum can be qualitatively linked to turbulence parameters that differ from solar minimum to solar minimum. Furthermore, Figure 3 shows that, due to the lower turbulence levels and HMF magnitude in 2009, the drift length scale for this period was larger than that during previous solar minima, leading us to conclude that drifts still play a role during this period, contrary to what was argued by, e.g., Potgieter et al. (2015) and references therein, and more in line with the findings of Zhao et al. (2014).

Overall, the intensities predicted by the current model for solar cycle 25 remain, at larger energies, at or below the intensities observed in 2009. This differs from what has been reported by Miyake et al. (2017), who expect intensities 19% higher than those observed during the 2009 solar minimum. The differences in the results presented here may be due to the fact that the effects of basic turbulence quantities on the diffusion and drift coefficients of CRs are taken into account in this study. At lower energies, $A > 0$ cycle 25 intensities are expected to be larger than in 2009, but only moderately so. This is a consequence of the fact that most modulation of galactic CRs occurs in the heliosheath (see, e.g., Stone et al. 2013), and as such, this result is only expected to change if there were large, solar cycle and magnetic polarity related changes in the boundary spectrum at 85 au. Webber et al. (2008) do indeed report that *Voyager* observed intensities for protons above ~150 MeV during $A < 0$ that were a factor of 1.5–1.7 higher than the corresponding $A > 0$ intensities. As this is not taken into account in the present study, the present results may even be an upper bound to what can potentially be observed in 2009.

To conclude, then, the present model can, in the near future, at the very least give some indication of the expected CR intensities based on a realistic ab initio approach to the modulation of CRs, and predict that the contribution of galactic CR protons to the space radiation environment in solar cycle 25 will be very similar to, or slightly less than, that during cycle 24.

Future work will involve extending the present model to be fully time dependent, incorporating time-dependent current sheet, tilt angle, solar wind profile, HMF, and turbulence quantities to model several full solar cycles and to refine the predictions made in the present study. The incorporation of the effects of the heliosheath on CR modulation in an ab initio way is also a priority for future studies. Furthermore, the current model will be used to study the time-dependent, ab initio modulation of other species of CRs, including galactic electrons, positrons, and in particular Jovian electrons, which make up the majority of CR electrons observed at Earth (see, e.g., Ferreira et al. 2001a, 2001b) and which have not yet been studied in an ab initio manner.

This work is based on the research supported in part by the National Research Foundation of South Africa (grant number 111731). Opinions expressed and conclusions arrived at are those of the authors and are not necessarily to be attributed to the NRF.

The authors would like to thank the Centre for High Performance Computing (CHPC) in South Africa for providing computational resources for this study.

ORCID iDs

N. E. Engelbrecht https://orcid.org/0000-0003-3659-7956

References

Adams, L. 1985, Microelectronics Journal, 16, 17
Adhikari, L., Zank, G. P., Bruno, R., et al. 2015, ApJ, 805, 63
Adriani, O., Barbarino, G. C., Bazilevskaya, G. A., et al. 2013, ApJ, 765, 91
Aggarwal, P., Taylor, D. K., Smith, C. W., et al. 2016, ApJ, 822, 94
Ahluwalia, H. S. 2016, AdSpR, 57, 710
Badhwar, G. D., Keith, J. E., & Cleghorn, T. F. 2001a, RadM, 33, 235
Badhwar, G. D., Nachtwey, D. S., & Yang, T. C. 2001b, AdSpR, 12, 195
Badhwar, G. D., & O'Neill, P. M. 1994, AdSpR, 14, 749
Bavassono, B., Pietropaolo, E., & Bruno, R. 2000a, JGR, 105, 15959
Bavassono, B., Pietropaolo, E., & Bruno, R. 2000b, JGR, 105, 12697
Bieber, J. W., Chen, J., Matthaeus, W. H., Smith, C. W., & Pomerantz, M. A. 1993, JGR, 98, 3585
Bieber, J. W., & Matthaeus, W. H. 1997, ApJ, 485, 655
Bieber, J. W., Matthaeus, W. H., Smith, C. W., et al. 1994, ApJ, 420, 294
Bieber, J. W., Wanner, W., & Matthaeus, W. H. 1996, JGR, 101, 2511
Breech, B. A., Matthaeus, W. H., Minnie, J., et al. 2008, JGRA, 113, A08105
Bruno, R., & Carbone, V. 2013, LRSP, 10, 2
Burger, R. A. 1990, in Physics of the Outer Heliosphere, ed. S. Grzedzielski & D. E. Page (Oxford: Pergamon), 179
Burger, R. A. 2012, ApJ, 760, 60
Burger, R. A., Krüger, T. P. J., Hitge, M., & Engelbrecht, N. E. 2008, ApJ, 674, 511

Burger, R. A., Nel, A. E., & Engelbrecht, N. E. 2014, in AGU Fall Meeting Abstracts (San Francisco, CA: AGU), SH51A–4152
Burger, R. A., Potgieter, M. S., & Heber, B. 2000, JGR, 105, 27447
Burger, R. A., & Visser, D. J. 2010, ApJ, 725, 1366
Caballero-Lopez, R. A., Moraal, H., & McDonald, F. B. 2010, ApJ, 725, 121
Cameron, R. H., Jiang, J., & Schussler, M. 2016, ApJL, 823, L22
Cannon, B. E., Smith, C. W., Isenberg, P. A., et al. 2014, ApJ, 787, 133
Cannon, B. E., Smith, C. W., Isenberg, P. A., et al. 2017, ApJ, 840, 13
Chen, J., & Bieber, J. W. 1993, ApJ, 405, 375
Cucinotta, F. A. 2014, PLoSO, 9, e96099
Cucinotta, F. A., Alp, M., Sulzman, F. M., & Wang, M. 2014, LSSR, 2, 54
Cucinotta, F. A., & Durante, M. 2006, Lancet Oncology, 7, 431
Cucinotta, F. A., Manuel, F. K., Jones, J., et al. 2001a, RadR, 156, 460
Cucinotta, F. A., Schimmerling, W., Wilson, J. W., et al. 2001b, RadR, 156, 682
Dasso, S., Milano, J., Matthaeus, W. H., & Smith, C. W. 2005, ApJL, 635, L181
Engelbrecht, N. E. 2017, ApJL, 849, L15
Engelbrecht, N. E., & Burger, R. A. 2010, AdSpR, 45, 1015
Engelbrecht, N. E., & Burger, R. A. 2013a, ApJ, 772, 46
Engelbrecht, N. E., & Burger, R. A. 2013b, ApJ, 779, 158
Engelbrecht, N. E., & Burger, R. A. 2015a, AdSpR, 55, 390
Engelbrecht, N. E., & Burger, R. A. 2015b, ApJ, 814, 152
Engelbrecht, N. E., Strauss, R. D., le Roux, J. A., & Burger, R. 2017, ApJ, 841, 107
Eraker, J. H. 1982, ApJ, 257, 862
Erdös, G., & Balogh, A. 2005, AdSpR, 35, 625
Ferreira, S. E. S., Potgieter, M. S., Burger, R. A., et al. 2001a, JGR, 106, 29313
Ferreira, S. E. S., Potgieter, M. S., Burger, R. A., Heber, B., & Fichtner, H. 2001b, JGR, 106, 24979
Fisk, L. A., & Schwadron, N. A. 1995, JGR, 100, 7865
Forman, M. A., Jokipii, J. R., & Owens, A. J. 1974, ApJ, 192, 535
Forsyth, R. J., Horbury, T. S., Balogh, A., & Smith, E. C. 1996, GeoRL, 23, 595
Gardiner, C. 2004, Stochastic Methods: A Handbook for the Natural and Social Sciences (Heidelberg: Springer)
Gleeson, L. J., & Axford, W. I. 1968, ApJ, 154, 1011
Golge, S., O'Neill, P. M., & Slaba, T. C. 2015, ICRC (The Hague), 34, 180
Guo, X., & Florinski, V. 2016, ApJ, 826, 65
Hathaway, D. H., & Upton, L. A. 2016, JGRA, 121, 10744
Heber, B., Dröge, W., Ferrando, P., et al. 1996, A&A, 316, 538
Hellweg, C. E., & Baumstark-Khan, C. 2007, NW, 94, 517
Holmes-Siedle, A., & Adams, L. 2009, Handbook of Radiation Effects (New York: Oxford Univ. Press)
Isenberg, P. A. 2005, ApJ, 623, 502
Jokipii, J. R. 1966, ApJ, 146, 480
Jokipii, J. R. 1993, ICRC (Calgary), 3, 497
Jokipii, J. R., & Thomas, B. 1981, ApJ, 243, 1115
Kóta, J. 2013, SSRv, 176, 391
Kóta, J., & Jokipii, J. R. 1983, ApJ, 265, 573
Kóta, J., & Jokipii, J. R. 2001, AdSpR, 27, 529
le Roux, J. A., & Webb, G. M. 2007, ApJ, 667, 930
Manuel, R., Ferreira, S. E. S., Potgieter, M. S., Strauss, R. D., & Engelbrecht, N. E. 2011, AdSpR, 47, 1529
Matthaeus, W. H., Bieber, J. W., Ruffolo, D., Chuychai, P., & Minnie, J. 2007, ApJ, 667, 956
Matthaeus, W. H., Gray, P. C., Pontius, D. H., Jr., & Bieber, J. W. 1995, PhRvL, 75, 2136
Matthaeus, W. H., Qin, G., Bieber, J. W., & Zank, G. P. 2003, ApJL, 590, L53
McComas, D. J., Barraclough, B. L., Funsten, H. O., et al. 2000, JGR, 105, 10419
McDonald, F. B., Heikkila, B., Lal, N., & Stone, E. C. 2000, JGR, 105, 1
McDonald, F. B., Moraal, H., Reinecke, J. P. L., Lal, N., & McGuire, R. E. 1992, JGR, 97, 1557
Minnie, J., Bieber, J. W., Matthaeus, W. H., & Burger, R. A. 2007a, ApJ, 663, 1049
Minnie, J., Bieber, J. W., Matthaeus, W. H., & Burger, R. A. 2007b, ApJ, 670, 1149
Miyake, S., Kataoka, R., & Sato, T. 2017, SpWea, 15, 589
Moloto, K. D. 2015, MSc thesis, North-West Univ.
Moraal, H. 2013, SSRv, 176, 299
Nagashima, K., & Morishita, I. 1980a, P&SS, 28, 177
Nagashima, K., & Morishita, I. 1980b, P&SS, 28, 195
O'Neill, P. M. 2006, AdSpR, 37, 1727
Oughton, S., Matthaeus, W. H., Smith, C. W., Bieber, J. W., & Isenberg, P. A. 2011, JGRA, 116, A08105
Oughton, S., Matthaeus, W. H., Wan, M., & Osman, K. T. 2015, RSPTA, 373
Palmer, I. D. 1982, RvGSP, 20, 335
Parker, E. N. 1958, ApJ, 128, 664
Parker, E. N. 1965, P&SS, 13, 9
Pei, C., Bieber, J. W., Burger, R. A., & Clem, J. 2010, JGR, 115, A12107
Perri, S, & Balogh, A. 2010, GeoRL, 37, L17102
Potgieter, M. S. 1996, JGR, 101, 24411
Potgieter, M. S. 2008, JASTP, 70, 207
Potgieter, M. S. 2013, SSRv, 176, 165
Potgieter, M. S., Vos, E. E., Munini, R., Boezio, M., & Di Felice, V. 2015, ApJ, 810, 141
Qin, G., Matthaeus, W. H., & Bieber, J. W. 2002a, ApJL, 578, L117
Qin, G., Matthaeus, W. H., & Bieber, J. W. 2002b, GeoRL, 29, 1048
Qin, G., & Shen, Z.-N. 2017, ApJ, 846, 56
Qin, G., & Zhang, L.-H. 2014, ApJ, 787, 12
Reinecke, J. P. L., & Potgieter, M. S. 1994, JGR, 99, 14761
Ruffolo, D., Pianpanit, T., Matthaeus, W. H., & Chuychai, P. 2012, ApJL, 747, L34
Schwadron, N. A., Blake, J. B., Case, A. W., et al. 2014, SpWea, 12, 622
Shalchi, A. 2006, A&A, 453, L43
Shalchi, A. 2009, Nonlinear Cosmic Ray Diffusion Theories (Germany: Springer)
Shalchi, A. 2010, ApJL, 720, L127
Shalchi, A., Bieber, J. W., & Matthaeus, W. H. 2004, ApJ, 604, 675
Shalchi, A., Li, G., & Zank, G. P. 2010, Ap&SS, 325, 99
Simpson, J. A., Hamilton, D., Lentz, G., et al. 1974, Sci, 183, 306
Smith, W. S., Matthaeus, W. H., Zank, G. P., et al. 2001, JGR, 106, 8253
Stone, E. C., Cummings, A. C., McDonald, F. B., et al. 2013, Sci, 341, 150
Strauss, R. D., & Effenberger, F. 2017, SSRv, 212, 151
Strauss, R. D., Potgieter, M. S., Busching, I., & Kopp, A. 2011a, ApJ, 735, 83
Strauss, R. D., Potgieter, M. S., Kopp, A., & Busching, I. 2011b, JGR, 116, A12105
Tautz, R. C., & Shalchi, A. 2012, ApJ, 744, 125
Taylor, G. I. 1922, Proc. Lond. Math. Soc., 20, 196
Teufel, A., & Schlickeiser, R. 2003, A&A, 397, 15
Usmanov, A. V., Goldstein, M. L., & Matthaeus, W. H. 2016, ApJ, 820, 17
Webber, W. R., Cummings, A. C., McDonald, F. B., et al. 2008, JGR, 113, A10108
Weinhorst, B., Shalchi, A., & Fichtner, H. 2008, ApJ, 677, 671
Weygand, A. V., Goldstein, M. L., & Matthaeus, W. H. 2016, ApJ, 820, 17
Weygand, J. M., Matthaeus, W. H., Dasso, S., & Kivelson, M. G. 2011, JGRA, 116, A08102
Wicks, R. T., Roberts, D. A., Mallet, A., et al. 2013, ApJ, 778, 177
Wiengarten, T., Oughton, S., Engelbrecht, N. E., et al. 2016, ApJ, 833, 17
Williams, L. L., & Zank, G. P. 1994, JGR, 99, 19229
Wilson, J. W., Shinn, J. L., Tripathi, R. K., et al. 2001, AcAau, 49, 289
Zank, G. P. 1999, SSRv, 89, 413
Zank, G. P., Adhikari, L., Hunana, P., et al. 2017, ApJ, 835, 147
Zank, G. P., Matthaeus, W. H., & Smith, C. W. 1996, JGR, 101, 17093
Zapp, E. N., Ramsey, C. R., Townsend, L. W., & Badhwar, G. D. 1998, AcAau, 43, 249
Zeitlin, C., Cleghorn, T., Cucinotta, F. A., et al. 2004, AdSpR, 33, 2204
Zeitlin, C., Hassler, D. M., Cucinotta, F. A., et al. 2013, Sci, 340, 1080
Zhang, M. 1997, ApJ, 488, 841
Zhang, M. 1999, ApJ, 513, 409
Zhang, M., Luo, X., & Pogorelov, N. 2015, PhPl, 22, 091501
Zhang, M., Qin, G., Rassoul, H., et al. 2007, P&SS, 55, 12
Zhao, L. L., Adhikari, L., Zank, G. P., Hu, Q., & Feng, X. S. 2018, ApJ, 856, 94
Zhao, L. L., Qin, G., Zhang, M., & Heber, B. 2014, JGRA, 119, 1493

CHAPTER 4

Numerical integration of stochastic differential equations: A parallel cosmic ray modulation implementation on Africa's fastest computer

The paper presented in this chapter has been published in Advances in Space Research: K.D. Moloto et al. — Advances in SpaceResearch 63 (2019) 626–639

Available online at www.sciencedirect.com

ScienceDirect

Advances in Space Research 63 (2019) 626–639

ADVANCES IN SPACE RESEARCH (a COSPAR publication)

www.elsevier.com/locate/asr

Numerical integration of stochastic differential equations: A parallel cosmic ray modulation implementation on Africa's fastest computer

K.D. Moloto [a], N.E. Engelbrecht [a,b,*], R.D. Strauss [a,b], D.M. Moeketsi [c], J.P. van den Berg [a]

[a] Center for Space Research, North-West University, Potchefstroom, South Africa
[b] National Institute for Theoretical Physics (NITheP), Gauteng, South Africa
[c] Centre for High Performance Computing (CHPC), CSIR Meraka Institute, Cape Town, South Africa

Received 20 June 2018; received in revised form 27 August 2018; accepted 30 August 2018
Available online 8 September 2018

Abstract

Three-dimensional studies of the transport and modulation of cosmic ray particles in turbulent astrospheres require large-scale simulations using specialized scientific codes. Essentially, a multi-dimensional Fokker-Planck type equation (a parabolic diffusion equation) must be integrated numerically. One such approach is to convert the relevant transport equation into a set of stochastic differential equations (SDEs), with the latter much easier to handle numerically. Due to the growing demand for high performance computing resources, research into the application of effective and suitable numerical algorithms to solve such equations is needed. We present a case study of the performance of a custom-written FORTRAN SDE numerical solver on the CHPC (Centre for High Performance Computing) Lengau cluster in South Africa for a realistic test problem with different set-ups. It is shown that SDE codes can scale very well on large parallel computing platforms. Finally, we consider an extremely computationally expensive application of the SDE approach to cosmic ray modulation, studying the behaviour of galactic cosmic ray proton latitude gradients and relative amplitudes in a physics-first manner. This is done using a modulation code that employs diffusion coefficients derived from first principles, which in turn are functions of turbulence quantities in reasonable agreement with spacecraft observations and modelled using a two-component turbulence transport model (TTM). We show that this approach leads to reduced latitude gradients qualitatively in line with spacecraft observations of the same, without making *ad hoc* assumptions as to anisotropic perpendicular diffusion coefficients as are often made in many cosmic ray modulation studies.

Keywords: Cosmic rays; Stochastic differential equations; Parallel computing; Code scaling and efficiency; MPI; Fortran 90

1. Introduction

Over the past 50 years, studies of the transport and modulation of cosmic ray particles (CRs) through turbulent, magnetized space and astrophysical plasmas have been performed by solving a Fokker-Planck type diffusion equation (Parker, 1965; Moraal, 2013). Due to the complexity of the plasma geometry, and the associated transport parameters, the relevant equation has to be solved numerically. This has been traditionally done using different finite difference numerical schemes to solve a multidimensional partial differential equation which involves diffusion processes (see, e.g., Kota and Jokipii, 1983; le Roux and Potgieter, 1995; Haasbroek and Potgieter,

* Corresponding author at: Center for Space Research, North-West University, Potchefstroom, South Africa.
E-mail addresses: katlego.moloto@nwu.ac.za (K.D. Moloto), n. eugene.engelbrecht@gmail.com (N.E. Engelbrecht), dutoit.strauss@nwu.ac.za (R.D. Strauss), dmoeketsi@csir.co.za (D.M. Moeketsi), 24182869@nwu.ac.za (J.P. van den Berg).

https://doi.org/10.1016/j.asr.2018.08.048
0273-1177/

1998; Burger et al., 2008; Wawrzynczak and Alania, 2010; Engelbrecht and Burger, 2013). However, problems arise when solving these equations in higher dimensions. In particular, the finite difference type schemes become less accurate and numerically unstable when increasing the number of dimensions (e.g. Kopp et al., 2012). These schemes also need large amounts of memory to store the required numerical grids (Strauss and Effenberger, 2017). To circumvent these issues, models using stochastic differential equations (SDEs) have become very popular in recent times to solve a variety of problems in space and astrophysics. For the finer details of the SDE approach, the reader is referred to Yamada et al. (1998), Zhang (1999a, b), Pei et al. (2010), Strauss et al. (2011b), Della Torre et al. (2012), Miyake et al. (2015), Engelbrecht and Burger (2015b), Luo et al. (2017), Strauss and Effenberger (2017), amongst others. In this work we focus on the implementation and performance of two SDE particle transport codes, initially described by Strauss et al. (2011a, 2012) and Engelbrecht and Burger (2015b), on the petascale cluster hosted by the Centre for High Performance Computing (CHPC, www.chpc.ac.za) in South Africa, an overview of which is given in Appendix A. Both particle transport codes implement the SDE approach in exactly the same manner. The Strauss et al. (2011a, 2012) code, however, is set up for a simpler set of transport parameters, and thus is more ideally suited for scaling analyses such as those presented in Appendix B of this paper. The second section of this paper is devoted to investigating the scaling of an SDE code using the Engelbrecht and Burger (2015b) code, which employs more complicated, physically-motivated CR transport coefficients derived from first principles, and utilizing outputs from a turbulence transport model as inputs for these coefficients. The scaling of this latter code will be tested by investigating the latitudinal and azimuthal transport of cosmic rays by investigating the latitude gradients and relative amplitudes of galactic protons computed with the latter SDE code. The latitude gradient, defined in terms of the CR differential intensity j_T by Zhang (1997) to be

$$G_\theta(r) = \frac{1}{\theta_1 - \theta_2} \ln \left[\frac{\langle j_T(r,\theta_2)\rangle_\phi}{\langle j_T(r,\theta_1)\rangle_\phi} \right] \times 100\%, \quad (1)$$

with $\theta_1 = 90^\circ$ and $\theta_2 = 10^\circ$ colatitude with angle brackets denoting an average over the subscripted coordinate, and the relative amplitude, defined by Zhang (1997) to be

$$\Delta j_T(r,\theta) = \frac{j_T^{max}(r,\theta,\phi) - j_T^{min}(r,\theta,\phi)}{\langle j_T(r,\theta,\phi)\rangle_\phi} \times 100\%, \quad (2)$$

where superscripts 'max' and 'min' denote maximum and minimum values for the differential intensity at a given radial distance and colatitude, represent uniquely computationally-expensive quantities to calculate using an SDE technique, and thus provide ideal measures for the scaling of such a code, especially when complex transport coefficients are employed. This is due to the fact that CR intensities at many different points need to be calculated so as to compute the averages required to calculate these quantities. To the best of our knowledge, this has not before been attempted with an SDE code, and would have proven well-nigh impossible to accomplish within a reasonable period of time without the computing resources of the CHPC. Furthermore, conclusions as to the transport of galactic cosmic rays will be drawn from the results so computed.

2. The propagation model

CRs are highly energetic charged particles with kinetic energy, $E \geqslant 1$ MeV, originating from various astrophysical sources, such as the Sun (e.g. Reames, 2013), the magnetosphere of Jupiter (referred to as Jovian electrons; e.g. Ferreira et al., 2001), the heliospheric termination shock (e.g. Florinski, 2009) or beyond the solar system (called galactic cosmic rays; e.g. Potgieter, 2013). For this paper, we show results for a model that is specifically set-up to simulate the transport of these galactic cosmic rays in the heliosphere. The basic idea is that the turbulent solar plasma fills an approximately spherical region of space (the heliosphere, Parker, 1958) and that the intensity of the CRs outside of this sphere is known, defining a Dirichlet boundary condition that is only dependent on energy. This boundary spectrum is referred to as the local interstellar spectrum (LIS, see Stone et al., 2013). For an illustration of this model's computational domain, see Dunzlaff et al. (2015).

The transport of CRs from the local interstellar spectrum (LIS) to any position in the heliosphere (which constitutes the computational domain) is governed by the Parker (1965) cosmic-ray transport equation (TPE), which is given in terms of the omnidirectional CR phase space density f_0 (related to the CR differential intensity by $j_T = p^2 f_0$). In the simplest scenario, f_0 is a function of time, position and particle momentum p (i.e. time and phase-space), and is given by

$$\frac{\partial f_0}{\partial t} = \nabla \cdot (\mathbf{K} \cdot \nabla f_0) - \mathbf{V}_{sw} \cdot \nabla f_0 + \frac{1}{3}(\nabla \cdot \mathbf{V}_{sw}) \frac{\partial f_0}{\partial \ln p}. \quad (3)$$

Eq. (3) describes various physical process which CRs undergo, such as diffusion, drift due to gradients and curvatures in the heliospheric magnetic field as well as along the heliospheric current sheet, convection by the solar wind, and adiabatic energy losses.

Due to the complexity of the Parker TPE, and the fact that the equation must be solved in higher dimensions to realistically capture the processes included therein (drifts, for instance, represent an inherently multi-dimensional problem and cannot be included in a one-dimensional modelling scenario), it must be integrated numerically. In the past, finite difference-type numerical schemes have been used extensively. The schemes, however, suffer from stability issues (especially in higher dimensions). For this reason, we have more recently developed a numerical model based

on the solution of a set of stochastic differential equations. With the mathematical details of this model published extensively elsewhere, we will give only the briefest introduction here.

The idea behind our numerical approach is the fact that any Fokker-Planck equation (such as Eq. (3)) can be written in terms of a set of Itō SDEs that are mathematically equivalent (see, e.g., Zhang, 1999b; Gardiner, 2004; Strauss and Effenberger, 2017)

$$dx_i = A_i(x_i)dt + \sum_j B_{i,j}(x_i)\cdot dW_i, \tag{4}$$

with x_i Itō processes (Gardiner, 2004) and where the subscript i denotes the three spatial coordinates (r,θ,ϕ) and energy E (or momentum). The quantity

$$dW_i(t) = \eta(t)\sqrt{dt} \tag{5}$$

represents the discretization of a Wiener process, which is a time-stationary Levy process where the temporal increments have a zero-mean Normal distribution (see, e.g., Gardiner, 2004; Strauss and Effenberger, 2017). Furthermore, η represents a Gaussian-distributed pseudo-random number that must be generated numerically (for more detail on this, see Section 3).

Instead of discretizing Eq. (3) and solving it on a numerical grid, we can now rather integrate Eq. (4) from some starting value $(\mathbf{x}^o, t^o)$ until this trajectory (which, being simply one mathematical realization of the set of SDEs, is usually referred to as a *pseudo-particle*) reaches the computational boundary at a different phase-space position $(\mathbf{x}^e, t^e)$. We do so using the so-called time-backwards approach (for more details see Strauss and Effenberger, 2017) and use the Euler-Maruyama scheme Maruyama (1955) to perform the numerical integration. However, solving Eq. (4) for a single pseudo-particle has no meaning: the integration process must be repeated for N such trajectories, where each trajectory will be different (and by definition independent) due to the unique set of Wiener processes that must be used to compute that specific trajectory. After performing the required integration N times, the cosmic ray distribution function at the initial point is calculated using (Strauss et al., 2011a; Strauss and Effenberger, 2017)

$$f_0(x_i^o, t^o) = \frac{1}{N}\sum_{k=1}^{N} f_B(x_{i,k}^e, t_k^e), \tag{6}$$

in discretized form, where f_B denotes the distribution function at the boundary. When this is calculated, the result is converted to a differential intensity using the relation $j_T = p^2 f_0$ (see, e.g., Moraal, 2013).

The components of the vector $\mathbf{A}$ and tensor $\mathbf{B}$ in Eq. (4) are related to the physical processes incorporated into the TPE. For a calculation of these quantities, see Pei et al. (2010), Strauss et al. (2011b) and Engelbrecht and Burger (2015b), amongst others. These, for a general heliospheric magnetic field geometry, are given by Pei et al. (2010) and Engelbrecht and Burger (2015b) as

$$\begin{aligned}
B_{1,1} &= \frac{\sqrt{2(\kappa_{\phi\phi}\kappa_{r\theta}^2 - 2\kappa_{r\phi}\kappa_{r\theta}\kappa_{\theta\phi} + \kappa_{rr}\kappa_{\theta\phi}^2 + \kappa_{\theta\theta}\kappa_{r\phi}^2 - \kappa_{rr}\kappa_{\theta\theta}\kappa_{\phi\phi})}}{\sqrt{\kappa_{\theta\phi}^2 - \kappa_{\theta\theta}\kappa_{\phi\phi}}},\\
B_{1,2} &= \frac{\kappa_{r\phi}\kappa_{\theta\phi} - \kappa_{r\theta}\kappa_{\phi\phi}}{\kappa_{\theta\phi}^2 - \kappa_{\theta\theta}\kappa_{\phi\phi}}\sqrt{2\left(\kappa_{\theta\theta} - \frac{\kappa_{\theta\phi}^2}{\kappa_{\phi\phi}}\right)},\\
B_{1,3} &= \frac{\sqrt{2}\kappa_{r\phi}}{\sqrt{\kappa_{\phi\phi}}},\\
B_{2,2} &= \frac{\sqrt{2(\kappa_{\theta\theta} - \kappa_{\theta\phi}^2/\kappa_{\phi\phi})}}{r},\\
B_{2,3} &= \frac{\kappa_{\theta\phi}}{r}\sqrt{\frac{2}{\kappa_{\phi\phi}}},\\
B_{3,3} &= \frac{\sqrt{2\kappa_{\phi\phi}}}{r\sin\theta},\\
B_{2,1} &= B_{3,1} = B_{3,2} = 0
\end{aligned} \tag{7}$$

and

$$\begin{aligned}
A_r &= \frac{1}{r^2}\frac{\partial}{\partial r}r^2\kappa_{rr} + \frac{1}{r\sin\theta}\frac{\partial}{\partial\phi}\kappa_{r\phi} + \frac{1}{r\sin\theta}\frac{\partial}{\partial\theta}\kappa_{r\theta}\sin\theta - V_{sw}\\
&\quad - V_{d,r},\\
A_\theta &= \frac{1}{r^2}\frac{\partial}{\partial r}r^2\kappa_{r\theta} + \frac{1}{r^2\sin\theta}\frac{\partial}{\partial\theta}\kappa_{\theta\theta}\sin\theta + \frac{1}{r^2\sin\theta}\frac{\partial}{\partial\phi}\kappa_{\theta\phi}\\
&\quad - \frac{V_{d,\theta}}{r},\\
A_\phi &= \frac{1}{r^2\sin^2\theta}\frac{\partial}{\partial\phi}\kappa_{\phi\phi} + \frac{1}{r^2\sin^2\theta}\frac{\partial}{\partial r}r\kappa_{\phi\phi} + \frac{1}{r^2\sin^2\theta}\frac{\partial}{\partial\theta}\kappa_{\theta\phi}\\
&\quad - \frac{V_{d,\phi}}{r\sin\theta},\\
A_E &= \frac{1}{3r^2}\frac{\partial}{\partial r}(r^2V_{sw})\frac{(E+2E_o)}{E+E_o}E,
\end{aligned} \tag{8}$$

with $\kappa_{i,j}$ the elements of the diffusion tensor $\mathbf{K}$ in Eq. (3), E_o the rest-mass energy of the species of cosmic-ray in question, and V_{sw} and V_d the solar wind and drift speeds. The above formulations for $\mathbf{B}$ and $\mathbf{A}$ reduce to what is employed in the Strauss et al. (2011b) SDE model when a Parker (1958) heliospheric magnetic field is assumed, as is done throughout this paper. The diffusion tensor is given by, e.g., Burger et al. (2008)

$$\begin{aligned}
\kappa_{rr} &= (\kappa_{\parallel}\cos^2\psi + \kappa_{\perp,3}\sin^2\psi)\cos^2\zeta + \kappa_{\perp,2}\sin^2\zeta \\
\kappa_{r\theta} &= (\kappa_{\parallel}\cos^2\psi + \kappa_{\perp,3}\sin^2\psi - \kappa_{\perp,2})\sin\zeta\cos\zeta - \kappa_A\sin\psi \\
\kappa_{r\phi} &= (-\kappa_{\parallel} + \kappa_{\perp,3})\sin\psi\cos\psi\cos\zeta - \kappa_A\cos\psi\sin\zeta \\
\kappa_{\theta r} &= (\kappa_{\parallel}\cos^2\psi + \kappa_{\perp,3}\sin^2\psi - \kappa_{\perp,2})\sin\zeta\cos\zeta + \kappa_A\sin\psi \\
\kappa_{\theta\theta} &= (\kappa_{\parallel}\cos^2\psi + \kappa_{\perp,3}\sin^2\psi)\sin^2\zeta + \kappa_{\perp,2}\cos^2\zeta \\
\kappa_{\theta\phi} &= (-\kappa_{\parallel} + \kappa_{\perp,3})\sin\psi\cos\psi\sin\zeta + \kappa_A\cos\psi\cos\zeta \\
\kappa_{\phi r} &= (-\kappa_{\parallel} + \kappa_{\perp,3})\sin\psi\cos\psi\cos\zeta + \kappa_A\cos\psi\sin\zeta \\
\kappa_{\phi\theta} &= (-\kappa_{\parallel} + \kappa_{\perp,3})\sin\psi\cos\psi\sin\zeta - \kappa_A\cos\psi\cos\zeta \\
\kappa_{\phi\phi} &= \kappa_{\parallel}\sin^2\psi + \kappa_{\perp,3}\cos^2\psi
\end{aligned} \tag{9}$$

with ψ denoting the HMF winding angle, and ζ, defined by

$$\begin{aligned}
\sin\zeta &= \frac{B_\theta}{\sqrt{B_r^2 + B_\theta^2}}, \\
\cos\zeta &= \frac{B_r}{\sqrt{B_r^2 + B_\theta^2}},
\end{aligned} \tag{10}$$

reducing to zero for a Parker field. The above diffusion tensor again reduces to what was used by Strauss et al. (2011b) when a Parker HMF is assumed. The quantities $\kappa_{\parallel}, \kappa_{\perp}$ and κ_A denote the diffusion coefficients parallel and perpendicular to the HMF, as well as the drift coefficient. For more details on the physical meaning of these parameters see, for instance, Jokipii and Thomas (1981), Shalchi (2009), Engelbrecht and Burger (2013), Burger (2012) and Engelbrecht et al. (2017).

The contents of the section above describe, in brief, the background, both theoretical and physical, needed to solve the Parker transport equation using stochastic differential equations (SDEs). The following section will delve into the details of the numerical implementation of this endeavour. In Appendix B, particular emphasis will be placed on the parallel scaling of such a SDE code, namely that presented by Strauss et al. (2011b). Although many studies state that such codes scale very well (e.g. Kopp et al., 2012; Engelbrecht and Burger, 2015b; Strauss and Effenberger, 2017), this has never before been explicitly demonstrated. Detail as to the numerical implementation of the SDE technique will also be given in the next section.

3. Numerical implementation

In order to solve any Fokker-Planck type equation numerically by means of an SDE approach, one has to integrate Eq. (4) for N independent Wiener processes, i.e. using N independent sets of pseudo-random numbers (see η in Eq. (5)). Starting from $(\mathbf{x}^o, t^o)$, one has to integrate along the path of this *pseudo-particle* until it exits the computational domain at $(\mathbf{x}^e, t^e)$. The solution of f, at $(\mathbf{x}^o, t^o)$, is then obtained by the convolution as given by Eq. (6). This process must be repeated for each phase-space position, $\mathbf{x}^o$, where the solution is required. Below we give an outline of how we have implemented this numerical scheme in a custom written FORTRAN 90 numerical solver. Although the application here is to particle transport, the basics of this scheme should be the same for any given set of SDEs.

3.1. Code initialization and parallel implementation

Because the different pseudo-particles (i.e. the different integrations of the same set of SDEs) are independent, we choose to integrate these, for the same phase-space position, on different compute nodes using MPI. As we want to integrate `N` pseudo-particles on `numtasks` different compute nodes, we therefore have to integrate `N_par=N/numtasks` particles on each node. The solutions from the different compute cores are then combined by using the `MPI reduce` routine. The whole integration process must now be repeated for the required number of phase-space positions, `M`. In total, `M*N` pseudo-particles will be integrated, and each compute core will integrate `M*N_par` of these. A generalized schematic representation of the algorithm is shown in Fig. 1, where the initialization and looping over `M` phase-space positions is shown in black, the parallel job distribution in red,[1] and looping over `N_par` particles on each node in blue. A FORTRAN 90 specific schematic is given in Fig. B.8.

3.2. The SDE solver

The green section in Fig. 1 shows the integration of the set of SDEs, starting from $\mathbf{x}^o$ and continuing until the pseudo-particle exits the computational domain. In comparison with finite difference-type numerical schemes, the SDE scheme (in essence Eq. (4)) is very simple to implement, although care has to be taken with the generation of pseudo-random numbers (see the next paragraph), while the coefficients (quantities $\mathbf{V}$ and $\mathbf{B}$) can become very complex and the derivatives thereof may have to be evaluated numerically. In fact, the latter statement is true for nearly any realistic set-up, while more complicated set-ups may even require the use of optimization schemes at every step of the numerical integration (for such an implementation, see Strauss et al., 2012).

3.3. Random number generation

The accuracy of the SDE solution is largely governed by the quality of the pseudorandom number generator and by the number of pseudo-particles that are integrated for each phase-space position. As a rule of thumb, the statistical error on the solution can be obtained by assuming an accuracy of $N \pm \sqrt{N}$. However, this is only true if the paths of the pseudo-particles are truly independent, i.e. if the

[1] For interpretation of color in Figs. 1 and B.8, the reader is referred to the web version of this article.

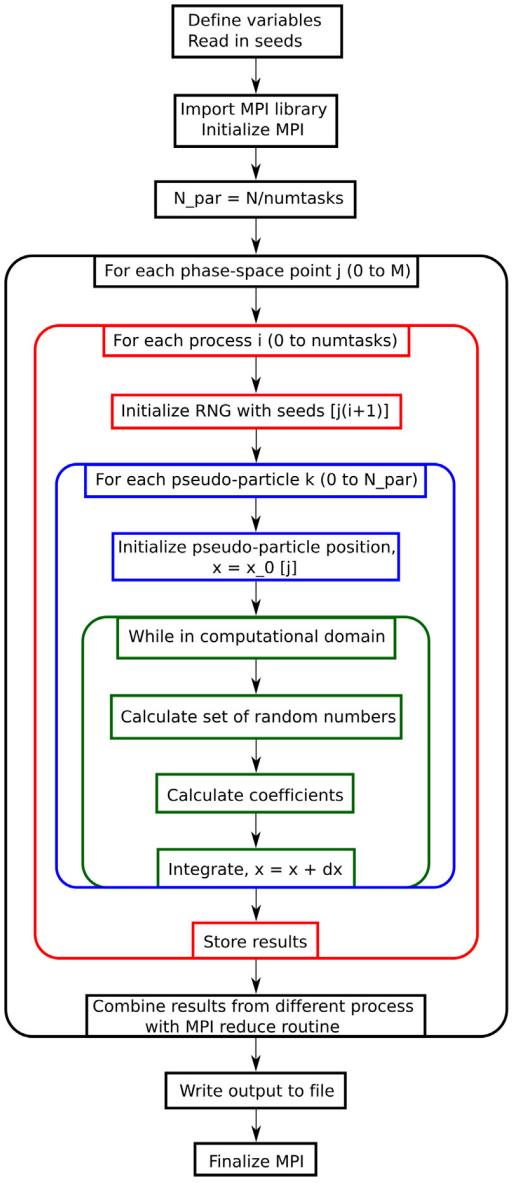

Fig. 1. A generalized schematic representation of the SDE model. Please see the text for more details.

different streams (i.e. the sequence of random numbers on each compute core) of random numbers are independent and without repetition. The different streams must thus be tested for two types of defects. Firstly there should be no apparent correlation between the elements in a single stream, and secondly there should be no correlation between streams on the different compute cores. Srinivasan et al. (2003) call these intra-stream and inter-stream correlations, respectively. In this work, we chose to implement a custom variation of the well-known MT 19937 version of Mersenne twister pseudo-random number generator (Matsumoto and Nishimura, 1988). Brugger et al. (2014) show that, for a robust seeding procedure, the MT 19937 masters both tests and an array of other tests for a good parallel pseudo-random number generator. We start off by generating a string of seed values with a length of `M*N_par` from `www.random.org`, which can be reused. The first step in the numerical model (see the first step shown in Fig. 1) is to load this seed-list and initialize the random number generator each time a new process is initialized on each compute core. That is to say, when solving phase-space position number `j` on compute core `i`, seed number `j(i+1)` is used. The actual bit-shifting is performed with the FORTRAN 90 code available from the developers of the Mersenne twister, see `http://www.math.sci.hiroshima-u.ac.jp/m-mat/MT/emt.html`. A detailed illustration of how the random number functions are called is shown in Fig. B.8. Lastly, the uniformly distributed pseudo-random numbers are transformed to a Gaussian distribution (a necessary requirement for a Wiener process) by applying the Box-Muller method (Box and Muller, 1958).

4. Galactic CR latitude gradients and relative amplitudes

The *Ulysses* mission led to many surprising discoveries as to the transport of cosmic rays in the heliosphere (see, e.g., Heber, 2013; Gieseler and Heber, 2016), notably that observed latitude gradients in galactic cosmic ray proton intensities are considerably lower than expected from then extant numerical cosmic ray modulation models (Heber et al., 316). The cosmic ray (CR) modulation community responded with several modifications to existing modulation models to explain this discrepancy. Two of the most successful of these were: the assumption of anisotropic perpendicular diffusion proposed by Jokipii (1973), Kóta and Jokipii (1995) and shown to successfully reproduce observed latitude gradients by, e.g., Potgieter et al. (1997) and Burger et al. (2000); or particle transport along heliospheric magnetic field lines that displayed non-Parkerian latitudinal excursions, as proposed by Fisk (1996). This latter mechanism was shown to also be able to reproduce observed galactic proton latitude gradients by, e.g., Burger and Hitge (2004) and Burger et al. (2008), as well as the linear relationship reported by Zhang (1997) between latitude gradients and CR relative amplitudes observed by *Ulysses*. Fisk-type fields, however, have been the subject of some controversy, as analyses of Ulysses data have not yet found direct evidence for the expected (see, e.g., Zurbuchen et al. (1997)) signatures of such fields Forsyth et al. (2002), Roberts et al. (2007), and Burger et al. (2008), even though magnetohydrodynamic simulations of the HMF do not rule out the possibility of such an HMF Lionello et al. (2006). Nevertheless, to date the strongest evidence for some kind of a Fisk type HMF arises from studies of the transport of CRs in the very inner heliosphere such as that performed by Sternal et al. (2011).

Relatively recently a third alternative to modelling galactic CR proton latitude gradients has come to light. Employing a 3D steady-state cosmic-ray modulation code that uses as inputs for the diffusion tensor turbulence quantities yielded by the two-component turbulence transport model of Oughton et al. (2011) which are in reasonable

agreement with observations of the same by *Ulysses* taken during the period in which the abovementioned latitude gradient observations were made, as well as with other existing turbulence data sets taken elsewhere in the heliosphere, Engelbrecht and Burger (2013) compute proton latitude gradients in reasonable agreement with the Ulysses observations, even though these authors assume isotropic perpendicular diffusion, and a purely Parker (1958) heliospheric magnetic field. This was simply due to the fact that the diffusion coefficients these authors employed, having been calculated from basic scattering theories, acquired a latitude dependence due to the latitude dependence of the turbulence quantities yielded by the TTM. This model, which employed an ADI (Alternating Direction Implicit, see Peaceman and Rachford (1955)) technique to solve the Parker TPE, was not ideally suited to a study of CR latitude gradients and relative amplitudes in the presence of a Fisk-type field due to numerical stability issues. This fact motivated Engelbrecht and Burger (2015b) to develop their stochastic, three-dimensional (3D) *ab initio* cosmic-ray modulation code. It should be noted that the Engelbrecht and Burger (2015b) stochastic code benchmarks well with the ADI code used by Engelbrecht and Burger (2013). A stochastic solver, though, presents unique challenges when used to compute quantities requiring averaged intensities. The calculation of latitude gradients (Eq. (1)) requires the calculation of CR intensities at enough longitudinal points to construct a meaningful average at two different colatitudes, while the calculation of relative amplitudes (Eq. (2)) requires a similar number of calculated intensities. Given the sheer amount of computation involved, the runtimes to calculate such quantities necessitate the use of a large computing cluster such as the CHPC. The focus of this part of the present study, then, is to calculate these quantities using the *ab initio* stochastic code of Engelbrecht and Burger (2015b), so as to demonstrate the sensitivity of these quantities to the number N of pseudoparticles used to calculate each individual intensity required in their calculation. Note that no direct comparisons with spacecraft observations are made, as the aim here is solely to demonstrate the abovementioned sensitivity of solutions to the number of pseudoparticles.

In the model set up so employed, the latitudinal solar wind speed profile is modelled using a hyperbolic tangent function, so that $V_{sw} = 400\ \mathrm{km{\cdot}s^{-1}}$ in the ecliptic plane, and $800\ \mathrm{km{\cdot}s^{-1}}$ over the poles, as observed by *Ulysses* (McComas et al., 2000), and a Parker heliospheric magnetic field is assumed. Furthermore, a tilt angle of $\alpha = 10^{\circ}$ is assumed, and current sheet drift is described using the approach of Burger (2012). We assume also, as a point of departure, a 100 AU heliosphere, and employ the Burger et al. (2008) local interstellar spectrum (LIS) at this boundary, so as to facilitate comparisons with the results of Engelbrecht and Burger (2013), thereby assuming steady state conditions for heliospheric plasma quantities. Future studies will relax this condition, following the approach outlined by Engelbrecht and Burger (2015b).

As to the diffusion tensor (Eq. (9)), the expression for the galactic proton parallel mean free path used here is based on the results derived from the quasilinear theory of Jokipii (1966) by Teufel and Schlickeiser (2003), as used by, e.g., Burger et al. (2008) and Engelbrecht and Burger (2013), assuming axisymmetric, anisotropic turbulence (see, e.g. Bieber et al., 1994). This mean free path is given by

$$\lambda_{\parallel} = \frac{3s}{\sqrt{\pi}(s-1)} \frac{R^2}{k_m} \left(\frac{B_o}{\delta B_{sl}}\right)^2 \cdot \left[\frac{1}{4\sqrt{\pi}} + \frac{2R^{-s}}{\sqrt{\pi}(2-s)(4-s)}\right], \tag{11}$$

where $R = R_L k_m, R_L$ being the proton gyroradius, $s = 5/3$ the slab spectrum inertial range spectral index, k_m the wavenumber corresponding to the lengthscale at which the inertial range commences, δB_{sl}^2 the slab variance, and B_o the uniform background (Parker) field. As a first approach, the perpendicular mean free path used by Engelbrecht and Burger (2013) is employed in this study. This expression is derived from the extended nonlinear guiding center theory (ENLGC) theory of Shalchi (2006), which is based on the NLGC theory proposed by Matthaeus et al. (2003), and yields results in good agreement with numerical test simulations of the perpendicular diffusion coefficient as well as with spacecraft observations of the same (see, e.g., Minnie et al., 2007a; Shalchi, 2006, 2009). This perpendicular mean free path is derived for a 2D turbulence power spectrum that is constant in the energy-containing range, has a Kolmogorov inertial range, and at the smallest wavenumbers displays an inner range with a k^q wavenumber dependence, with $q = 3$ in this study (see, e.g., Matthaeus et al., 2007). The expression for $\lambda_{\perp}$ is given by (Engelbrecht and Burger, 2013, 2015a)

$$\lambda_{\perp} = \frac{2a^2}{B_o^2} \frac{C_0 \lambda_{2D} \delta B_{2D}^2}{\lambda_{\perp}} [h_{\perp,1} + h_{\perp,2} + h_{\perp,3}], \tag{12}$$

where

$$h_{\perp,1} = \frac{\lambda_{\parallel}\lambda_{\perp}}{(1+q)\lambda_{out}^2} F_1\left(1, \frac{1+q}{2}, \frac{3+q}{2}; -x_0^{-2}\right),$$
$$h_{\perp,2} = \sqrt{3\lambda_{\parallel}\lambda_{\perp}}[\arctan(x_0) - \arctan(y_0)],$$
$$h_{\perp,3} = \frac{3\lambda_{2D}}{(1+v)^2} F_1\left(1, \frac{1+v}{2}, \frac{3+v}{2}; -y_0^2\right), \tag{13}$$

and

$$x_0 = \frac{\sqrt{3}\lambda_{out}}{\sqrt{\lambda_{\parallel}\lambda_{\perp}}}, \tag{14}$$

$$y_0 = \frac{\sqrt{3}\lambda_{2D}}{\sqrt{\lambda_{\parallel}\lambda_{\perp}}}, \tag{15}$$

with

$$C_0 = \left[\left(1 - \frac{q}{1+q}\left(\frac{\lambda_{2D}}{\lambda_{out}}\right) + \frac{1}{v-1}\right)\right]^{-1} \quad (16)$$

The quantities δB_{2D}^2 and λ_{2D} denote the 2D variance and the spectral turnover scale between the energy and inertial ranges, respectively, while λ_{out} represents the turnover lengthscale between the inner and energy-containing ranges. This last quantity is set to $\lambda_{out} = 1000\lambda_{2D}$. Furthermore, v is equal to half the Kolmogorov inertial range spectral index, and $a^2 = 1/3$ a numerical factor (see Matthaeus et al., 2003). Note that the diffusion coefficients parallel ($\kappa_\parallel$) and perpendicular ($\kappa_\perp$) to the HMF are related to the corresponding parallel and perpendicular mean free paths by $\kappa_{\parallel,\perp} = (v/3)\lambda_{\parallel,\perp}$, with v the particle speed. Drift coefficients (κ_A) are modelled to take into account the fact that these coefficients are reduced in the presence of turbulence (see, e.g., Minnie et al. (2007b)), following the approach of Engelbrecht et al. (2017). These are given by

$$\kappa_A = \frac{v}{3} R_L \frac{1}{1 + (\lambda_\perp/R_L)^2 (\delta B/B_o)^2}, \quad (17)$$

where δB^2 denotes the total (slab + 2D) transverse variance. In this the present study differs from that of Engelbrecht and Burger (2013), who model the effects of turbulence on drift following the approach of Burger and Visser (2010). The abovementioned diffusion and drift coefficients are extremely sensitive to assumptions made as to the behaviour of the turbulence power spectra throughout the heliosphere (see, e.g., Shalchi et al. (2010), Engelbrecht and Burger (2015a,b)), and hence require as inputs values for turbulence quantities such as the variance which influence the turbulence power spectra. These turbulence quantities are here calculated using the two-component Oughton et al. (2011) turbulence transport model. This model is solved as described by Engelbrecht and Burger (2013) and Engelbrecht and Burger (2015b), utilizing the same boundary values, and modelling turbulence-related terms in the same way, for the generic solar minimum conditions described above. Note that the effect of pickup ion-driven turbulence is here neglected, as fluctuations on such scales are assumed to not greatly affect the transport of galactic CR protons (see, e.g., Engelbrecht and Burger (2015b) and Engelbrecht (2017)).

Fig. 2 shows galactic CR proton differential intensities calculated at 1 AU and 0° azimuth in the ecliptic plane using the Engelbrecht and Burger (2015b) code, for positive and negative magnetic polarity cycles (left and right panels, respectively), choosing the number of pseudoparticles to be $N = 10\,000, N = 100\,000, N = 1\,000\,000$ and $N = 10\,000\,000$. Clearly the choice of $N > 10^4$ has little to no effect on spot intensities such as those shown here. The effects on computed latitude gradients and relative amplitudes are more clearly visible, shown in Fig. 3 as function of particle rigidity. Latitude gradients are not very sensitive to the choice of N during in $A < 0$ conditions, and during $A > 0$ these effects only become visible below ~ 0.5 GV. The relative amplitudes, however, are extremely sensitive to N. The expected value for this quantity, when calculated assuming a Parker field and a spherically-symmetric model heliosphere, is zero (see, e.g. Zhang, 1997). As such, then, the SDE code only begins to give realistic results when $N = 10\,000\,000$, with the error decreasing roughly as $\sim 1/\sqrt{N}$, as expected from Strauss and Effenberger (2017). This sensitivity is due to the fact that, from Eq. (2), this quantity depends on the difference in maximum and minimum intensities calculated as function of azimuthal angle at a specified radial distance and colatitude, and thus is extremely sensitive to any statistical variations in the computed intensity spectra. Comparison of the results shown in Fig. 2 with those in Fig. 3 clearly shows that pseudo-particle numbers shown to be sufficient for the calculation of differential intensity spectra at any given point in the model heliosphere are not necessarily sufficient to calculate averaged quantities such as CR relative amplitudes. Considering now specifically the results calculated assuming $N = 10^7$, the $A > 0$ latitude gradients are comparable with the observations reported by Heber et al. (316) and the simulations of Engelbrecht and

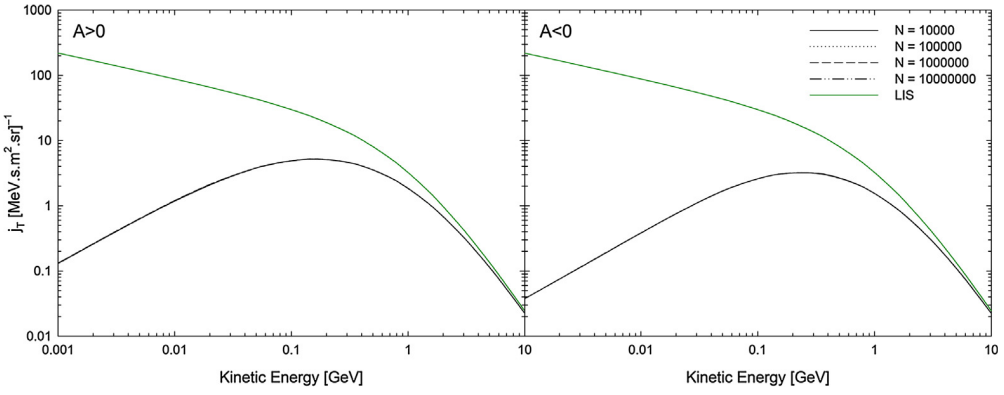

Fig. 2. Galactic CR proton differential intensities calculated at 1 AU and 0° azimuth in the ecliptic plane during $A > 0$ (left panel) and $A < 0$ (right panel), using the Engelbrecht and Burger (2015b) SDE solver. Runs are done for $N = 10\,000, N = 100\,000, N = 1\,000\,000$ and $N = 10\,000\,000$.

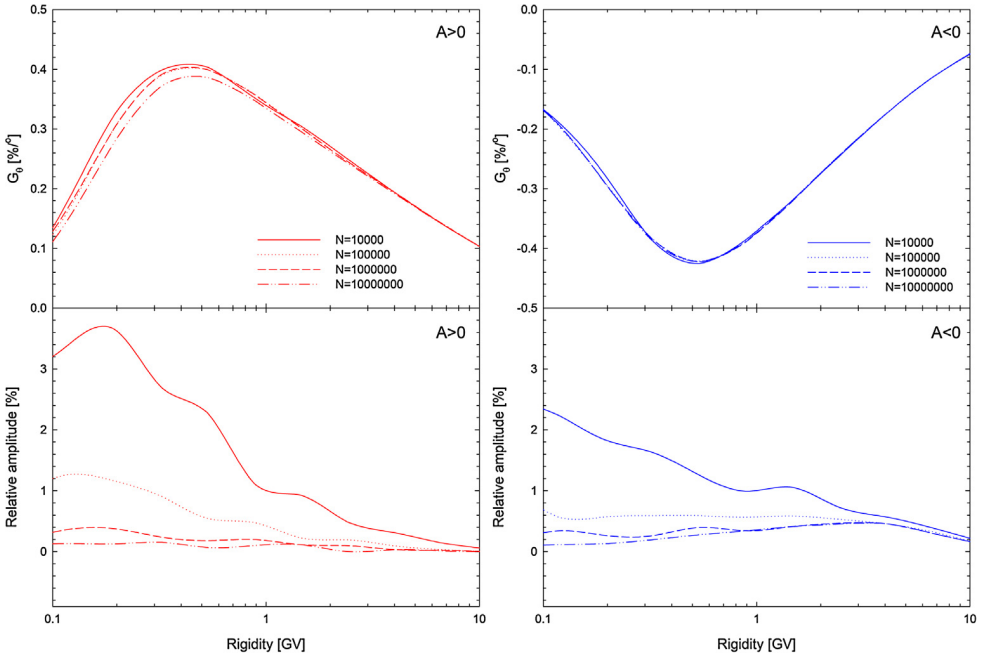

Fig. 3. Top panels: Galactic CR proton latitude gradients calculated at 2 AU and 50° colatitude during $A > 0$ (left panel) and $A < 0$ (right panel). Bottom panels: Galactic CR proton relative amplitudes calculated at 2 AU and 50° colatitude during $A > 0$ (left panel) and $A < 0$ (right panel). Quantities shown here are computed using the Engelbrecht and Burger (2015b) SDE solver. Runs are done for $N = 10000, N = 100000, N = 1000000$ and $N = 10000000$.

Burger (2013), albeit with a peak at a lower rigidity than that reported by those authors. During $A < 0$, the computed latitude gradients are negative, as expected (see, e.g., Burger et al., 2000; Heber, 2013; Gieseler and Heber, 2016), but are larger in absolute value than expected. Relative amplitudes are close to zero, as expected for a purely Parker field.

5. Discussion and conclusions

We have discussed the computational implementation of our SDE solver on the Lengau cluster of the CHPC in South Africa. The model is usually applied to the study of CR transport in the heliosphere, but aspects thereof are applicable to any diffusion equation. The independence of the different pseudo-particles make this approach ideally suited to be executed on parallel computing architectures because we require almost no communication between the different nodes or compute cores. Moreover, we require very little RAM, as only a hand-full of variables need to be defined, and these are not stored on a grid (as is the case with finite difference schemes), but are continuously updated along the trajectory of a pseudo-particle. Therefore, as expected, the code scales well when executed on the Lengau cluster, even when a realistic set-up is used. Due to the longer processing times for scenarios with more pseudo-particles (systems with larger N), the relative overhead decreases, and the code scales better. Further optimization of the model and code is, of course, possible, and we will continue to develop and refine the algorithm further.

Furthermore, we have demonstrated the effects of pseudo-particle number on galactic CR proton latitude gradients and relative amplitudes calculated with an ab initio SDE code, showing that values of N which are sufficient for calculating spot differential intensity spectra are not sufficient for calculating averaged quantities like CR relative amplitudes. Specifically, we show that at least 10^7 pseudo-particles are required to calculate accurate relative amplitudes. It has also been demonstrated that using latitude-dependent turbulence quantities calculated using a turbulence transport model as inputs for theoretically well-motivated diffusion and drift coefficients naturally leads to a reduction in computed latitude gradients, without making essentially *ad hoc* assumptions as to anisotropic perpendicular diffusion coefficients. Such a model, however, still leads to zero relative amplitudes, contrary to the observations reported on by Zhang (1997), due to the fact that no inherent azimuthal dependences exist in the model as it is implemented here. Based on the results of Sternal et al. (2011), such dependences would naturally arise if a Fisk-type field such as that proposed by Hitge and Burger (2010) were employed. The implementation of such a field in the Engelbrecht and Burger (2015b) code, along with a study of its effects on relative amplitudes and latitude gradients computed for CR protons and electrons, will be the subject of future investigation.

Acknowledgements

We would like to thank our co-workers on the SDE project for valuable research discussions. Also, Eric Mbele and Oscar Monama, for technical assistance and the CHPC for access to the new cluster. DMM would also like to thank the CHPC for financial support. This work is based on

the research supported partially by the National Research Foundation of South Africa (Grant No. 111731). Opinions expressed and conclusions arrived at are those of the authors and are not necessarily to be attributed to the NRF.

Appendix A. Africa's first petascale cluster

A.1. A brief history

The Centre for High Performance Computing (CHPC) is part of the National Integrated Cyber Infrastructure System of the government of South Africa. It was established in 2007 by the South African Department of Science and Technology and is managed by the Council for Scientific and Industrial Research (CSIR, www.csir.co.za). The mandate of the centre is to provide computational resources to the South African research community and drive human capital development in high performance computing.

Fig. A.4 summarizes the time evolution of the CHPC system's Linpack Performance from 2007 to 2017. Note the exponential increase in computing resources over time. The first computational procurement of the centre in 2007 was the International Business Machines (IBM) e1350 Linux Cluster, called Iqudu ("iqudu" is the isiXhosa word for the "kudu" antelope). The cluster was equipped with 160 nodes, each one of which equipped with dual-core Advanced Microprocessor Devices (AMD) Opteron processors with a total of 640 CPU cores and 16 GB of Random Access Memory (RAM). The cluster gave a peak performance of 2.5 Tflop/s with a storage capacity of 94 TB. This system was extensively used by the first flagship projects, identified by the CHPC, to enable scientists in these fields to embark on projects which were previously impossible. The selected flagship projects were in the fields of Computational Space and Astrophysics, Ocean and Climate Modelling, and Material Modelling (Potgieter, 2008). Due to increased demand for computational resources by the user community, the CHPC launched a SUN microsystem supercomputer in 2009, called the Tsessebe Cluster (the "tsessebe" is the fastest African antelope) with a peak performance of 24.9 Tflop/s. In 2011, the system was upgraded to 64.44 Tflop/s. This enabled the broader user community, from academia and industry, to have more access to supercomputing resources.

A.2. An African first

Most recently, in 2016, the CHPC has expanded its computing capability to an almost peta-scale system, called the Lengau Cluster ("Lengau" is the Tswana word for "Cheetah", the fastest land animal). The cluster consists of Dell servers, powered by Intel Xeon processors, using FDR InfiniBand by Mellanox, and is managed by a Bright Cluster Manager. The system consists of a total of 19 racks containing 1008 standard compute nodes (24 cores/node with a total number of 24,192 compute cores and 128 GB RAM/node), and 5 FAT nodes (56 cores/node for a total of 280 compute cores and 1024 GB memory/node). This set-up gives a theoretical peak Linpack performance of 784.5 Tflop/s. With the 2017 upgrades of the cluster, which involved the addition of 5 new compute racks (with 72 nodes on each rack), the number of nodes increased to 1368, and hence the total number of cores to 32,832. The system now has a peak performance of 1.029 Pflop/s, making it the first peta-scale system in Africa (www.top500.org). The Lengau cluster is currently running Linux CentOS 7.3, while computational tasks are managed by the PBS pro scheduler 13.0. The system is mainly used by researchers from academia in South Africa. System access to academia from Africa is free, but these researchers must acknowledge the use of the CHPC in all research-related outputs, including peer-reviewed publications, completed post-graduate degrees, and so forth. International users from outside Africa are also welcome if they participate in a research project with South African partners. The CHPC also provides limited access to industry for contract projects. To apply for an account, potential users should familiarize themselves with the CHPC user policy (http://wiki.chpc.ac.za/) and visit https://users.chpc.ac.za/. Note that computational time is

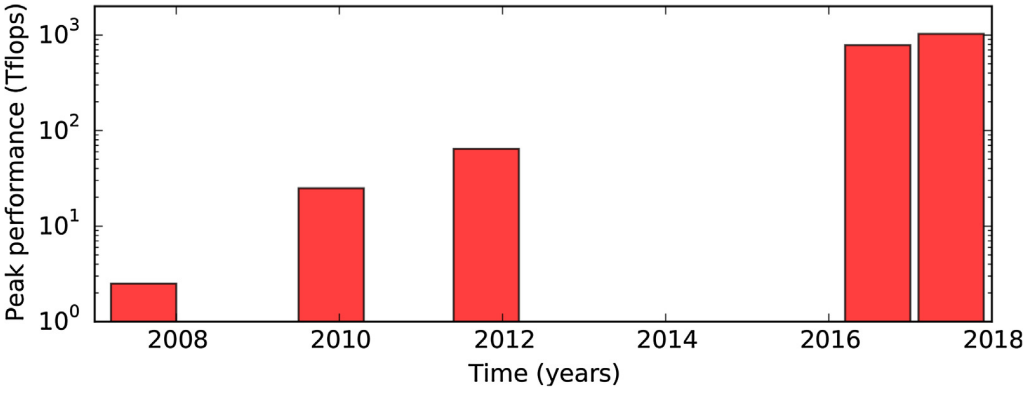

Fig. A.4. The benchmark performance of the CHPC system over time.

only allocated after the submission and acceptance of a suitable research proposal.

Appendix B. Scaling results

In this section we test the performance of the SDE model on the CHPC Lengau Cluster for a realistic set-up that is identical to that of Strauss et al. (2012). The code is compiled using the most recent version of Intel Parallel Studio installed on the cluster.

We have tested the code for different levels of optimization, from no optimization, `-O0`, to level 2 optimization, `-O2`. The results presented here were compiled with the latter, as it is the fastest, and we have found that the level of optimization did not effect the results computed with the code. Computations were performed for the SDE code with three different set-ups, namely: a small system with $N = 100$ pseudo-particles, a medium sized system with $N = 1000$ and big system with $N = 10000$.

Outputs from the model are shown in the top panel Fig. A.5. The boundary spectrum is shown as the solid black line, while the different symbols show the computed spectrum at a given spatial position (this could be, for example, at Earth). In the bottom panel of the figure, the ratio of the computed solutions (relative to the $N = 10000$ solution) is shown to illustrate the statistical nature of the solution. Depending on the application, and how accurate a solution is needed, different values of N might be used. For production runs, we usually use at least $N = 10000$.

The code's execution time on the cluster was then measured between 1 and 9 nodes (i.e. between 24 and 216 compute cores). This was done by using the `time` function in the submit script, as well as the timing calculated directly from the code. Both of these give essentially the same result. The corresponding speedup, S, and parallel efficiency, E, of the SDE code were calculated using

$$S(p) := \frac{T_1}{T_p} \tag{B.1}$$

and

$$E(p) := \frac{T_1}{pT_p} = \frac{S(p)}{p} \tag{B.2}$$

where p in the number of nodes and T_1 and T_p are the execution times for sequential execution and execution on p parallel nodes respectively (Lu and Cai, 2001).

The left panel of Fig. A.6 depicts the execution time of the SDE code and the right panel the computed speedup against the number of compute nodes, noting again that

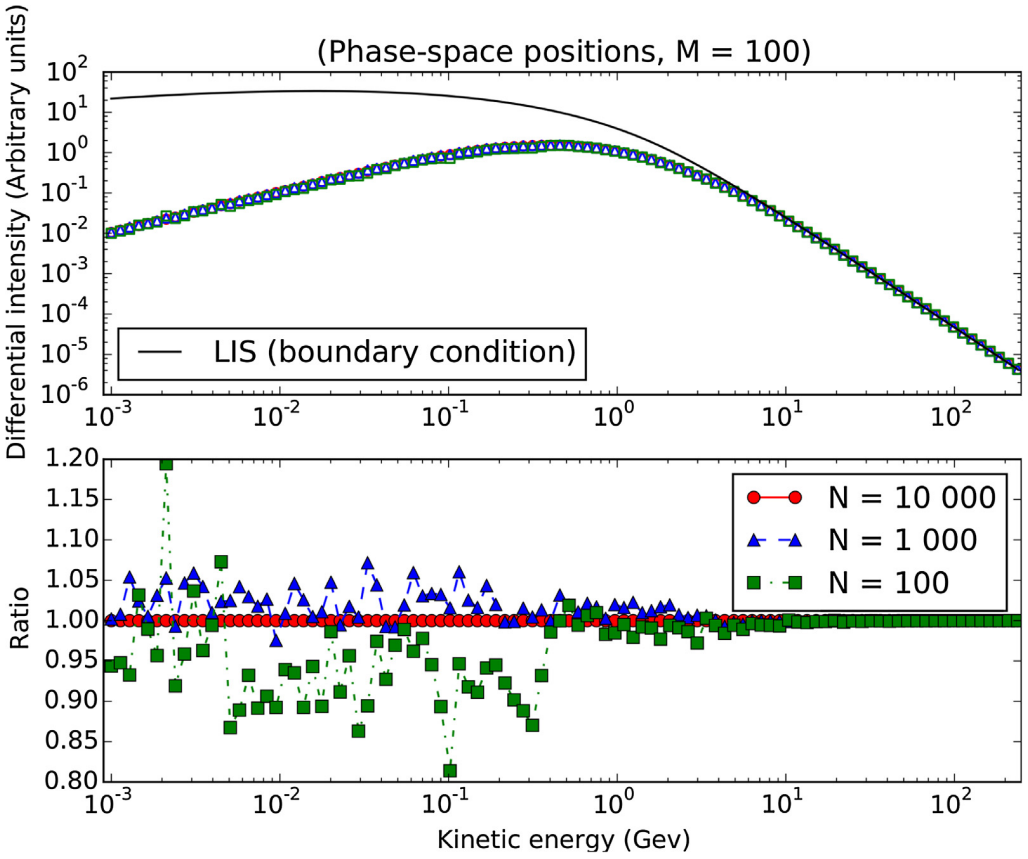

Fig. A.5. The top panel shows solutions of our test problem for a varying number of pseudo-particles. In the bottom panel, the ratio of the solutions (relative to the $N = 10000$ scenario) are shown to illustrate the statistical nature thereof.

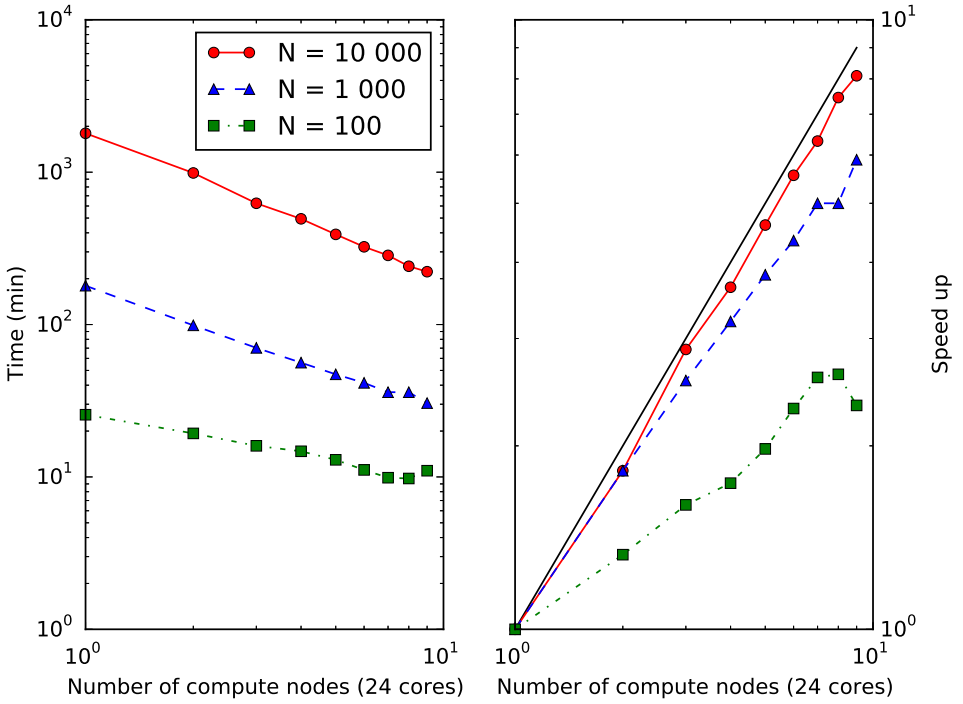

Fig. A.6. The execution time of the SDE model (left panel) and the calculated speed-up (right panel) for code set-ups of $N = 100, N = 1000$ and $N = 10000$. The solid line in the right panel shows the case of ideal speed-up.

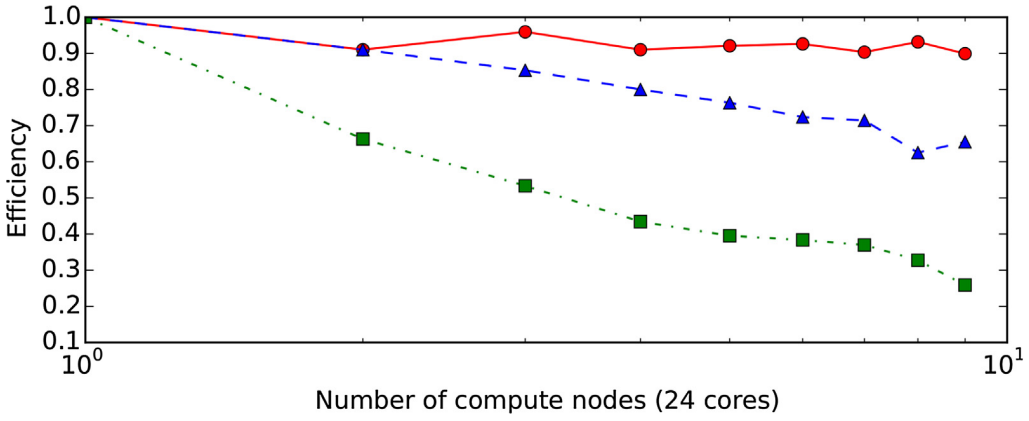

Fig. B.7. The calculated efficiency of the SDE model for different set-ups of $N = 100, N = 1000$ and $N = 10000$.

each node has 24 CPUs. These runs are for the small ($N = 100$ pseudo-particles), medium ($N = 1000$) and large ($N = 10000$) SDE systems. When using less than 5 compute nodes, all three set-ups scale linearly with increasing resources, but with the largest system clearly the most effective. When using more than 5 nodes, the linear scaling of the small and medium systems breaks down, while the $N = 10000$ scenario continues to scale extremely well with an increasing number of nodes.

The corresponding parallel efficiencies of these systems are calculated and shown in Fig. B.7. From this, it is evident that the system with the largest number of pseudo-particles is the most effective on the cluster, while a nearly linear speedup and higher efficiency is achieved. For a small system, the model becomes increasingly ineffective, and does not scale very well. For example, when using 9 compute nodes, the 10000 pseudo-particle code has a parallel efficiency of about 0.90 (90%), which is much better than the corresponding efficiency of 0.14 (14%) when using 100 pseudo-particles. In essence, by using more pseudo-particles, the code's relative overhead is decreased and hence it scales much better. Overall, the computational effectiveness allows us to tackle extremely computationally expensive simulations, such as those of cosmic ray latitude gradients discussed in Section 1 (Fig. B.8).

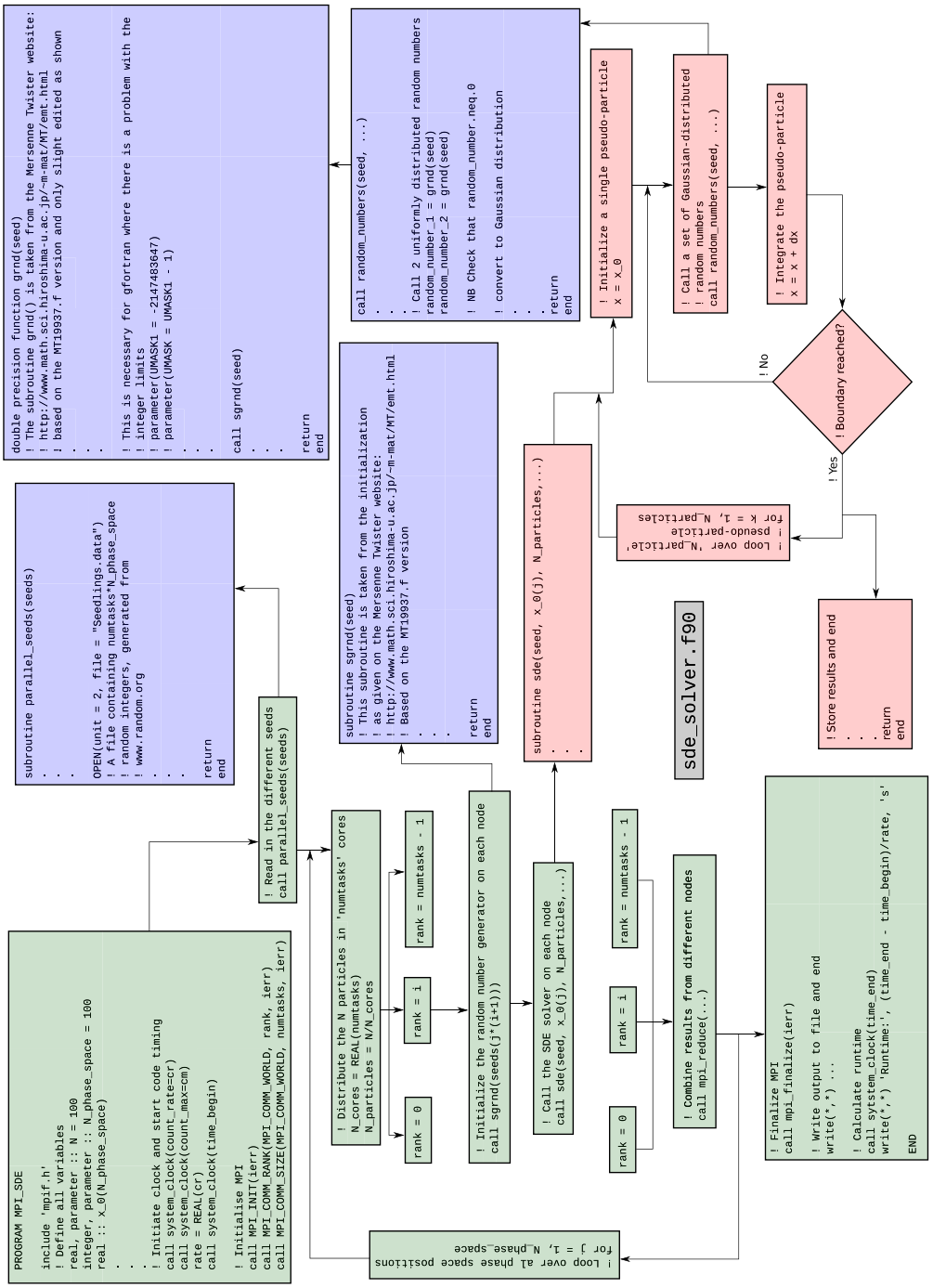

Fig. B.8. A FORTRAN 90 specific schematic representation of the SDE model.

References

Bieber, J.W., Matthaeus, W.H., Smith, C.W., Wanner, W., Kallenrode, M.B., Wibberenz, G., 1994. Proton and electron mean free paths: the Palmer consensus revisited. Astrophys. J. 420, 294–306.

Box, G.E.P., Muller, M.E., 1958. A note in the generation of normal deviates. Ann. Math. Stat. 21, 455–456.

Burger, R.A., 2012. Modeling drift along the heliospheric wavy neutral sheet. Astrophys. J. 760, 60.

Burger, R.A., Hitge, M., 2004. The effect of a Fisk-type heliospheric magnetic field on cosmic-ray modulation. Astrophys. J. Lett. 617, L73–L76.

Burger, R.A., Visser, D.J., 2010. Reduction of drift effects due to solar-wind turbulence. Astrophys. J. 725, 1366–1372.

Burger, R.A., Potgieter, M.S., Heber, B., 2000. Rigidity dependence of cosmic ray proton latitudinal gradients measured by the Ulysses spacecraft: implications for the diffusion tensor. J. Geophys. Res. 105, 27447–27455.

Burger, R.A., Kruger, T.P.J., Hitge, M., Engelbrecht, N.E., 2008. A Fisk-Parker hybrid heliospheric magnetic field with a solar cycle dependence. Astrophys. J. 674, 511–519.

Brugger, C., Weithoffer, S., de Schryver, C., Wasenmüller, U., Wehn, N., 2014. On parallel random number generation for accelerating simulations of communication systems. Adv. Radio Sci. 12, 75–81.

Della Torre, S., Bobik, P., Boschini, M.J., Consolandi, C., Gervasi, M., Grandi, D., Kudela, K., Pensotti, S., Rancoita, P.G., Rozza, D., Tacconi, M., 2012. Effects of solar modulation on the cosmic ray positron fraction. Adv. Space. Res. 49, 1587–1592.

Dunzlaff, P., Strauss, R.D., Potgieter, M.S., 2015. Solving Parker's transport equation with stochastic differential equations on GPUs. Comput. Phys. Commun. 192, 156–165.

Engelbrecht, N.E., Burger, R.A., 2013. An ab initio model for cosmic-ray modulation. Astrophys. J. 772, 46.

Engelbrecht, N.E., Burger, R.A., 2015a. A comparison of turbulence-reduced drift coefficients of importance for the modulation of galactic cosmic-ray protons in the supersonic solar wind. Adv. Space. Res. 55, 390–400.

Engelbrecht, N.E., Burger, R.A., 2015b. Sensitivity of cosmic-ray proton spectra to the low-wavenumber behavior of the 2D turbulence power spectrum. Astrophys. J. 814, 152.

Engelbrecht, N.E., Strauss, R.D., le Roux, J.A., Burger, R.A., 2017. Toward a greater understanding of the reduction of drift coefficients in the presence of turbulence. Astrophys. J. 841, 107.

Engelbrecht, N.E., 2017. On the effects of pickup ion-driven waves on the diffusion tensor of low-energy electrons in the heliosphere. Astrophys. J. Lett. 849, L15.

Ferreira, S.E.S., Potgieter, M.S., Burger, R.A., Heber, B., Fichtner, H., 2001. Modulation of Jovian and galactic electrons in the heliosphere: 1. Latitudinal transport of a few MeV electrons. J. Geophys. Res. 106, 24979–24988.

Fisk, L.A., 1996. Motion of the footpoints of heliospheric magnetic field lines at the Sun: implications for recurrent energetic particle events at high heliographic latitudes. J. Geophys. Res. 101, 15547–15553.

Florinski, V., 2009. Pickup ion acceleration at the termination shock and in the heliosheath. Space Sci. Rev. 143, 111–124.

Forsyth, R.J., Balogh, A., Smith, E.J., 2002. The underlying direction of the heliospheric magnetic field through the Ulysses first orbit. J. Geophys. Res. 107, 1405.

Gardiner, C., 2004. Stochastic Methods: A Handbook for the Natural and Social Sciences. Springer-Verlag, Berlin Heidelberg.

Gieseler, J., Heber, B., 2016. Spatial gradients of GCR protons in the inner heliosphere derived from Ulysses COSPIN/KET and PAMELA measurements. Astron. Astrophys. 589, 832.

Haasbroek, L.J., Potgieter, M.S., 1998. A new model to study galactic cosmic ray modulation in an asymmetrically bounded heliosphere. J. Geophys. Res. 103, 2099–2104.

Heber, B., 2013. Cosmic rays through the solar hale cycle: insights from Ulysses. Space. Sci. Rev. 176, 265–278.

Heber, B., Dröge, W., Ferrando, P., Haasbroek, L.J., Kunow, R., Müller-Mellin, R., Paizis, C., Potgieter, M.S., Raviart, A., Wibberenz, G., 316. Spatial variation of > 40 MeV/n nuclei fluxes observed during the Ulysses rapid latitude scan. Astron. Astrophys. 316, 538–546.

Hitge, M., Burger, R.A., 2010. Cosmic ray modulation with a Fisk-type heliospheric magnetic field and a latitude-dependent solar wind speed. Adv. Space Res. 45, 18–27.

Jokipii, J.R., Thomas, B., 1981. Effects of drift on the transport of cosmic rays. IV - Modulation by a wavy interplanetary current sheet. Astrophys. J. 243, 1115–1122.

Jokipii, J.R., 1966. Cosmic-ray propagation. I. Charged particles in a random magnetic field. Astrophys. J. 146 (2), 480–487.

Jokipii, J.R., 1973. Radial variation of magnetic fluctuations and the cosmic-ray diffusion tensor in the solar wind. Astrophys. J. 182, 585–600.

Kota, J., Jokipii, J.R., 1983. Effects of drift on the transport of cosmic rays. VI – A three-dimensional model including diffusion. Astrophys. J. 265, 573–581.

Kóta, J., Jokipii, J.R., 1995. 3-D distribution of cosmic rays in the outer heliosphere. In: Iucci, N., Lamanna, E. (Eds.), 24th International Cosmic Ray Conference, vol. 4, held August 28–September 8, 1995 in Rome, Italy. International Union of Pure and Applied Physics, p.680.

Kopp, A., Büsching, I., Strauss, R.D., Potgieter, M.S., 2012. A stochastic differential equation code for multidimensional Fokker-Planck type problems. Comput. Phys. Commun. 183, 530–542.

le Roux, J.A., Potgieter, M.S., 1995. The simulation of complete 11 and 12 year modulation cycles for cosmic rays in the heliosphere using a drift model with global merged interaction regions. Astrophys. J. 442, 847–851.

Lionello, R., Linker, J.A., Mikić, Z., Riley, P., 2006. The latitudinal excursion of coronal magnetic field lines in response to differential rotation: MHD simulations. Astrophys. J. Lett. 642, L69–L72.

Lu, Q.M., Cai, D.S., 2001. Implementation of parallel plasma particle-in-cell codes on PC cluster. Comput. Phys. Commun. 135, 93–104.

Luo, X., Potgieter, M.S., Zhang, M., Feng, X., 2017. A numerical study of Forbush decreases with a 3D cosmic-ray modulation model based on an SDE approach. Astrophys. J. 839, 53.

Maruyama, G., 1955. Continuous Markov processes and stochastic equations. Rend. Circ. Mat. Palermo. 4, 48–90.

Matthaeus, W.H., Qin, G., Bieber, J.W., Zank, G.P., 2003. Nonlinear collisionless perpendicular diffusion of charged particles. Astrophys. J. Lett. 590, L53–L56.

Matthaeus, W.H., Bieber, J.W., Ruffolo, D., Chuychai, P., Minnie, J., 2007. Spectral properties and length scales of two-dimensional magnetic field models. Astrophys. J. 667, 956–962.

Matsumoto, M., Nishimura, T., 1988. Mersenne twister: a 623-dimensionally equidistributed uniform pseudorandom number generator. ACM Trans. Model. Comput. Simul. 31, 1192–1201.

McComas, D.J., Barraclough, B.L., Funsten, H.O., Gosling, J.T., Santiago-Muñoz, E., Skoug, R.M., Goldstein, B.E., Neugebauer, M., Riley, P., Balogh, A., 2000. Solar wind observations over Ulysses' first full polar orbit. J. Geophys. Res. 105, 10419–10434.

Minnie, J., Bieber, J.W., Matthaeus, W.H., Burger, R.A., 2007a. On the ability of different diffusion theories to account for directly simulated diffusion coefficients. Astrophys. J. 663, 1049–1054.

Minnie, J., Bieber, J.W., Matthaeus, W.H., Burger, R.A., 2007b. Suppression of particle drifts by turbulence. Astrophys. J. 670, 1149–1158.

Miyake, S., Muraishi, H., Yanagita, S., 2015. A stochastic simulation of the propagation of Galactic cosmic rays reflecting the discreteness of cosmic ray sources Age and path length distribution. Astron. Astrophys. 573, A134.

Moraal, H., 2013. Cosmic ray modulation equations. Space Sci. Rev. 176, 299–319.

Oughton, S., Matthaeus, W.H., Smith, C.W., Bieber, J.W., Isenberg, P.A., 2011. Transport of solar wind fluctuations: a two-component model. J. Geophys. Res. 116, 8105.

Parker, E.N., 1958. Dynamics of the interplanetary gas and magnetic fields. Astrophys. J. 128, 664–676.

Parker, E.N., 1965. The passage of energetic charged particles through interplanetary space. Planet. Space Sci. 13, 9–49.

Peaceman, D.W., Rachford, H.H., 1955. The numerical solution of parabolic and elliptic differential equations. J. Soc. Ind. Appl. Math. 3 (1), 28–41.

Pei, C., Bieber, J.W., Burger, R.A., Clem, J., 2010. A general time-dependent stochastic method for solving Parker's transport equation in spherical coordinates. J. Geophys. Res. 115, A12107.

Potgieter, M.S., Haasbroek, L.J., Ferrando, P., Heber, B., 1997. The modelling of the latitude dependence of cosmic ray protons and electrons in the inner heliosphere. Adv. Space Res. 19 (6), 917–920.

Potgieter, M.S., 2008. Probing the Universe with cosmic rays using high performance computing. S. Afr. J. Sci. 104, 465–471.

Potgieter, M.S., 2013. Cosmic rays in the inner heliosphere: insights from observations, theory and models. Space Sci. Rev. 176, 165–176.

Reames, D.V., 2013. The two sources of solar energetic particles. Space Sci. Rev. 175, 53–92.

Roberts, D.A., Giacalone, J., Jokipii, J.R., Goldstein, M.L., Zepp, T.D., 2007. Spectra of polar heliospheric magnetic fields and implications for field structure. J. Geophys. Res. 112, 8103.

Shalchi, A., 2006. Extended nonlinear guiding center theory of perpendicular diffusion. Astron. Astrophys. 453, L43–L46.
Shalchi, A., 2009. Nonlinear Cosmic Ray Diffusion Theories. Springer, Germany.
Shalchi, A., Li, G., Zank, G.P., 2010. Analytic forms of the perpendicular cosmic ray diffusion coefficient for an arbitrary turbulence spectrum and applications on transport of Galactic protons and acceleration at interplanetary shocks. Astrophys. Space Sci. 325, 99–111.
Srinivasan, A., Mascagni, M., Ceperley, D., 2003. Testing parallel random number generators. Parallel Comput. 29, 69–94.
Sternal, O., Engelbrecht, N.E., Burger, R.A., Ferreira, S.E.S., Fichtner, H., Heber, B., Kopp, A., Potgieter, M.S., Scherer, K., 2011. Possible evidence for a Fisk-type heliospheric magnetic field. I. Analyzing Ulysses/KET electron observations. Astrophys. J. 741, 23.
Stone, E.C., Cummings, A.C., McDonald, F.B., Heikkila, B.C., Lal, N., Webber, W.R., 2013. Voyager 1 observes low-energy galactic cosmic rays in a region depleted of heliospheric ions. Science 341, 150–153.
Strauss, R.D., Effenberger, F., 2017. A Hitch-hiker's guide to stochastic differential equations. Space Sci. Rev., 1–42
Strauss, R.D., Potgieter, M.S., Büsching, I., Kopp, A., 2011a. Modeling the modulation of galactic and Jovian electrons by stochastic processes. Astrophys. J. 735, 83–96.
Strauss, R.D., Potgieter, M.S., Kopp, A., Büsching, I., 2011b. On the propagation times and energy losses of cosmic rays in the heliosphere. J. Geophys. Res. 116, A12105.
Strauss, R.D., Potgieter, M.S., Büsching, I., Kopp, A., 2012. Modelling heliospheric current sheet drift in stochastic cosmic ray transport models. Astrophys. Space Sci. 339, 223–236.
Teufel, A., Schlickeiser, R., 2003. Analytic calculation of the parallel mean free path of heliospheric cosmic rays. II. Dynamical magnetic slab turbulence and random sweeping slab turbulence with finite wave power at small wavenumbers. Astron. Astrophys. 397, 15–25.
Wawrzynczak, A., Alania, M.V., 2010. Modeling and data analysis of a Forbush decrease. Adv. Space Sci. 45, 622–631.
Yamada, Y., Yanagita, S., Yoshida, T., 1998. A stochastic view of the solar modulation phenomena of cosmic rays. Geophys. Res. Lett. 25, 2353–2356.
Zhang, M., 1997. A linear relationship between the latitude gradient and 26 day recurrent variation in the fluxes of galactic cosmic rays and anomalous nuclear components. I. Observations. Astrophys. J. 488, 841–853.
Zhang, M., 1999a. A path integral approach to the theory of heliospheric cosmic-ray modulation. Astrophys. J. 510, 715–725.
Zhang, M., 1999b. A Markov stochastic process theory of cosmic-ray modulation. Astrophys. J. 513, 409–420.
Zurbuchen, T.H., Schwadron, N.A., Fisk, L.A., 1997. Direct observational evidence for a heliospheric magnetic field with large excursions in latitude. J. Geophys. Res. 102, 24175–24181.

CHAPTER 5

A fully time-dependent ab initio cosmic-ray modulation model applied to historical cosmic-ray modulation

The paper presented in this chapter has been published in The Astrophysical Journal: K. D. Moloto and N. E. Engelbrecht — The Astrophysical Journal, 894:121

The Astrophysical Journal, 894:121 (12pp), 2020 May 10 https://doi.org/10.3847/1538-4357/ab87a2

A Fully Time-dependent Ab Initio Cosmic-Ray Modulation Model Applied to Historical Cosmic-Ray Modulation

K. D. Moloto[1] and N. Eugene Engelbrecht[1,2]
[1] Center for Space Research, North-West University, Potchefstroom, 2522, South Africa; n.eugene.engelbrecht@gmail.com
[2] National Institute for Theoretical Physics (NITheP), Gauteng, South Africa
Received 2020 March 12; revised 2020 April 6; accepted 2020 April 6; published 2020 May 14

Abstract

Cosmogenic nuclide records can in principle allow for the estimation of the behavior of the heliospheric magnetic field (HMF) in the distant past. This requires careful modeling of cosmic-ray transport in a manner that is as realistic as possible, taking into account as many of the factors affecting the transport of cosmic-rays (CRs) as possible. The present study presents a 3D time-dependent ab initio CR modulation code that utilizes as inputs simple theoretically and observationally motivated temporal profiles to model large-scale (such as the tilt angle) and small-scale (such as the magnetic variance) parameters relevant to CR transport. Galactic CR proton differential intensities computed using this model for the period 1977–2001 are in reasonable to good agreement with spacecraft observations, reproducing the major salient features of the observed CR intensity temporal profile. To investigate pre-space-age cosmic-ray modulation, and to test conclusions previously drawn regarding the relative importance of drift effects on said modulation, historic estimates of the past HMF presented by McCracken & Beer were used as inputs for the model. The resulting CR temporal intensity profile displays clear evidence of drift effects, with a sharp peak in intensities during the Dalton Minimum.

Unified Astronomy Thesaurus concepts: Heliosphere (711); Cosmic rays (329); Solar cycle (1487)

1. Introduction

Estimates of the historical behavior of the heliospheric magnetic field (HMF), prior to the advent of direct observations thereof during the space age, provide a valuable basis for the comparison of recent solar activity with that of the past (see, e.g., Svalgaard & Cliver 2010; Barnard et al. 2011, 2018; Cliver & Herbst 2018). Insights from such studies can also in turn be used to attempt to extrapolate the potential future behavior of the HMF and other related quantities (e.g., Abreu et al. 2008; Steinhilber et al. 2012; Goelzer et al. 2013; Smith et al. 2014; Ahluwalia 2016). Such information could also potentially be used to predict future galactic cosmic-ray (GCR) intensities, which would prove essential when planning future, long-term manned missions in space (see, e.g., Schwadron et al. 2014; Moloto et al. 2018, and references therein). Several methods are used to deduce the historical changes in the HMF magnitude near Earth. Estimates calculated using reconstructed sunspot data (e.g., Goelzer et al. 2013; Usoskin 2017) or various geomagnetic indices (e.g., Svalgaard & Cliver 2007; Lockwood et al. 2018) tend to be in agreement, while modulation theory-derived estimates based on comparisons with cosmogenic nuclides like ^{10}Be, where the HMF magnitude is calculated by inverting some solution of the Parker (1965) CR transport equation (TPE), have been more contentious (see the review by Cliver & Herbst 2018 and references therein). These cosmogenic nuclides are direct products of the interactions of CRs with atmospheric molecules, and as such provide a measure of cosmic-ray fluxes in the past (for more details, see, e.g., Beer et al. 2012; Wieler 2017). The last-mentioned approach to calculating estimates for the HMF magnitude is the focus of this study. In prior studies, two techniques have been employed to accomplish this inversion. The first entails the comparison of modulation potentials calculated using the force field solution of the Parker TPE (Gleeson & Axford 1968) with those inferred from cosmogenic nuclide measurements (see, e.g., Steinhilber et al. 2008; Muscheler et al. 2016). Assumptions are made as to the magnetic field dependence of the CR effective diffusion coefficient and relevant local interstellar spectra, and inferences are drawn as to the behavior of the HMF magnitude therefrom (see, e.g., Steinhilber et al. 2010; Cliver & Herbst 2018, and references therein). Although this approach yields reasonable results, it suffers from some disadvantages. First, the force field approach represents a steady-state, one-dimensional solution to the Parker TPE (see Moraal 2013), and as such neglects much of the physics of CR transport such as drift, which has a demonstrable effect on CR intensities (see, e.g., Jokipii & Levy 1977; Caballero-Lopez & Moraal 2004; Caballero-Lopez et al. 2019). Furthermore, any result calculated using this approach will be sensitive to the form of the local interstellar spectrum assumed (e.g., Asvestari et al. 2017; Herbst et al. 2017), which may change over long time periods. Lastly, the simple magnetic field dependences required of diffusion coefficients to simply invert force field solutions are not necessarily realistic, as theory often predicts more complicated dependences of these coefficients on various turbulence quantities as well as on the HMF magnitude (see, e.g., Shalchi 2009; Engelbrecht & Burger 2015b; Wiengarten et al. 2016; Engelbrecht 2017), which also change as a function of solar cycle (see, e.g., Zhao et al. 2018). The second approach to this problem, proposed by Caballero-Lopez et al. (2004a), employs a 2D, time-dependent solution of the Parker TPE described by Caballero-Lopez et al. (2004b) to calculate CR differential intensities, assuming various simple HMF magnitude dependences for the diffusion coefficients employed. These differential intensities, calculated for GCR H and He, were then converted to ^{10}Be concentrations using the ^{10}Be yield function proposed by Webber & Higbie (2003). Comparisons were made to 22 yr averaged ^{10}Be concentrations (see McCracken et al. 2004, for a description of the data used), so Caballero-Lopez et al. (2004a) assumed a constant solar

The Astrophysical Journal, 894:121 (12pp), 2020 May 10 Moloto & Engelbrecht

cycle average tilt angle of 40° in their calculations, which were performed twice, assuming first an $A > 0$ and then an $A < 0$ magnetic polarity, where $A > 0$ denotes a polarity cycle where the HMF points away from the Sun in the northern hemisphere of the heliosphere and toward the Sun in the southern hemisphere of the heliosphere, and vice versa for $A < 0$. These two temporal intensity profiles were then averaged, and the result compared to ^{10}Be concentration data. The HMF temporal profile reported by these authors was then calculated from the diffusion coefficients needed to produce a reasonable fit to the ^{10}Be data. This analysis also forms the basis of subsequent analyses that underlie the historical HMF temporal profiles reported by McCracken (2007) and McCracken & Beer (2015).

The aim of this study is to partially revisit the calculations of Caballero-Lopez et al. (2004a) and the conclusions as to very long-term GCR modulation those authors drew, in particular their assessment of the importance of drift effects, which they concluded did not have a large effect on their results. Furthermore, since the publication of this study, more observational information as to turbulence quantities relevant to CR transport has been reported in the literature (see, e.g., Matthaeus & Velli 2011; Bruno & Carbone 2013; Oughton et al. 2015; Zhao et al. 2018), and more insight as to the spatial variations of these quantities has been acquired through turbulence transport modeling (see, e.g., Oughton et al. 2011; Adhikari et al. 2015; Usmanov et al. 2016; Wiengarten et al. 2016; Zank et al. 2017, 2018). Advances have also been made in terms of theoretical descriptions of diffusion (e.g., Shalchi 2010; Ruffolo et al. 2012; Qin & Zhang 2014) and the effects of turbulence on particle drift coefficients (e.g., Engelbrecht & Burger 2015a; Engelbrecht et al. 2017), which have been used in various CR modulation studies that compute intensities for different GCR species in reasonable to good agreement with spacecraft observations (see, e.g., Engelbrecht & Burger 2013a, 2013b; Qin & Shen 2017; Moloto et al. 2018; Shen et al. 2019). Lastly, the advent of stochastic techniques to solve the Parker TPE, already commonly employed in CR modulation studies (e.g., Pei et al. 2010; Strauss et al. 2011; Engelbrecht & Burger 2015b; Boschini et al. 2019), greatly facilitates the study of very long term CR modulation.

In this study, the aim is not to minutely reproduce every feature in the observed CR temporal intensity profiles. Given the uncertainties implicit to any modulation study (see, e.g., Kóta 2013), this is not yet possible. The aim here is to present a model robust enough to reproduce the major salient features of time-dependent CR modulation in such a way as to allow for the meaningful extrapolation of the model to prior times using extremely limited inputs. To that end, a 3D fully time-dependent Stochastic Differential Equation (SDE) CR modulation code is employed to solve the Parker TPE over several solar cycles during the space age, adapting the steady-state code of Engelbrecht & Burger (2015b) so as to incorporate relatively simple, observationally and theoretically motivated time-dependent models for plasma quantities such as the HMF magnitude and magnetic variance, thereby creating a model whereby the time-dependent modulation of galactic cosmic rays during the space age can be better understood. This route differs from that employed by Moloto et al. (2018), which was also based on the Engelbrecht & Burger (2015b) SDE code, but instead took an effective-value approach (see, e.g., Nagashima & Morishita 1980a, 1980b) to model these plasma quantities. This approach assumes constant average values for heliospheric quantities (such as the tilt angle) calculated over the residence time of CRs in the heliosphere, and yielded differential intensities in reasonable to good agreement with spacecraft observations of the same taken during the last three solar minima. Furthermore, Moloto et al. (2018) could also successfully reproduce the unusually high galactic proton intensities in 2009 reported by Adriani et al. (2013). Extending such a study to take into account heliospheric modulation conditions over many solar cycles, however, requires an approach that more accurately models the time dependence of these conditions throughout the heliosphere, which is now rendered possible due to the unique advantages afforded by the stochastic approach to solving the Parker TPE, which includes unconditional stability, ease of parallelization, and the fact that individual pseudoparticle trajectories are statistically independent of one another (see, e.g., Zhang 1999b; Gardiner 2004; Strauss & Effenberger 2017; Moloto et al. 2019). This model is described in the second section of this study. In the third section, selected results computed using the abovementioned model will be compared with various spacecraft observations, including a temporal intensity profile and differential intensity energy spectra. Comparisons are also made with observed intensity-tilt data, so as to ascertain whether the model correctly describes the interplay between various modulation mechanisms, such as diffusion and drift, relevant to CR transport.

To investigate the effects of these various mechanisms on the long term modulation of CRs, an existing long term temporal profile for the HMF magnitude is employed as an input for the model. In this study, the PCR2 HMF profile of McCracken & Beer (2015) is used. This provides annual values for the HMF magnitude, calculated from annual ^{10}Be concentrations that have been cleared of the signatures of impulsive events due to, e.g., geomagnetic storms and nuclear weapons tests. Furthermore, a historical temporal profile for the heliospheric tilt angle is utilized so as to test the effects of current sheet drift on the resulting computed GCR intensities, and reconstructed using the sunspot record as proposed by Asvestari & Usoskin (2016). The resulting intensities are then compared with those calculated by employing some of the assumptions employed by Caballero-Lopez et al. (2004a). The study closes with a section devoted to a summary of the above results, and the conclusions drawn therefrom.

2. The Modulation Model

In the present study, the Parker (1965) cosmic-ray TPE is solved stochastically, modifying the model presented by Engelbrecht & Burger (2015b). This equation, neglecting possible sources of CRs such as the Jovian magnetosphere, is given by

$$\frac{\partial f_0}{\partial t} = \nabla \cdot (\boldsymbol{K} \cdot \nabla f_0) - \boldsymbol{V}_{\rm sw} \cdot \nabla f_0 + \frac{1}{3}(\nabla \cdot \boldsymbol{V}_{\rm sw}) \frac{\partial f_0}{\partial \ln p}, \quad (1)$$

where p and $\boldsymbol{r}$ denote particle momentum and position, $f_0(\boldsymbol{r}, p, t)$ is the omnidirectional cosmic-ray distribution function, such that the cosmic-ray differential intensity is $j_T = p^2 f_0$ (see, e.g., Moraal 2013), and $\boldsymbol{V}_{\rm sw}$ and $\boldsymbol{K}$ denote, respectively, the solar wind velocity and heliospheric diffusion tensor. Various processes modulating an initial, boundary CR differential intensity j_B are described by this TPE, including CR drift due to gradients and curvatures of the heliospheric

The Astrophysical Journal, 894:121 (12pp), 2020 May 10 Moloto & Engelbrecht

magnetic field and along the heliospheric current sheet, diffusion (both described by the first term on the right-hand side of Equation (1)), the outward convection of cosmic rays by the solar wind (second term on the right-hand side of Equation (1)), and adiabatic cooling (third term on the right-hand side of Equation (1)). Equation (1) can be written in terms of a set of equivalent Itō SDEs (see, e.g., Strauss & Effenberger 2017, and references therein) given by

$$dx_i = A_i(x_i)dt + \sum_j B_{i,j}(x_i) \cdot dW_i, \tag{2}$$

with subscripts $i \in [r, \theta, \phi, E]$ referring to heliocentric spherical polar coordinates (r, θ, ϕ) and CR kinetic energy E, $x_i(t)$ are Itō processes (see, e.g., Gardiner 2004), and dW_i satisfy a Weiner process, such that (Strauss & Effenberger 2017)

$$dW_i(t) = \eta(t)\sqrt{dt}, \tag{3}$$

where η (t) represents a pseudo-random, Gaussian distributed number between zero and one. Pseudo-random numbers are here generated using the Mersenne Twister algorithm developed by Matsumoto & Nishimura (1998). Equation (2) is solved in the time-backward manner using the Euler–Maruyama approximation (Maruyama 1955). Therefore, the evolution of a sufficiently large number of pseudo-particles N at a particular energy/rigidity, and at a pre-specified point in phase-space and time (x_i^o, t^o) (e.g., at Earth), are followed to their exit positions, times, and energies at a pre-specified boundary (x_i^e, t^e). Then the CR intensity at the initial point can be calculated using (Strauss & Effenberger 2017)

$$j(x_i^o, t^o) = \frac{1}{N}\sum_{k=1}^{N} j_B(x_{i,k}^e, t_k^e), \tag{4}$$

using the assumed boundary CR intensity. Note that $N = 10{,}000$ is used throughout this study. The tensor $\boldsymbol{B}$ and vector $\boldsymbol{A}$ are related to the CR transport coefficients, and are given by, e.g., Pei et al. (2010) and Engelbrecht & Burger (2015b), such that, for a fully 3D HMF,

$$\begin{aligned}
B_{1,1} &= \frac{\sqrt{2(\kappa_{\phi\phi}\kappa_{r\theta}^2 - 2\kappa_{r\phi}\kappa_{r\theta}\kappa_{\theta\phi} + \kappa_{rr}\kappa_{\theta\phi}^2 + \kappa_{\theta\theta}\kappa_{r\phi}^2 - \kappa_{rr}\kappa_{\theta\theta}\kappa_{\phi\phi})}}{\sqrt{\kappa_{\theta\phi}^2 - \kappa_{\theta\theta}\kappa_{\phi\phi}}},\\
B_{1,2} &= \frac{\kappa_{r\phi}\kappa_{\theta\phi} - \kappa_{r\theta}\kappa_{\phi\phi}}{\kappa_{\theta\phi}^2 - \kappa_{\theta\theta}\kappa_{\phi\phi}}\sqrt{2\left(\kappa_{\theta\theta} - \frac{\kappa_{\theta\phi}^2}{\kappa_{\phi\phi}}\right)},\\
B_{1,3} &= \frac{\sqrt{2}\,\kappa_{r\phi}}{\sqrt{\kappa_{\phi\phi}}},\\
B_{2,2} &= \frac{\sqrt{2(\kappa_{\theta\theta} - \kappa_{\theta\phi}^2/\kappa_{\phi\phi})}}{r},\\
B_{2,3} &= \frac{\kappa_{\theta\phi}}{r}\sqrt{\frac{2}{\kappa_{\phi\phi}}},\\
B_{3,3} &= \frac{\sqrt{2\kappa_{\phi\phi}}}{r\sin\theta},\\
B_{2,1} &= B_{3,1} = B_{3,2} = 0
\end{aligned} \tag{5}$$

where κ denotes one of the elements of the diffusion tensor $\boldsymbol{K}$ in Equation (1) in heliocentric spherical coordinates. The present study employs the diffusion tensor transformation proposed by Burger et al. (2008) to convert the diffusion tensor in HMF-aligned coordinates $\boldsymbol{K}'$, given by

$$\boldsymbol{K}' = \begin{bmatrix} \kappa_{\parallel} & 0 & 0 \\ 0 & \kappa_{\perp,2} & \kappa_A \\ 0 & -\kappa_A & \kappa_{\perp,3} \end{bmatrix}, \tag{6}$$

where parallel and perpendicular subscripts denote diffusion coefficients parallel and perpendicular to the assumed HMF, and κ_A the drift coefficient (see, e.g., Forman et al. 1974), to a diffusion tensor in spherical coordinates. Note that elements of the above tensor are related to the mean free paths (MFPs) discussed below by $\kappa = v\lambda/3$, with v the particle speed. The vector $\boldsymbol{A}$ is given by (Engelbrecht & Burger 2015b)

$$\begin{aligned}
A_r &= \frac{1}{r^2}\frac{\partial}{\partial r}r^2\kappa_{rr} + \frac{1}{r\sin\theta}\frac{\partial}{\partial\phi}\kappa_{r\phi}\\
&\quad + \frac{1}{r\sin\theta}\frac{\partial}{\partial\theta}\kappa_{r\theta}\sin\theta - V_{\rm sw} - V_{d,r},\\
A_\theta &= \frac{1}{r^2}\frac{\partial}{\partial r}r^2\kappa_{r\theta} + \frac{1}{r^2\sin\theta}\frac{\partial}{\partial\theta}\kappa_{\theta\theta}\sin\theta\\
&\quad + \frac{1}{r^2\sin\theta}\frac{\partial}{\partial\phi}\kappa_{\theta\phi} - \frac{V_{d,\theta}}{r},\\
A_\phi &= \frac{1}{r^2\sin^2\theta}\frac{\partial}{\partial\phi}\kappa_{\phi\phi} + \frac{1}{r^2\sin^2\theta}\frac{\partial}{\partial r}r\kappa_{\phi\phi}\\
&\quad + \frac{1}{r^2\sin^2\theta}\frac{\partial}{\partial\theta}\kappa_{\theta\phi} - \frac{V_{d,\phi}}{r\sin\theta},\\
A_E &= \frac{1}{3r^2}\frac{\partial}{\partial r}(r^2V_{\rm sw})\frac{(E+2E_o)}{E+E_o}E,
\end{aligned} \tag{7}$$

with E_o the CR rest-mass energy. Note that the signs of A_E, as well as of the solar wind and drift speeds $V_{\rm sw}$ and V_d, are chosen so as to render explicitly the time-backward nature of the approach taken to solving Equation (2), and thus Equation (1), in this study.

Any attempt at modeling the time-dependent transport of CRs in the heliosphere must take into account the observed solar cycle dependences of both large and small scale heliospheric plasma quantities. The top panel of Figure 1 shows almost 45 yr worth of OMNI observations of the HMF magnitude B_o at Earth (solid green line), as well as observations of the line-of-sight model tilt angle α (solid blue line; Hoeksema 1995). The former quantity displays a clear, almost sinusoidal ∼11 yr cycle, with an average magnitude of ∼5 nT at Earth during solar minimum conditions, but increasing to ∼10 nT during solar maximum conditions. The HMF also displays a further ∼22 yr cycle, where it reverses its polarity in the north/south hemispheres of the heliosphere (see, e.g., Parker 2001). Overall, the Parker (1958) model accurately describes the spatial evolution of the HMF in the heliosphere (see, e.g., Ness 2006), although alternative models have been proposed (see, e.g., Smith & Bieber 1991; Fisk 1996; Hitge & Burger 2010). The tilt angle also displays a clear ∼11 yr periodicity, but the rising slope of this quantity as solar activity increases toward solar maximum is markedly different from that observed as solar activity decreases (see, e.g., Cliver & Ling 2001). Ulysses observations of the solar wind speed $V_{\rm sw}$ show a clear latitude dependence in this quantity during solar minimum, with a slow ∼400 km s^{-1} solar wind in the equatorial regions, and a fast ∼800 km s^{-1} wind at high latitudes. During solar maximum conditions this is no longer

The Astrophysical Journal, 894:121 (12pp), 2020 May 10 Moloto & Engelbrecht

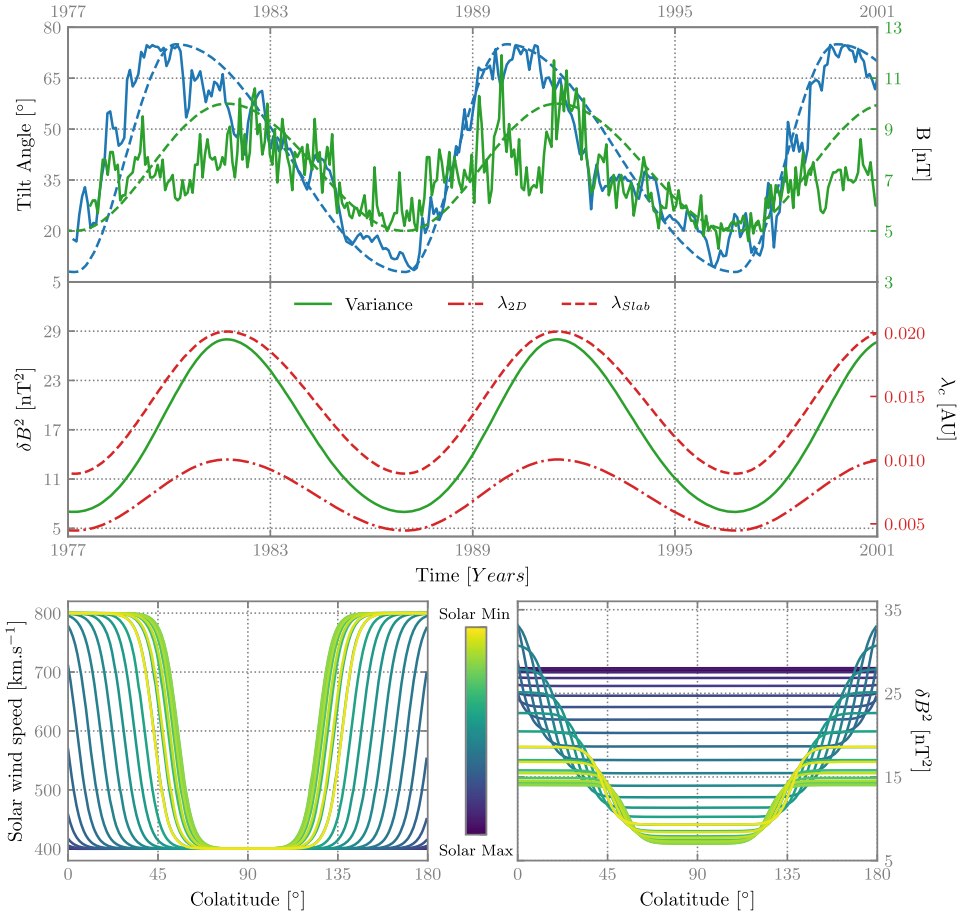

Figure 1. Top panel: heliospheric tilt angle α (blue dashed line, Equation (8)) and HMF magnitude at Earth (green line, Equation (9)), as a function of time, along with OMNI and Wilcox Solar Observatory (http://wso.stanford.edu) observations (solid green and blue lines, respectively). Middle panel: temporal scalings employed in the present study for the total variance (green line) and slab/2D correlation scales (red dashed/dotted–dashed lines). Bottom left panel: solar wind speed profile (Equation (10)) employed in this study as a function of colatitude. Green lines indicate solar minimum profiles, fading toward the bluer solar maximum profiles that are essentially colatitude-independent. Bottom right panel: same as bottom left panel, but denoting the colatitudinal profile for the total variance employed here.

the case, as no clear latitude dependence can be distinguished (see, e.g., McComas et al. 2000, for more detail). The magnetic variance, a key turbulence input for diffusion coefficients, has also been observed to vary with solar cycle, displaying the same temporal dependence as the HMF (see, e.g., Burlaga 2001; Zhao et al. 2018), while the magnetic correlation scale has been shown to display a similar solar cycle dependence (e.g., Matthaeus et al. 1986; Burger & Engelbrecht 2018), although not all studies of this quantity report this (e.g., Wicks et al. 2010).

As a first approach, the 1 au values of the abovementioned quantities are modeled using relatively simple temporal dependences, chosen to mimic the most salient observational features continuously, so as to facilitate their use in a time-backward SDE modulation code, as well as to allow for ease of implementation when longer-term inputs for heliospheric quantities, such as those presented by, e.g., McCracken & Beer (2015) for the HMF magnitude at Earth, are considered later in this study. These values are then assumed to propagate outwards at the solar wind speed, so that the value of a quantity required to calculate the transport parameters for the ith pseudoparticle at some position (r_i, θ_i, ϕ_i) and time T_i can be related, with appropriate scaling, to the value of that quantity at Earth at a time $T = T_i - T_\eta$, where $T_\eta = r_i/V_{sw}$, assuming a radially constant solar wind speed, which is approximately accurate within the termination shock. Essentially, the aim is to calculate the appropriate large and small scale plasma quantity values at the time and location of a pseudoparticle, so as to calculate its transport parameters in a temporally and spatially dependent manner, taking advantage of the Markovian nature of the Levy flights implicit to the stochastic approach to solving the Parker TPE (see Zhang 1999a, 1999b). This involves renormalizing the expressions used to model the various quantities with every Levy flight, with the appropriate spatial dependences, so that they assume their correct values at the location of the pseudoparticle. An example of this would be to calculate the "local" tilt angle for a pseudoparticle at position (r_i, θ_i, ϕ_i) and time T_i. This would then be equal to the tilt angle at 1 au at time T, and the latter angle would then be used to calculate the current sheet angle, and thus the current sheet drift velocity, at position (r_i, θ_i, ϕ_i) and time T_i. For quantities with explicit spatial dependences, like the HMF magnitude, the field at (r_i, θ_i, ϕ_i) and time T_i would be the Parker (1958) field normalized to the value at Earth at time T. This implies a "different" Parker field for each time T_i and for each pseudoparticle, but ensures that the transport parameters for each pseudoparticle, at each T_i, are correct at each position (r_i, θ_i, ϕ_i). As an ensemble, then, all pseudoparticles experience a time-dependent Parker field. A similar approach is taken by, e.g., Qin & Shen (2017).

The Astrophysical Journal, 894:121 (12pp), 2020 May 10 Moloto & Engelbrecht

The tilt angle of the heliospheric current sheet is modeled as

$$\alpha(T) = \alpha_{\min} + \left(\frac{\pi}{4.8} - \frac{\alpha_{\min}}{2}\right) \times \begin{cases} 1 - \cos\left(\frac{\pi}{6.8}(T - 9.8)\right), & 0 \leqslant T \leqslant 6.8 \\ 1 - \cos\left(\frac{\pi}{3.0}T\right), & 6.8 < T \leqslant 9.8 \end{cases} \quad (8)$$

based on Burger et al. (2008), where the angles are expressed in radians and $\alpha_{\min} = \pi/22.8$ for the present case, and times are in fractional years past solar minimum. The tilt angle is therefore assumed to vary between 7.°9 (the mean solar minimum tilt angle) and 75° (the limit to which the radial model tilt angle extends) as shown in the top panel of Figure 1. The temporal variations in the Parker (1958) HMF magnitude at Earth and the time evolution of the latitudinal dependence of $V_{\rm sw}$ are modeled as

$$L = \begin{cases} \cos\left(\frac{\pi}{4.5}(T - 9.8)\right), & 0 \leqslant T \leqslant 4.5 \\ \cos\left(\frac{\pi}{5.3}T\right), & 4.5 < T \leqslant 9.8 \end{cases} \quad (9)$$

such that the magnetic field and tilt angle minima are in phase and the magnetic field maxima lag the tilt angle maxima by ~2.5 yr, as observed in the data, and with B_o varying between 5 and 10 nT from solar minimum to solar maximum (shown in the top panel of Figure 1). As a first approach, the HMF polarity is modeled to change at times where the HMF magnitude at Earth is at its maximum (for an alternative approach to this, see Shen & Qin 2018). The solar wind speed latitudinal dependence is modeled as a function of colatitude θ using

$$V_{\rm sw}(\theta) = 400 \begin{cases} \frac{3}{2} - \frac{1}{2}\tanh\left[8\left(\theta - \frac{\pi}{2} + L + \delta_t\right)\right], & \theta \leqslant \frac{\pi}{2}; \\ \frac{3}{2} + \frac{1}{2}\tanh\left[8\left(\theta - \frac{\pi}{2} - L - \delta_t\right)\right], & \theta > \frac{\pi}{2} \end{cases} \quad (10)$$

in units of km s^{-1}, with $\delta_t = \pi/9$ radians, as shown in the bottom left panel of Figure 1. Due to the influence of L, the profile of $V_{\rm sw}$ gradually becomes essentially independent of colatitude toward solar maximum conditions, as evinced by the shaded transition seen in this figure. Note that, as a simplifying assumption, no attempt is made here to model the effects of global merged interaction regions or corotating interaction regions. The magnetic variance δB^2 at Earth is related to the magnetic field magnitude by $\delta B^2 = 0.28B^2$, following Burlaga (2001), Smith et al. (2006), and Zhao et al. (2018), and temporal scalings for the correlation scales are modeled to follow the temporal dependence of the HMF magnitude, following Matthaeus et al. (1986) and Burger & Engelbrecht (2018). These are illustrated in the middle panel of Figure 1. As a function of colatitude, the variance is scaled to follow the solar wind speed profile, with larger variances corresponding to regions with larger solar wind speeds, as observed (see, e.g., Forsyth et al. 1996; Erdös & Balogh 2005), and shown at 1 au in the bottom right panel of Figure 1. Toward solar maximum, the total variance is modeled to be essentially latitude-independent, assuming larger values during this period than during solar minimum periods, as reported by, e.g., Zhao et al. (2018).

The spatial scalings for magnetic variances and correlation scales employed here are shown as a function of heliocentric radial distance in the solar ecliptic plane and at high latitudes in the top panels of Figure 2. The radial dependences for both of these quantities are parametrically modeled to follow the results of the Zank et al. (2018) turbulence transport model. Slab and 2D magnetic variances are modeled as multistage power laws, such that

$$\chi = \chi_0 \left(\frac{r}{r_0}\right)^{\epsilon_1} \left[\frac{1 + \left(\frac{r}{r_{c1}}\right)^{f_1}}{1 + \left(\frac{r_0}{r_{c1}}\right)^{f_1}}\right]^{\frac{(\epsilon_2 - \epsilon_1)}{f_1}} \times \left[\frac{1 + \left(\frac{r}{r_{c2}}\right)^{f_2}}{1 + \left(\frac{r_0}{r_{c2}}\right)^{f_2}}\right]^{\frac{(\epsilon_3 - \epsilon_2)}{f_2}} \times \left[\frac{1 + \left(\frac{r}{r_{c3}}\right)^{f_3}}{1 + \left(\frac{r_0}{r_{c3}}\right)^{f_3}}\right]^{\frac{(\epsilon_4 - \epsilon_3)}{f_3}}, \quad (11)$$

where χ is the value of either the slab or the 2D variance throughout the heliosphere, χ_0 is its value at $r_0 = 1$ au; ϵ_1, ϵ_2, ϵ_3, and ϵ_4 are the exponents of the three different radial dependencies; r_{c1}, r_{c2}, and r_{c3} are the radial distances at which the radial dependence changes from r^{ϵ_1} to r^{ϵ_2} to r^{ϵ_3} to r^{ϵ_4}; and f_1, f_2, and f_2 determine how sharp these transitions are. Large values for f result in abrupt transitions, while smaller values result in smoother transitions. Values used here for these parameters are listed in Table 1. In the ecliptic plane, the variances modeled thus are within the broad range of observations reported by Zank et al. (1996). For the correlation scales, the radial scalings reported by Zank et al. (2018) are employed, with the 1 au values adjusted to fall within the uncertainties of spacecraft observations reported by Weygand et al. (2011), and following the trend of Voyager observations reported by Smith et al. (2001).

Current sheet drift is implemented following the approach proposed by Burger (2012) to calculate the drift velocity V_d in Equation (7). The heliospheric current sheet angle is modeled as by Kóta & Jokipii (1983), but now with a time-dependent tilt angle from Equation (8) such that

$$\theta_{ns}(T) = \frac{\pi}{2} - \tan^{-1}(\tan\alpha(T)\sin\phi^*(T)), \quad (12)$$

where, after Burger et al. (2008), we employ

$$\phi^* = \phi + \phi_0 + r\frac{\Omega}{V_{\rm sw}}. \quad (13)$$

with $\phi_0 = 0°$, thereby allowing for the inclusion in the model of the effects of a fully time-dependent heliospheric current sheet. Diffusion coefficients are modeled as by Moloto et al. (2018). A composite slab/2D model for transverse magnetostatic turbulence

The Astrophysical Journal, 894:121 (12pp), 2020 May 10 Moloto & Engelbrecht

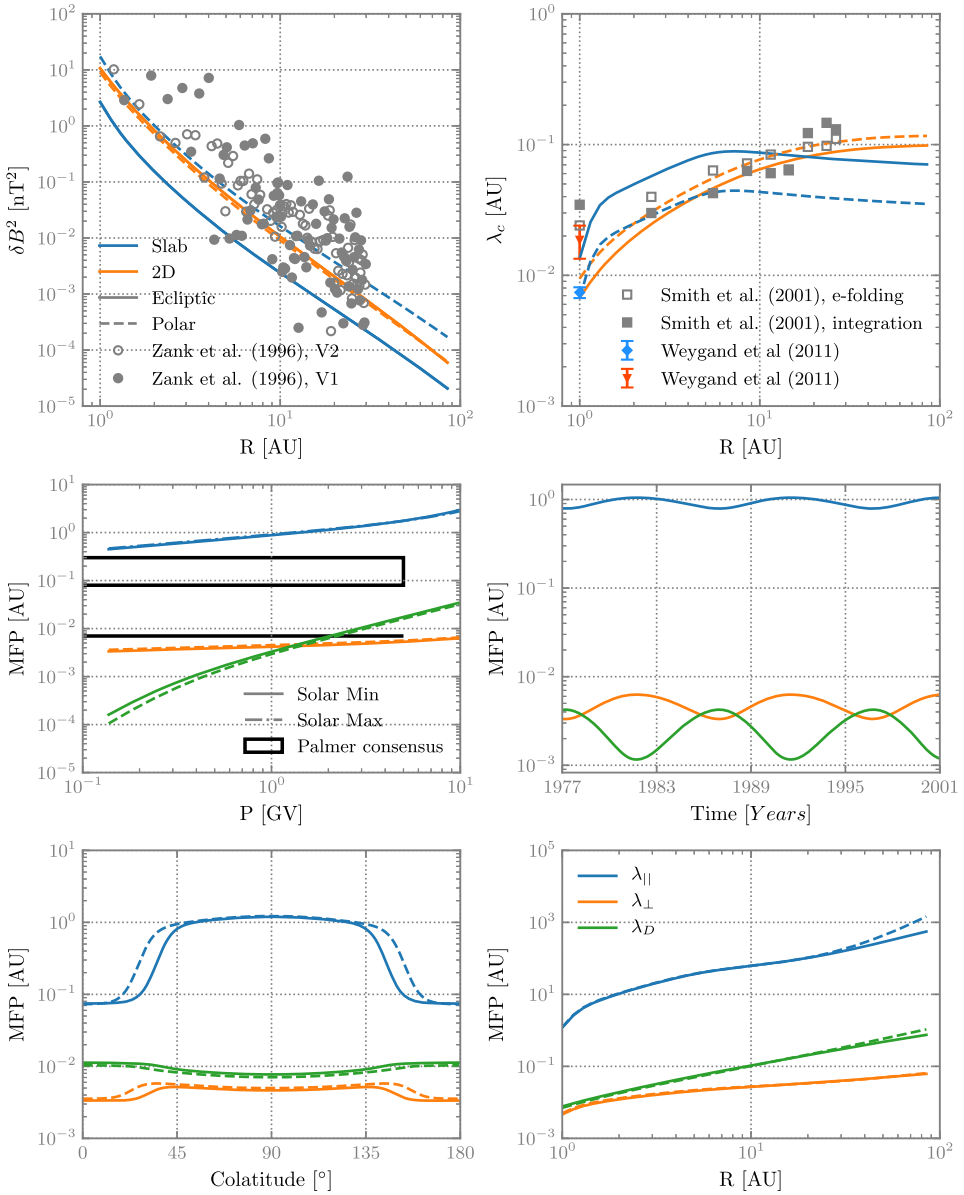

Figure 2. Top panels: Parametric fits to the Zank et al. (2017) turbulence transport model outputs corresponding to magnetic variances (left panel) and correlation scales (right panel) as a function of heliocentric radial distance in the ecliptic plane (blue lines) and at high latitudes (orange lines). Observations of these quantities reported by Zank et al. (1996), Smith et al. (2001), and Weygand et al. (2011) are included where applicable. Middle and bottom panels: Proton parallel and perpendicular MFPS (blue and orange lines) and drift scales (green lines). Middle left panel shows these as a function of rigidity at Earth, middle right panel shows them as a function of time, bottom left panel shows the 1.28 GV MFPs as function of colatitude at 1 au, and the bottom left panel shows the 1.28 GV MFPs as function of radial distance in the ecliptic plane. Black line and box in the middle left panel denote Palmer (1982) consensus values for $\lambda_\perp$ and $\lambda_{||}$, respectively.

is assumed (see, e.g., Matthaeus et al. 1995), as well as slab/2D turbulence power spectra with wavenumber-independent energy-containing ranges, and Kolmogorov inertial ranges. This latter assumption does not perfectly reflect spacecraft observations of the same (see, e.g., Bieber et al. 1993; Matthaeus et al. 2007; Bruno & Carbone 2013), but leads to relatively simple, tractable expressions for the parallel and perpendicular MFPs. For more detail on diffusion coefficients derived assuming more realistic forms for the turbulence power spectra, see Shalchi et al. (2010), Engelbrecht & Burger (2015b), and Strauss et al. (2016). In brief, then, the parallel MFP expression used here is that constructed by Burger et al. (2008) from the quasilinear theory results presented by Teufel & Schlickeiser (2003), and given by

$$\lambda_{||} = \frac{3s}{(s-1)} \frac{R^2}{k_m} \frac{B_o^2}{\delta B_{\rm sl}^2} \left[\frac{1}{4\pi} + \frac{2R^{-s}}{\pi(2-s)(4-s)} \right], \qquad (14)$$

where $s = 5/3$, $R = R_L k_m$, and $k_m = 1/\lambda_{\rm sl}$ the wavenumber at which the slab spectrum inertial range commences, and R_L is the maximal proton Larmor radius. To model the perpendicular MFP, we use the Nonlinear Guiding Center result of Shalchi et al. (2004), as modified by Burger et al. (2008) to take into account a general ratio of slab to 2D energies (see, e.g., Bieber et al. 1994, 1996). This expression is similar to that derived by

The Astrophysical Journal, 894:121 (12pp), 2020 May 10 Moloto & Engelbrecht

Table 1
Values Used in Equation (11) to Obtained Parametric Scalings for the Magnetic Variances and Correlation Scales Shown in Figure 2

χ	χ_0	ϵ_1	ϵ_2	ϵ_3	ϵ_4	f_1	f_2	f_3	r_{c1} (au)	r_{c2} (au)	r_{c3} (au)
$\delta B^2_{\rm slab}$	$20\% \times \delta B^2$	−7.1	−3.2	−2.0	⋯	5.1	2.2	⋯	1.1	4.0	⋯
$\delta B^2_{\rm 2D}$	$80\% \times \delta B^2$	−5.1	−3.2	−2.2	⋯	4.5	2.2	⋯	1.1	4.0	⋯
$\lambda_{\rm slab}$	13.4×10^{-3} (au)	7.1	0.6	−0.26	−0.04	11.5	5.2	1.0	1.12	5.5	10.0
$\lambda_{\rm 2D}$	6.7×10^{-3} (au)	2.8	1.4	0.97	−0.05	5.5	2.9	1.2	1.1	2.0	10.0

Zank et al. (2004), and is given by

$$\lambda_\perp = \left[\alpha^2\sqrt{3\pi}\,\frac{2\nu-1}{\nu}\,\frac{\Gamma(\nu)}{\Gamma(\nu-1/2)}\,\lambda_{\rm 2D}\,\frac{\delta B^2_{\rm 2D}}{B_0^2}\right]^{2/3}\lambda_\parallel^{1/3}, \quad (15)$$

where $\nu = 5/6$ denotes half the Kolmogorov inertial range spectral index, and we assume that $\alpha^2 = 1/3$ (Matthaeus et al. 2003). Drift coefficients, reduced in the presence of turbulence, are modeled following the approach of Engelbrecht et al. (2017), so that the lengthscale corresponding to the drift coefficient is given by

$$\lambda_D = R_L\left[1 + \frac{\lambda_\perp^2}{R_L^2}\,\frac{\delta B_T^2}{B_0^2}\right]^{-1}, \quad (16)$$

with δB_T^2 being the total magnetic variance. This expression is chosen as it provides results in reasonable agreement with numerical test particle simulations done by Minnie et al. (2007) and Tautz & Shalchi (2012) for the range of turbulence conditions expected in the supersonic solar wind, and due to the fact that its use in a CR modulation code has been shown by Moloto et al. (2018) to lead to computed CR intensities in reasonable agreement with spacecraft observations.

The diffusion and drift lengthscales discussed above are shown as a function of rigidity at Earth (middle left panel), time at Earth (middle right panel), colatitude at Earth (bottom left panel) and radial distance in the ecliptic plane (bottom right panel) in Figure 2, using as inputs the various spatial and temporal scalings for large and small scale heliospheric plasma quantities discussed above. As a function of rigidity and spatial coordinates, lengthscales corresponding to solar maximum conditions are indicated with dashed lines, while solid lines indicate solar minimum lengthscales, with the Palmer (1982) consensus range indicated by solid black lines. The parallel MFP shows the expected $P^{1/3}$ rigidity dependence, while the perpendicular MFP remains relatively constant. Both quantities show relatively minor changes from solar minimum to solar maximum. The drift scale corresponds closely to the weak-scattering value (R_L) at larger rigidities, declining from this scaling at lower rigidities. This quantity varies more considerably as function of solar cycle, assuming smaller values at solar maximum due to the higher turbulence models during this period. As a function of time at 1.28 GV, the parallel and perpendicular MFPs show relatively minor, sinusoidal variations, in agreement with the findings reported by Zhao et al. (2018), who employ expressions for these quantities similar to Equations (14) and (15). Notably, $\lambda_\parallel$ and $\lambda_\perp$ peak during solar maximum, and reach their minima at solar minimum. This is due to the fact that, even though the former is a function of $B_o^2/\delta B_{\rm sl}^2$, it also scales as $\sim\lambda_{\rm sl}^{s-1}$ at this rigidity, while $\lambda_\perp$ is a function of $\delta B^2_{\rm 2D}/B_o^2$ as well as $\lambda_\parallel^{1/3}$. The drift scale shows a clear solar cycle dependence which inversely follows that assumed for the HMF as shown in Figure 1. Interestingly, the drift scale assumes a minimum value at solar maximum, which would lead to a natural reduction of drift effects during this period. In terms of colatitudinal dependences, the 1.28 GV parallel MFP assumes larger values in the ecliptic plane than over the poles, reflecting the smaller values of $\delta B_{\rm sl}^2$ as modeled in the colatitudes dominated by the slow solar wind. The perpendicular MFP behaves similarly, due to its $\lambda_\parallel^{1/3}$ dependence. The colatitudinal profiles of both these quantities change considerably from solar minimum to maximum, reflecting the different colatitudinal scalings of the various turbulence quantities assumed here during these periods. Drift scales are smaller in the ecliptic than over the poles during solar minimum, while during solar maximum this quantity scales more uniformly as a function of colatitude, reflecting the colatitude dependence of the HMF magnitude. In terms of the radial dependences of the 1.28 GV MFPs and drift scale in the ecliptic plane, the parallel MFP displays a relatively gradual increase toward the outer modulation volume boundary, with slightly larger solar minimum values beyond ∼20 au. The perpendicular MFP remains relatively constant as a function of heliocentric radial distance, and only a relatively minor solar cycle dependence at the largest radial distances shown. The drift scale, as before, is larger during solar minimum than during solar maximum, and, due to the radial decrease of the magnetic variances, behaves as the Larmor radius would at larger radial distances.

Both observational and computational studies have shown that a considerable amount of cosmic-ray modulation occurs in the heliosheath (see, e.g., McDonald et al. 2000; Caballero-Lopez et al. 2004b; Stone et al. 2013; Zhang et al. 2015). Due to the fact that at the time of writing no self-consistent approach exists to model the unique turbulence conditions and their transport in this region (see, e.g.,the observational study of Burlaga et al. 2018) along the lines of, e.g., Wiengarten et al. (2016), this study confines itself to the study of modulation effects within the nominal termination shock boundary. This is also motivated by that fact that most scattering theories currently employed to derive CR diffusion coefficients are derived under the implicit assumption of transverse turbulence (see, e.g., Shalchi 2009, for a comprehensive review). Such coefficients would not necessarily be applicable in conditions of mostly compressive turbulence. Therefore this study employs a boundary spectrum at 85 au, within the termination shock, in much the same way as Engelbrecht & Burger (2015b), Guo & Florinski (2016), Qin & Shen (2017), Shen & Qin (2018), and Shen et al. (2019). The input spectrum employed is that employed by Moloto et al. (2018), and is constructed to agree with Voyager proton observations reported by Webber et al. (2008) at 85 au:

$$j_B(85\ {\rm au}) = \frac{17.0(P/P_o)^{-2.4}}{2.2 + 2.1(P/P_o)^3}, \quad (17)$$

with units of particles m^2 s^{-1} sr^{-1} MeV^{-1}, where $P_o = 1$ GV and P in GV. It should be noted that Webber et al. (2008) report 11 year cycle-related increases of ∼60%–70% from

The Astrophysical Journal, 894:121 (12pp), 2020 May 10 Moloto & Engelbrecht

solar maximum to minimum for protons with energies of 400–540 GeV/nuc and lower. Given that Equation (17) was constructed to agree with Voyager 2 observations taken in 2008, this spectrum would correspond to solar minimum conditions, and could therefore potentially overestimate galactic proton intensities at 85 au during periods of high solar activity. However, in the present study no temporal adjustments to the input spectrum are made, as such adjustments amount to assumptions as to time-dependent modulation conditions in the heliosheath, which are not currently well understood. The following section presents results calculated using the model described above, compared with selected spacecraft observations taken between 1977 and 2001.

3. Results

To compare model results with observations, we focus on the time frame from 1975 to 2002 (cycles 21 and 22), which do not display the unusual behavior seen in the last solar minimum. The top panel of Figure 3 shows the results computed using the model described above, calculated for 1.28 GV galactic CR protons, and compared to the IMP-8 1.28 GV proton proxy intensities reported by Gieseler et al. (2017). At this energy, both diffusion and drift are expected to play a role in the transport of these particles. Our model clearly reproduces all the salient features observed in the data, reproducing the peaked and broad solar minimum intensity profiles associated with the negative and positive magnetic polarity cycles, and thus the 22 yr cycle that is due to particle drifts (see, e.g., Jokipii & Thomas 1981; Kóta & Jokipii 1983; Reinecke & Potgieter 1994) while also yielding results in reasonable agreement with intensities during solar maximum, where diffusion is expected to dominate modulation processes. The rapid decrease of intensities from solar minimum to solar maximum and the much slower increase from solar maximum to solar minimum is also reproduced. However, the model results are not in perfect agreement with all observations. This is especially the case during solar maximum, and during periods of decreasing solar activity, and may be due to the fact that GMIRs, which can cause large drop-offs in CR intensities (see, e.g., le Roux & Potgieter 1995; Cane 2000), are not taken into account here when modeling transport conditions. Other reasons for this could be that the heliospheric plasma quantities simply vary too much during these periods to be accurately modeled using the smooth functions employed in this study, as evinced by a comparison of the observations for, say, the HMF magnitude at Earth during solar maximum seen in the top panel of Figure 1 with the fit employed, or an overestimation of the boundary spectrum (Equation (17)) during periods of higher solar activity.

The middle left and right panels of Figure 3 show intensity-tilt loops, calculated using the Gieseler et al. (2017) data for cycles 21 and 22 respectively (solid black lines) compared to computed results (gray dashed lines) for similar polarity cycles: $A > 0$ to $A < 0$ for cycle 21 and vice versa for cycle 22. Arrows on the figures indicate the direction of the passing of time from solar minimum, through solar maximum, and back to solar minimum. The intensity-tilt loops calculated using the Gieseler et al. (2017) spacecraft data agree qualitatively with those calculated by Smith (2006) using neutron monitor data. For cycle 21, which is an $A > 0$ to $A < 0$ solar cycle that stretches from ~1976–1986/7, starting at the top left of the panel, the intensity decreases slowly with increasing tilt angle until the tilt is ~70°. Above this tilt angle the overall solar magnetic polarity begins to change from positive to negative as indicated by the direction of the arrows, and during this period of maximum solar activity, roughly a third of the overall intensity modulation occurs. As the tilt begins to decrease again, the intensity increases slowly until the tilt angle becomes less than ~20°. Here the intensities begin a rapid increase back to their largest solar minimum value. The computed results follow the data fairly well and most of the deviations from data can potentially be attributed to GMIRs, which are not modeled here. The shape and clockwise rotation of the intensity-tilt loop is in qualitative agreement with the analyses done by le Roux & Potgieter (1990), using a time-dependent, 2D modulation code, and by Moloto (2015), using 3D, steady-state modulation codes.

For cycle 22, which was an $A < 0$ to $A > 0$ cycle, the situation is different. The intensities decrease with a much steeper gradient until the field reversal from $A < 0$ to $A > 0$ begins. At this time more than two-thirds of the overall modulation has already occurred and subsequently little in the way of additional decreases in intensities occurred during the field polarity reversal period. After the polarity reversal the intensities increase at roughly the rate at which they decreased during the decrease phase. Instead of changing in an counter-clockwise manner, the intensities continue to change in a clockwise sense, contrary to the expectations based on the analyses mentioned earlier. This may be due to the fact that the present model solves the Parker transport equation time-dependently in three dimensions, combined with the use of the Engelbrecht et al. (2017) turbulence-reduced drift coefficient, which, due to the temporal dependences assumed here, would also display a time-dependence (as shown in Figure 2) not seen in ad hoc drift reduction factors usually used in modulation studies. The computed results are again in fair agreement with the data and are able to reproduce the clockwise rotation seen in the data. There is a clear crossing of the $A < 0$ descending phase and the $A > 0$ ascending phase at ~30° that produces the same rotation as the data. This feature is mainly due to the asymmetric ascending and descending phases of the tilt angle shown in Figure 1. To summarize then, model results qualitatively reproduce the observed salient features of intensity-tilt loops reported by Lockwood & Webber (2005), Webber et al. (2005), and Smith (2006) for neutron monitor data, with the implication that the model can relatively accurately reproduce the interplay of diffusion and drift in the heliosphere over several solar cycles, at least at the energies considered here.

The bottom panel of Figure 3 shows the boundary spectrum employed in this study (Equation (17), black line) as well as the 1 au computed differential intensity spectra compared with various spacecraft data taken during the periods marked in various colors corresponding to the bars indicated in the top panel of the figure. Observations shown are from IMP-8 McDonald et al. (1992), the BESS spectrometer Shikaze et al. (2007), the Balloon Borne Magnet Facility Webber et al. (1989), and Voyager 2 at 85 au Webber et al. (2008). The boundary spectrum is constructed to pass through the Voyager data. Model results for both $A > 0$ (1977, 1997) and $A < 0$ (1987) solar minima are in good agreement with observations at all energies shown. The model results for the latter period are shown as a band, in order to accurately compare these with

The Astrophysical Journal, 894:121 (12pp), 2020 May 10 Moloto & Engelbrecht

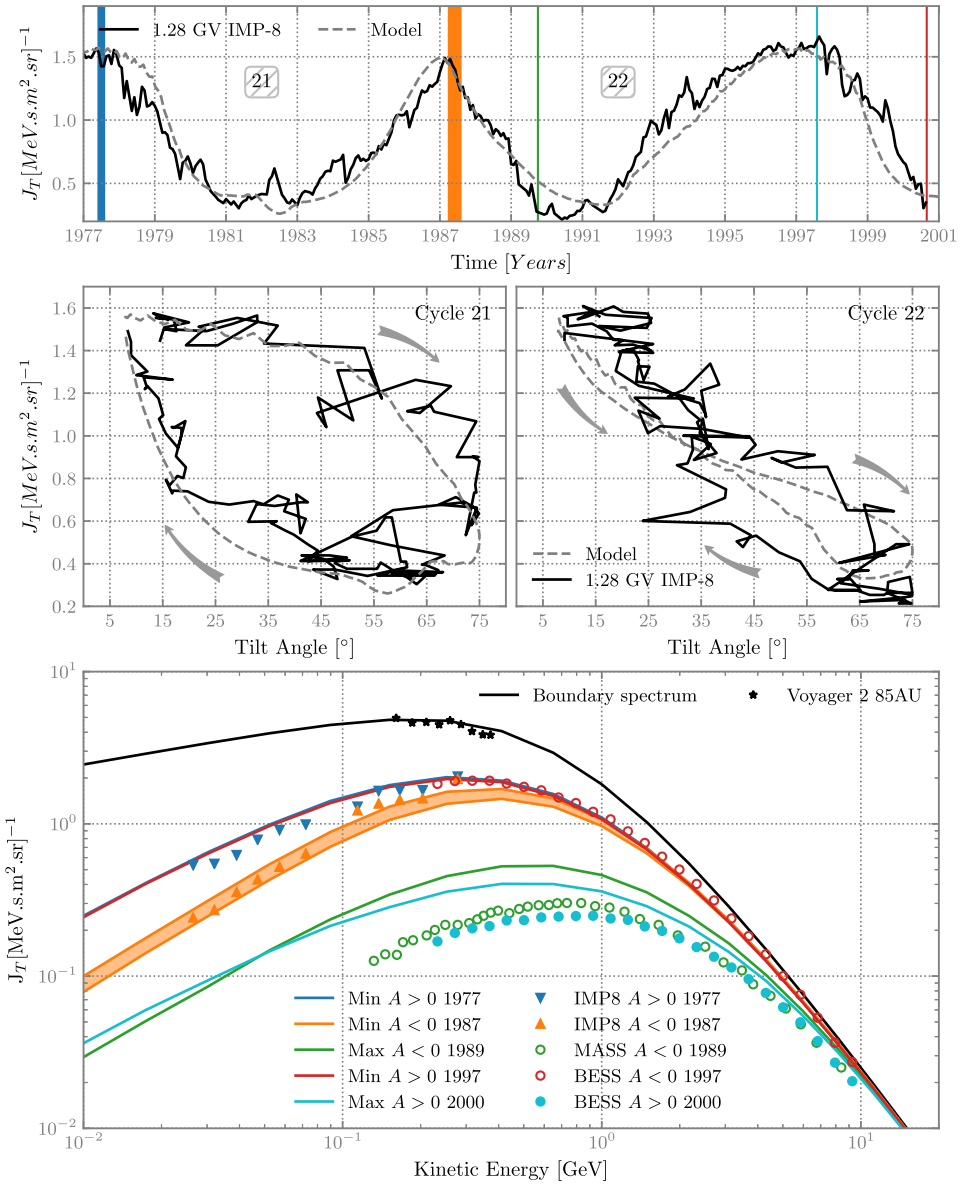

Figure 3. Top panel: 1.28 GV galactic proton intensities calculated with the current model (dashed line) compared with Gieseler et al. (2017) spacecraft observations. Colored bars indicate time periods during which observations shown in the bottom panel were taken. Middle panels: 1.28 GV Gieseler et al. (2017) intensities as function of observed tilt angle, compared with model results (dashed lines) for cycle 21 (left panel) and cycle 22 (right panel). Arrows indicate direction of the passing of time from solar minimum, through solar maximum, and back to solar minimum. Bottom panel: Boundary spectrum (Equation (17), black line) and 1 au model GCR proton differential intensity spectra calculated for comparison with spacecraft observations of the same taken during the time intervals indicated in the top panel of this Figure, as function of kinetic energy. Observations shown are taken from Webber et al. (1989, 2008), McDonald et al. (1992), and Shikaze et al. (2007).

observations taken over several months by McDonald et al. (1992). During both solar maxima, model results are larger than both data sets here considered, but display similar energy dependences, with computed 1989 intensities above ∼0.1 GeV remaining larger than computed 2000 intensities, as seen in the data. The reason for this lies partly in the HMF temporal profile employed in this study (top panel of Figure 1), which is in reasonable agreement with observed magnetic field magnitudes during solar minimum, but less so during solar maximum, when this quantity fluctuates greatly. This is specifically the case during the period preceding 1989, and is reflected in the overall overshoot of the data by the computed 1.28 GV intensities from 1989 to 1991 seen in the top panel of Figure 3. Another reason for this could be that the boundary spectrum overestimates galactic proton intensities at 85 au during periods of higher solar activity. Overall, then, the model yields results in reasonable to good agreement with observation, and can reproduce the salient features of the observed temporal profile of GCR proton intensities. Agreement of model outputs with observation only suffers in the instances where the model inputs, such as the temporal profile for the HMF magnitude, are in poor agreement with observations.

4. Long-term Modulation

In order to study the very long term modulation of galactic cosmic rays, we employ the annual historic PCR2 HMF magnitudes presented by McCracken & Beer (2015) as inputs to the model. As this model requires continuous inputs to reflect the residence times of ∼1 yr of GCRs in the heliosphere (see, e.g., Florinski & Pogorelov 2009; Strauss et al. 2011), a

The Astrophysical Journal, 894:121 (12pp), 2020 May 10 Moloto & Engelbrecht

simple linear interpolation is performed between each data point. Magnetic polarity changes are again assumed to occur during peaks in the HMF magnitude. The current sheet angle is again modeled using Equation (12). Turbulence quantities are modeled as outlined in Section 2, following the McCracken & Beer (2015) temporal profile, and diffusion and drift lengthscales are again modeled as outlined in that section. To model the historical behavior of the tilt angle, we follow an approach motivated by that of Asvestari & Usoskin (2016), who developed a model to reconstruct the HCS tilt angle using the phase of the sunspot solar cycle. The model solely describes the cyclic behavior of the tilt angle based on the phase of the solar cycle, as calculated using the sunspot record. Asvestari & Usoskin (2016) argue that, although the sunspot number varies significantly from cycle to cycle, the tilt angle exhibits roughly the same variations over all cycles, in accord with the idea of a regular cyclic behavior as is seen in space age observations of this quantity (see, e.g., Hoeksema 1995; Cliver & Ling 2001). This makes it possible to reconstruct the tilt angle variability using only the solar cycle phase. Based on this idea we adapt the Burger et al. (2008) tilt angle model into the form

$$\alpha(T) = \alpha_{\min} + \left(\frac{\pi}{4.8} - \frac{\alpha_{\min}}{2}\right) \times \begin{cases} 1 - \cos\left(\frac{\pi}{D_\phi}(T - L_\phi)\right), & 0 \leqslant T \leqslant D_\phi \\ 1 - \cos\left(\frac{\pi}{A_\phi}T\right), & D_\phi \leqslant T \leqslant L_\phi \end{cases}, \quad (18)$$

where A_ϕ, D_ϕ, and L_ϕ respectively represent the sunspot number ascending phase, the descending phase and the phase length. The dates and values for the cycle minima and maxima are sensitive to the methods and input data used to find them. The values we use for sunspot number maxima and minima are those found using the 13 month running mean (see, e.g., Hathaway 2015, and references therein). These dates and the values for sunspot cycle maxima and minima are given in Tables 1 and 2 of Hathaway (2015). Based on this reconstruction, then, the present study limits itself to considering GCR modulation back to 1775 only, even though McCracken & Beer (2015) provide HMF values dating back to 1391. The temporal profiles for the HMF magnitude and tilt angle discussed here are shown in the top panel of Figure 4, along with the space age observations first shown in the top panel of Figure 1, to guide the eye. The reconstructed tilt angle displays a clear solar cycle variation of varying phase, in step with the sunspot record. Peaks in the HMF magnitude occur roughly when tilt angle values approach their local maxima, in accord with space age observations.

The middle panel of Figure 4 shows 1.28 GV galactic proton intensities calculated using the full model outlined above (gray line), compared to those calculated using the same model, but assuming a constant 40° tilt angle (pink line), an assumption made by Caballero-Lopez et al. (2004a), along with the Gieseler et al. (2017) spacecraft observations, to again guide the eye. The full model solution shows a clear solar cycle dependence, and clearly displays the peak/plateau $A < 0$/$A > 0$ profile indicative of the charge-sign dependent effects of drift due to the helisopheric current sheet/gradients and curvatures in the HMF, and familiar from neutron monitor observations (e.g., Potgieter 2013, and references therein). It is interesting to note that the full model yields a sharp increase in GCR intensity during the Dalton Minimum (see, e.g., Usoskin 2017). Solar cycle variations in the 1.28 GV proton intensity are more pronounced than when only the tilt angle is kept at a constant 40° (pink line). Constant α results are in reasonable agreement with full model results during $A > 0$ magnetic polarity cycles, but do not show the peaks expected during $A < 0$ cycles, and does not peak during the Dalton Minimum. Full model results are also compared to results calculated following the approach of Caballero-Lopez et al. (2004a), viz. by running the model twice, assuming that $A < 0$ for the whole time span considered, and assuming that $A > 0$ for the whole time span, and then taking the average of the two runs (again assuming that $\alpha = 40°$). The averaged results do indeed vary with solar cycle, but less so than those calculated using the full model, and produces only a relatively small peak during the Dalton Minimum. Furthermore, there is no indication of the peak/plateau signature of drift effects in the averaged intensity profile.

5. Summary and Conclusions

In the present study, a new, 3D time-dependent ab initio CR modulation model is presented. This model employs, as a first approach, simple observationally motivated temporal scalings for large scale heliospheric quantities such as the HMF magnitude, tilt angle, and solar wind speed profile, as well as for turbulence quantities such as the magnetic variances and correlation scales. Spatial dependences for these quantities are also modeled to take into account theory and observations. Galactic CR proton differential intensities calculated using this model are in reasonable to good agreement with spacecraft observations, reproducing the major salient features of the observed CR intensity temporal profile. This model was then employed, using the historic magnetic field data presented by McCracken & Beer (2015), to calculate GCR proton intensities dating back to 1775 in several ways. In order to test conclusions drawn as to the role of drift in the historic modulation of GCRs by Caballero-Lopez et al. (2004a), model results were computed using historical tilt angles reconstructed using sunspot observations along the lines proposed by Asvestari & Usoskin (2016). These results displayed a clear signature of drift effects, displaying the characteristic peak/plateau temporal profiles seen during periods of negative/positive magnetic polarity in space age GCR observations. When intensities were calculated using the approach employed by Caballero-Lopez et al. (2004a), who assumed a constant tilt angle and averaged model runs for $A > 0$ and $A < 0$, no sign of particle drift effects in the resulting intensity profiles was discernible, and solar cycle-related fluctuations in the resulting intensities were considerably smaller than in the case of the full model, where a varying tilt angle was employed. This leads us to conclude that drift effects cannot be ignored when endeavouring to estimate historic changes in the HMF magnitude by modeling cosmic ray fluxes in the past. The importance of drift effects also implies the need to revisit previous estimates of the historic behavior of the HMF magnitude based on the force field solution to the Parker TPE, as this one-dimensional approach cannot a priori take into account drift effects.

In the future, this model will be employed to revisit the study of Caballero-Lopez et al. (2004a) using the annual ^{10}Be concentration data presented by McCracken & Beer (2015), to calculate a new estimation of the historical HMF magnitudes.

The Astrophysical Journal, 894:121 (12pp), 2020 May 10 Moloto & Engelbrecht

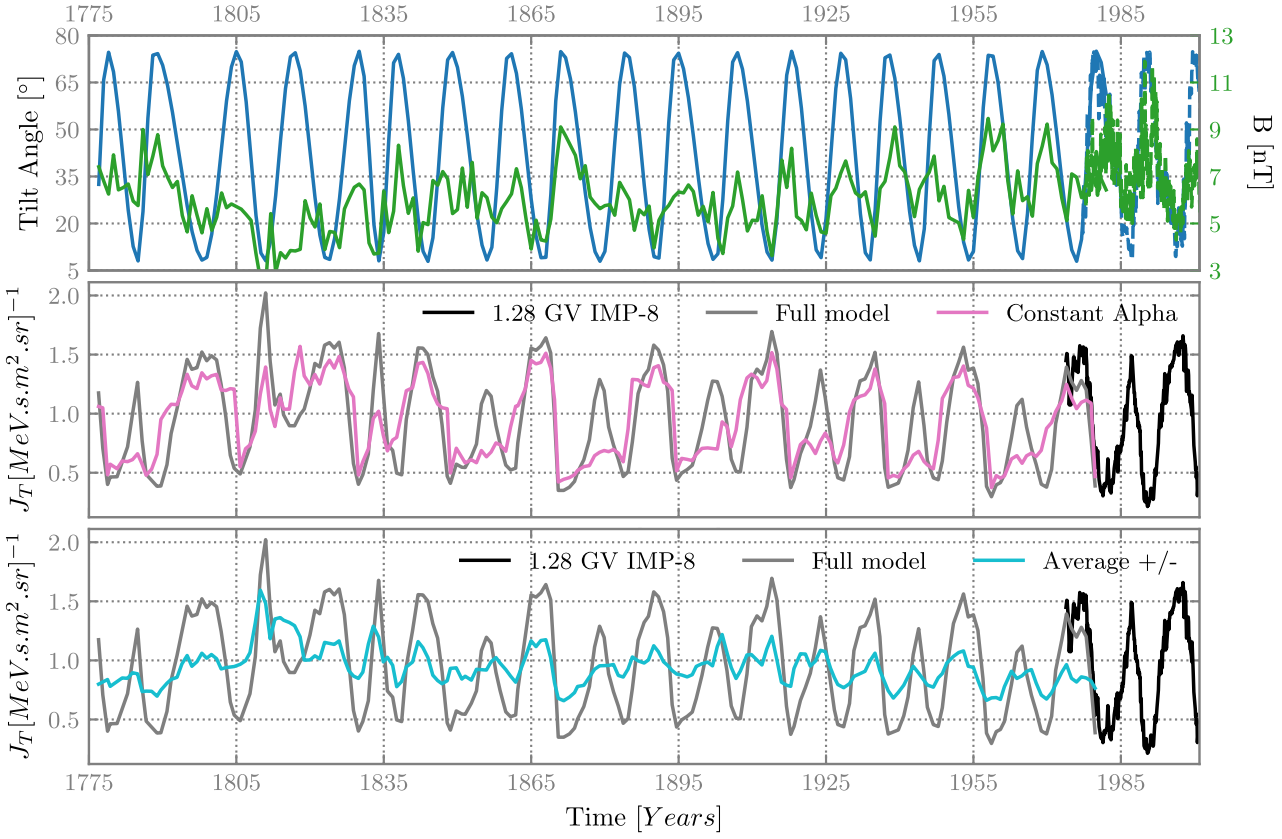

Figure 4. Top panel: Historic tilt angles employed in this study (blue line), calculated using Equation (18) using the sunspot number phase as proposed by Asvestari & Usoskin (2016). Green line denotes the historic HMF magnitude as reported by McCracken & Beer (2015), used as input for the model. Space age observations of these quantities shown in Figure 1 are also included, to guide the eye. Middle panel: 1.28 GV GCR proton intensities calculated using the full model (gray line), and when assuming a constant 40° tilt angle (pink line), alongside the Gieseler et al. (2017) spacecraft observations. Bottom panel: 1.28 GV GCR proton intensities calculated using the full model (gray line), and when taking an average of $A > 0$ and $A < 0$ intensity profiles calculated assuming that $\alpha = 40°$ (teal line).

To this end, several refinements to the model will be made, including the incorporation of more recent developments as to models for the diffusion coefficients (e.g., Engelbrecht & Burger 2015b; Strauss et al. 2016; Shalchi 2020) and the incorporation of temporal effects on the boundary spectrum. Furthermore, heavier CR elements such as He will need to be considered (see, e.g., Boschini et al. 2019; Shen et al. 2019), refinements to how current sheet drift is modeled will be made (e.g., by Engelbrecht et al. 2019), and recent advances in modeling the production of cosmogenic nuclides in the atmosphere (e.g., Poluianov et al. 2016) will be taken into account.

This work is based on the research supported in part by the National Research Foundation of South Africa (grant Nos. 111731 and 121920). Opinions expressed and conclusions arrived at are those of the authors and are not necessarily to be attributed to the NRF.

The authors would like to thank the Centre for High Performance Computing (CHPC) in South Africa for providing computational resources for this study.

The authors would like to thank an anonymous referee for a careful and insightful review of this work.

ORCID iDs

K. D. Moloto https://orcid.org/0000-0002-4840-6355
N. Eugene Engelbrecht https://orcid.org/0000-0003-3659-7956

References

Abreu, J. A., Beer, J., Steinhilber, F., Tobias, S. M., & Weiss, N. O. 2008, GeoRL, 35, L20109
Adhikari, L., Zank, G. P., Bruno, R., et al. 2015, ApJ, 805, 63
Adriani, O., Barbarino, G. C., Bazilevskaya, G. A., et al. 2013, ApJ, 765, 91
Ahluwalia, H. S. 2016, AdSpR, 57, 710
Asvestari, E., Gil, A., Kovaltsov, G. A., & Usoskin, I. G. 2017, JGRA, 122, 9790
Asvestari, E., & Usoskin, I. G. 2016, JSWSC, 6, A15
Barnard, L., Lockwood, M., Hapgood, M. A., et al. 2011, GeoRL, 38, L16103
Barnard, L., McCracken, K. G., Owens, M. J., & Lockwood, M. 2018, JSWSC, 8, A23
Beer, J., McCracken, K. G., & von Steiger, R. 2012, Cosmogenic Radionuclides—Theory and Applications in the Terrestrial and Space Environments (Berlin: Springer)
Bieber, J. W., Chen, J., Matthaeus, W. H., Smith, C. W., & Pomerantz, M. A. 1993, JGR, 98, 3585
Bieber, J. W., Matthaeus, W. H., Smith, C. W., et al. 1994, ApJ, 420, 294
Bieber, J. W., Wanner, W., & Matthaeus, W. H. 1996, JGR, 101, 2511
Boschini, M. J., della Torre, S., Gervasi, M., La Vacca, G., & Rancoita, P. G. 2019, AdSpR, 64, 2459
Bruno, R., & Carbone, V. 2013, LRSP, 10, 2
Burger, R. A. 2012, ApJ, 760, 60
Burger, R. A., & Engelbrecht, N. E. 2018, in AGU Fall Meeting (San Francisco, CA: AGU), SH21C-3300
Burger, R. A., Krüger, T. P. J., Hitge, M., & Engelbrecht, N. E. 2008, ApJ, 674, 511
Burlaga, L. F. 2001, JGR, 106, 917
Burlaga, L. F., Florinski, V., & Ness, N. F. 2018, ApJ, 854, 20
Caballero-Lopez, R. A., Engelbrecht, N. E., & Richardson, J. D. 2019, ApJ, 883, 73
Caballero-Lopez, R. A., & Moraal, H. 2004, JGRA, 109, A01101

Caballero-Lopez, R. A., Moraal, H., McCracken, K. G., & McDonald, F. B. 2004a, JGRA, 109, A12102
Caballero-Lopez, R. A., Moraal, H., & McDonald, F. B. 2004b, JGRA, 109, A05105
Cane, H. V. 2000, SSRv, 93, 55
Cliver, E. W., & Herbst, K. 2018, SSRv, 214, 56
Cliver, E. W., & Ling, A. G. 2001, ApJL, 551, L189
Engelbrecht, N. E. 2017, ApJL, 849, L15
Engelbrecht, N. E., & Burger, R. A. 2013a, ApJ, 772, 46
Engelbrecht, N. E., & Burger, R. A. 2013b, ApJ, 779, 158
Engelbrecht, N. E., & Burger, R. A. 2015a, AdSpR, 55, 390
Engelbrecht, N. E., & Burger, R. A. 2015b, ApJ, 814, 152
Engelbrecht, N. E., Mohlolo, S. T., & Ferreira, S. E. S. 2019, ApJL, 884, L54
Engelbrecht, N. E., Strauss, R. D., le Roux, J. A., & Burger, R. A. 2017, ApJ, 841, 107
Erdös, G., & Balogh, A. 2005, AdSpR, 35, 625
Fisk, L. A. 1996, JGR, 101, 15547
Florinski, V., & Pogorelov, N. V. 2009, ApJ, 701, 642
Forman, M. A., Jokipii, J. R., & Owens, A. J. 1974, ApJ, 192, 535
Forsyth, R. J., Horbury, T. S., Balogh, A., & Smith, E. C. 1996, GeoRL, 23, 595
Gardiner, C. 2004, Stochastic Methods: A Handbook for the Natural and Social Sciences (Berlin: Springer)
Gieseler, J., Heber, B., & Herbst, K. 2017, JGRA, 122, 10964
Gleeson, L. J., & Axford, W. I. 1968, ApJ, 154, 1011
Goelzer, M. L., Smith, C. W., Scwadron, N. A., & McCracken, K. G. 2013, JGRA, 118, 7525
Guo, X., & Florinski, V. 2016, ApJ, 826, 65
Hathaway, D. H. 2015, LRSP, 12, 4
Herbst, K., Muscheler, R., & Heber, B. 2017, JGRA, 122, 23
Hitge, M., & Burger, R. A. 2010, AdSpR, 45, 18
Hoeksema, J. T. 1995, SSRv, 72, 137
Jokipii, J. R., & Levy, E. H. 1977, ApJL, 213, L85
Jokipii, J. R., & Thomas, B. 1981, ApJ, 243, 1115
Kóta, J. 2013, SSRv, 176, 391
Kóta, J., & Jokipii, J. R. 1983, ApJ, 265, 573
le Roux, J. A., & Potgieter, M. S. 1990, ApJ, 361, 275
le Roux, J. A., & Potgieter, M. S. 1995, ApJ, 442, 847
Lockwood, J. A., & Webber, W. R. 2005, JGRA, 110, 4102
Lockwood, M., Owens, M. J., Barnard, L. A., et al. 2018, JSWSC, 8, A12
Maruyama, G. 1955, Rend. Circ. Mat. Palermo, 4, 48
Matsumoto, M., & Nishimura, T. 1998, Trans. Model. Comput. Simul., 8, 3
Matthaeus, W. H., Bieber, J. W., Ruffolo, D., Chuychai, P., & Minnie, J. 2007, ApJ, 667, 956
Matthaeus, W. H., Goldstein, M. L., & King, J. H. 1986, JGR, 91, 59
Matthaeus, W. H., Gray, P. C., Pontius, D. H., Jr., & Bieber, J. W. 1995, PhRvL, 75, 2136
Matthaeus, W. H., Qin, G., Bieber, J. W., & Zank, G. P. 2003, ApJL, 590, L53
Matthaeus, W. H., & Velli, M. 2011, SSRv, 160, 145
McComas, D. J., Barraclough, B. L., Funsten, H. O., et al. 2000, JGR, 105, 10419
McCracken, K. G. 2007, JGRA, 112, A09106
McCracken, K. G., & Beer, J. 2015, SoPh, 290, 3051
McCracken, K. G., McDonald, F. B., Beer, J., Raisbeck, G., & Yiou, F. 2004, JGRA, 109, A12103
McDonald, F. B., Heikkila, B., Lal, N., & Stone, E. C. 2000, JGR, 105, 1
McDonald, F. B., Moraal, H., Reinecke, J. P. L., Lal, N., & McGuire, R. E. 1992, JGR, 97, 1557
Minnie, J., Bieber, J. W., Matthaeus, W. H., & Burger, R. A. 2007, ApJ, 670, 1149
Moloto, K. D. 2015, MSc thesis, North-West Univ.
Moloto, K. D., Engelbrecht, N. E., & Burger, R. A. 2018, ApJ, 859, 107
Moloto, K. D., Engelbrecht, N. E., Strauss, R. D., Moeketsi, D. M., & van den Berg, J. P. 2019, AdSpR, 63, 626
Moraal, H. 2013, SSRv, 176, 299
Muscheler, R., Adolphi, F., Herbst, K., & Nilsson, A. 2016, SoPh, 291, 3025
Nagashima, K., & Morishita, I. 1980a, P&SS, 28, 177
Nagashima, K., & Morishita, I. 1980b, P&SS, 28, 195
Ness, N. F. 2006, in The Physics of the Heliospheric Boundaries, ed. V. V. Izmodenov & R. Kallenbach (Noordwijk: ESA), 183
Oughton, S., Matthaeus, W. H., Smith, C. W., Bieber, J. W., & Isenberg, P. A. 2011, JGRA, 116, A08105
Oughton, S., Matthaeus, W. H., Wan, M., & Osman, K. T. 2015, RSPTA, 373, 20140152
Palmer, I. D. 1982, RvGSP, 20, 335
Parker, E. N. 1958, ApJ, 128, 664
Parker, E. N. 1965, P&SS, 13, 9
Parker, E. N. 2001, JGR, 106, 15797
Pei, C., Bieber, J. W., Burger, R. A., & Clem, J. 2010, JGRA, 115, A12107
Poluianov, S. V., Kovaltsov, G. A., Mishev, A. L., & Usoskin, I. G. 2016, JGRD, 121, 8125
Potgieter, M. S. 2013, SSRv, 176, 165
Qin, G., & Shen, Z.-N. 2017, ApJ, 846, 56
Qin, G., & Zhang, L.-H. 2014, ApJ, 787, 12
Reinecke, J. P. L., & Potgieter, M. S. 1994, JGR, 99, 14761
Ruffolo, D., Pianpanit, T., Matthaeus, W. H., & Chuychai, P. 2012, ApJL, 747, L34
Schwadron, N. A., Blake, J. B., Case, A. W., et al. 2014, SpWea, 12, 622
Shalchi, A. 2009, Nonlinear Cosmic Ray Diffusion Theories (Berlin: Springer)
Shalchi, A. 2010, ApJL, 720, L127
Shalchi, A. 2020, SSRv, 216, 23
Shalchi, A., Bieber, J. W., & Matthaeus, W. H. 2004, ApJ, 604, 675
Shalchi, A., Li, G., & Zank, G. P. 2010, Ap&SS, 325, 99
Shen, Z.-N., & Qin, G. 2018, ApJ, 854, 137
Shen, Z.-N., Qin, G., Zhou, P., & Wei, F. 2019, ApJ, 887, 132
Shikaze, Y., Haino, S., Abe, K., et al. 2007, APh, 28, 154
Smith, C. W., & Bieber, J. W. 1991, ApJ, 370, 435
Smith, C. W., Isenberg, P. A., Matthaeus, W. H., & Richardson, J. D. 2006, ApJ, 638, 508
Smith, C. W., Matthaeus, W. H., Zank, G. P., et al. 2001, JGR, 106, 8253
Smith, C. W., McCracken, K. G., Schwadron, N. A., & Goelzer, M. L. 2014, SpWea, 12, 499
Smith, E. J. 2006, in AIP Conf. Ser. 858, Physics of the Inner Heliosheath, ed. J. Heerikhuisen et al. (Melville, NY: AIP), 104
Steinhilber, F., Abreu, J. A., & Beer, J. 2008, ASTRA, 4, 1
Steinhilber, F., Abreu, J. A., Beer, J., et al. 2012, PNAS, 109, 5967
Steinhilber, F., Abreu, J. A., Beer, J., & McCracken, K. G. 2010, JGRA, 115, A01104
Stone, E. C., Cummings, A. C., McDonald, F. B., et al. 2013, Sci, 341, 150
Strauss, R. D., & Effenberger, F. 2017, SSRv, 212, 151
Strauss, R. D., le Roux, J. A., Engelbrecht, N. E., Ruffolo, D., & Dunzlaff, P. 2016, ApJ, 825, 43
Strauss, R. D., Potgieter, M. S., Kopp, A., & Busching, I. 2011, JGRA, 116, A12105
Svalgaard, L., & Cliver, E. W. 2007, AdSpR, 40, 1112
Svalgaard, L., & Cliver, E. W. 2010, JGRA, 115, A09111
Tautz, R. C., & Shalchi, A. 2012, ApJ, 744, 125
Teufel, A., & Schlickeiser, R. 2003, A&A, 397, 15
Usmanov, A. V., Goldstein, M. L., & Matthaeus, W. H. 2016, ApJ, 820, 17
Usoskin, I. G. 2017, LRSP, 14, 3
Webber, W. R., Cummings, A. C., McDonald, F. B., Stone, E. C., Heikkila, B. C., & Lal, N. 2008, JGRA, 113, A10108
Webber, W. R., Golden, R. L., Stochaj, S. J., Ormes, J. F., & Strittmatter, R. E. 1989, ApJ, 380, 230
Webber, W. R., Heber, B., & Lockwood, J. A. 2005, JGRA, 110, A12107
Webber, W. R., & Higbie, N. 2003, JGRA, 108, 1355
Weygand, J. M., Matthaeus, W. H., Dasso., S., & Kivelson, M. G. 2011, JGRA, 116, A03305
Wicks, R. T., Owens, M. J., & Horbury, T. S. 2010, SoPh, 262, 191
Wieler, R. 2017, in Encyclopedia of Geochemistry, ed. W. White (Cham: Springer)
Wiengarten, T., Oughton, S., Engelbrecht, N. E., et al. 2016, ApJ, 833, 17
Zank, G. P., Adhikari, L., Hunana, P., et al. 2017, ApJ, 835, 147
Zank, G. P., Adhikari, L., Zhao, L.-L., et al. 2018, ApJ, 869, 23
Zank, G. P., Li, G., Florinski, V., et al. 2004, JGRA, 109, A04107
Zank, G. P., Matthaeus, W. H., & Smith, C. W. 1996, JGR, 101, 17093
Zhang, M. 1999a, ApJ, 510, 715
Zhang, M. 1999b, ApJ, 513, 409
Zhang, M., Luo, X., & Pogorelov, N. 2015, PhPl, 22, 091501
Zhao, L. L., Adhikari, L., Zank, G. P., Hu, Q., & Feng, X. S. 2018, ApJ, 856, 94

CHAPTER 6

Summary and conclusions

THE development of a fully time-dependent cosmic ray modulation model was considered in this thesis. The main research results were published in peer-reviewed journals. The conclusions and take-ways from each chapter are discussed briefly below.

The relevant heliospheric background was introduced in **Chapter 2**, This lay the foundations for the topics discussed in the chapters that followed.

A simplified *ab initio* cosmic-ray (CR) proton modulation model was introduced in **Chapter 3**, using a steady-state three-dimensional stochastic solver of the Parker transport equation originally developed by *Engelbrecht and Burger* [2015]. Diffusion coefficients derived using the well-tested Quasilinear and Nonlinear Guiding Center Theories are employed. By pairing effective values for the solar wind speed, magnetic field magnitude and tilt angle with parametric fits to results from a turbulence transport model taking into account observational values for turbulence quantities, the model computes galactic cosmic ray proton differential intensities that are in reasonable to good agreement with spacecraft observations at Earth for all three solar minima under consideration. The self-consistent treatment of turbulence quantities from one solar cycle to the next naturally leads to the larger intensities relative to previous solar minima observed during the unusual solar minimum of 2009, implying that the unusually high cosmic ray intensities for this period can be qualitatively linked to turbulence parameters that differ from solar minimum to solar minimum. It is also shown that drift effects still play an import role during this solar minimum.

Various predictions were also made for differential intensities during the current solar minimum to test the potential predictive capability of the model. The model showed, for reasonable extrapolations of the behaviour of the heliospheric magnetic field magnitude, turbulence quantities, and tilt angel, that the expected contribution of galactic CR protons to the space radiation environment, and therefore their differential intensity spectra, in

solar cycle 25 will be very similar to, or slightly less than what was observed during cycle 24. Intensities at larger energies are expected to remain at or below the intensities observed in 2009 and to only be moderately higher for lower energies. This differs from predictions reported by previous studies, who expect intensities to be 19% higher than those observed during the 2009 solar minimum [*Miyake et al.*, 2017].

It should be noted, however, that the current model does not take into account any polarity or solar cycle dependence of the boundary spectrum at 85 au. Based on *Voyager* observations near the termination shock reported by *Webber et al.* [2008], $A < 0$ intensities are expected to be a factor of $1.5 - 1.7$ higher than the corresponding $A > 0$ intensities for protons above $\sim$150 MeV. Therefore the results presented in this study could even be an upper bound of what can potentially be observed in the current solar minimum. Although this particular model in its current form does not address the radiation health risks posed by intermittent solar particle events, it may prove a useful tool in long-duration space mission planing, where exposure to cosmic-ray radiation remains a challenge and a hazard to be mitigated.

In **Chapter 4** it is shown that using latitude-dependent turbulence quantities calculated using a turbulence transport model as inputs for theoretically well-motivated diffusion and drift coefficients naturally leads to a reduction in computed latitude gradients, without making any assumptions as to anisotropic perpendicular diffusion coefficients as is usually done in the literature [see, e.g., *Burger et al.*, 2000]. However, the choice of a pure Parker magnetic field, without any azimuthal dependences, means that the model still computes zero relative amplitudes, contrary to the observations reported by *Zhang* [1997]. It would be interesting to see if the future implementation of a *Fisk* [1996]-type field changes these results.

It is also demonstrated that three orders of magnitude more computational resources are needed to calculate relative amplitudes than to calculate spot differential intensity spectra. It is therefore important to take advantage of the flexibility of the SDE solver to optimize for specific research problems within the field of numerical cosmic-ray modulation studies. Overall the model is demonstrated to be ideally suited to execution on parallel computing architectures. Due to the fact that defined variables are not stored on a grid (as is the case with finite difference schemes), but are continuously updated along the trajectory of a pseudo-particle, the model requires very little memory and thus very little to almost no communication between the different nodes or compute cores. Therefore, as expected from a stochastic solver, the code scales well when executed on the Lengau cluster at the CHPC, even when a realistic, computationally-expensive set-up is used.

Finally, a three-dimensional, fully time-dependent *ab initio* cosmic ray modulation model was introduced in **Chapter 5**. This model employs, as a first approach, simple observationally-motivated temporal scalings for large scale heliospheric quantities such as the HMF magnitude, tilt angle, and solar wind speed profile, as well as for turbulence quantities such as the magnetic variances and correlation scales. Spatial dependences for basic turbulence quantities are modelled using parametric fits to outputs from the *Zank et al.* [2017] turbulence transport model, and the QLT/NLGC diffusion coefficients employed by *Moloto et al.* [2018] were utilised. Galactic CR proton differential intensities calculated using these scalings for the period extending from 1977 to 2001 are in reasonable to good agreement with spacecraft observations, reproducing the major salient features of the observed CR intensity temporal profile.

The relative importance of drift effects on cosmic ray modulation in the pre-space age era were tested by employing historic magnetic field magnitudes derived from calculations based on observed cosmogenic nuclide counts presented by *McCracken and Beer* [2015] and tilt angles reconstructed using sunspot observations as a temporal proxy. These results displayed a clear signature of drift effects, yielding the characteristic peak/plateau temporal profiles seen during periods of negative/positive magnetic polarity in space age GCR observations. The intensity profiles also peak during the Dalton minimum as would be expected from the inverse relation to solar cycle activity. This leads to the important conclusion that drift effects cannot be ignored when endeavouring to estimate historic changes in the HMF magnitude by modelling cosmic ray fluxes in the past. The importance of drift effects also implies the need to revisit previous estimates of the historic behaviour of the HMF magnitude based on the force field solution to the Parker TPE, as this one-dimensional approach cannot *a priori* take into account drift effects. Possible refinements and improvements to the model include the incorporation of more recent developments as to models for the diffusion coefficients, an improved way of dealing with current sheet drift and the consideration of the modulation of heavier elements in the model.

To conclude, the study of long-term cosmic ray modulation requires a self-consistent, physics-first approach for dealing with the various large and small scale plasma quantities that govern the transport of cosmic rays in the heliosphere, as well as the transport parameters such as diffusion and drift coefficients. These quantities are the main drivers of cosmic-ray modulation over time scales associated with the solar activity cycle and the solar magnetic cycle, and their influence on cosmic-ray modulation over the long-term cannot be understated.

References

Burger, R. A., M. S. Potgieter, and B. Heber, Rigidity dependence of cosmic ray proton latitudinal gradients measured by the Ulysses spacecraft: Implications for the diffusion tensor, *J. Geophys. Res.*, *105*, 27,447–27,455, 2000.

Engelbrecht, N. E., and R. A. Burger, A comparison of turbulence-reduced drift coefficients of importance for the modulation of galactic cosmic-ray protons in the supersonic solar wind, *55*, 390–400, doi:10.1016/j.asr.2014.09.019, 2015.

Fisk, L. A., Motion of the footpoints of heliospheric magnetic field lines at the Sun: Implications for recurrent energetic particle events at high heliographic latitudes, *J. Geophys. Res.*, *101*, 15,547–15,553, 1996.

McCracken, K. G., and J. Beer, The Annual Cosmic-Radiation Intensities 1391 - 2014; The Annual Heliospheric Magnetic Field Strengths 1391 - 1983, and Identification of Solar Cosmic-Ray Events in the Cosmogenic Record 1800 - 1983, *Solar Phys.*, *290*(10), 3051–3069, doi:10.1007/s11207-015-0777-x, 2015.

Miyake, S., R. Kataoka, and T. Sato, Cosmic ray modulation and radiation dose of aircrews during the solar cycle 24/25, *Space Weather*, *15*(4), 589–605, doi:10.1002/2016SW001588, 2017.

Moloto, K. D., N. E. Engelbrecht, and R. A. Burger, A Simplified Ab Initio Cosmic-ray Modulation Model with Simulated Time Dependence and Predictive Capability, *Astrophys. J.*, *859*(2), 107, doi:10.3847/1538-4357/aac174, 2018.

Webber, W. R., A. C. Cummings, F. B. McDonald, E. C. Stone, B. Heikkila, and N. Lal, Galactic cosmic ray H and He nuclei energy spectra measured by Voyagers 1 and 2 near the heliospheric termination shock in positive and negative solar magnetic polarity cycles, *J. Geophys. Res.*, *113*(A10), A10108, doi:10.1029/2008JA013395, 2008.

Zank, G. P., L. Adhikari, P. Hunana, D. Shiota, R. Bruno, and D. Telloni, Theory and transport of nearly incompressible magnetohydrodynamic turbulence, *Astrophys. J.*, *835*, 147, doi:10.3847/1538-4357/835/2/147, 2017.

Zhang, M., A linear relationship between the latitude gradient and 26 day recurrent variation in the fluxes of galactic cosmic rays and anomalous nuclear components. I. Observations, *Astrophys. J.*, *488*(2), 841–853, 1997.